ON THE ORIGINS OF COSMIC DUST AND THE EVOLUTION OF NEARBY GALAXIES WITH THE HERSCHEL SPACE OBSERVATORY

by

Christopher Jonathan Redfern Clark

A THESIS SUBMITTED TO CARDIFF UNIVERSITY
FOR THE DEGREE OF DOCTOR OF PHILOSOPHY

OCTOBER 2014

‘Beep. Beep. Beep.’

Sputnik I

DEDICATION

'God does not play dice.'

ALBERT EINSTEIN

'Einstein, stop telling God what to do with his dice.'

NIELS BOHR

WELL, here's the part of the thesis where traditionally I'm supposed to tearfully wax lyrical about all the wonderful people in my life, without whom I would not be where I am today[1]. And, well, who am I to go against tradition?

At the risk of sounding like I'm working my way through a stereotypical award ceremony acceptance speech, I really *do* want to thank my Mum and Dad. They did an excellent good job of raising a unrepentant contrarian, determined to find things out for himself, and bloody well make up his own damn mind – and for that I am very grateful. I'm similarly thankful to Grandad, who did his utmost to to get me interested in science (with a pretty decent degree of success, by the looks of it), and to Nana, whose patience and level-headedness have served as an inspiration (when dealing with both intractable scientific problems, and equally-intractable undergraduate students).

Cardiff has been my brilliant home for the past 7 years, and the Cardiff University School of Physics and Astronomy has been a fantastic place to study. In

---

[1] Namely, a drained, quasi-human husk who dreams in Python and LaTeX. Honestly, a few days ago I was woken by my alarm clock, and whilst struggling to turn it off I grumbled, 'Ugh, why won't it compile?'

particular, I cannot image a better, or more welcoming, working environment than the galaxies office. There has always been someone happy to lend a hand on those occasions when science has decided to be a particularly vexatious mistress. More importantly, my splendid officemates have provided a steady stream of persiflage, office golf™, internet quizzes, bizarre Christmas presents, and – best of all – cat videos[2]. So thank you Andreas, Chris, Eliabetta, Ezzy, George, Mat, Olivia, and Simon; with particular thanks to Matt and Robbie, the invaluable gurus-over-my-shoulder, whose boundless knowledge I have relied upon throughout[3]. I would, however, like to take this oppertunty to express my unending disdain and limitless contempt for `Frodo` (my computer); when the time comes for you to pass to the great office in the sky, I hope to be the one who sends you – preferably by means of a great big sledgehammer[4]. Although I suspect that the omnipotent computing support dynamic duo of Richard and Rodney might object.

The postgrads and postdocs of this department have made my time as a PhD student a happy one. The institutions of coffee time, cake day™, postgrad lunch, and Friday pub have become pillars of my week. Without you all, my time here would not have been half so memorable as it has been, so thank you Andrew, Chris, Ciara[5], Craig, Dave, Dave, Duncan, Edward, Ellis, Erin, Frank, Fraser, Geraint, Gernot, Ian, Jo[6], Laura[7], Mark, Mark, Martyn, Matt, Maxime, Oli[8], Patricia[9], Peri, Pete, Peter, Ryan, Sam, Seamus, Seb, Scott, Tom, Tom, Tom, and all of the other people I have no doubt neglected to include. I should also say that amongst the great unwashed hoards of undergraduates who insist upon clogging up the department's corridors for half the year, there are a few diamonds in the rough who it has been my pleasure to teach and know. And, of course, I would be utterly mad if I didn't pay tribute to the admin and technical staff of department, its true puppet-masters, without whom we would long ago all have died of dysentery or somesuch; particular thanks to Steven, who is officially the best lab technician in

---

[2] `https://new.livestream.com/FosterKittenCam`

[3] Or, in Robbie's case, until he ran off to the loving, cash-filled embrace of industry.

[4] Wreathed in flame.

[5] Pseudo-benevolent ruler of Obs Tech.

[6] And her chocolate brownies.

[7] Cake Queen extraordinaire

[8] King of pulchritudinous shirts.

[9] Sponsored by Old Rosie.

the country[10], and Nicola, who is no doubt already plotting to get me helping out at UCAS days again.

I have also benefited immensely from the wisdom of the department's academic staff, both as an undergraduate and postgraduate. Steve Eales and Jon Davies have freely shared their vast expertise (and delicious post-hike barbecued food) throughout; whilst Mike Disney has always been on hand to remind us all that no matter what it is about the Universe you're trying to understand, there's no doubt a whole bunch low-surface-brightness galaxies totally messing up your findings.

No discussion of the academics to whom I owe a great deal would be complete without mention of Loretta Dunne. Her contribution to global intercontinental email traffic has been truly astounding – but no less so than her insight and guidance, which have no doubt have made me a better scientist. I would also like to mention the marvellous people of .Astronomy[11]; a community which has made me continually consider what sort of astronomer I want to be. And I'm grateful to my examiners, Steven Phillipps and Enzo Pascale, for the improvements to this thesis that have arisen from their comments.

This list would be woefully incomplete without mention of the fellow physics students who made my undergraduate degree so enjoyable[12]. Likewise, the people I've lived with during my time in Cardiff (namely Amlyn, Becca, Huw, Ian, Jake, Jonny, Megan, Nye, Penny, Phil, and Ruth) have kept my life outside physics thoroughly entertaining.

Last, but quite the opposite of least, my heartfelt gratitude goes out to my supervisor, Haley Gomez. Despite knowing full well what she was letting herself in for, she took me on as her student, and has been the most magnificent teacher I could possibly hope for – tolerating my stubbornness, know-it-all-ism, and fondness for really rather odd sentence structure. Thank you so very much.

Well, I suppose there's nothing left now except to actually, you know, get on with the thesis. For those of you who can't be bothered to slog through all ~ 250 pages, Figures 6.7 and 3.2 are really quite spectacularly lurid, Chapter 3 is mostly pretty pictures, and Figures 7.9 and 7.11 more or less explain everything.

---

[10] `http://www.astro.cardiff.ac.uk/newsandevents/?page=news_detail&news=0141`

[11] `http://dotastronomy.com/`

[12] No, I'm not listing all of you by name, for you are legion.

ACKNOWLEDGEMENTS

'If I have seen further, it is by standing on the shoulders of giants.'

SIR ISAAC NEWTON

THIS work was made possible by support from the STFC Doctoral Training Grant scheme – and by extension, the kind people of the United Kingdom. This work made use of the invaluable Astropy[13], a community-developed core Python package for astronomy (Astropy Collaboration et al., 2013). The beautiful images of shiny spacey things found in this work were achieved by means of APLpy[14], an open-source astronomical image plotting package for Python. Despite being an oft-frustrating tool (open-source documentation has its downsides), the plots that fill this work were made possible by MatPlotLib[15] (Hunter, 2007). There are precious few sums in this work that weren't done by means of NumPy[16] (Walt et al., 2011) and SciPy[17]. This work made quite frankly gratuitous use of TOPCAT[18] (Taylor, 2005), which was initially developed under the UK Starlink project, and has since been supported by PPARC, the VOTech project, the AstroGrid project, the AIDA project, the STFC, the GAVO project, the European Space Agency, and the GENIUS project. Also used, and much appreciated, were the invaluable SIMBAD[19] database (Wenger et al., 2000) and the VizieR[20] catalogue

---

[13] `http://www.astropy.org/`
[14] `http://aplpy.github.io/`
[15] `http://matplotlib.org/`
[16] `http://www.numpy.org/`
[17] `http://www.scipy.org/`
[18] `http://www.star.bris.ac.uk/~mbt/topcat/`
[19] `http://simbad.u-strasbg.fr/simbad/`
[20] `http://vizier.u-strasbg.fr/viz-bin/VizieR`

access tool (Ochsenbein et al., 2000), both operated at CDS, Strasbourg, France. In the course of this work, observations of objects near and far were viewed in SAOImage DS9[21], developed by the Smithsonian Astrophysical Observatory with support from the Chandra X-ray Science Center (CXC), the High Energy Astrophysics Science Archive Center (HEASARC), and the JWST Mission office at the Space Telescope Science Institute (STSI). And despite its 1990s stylings, use was made of the NASA/IPAC Extragalactic Database (NED[22]), along with the slightly more 21st century NASA/IPAC Infrared Science Archive (IRSA[23]), both of which are operated by the Jet Propulsion Laboratory, California Institute of Technology, under contract with the National Aeronautics and Space Administration.

H-ATLAS[24] is a project with *Herschel*, which is an ESA space observatory with science instruments provided by European-led Principal Investigator consortia and with important participation from NASA. GAMA[25] is a joint European-Australasian project based around a spectroscopic campaign using the Anglo-Australian Telescope. The GAMA input catalogue is based on data taken from the Sloan Digital Sky Survey and the UKIRT Infrared Deep Sky Survey. Complementary imaging of the GAMA regions is being obtained by a number of independent survey programs including GALEX MIS, VST KIDS, VISTA VIKING, WISE, *Herschel*-ATLAS, GMRT, and ASKAP, providing UV to radio coverage. GAMA is funded by the STFC (UK), the ARC (Australia), the AAO, and the participating institutions.

I gratefully acknowledge Martha Haynes, Riccardo Giovanelli, and the ALFALFA team for supplying the latest ALFALFA survey data, and I kindly thank Tracey DeLaney, Marcel Clemens, Luca Cortese, Allison Kirkpatrick, Ivan Baldry, and Lee Kelvin for helpful conversations.

---

[21] `http://ds9.si.edu/site/Home.html`

[22] `http://ned.ipac.caltech.edu/`

[23] `http://irsa.ipac.caltech.edu/frontpage/`

[24] `http://www.h-atlas.org/`

[25] `http://www.gama-survey.org/`

PUBLICATIONS

> *'Reading maketh a full man; conference a ready man; and writing an exact man.'*
>
> FRANCIS BACON

FIRST AUTHOR

Clark C. J. R., Gomez H. L., Dunne L., et al., 2014, *A Blind Survey of the Local Dusty Universe with Herschel-ATLAS*, in proceedings of 'The Life Cycle of Dust in the Universe', PoS, LCDU2013, 073

Clark C. J. R., Dunne L., Gomez H. L., et al., 2014, *Herschel-ATLAS: The Surprising Diversity of Dust-Selected Galaxies in the Local Submillimetre Universe*, submitted to MNRAS

SECOND AUTHOR

[26]Gomez H. L., Clark C. J. R., Nozawa T., et al., 2012, *Dust in Historical Galactic Type-Ia Supernova Remnants with Herschel*, MNRAS, 420, 3557

CO-AUTHOR

[27]Gomez H. L., Krause H. O., Barlow M. J., Swinyard B. M., Owen P. J., Clark C. J. R., et al., 2012, *A Cool Dust Factory in the Crab Nebula: A Herschel Study of the Filaments*, ApJ, 760, 96

---

[26] Lead scientist.

[27] Important scientific contributions.

López-Caniego M., González-Nuevo J., Massardi M., et al., 2013, *Mining the Herschel-ATLAS: submillimetre-selected blazars in equatorial fields*, MNRAS, 430, 1566

Agius N. K., Sansom A. E., Popescu C. C., et al., 2013, *GAMA/H-ATLAS: linking the properties of submm detected and undetected early-type galaxies: I. z 0.06 sample*, MNRAS, 431, 1929

[28]Bourne N., Dunne L., Bendo G. J., Smith M. W. L., Clark C. J. R., et al., 2013, *Herschel-ATLAS: correlations between dust and gas in local submm-selected galaxies*, MNRAS, 436, 479

Peason E. A., Eales S. A., Dunne L., *Herschel-ATLAS: estimating redshifts of Herschel sources from sub-mm fluxes*, MNRAS 435 2753

Eales A., Fullard A., Smith M. W. L., Baldry I., Bourne N., et al., 2014, *Over 80% of all the stars in the Universe formed in disks*, submitted to Science

[29]de Vis P., Dunne L., Maddox S., Clark C. J. R., et al., 2014, *Gas, Dust, and Stars: Building the Relations for Galaxy Evolution*, in prep.

---

[28] Important scientific contributions.

[29] Important scientific contributions.

ABSTRACT

USING multiwavelength observations, centred around the unique far-infrared and submillimetre window provided by the *Herschel* Space Observatory, this thesis investigates the origins and evolution of cosmic dust in the local Universe – by examining individual sources of dust in our own galaxy, and by studying dust in nearby galaxies.

Herschel observations of the remnants of Kepler's (SN1604) and Tycho's (SN1572) supernovæ, both Type-Ia explosions, are searched for evidence of dust creation by these events. Being the only Type-Ia supernovæ known to have occurred in our Galaxy within the past 1,000 years, these remnants are the only ones both close enough to resolve, and young enough that they are dominated by their ejecta dynamics. There is no indication of any recently manufactured dust associated with either supernova remnant. It therefore appears that Type-Ia supernovæ do not contribute significantly to the dust budgets of galaxies.

The Crab Nebula, the result of a Type-II supernova (SN1054), is also investigated using *Herschel* and multiwavelength data. After accounting for other sources of emission, a temperature of $T_d = 63.1\,\mathrm{K}$ and mass of $M_d = 0.21\,\mathrm{M}_\odot$ is derived for the Crab Nebula's dust component. A map of the distribution of dust in the Crab Nebula, the first of its kind, is created by means of a resolved component separation, revealing that the dust is located in the dense filamentary ejecta. We can be confident that this dust will survive in the long term, and be injected into the galactic dust budget. This is the first detection of manufactured supernova dust for which this can be said.

I next use the *Herschel*-ATLAS to assemble HAPLESS: the *Herschel*-ATLAS Phase-1 Limited Extent Spatial Sample – a blind, volume-limited, dust-selected sample of nearby galaxies. The majority of this sample is made up of curious very blue galaxies. Often irregular and/or flocculent in morphology, with extremely

blue UV-NIR colours, these galaxies appear to be prominent in the local dusty universe.

In the absence of reliable photometry for the HAPLESS galaxies, I describe the function and testing of a purpose-built photometric pipeline – CAAPR: Chris' Adequate Aperture Photometry Routine. The photometry conducted with CAAPR exhibits flux greater by factors of, on average, 1.6 in the FUV and 1.4 in *r*-band, relative to the previously-available photometry.

In comparison to other surveys of dust in local galaxies, the HAPLESS systems show a strong propensity towards very late morphological types and extremely blue FUV-K_S colours. The dust in the HAPLESS galaxies appears to be very cold, with a median temperature of 14.6 K. They are also exceptionally dust rich, with a median dust mass of $5.3 \times 10^6\,\mathrm{M_\odot}$, and a median $M_d/M_\star$ of 4.4×10^{-3} – greater by a factor of 1.8–3.7 than that seen in other local surveys. The curious very blue HAPLESS galaxies, whilst accounting for only 6% of the stellar mass in our sample, contain over 35% of the dust mass. I show that the more dust-rich a galaxy (as defined by $M_d/M_\star$), the *smaller* the fraction of its UV luminosity that suffers dust absorption – this effect is observed to be particularly dramatic in the case of the curious very blue objects. Either the emissivity or geometry of the dust in these systems must be highly unusual.

HAPLESS suggests a dust mass volume density of the local universe of $(3.7 \pm 0.7) \times 10^5\,\mathrm{M_\odot\,Mpc^{-3}}$; the largest value reported to date. The HAPLESS 250 µm luminosity function is in good agreement with surveys of far larger volumes, suggesting that we do not sample an over-dense region of space.

The HAPLESS galaxies are extraordinarily gas rich; the median HAPLESS gas fraction is 0.52, and 19% of the sample have gas fractions > 0.8. The median HAPLESS gas-to-dust ratio is ≈ 260, 2–3 times larger than in other local surveys. The very blue galaxies of the sample are found to be particularly gas rich; a chemical and dust evolution model indicates that they are at an early stage of converting their gas into stars. A dust-selected survey such as *H*-ATLAS is a particularly efficient way of identifying young systems of this kind, which should therefore provide valuable insights into the chemical evolution of young galaxies.

CONTENTS

LIST OF TABLES

LIST OF FIGURES

CHAPTER 1
INTRODUCTION

> *'An object may not only contain stars, but also nebulosity not composed of them.'*
>
> SIR WILLIAM HERSCHEL

HALF of all the photons emitted by stars since the Big Bang have been absorbed by grains of cosmic dust. In the space of a century, dust has gone from being a nuisance, an obstacle in the way of conducting 'real' astronomy, to becoming one of the most powerful ways we have of understanding the evolution of matter.

Dust enshrouds some of the most fascinating and important environments in the Universe. New stars are born in dense interstellar clouds, impenetrable to optical light due to the effects of dust. The optical and ultraviolet emission of the most aggressively star-forming galaxies in the Universe is almost totally obscured by the large amounts of dust they contain. But as dust absorbs these shorter wavelengths of light, it thermally re-radiates them at longer, far-infrared and submillimetre wavelengths – to which dust is entirely transparent. So by observing this longer-wavelength emission we have a way to retrieve the 'stolen starlight' and probe regions of space that were hitherto hidden from view.

Dust also provides us with a way to understand the chemical evolution of the universe, in which it plays a vital role. The Big Bang created only the simplest of elements; hydrogen, helium, and lithium. All of the heavier elements in existence today – the so-called 'metals' – were forged by the lives, and deaths, of stars. It is in the deaths-throes of stars that dust is made; and of all the atoms of heavy elements found in interstellar space, half are locked up in dust (Whittet, 1992).

FIGURE 1.1 The Andromeda Galaxy, as it appears in optical (*upper*), showing emission primarily from stars, and in the submillimetre (*lower*), showing the emission from dust. The dust lanes stand out as being dark in the optical; absorbing the light from the stars located behind them, and the star-formation occurring within them. Reproduced from Smith et al. (2012b), with permission.

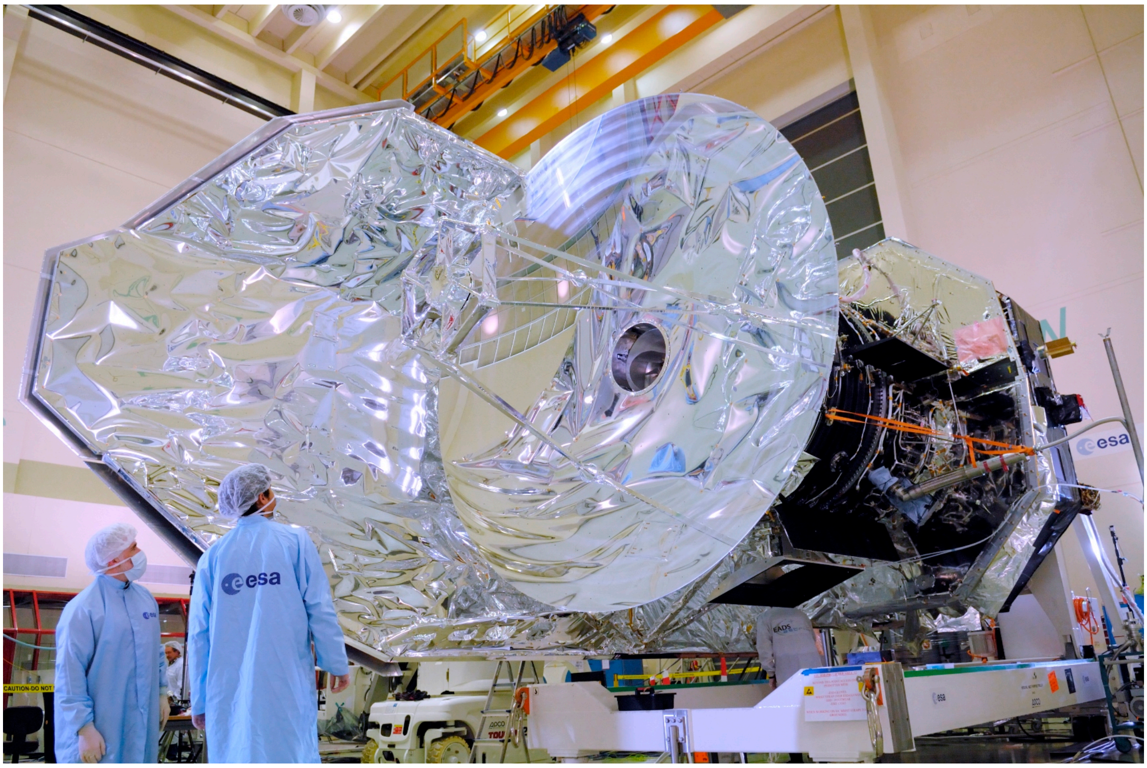

FIGURE 1.2 *Herschel* in the final stages of construction at the European Space Technology and Engineering Centre (ESTEC) in Noorwijk, the Netherlands. Image credit: ESA.

Dust is also vital for converting basic elements into complex molecules. It catalyses the formation of molecular hydrogen (Gould & Salpeter, 1963), the raw material from which stars are made; and most of the water in the Universe was formed on the surface of dust grains. So as well as serving as a window with which to watch the births of stars, dust also enables that very process, and furthermore acts as the production site, and reservoir, of the complex materials which go on to to form planets around those stars – and whatever life they carry.

In this thesis, I use far-infrared and submillimetre observations, undertaken by the *Herschel* Space Observatory, to investigate the origins and evolution of dust in galaxies.

1.1 THE HERSCHEL SPACE OBSERVATORY

The *Herschel* Space Obervatory (Pilbratt et al., 2010), operated by the European Space Agency (ESA), was launched on 14th May 2009. *Herschel* is the largest telescope ever sent into space; its 3.5 m primary mirror (see Figure 1.2) has a diameter 50% greater than (therefore providing more than double the collecting area of)

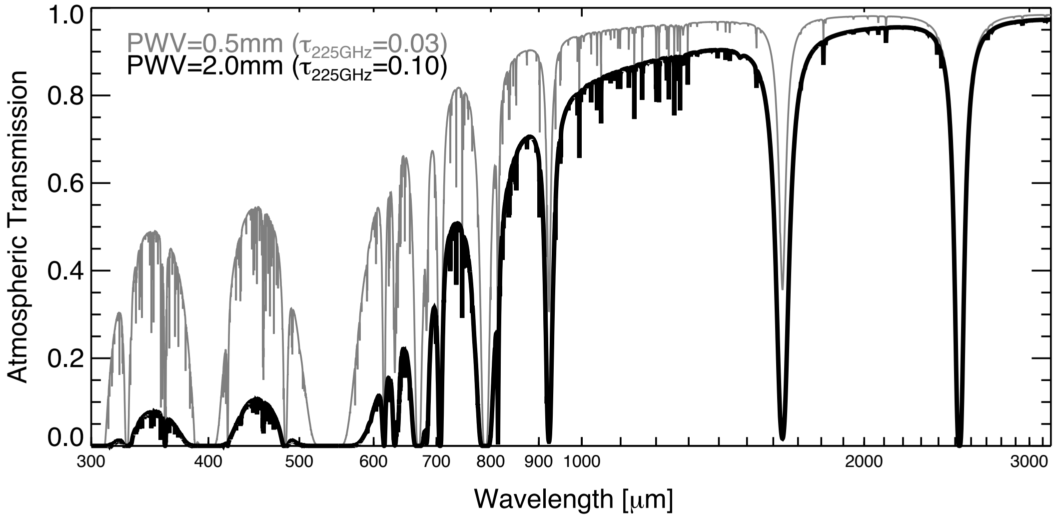

FIGURE 1.3 The atmospheric transmission of submm and mm wavelengths at the summit of Mauna Kea, one of the best locations on Earth for observations in this part of the spectrum. There are limited atmospheric windows available, and they are mostly at longer wavelengths – where dust emission is typically many times fainter (Section 1.2.1) than at shorter wavelengths, at which observations are either even more difficult, or altogether impossible. Below the 300 μm x-axis limit of this plot, in the FIR regime, transmission is essentially nil until wavelengths of $\lesssim$25 μm. Note the extreme dependence of submm atmospheric transmission upon the level of Precipitable Water Vapour (PWV) in the atmosphere, as indicated by the two lines plotted. Note also that both of the lines represent *exceptionally good* observing conditions – optical depths of $\tau_{225} \leq 0.1$ (the black line) account for < 10% of nights on Mauna Kea, whilst conditions as good as $\tau_{225} \leq 0.03$ (the grey line) are extremely rare, representing the best few nights each year. Reproduced from Casey et al. (2014), with permission.

the 2.4 m primary mirror of the *Hubble* Space Telescope, the previous record holder. The justification for *Herschel*'s exceptionally large mirror, and the reason it was necessary for the telescope to operate in space, is the nature of the Far-InfraRed (FIR, $50 \gtrsim \lambda \gtrsim 200$ μm) and sub-millimetre (submm, $200 \gtrsim \lambda \gtrsim 1000$ μm) wavelengths *Herschel* is designed to observe.

The FIR and submm wavelength range is the region of the electromagnetic spectrum that encompasses the emission from the 90% (Devereux & Young, 1990) of cosmic dust (Section 1.2) too cold to be detected at shorter InfraRed (IR) wavelengths. However, these wavelengths are notoriously difficult to observe (Swinyard & Wild, 2010). Some atmospheric windows exist in the submm regime, allowing limited observations to be made from exceptionally arid, high-altitude Earth-based sites such as the Atacama Plateau, and summit of Mauna Kea, as illustrated in Figure 1.3. However, even when observing at the best-suited locations on the planet, significant levels of atmospheric absorption and background emission must still be overcome. In the FIR, however, observations remain impossible, even from locations such as these. Moreover, atmosphere notwithstanding, it is more difficult to create instrumentation capable of detecting astronomical FIR and submm emission than for any other part of the spectrum (Section 1.1.1). As a result of these difficulties, the FIR and submm represent the last part of the electromagnetic spectrum to be explored by astronomers.

Herschel represents a major advance in FIR and submm astronomy. Named for 18th Century astronomer Sir William Herschel, the discoverer of infrared light (and one of the first astronomers to consider objects beyond our Solar System worthy of serious study), the design concept for *Herschel* was first proposed in 1982, and selected in 1993 to be the fourth cornerstone mission of ESA's science program. The 3.5 m diameter of the primary mirror is over 4 times greater than that of any previous orbital telescope operating in this wavelength range, and was limited only by the space available inside the Ariane V rocket used to launch *Herschel* into orbit.

Having the largest possible mirror is a vital aspect of *Herschel*'s design – an aperture of a given size will have diffraction-limited resolution $\sim$1,000 times worse at submm wavelengths than it will in the optical. *Herschel* requires the best possible resolution not only to permit the study of objects of smaller angular sizes, but also for the sake of sensitivity. Observations at poor angular resolution are particularly susceptible to confusion noise – the effect whereby unresolved sources (such as distant galaxies) 'overlap', preventing the detection of individual objects fainter than a certain limit. Sharper images, provided by improved resolution, reduce this effect.

Observations at submm wavelengths are especially vulnerable to confusion noise due to negative k-correction – a phenomena which causes distant objects to appear as bright as more nearby sources. Naïvely, the apparent brightness of an object decreases with the inverse square of its distance. But for a typical submm source, a progressively more luminous part of the Spectral Energy Distribution (SED) will be sampled (at a given wavelength of observation) as the SED gets redshifted – counteracting the effect of a source's distance. By making distant objects appear as bright as those nearby, negative k-correction dramatically increases the number of distant galaxies that can be detected by *Herschel* at a given observational depth. Whilst this is hugely beneficial to the study of the early universe, it also has the effect of worsening confusion noise.

In order to further increase the sensitivity it can achieve, *Herschel*'s instruments are cooled to extremely low temperatures. Instrumental noise is a significant problem for FIR and submm telescopes. Observing in the FIR and submm allows us to detect the thermal emission from objects at temperatures of $\lesssim 100\,\mathrm{K}$; however, this includes the temperature of *Herschel* itself. *Herschel* therefore emits light in the very wavelengths it is designed to detect. This has been compared to trying to detect optical light using a camera that is on fire. To mitigate this effect, *Herschel*'s instruments are cooled using a multi-stage cryostat; the bulk of the instrumentation operates at 1.7 K, whilst the detectors are cooled to an operating temperature of 300 mK; cold enough that their own FIR and submm thermal emission is rendered minimal, greatly reducing instrumental noise (the 85 K primary mirror actually represents the primary source of instrumental noise during normal operation). This cooling is achieved using a reservoir of liquid helium that gradually boils away into space, taking with it the small amounts of heat that *Herschel* generates though its operation, and absorbs from the Sun (which is itself minimised by means of a sunshield). However, this reservoir is limited, and dictates the lifetime of *Herschel*'s mission – the last of the liquid helium was exhausted on 29th April 2013, almost 4 years after launch.

1.1.1 HERSCHEL'S INSTRUMENTS

Herschel carries three instruments – SPIRE, PACS, and HIFI – which in combination provide full photometric and spectroscopic coverage of the 52–670 µm wavelength range. Here, for completeness, I describe all of the instruments on board *Herschel*; however, only data from the photometers is used in this work.

1.1.1.1 HIFI

The Heterodyne Instrument for the Far-Infrared (HIFI, de Graauw et al., 2010) is *Herschel*'s dedicated spectrometer. HIFI observed across two wavelength ranges, 157–212 µm and 240–625 µm, at a spectral resolution of $\lambda / \Delta\lambda \sim 10^7$. HIFI was designed to study the astrochemistry of the densest regions of the InterStellar Medium (ISM), where effectively all short-wavelength photons are absorbed, by studying the FIR cooling lines of the various atomic and molecular species found there. HIFI was also well-suited to the study of cool Solar System objects.

1.1.1.2 SPIRE

The Spectral and Photometric Imaging REceiver (SPIRE[1], Griffin et al., 2010) is *Herschel*'s longest-wavelength instrument, designed to observe in the hitherto under-exploited submm regime, across a wavelength range of 190–670 μm. This wavelength range covers the beginning of the Rayleigh-Jeans slope of cold interstellar dust, allowing for the accurate determination of dust temperatures, and permitting SPIRE to take full advantage of the effects of negative k-correction. SPIRE consists of both a spectrometer and photometer; in both cases, the detectors used are bolometers.

As previously described, the submm is an extremely difficult part of the spectrum in which to conduct observations. At shorter wavelengths, it is possible to use photoconductors, instruments for which the amount of incident radiation alters the electrical conductivity of the detector, an effect which can be measured. However, in order for photoconductors to function, the energy of the incident photons must be at least as great as the energy required to excite an electron across the photoconductor's band gap. However, the long wavelength of submm photons means that they posses insufficient energy to achieve this. At wavelengths longer than the submm, it becomes possible to use antennae to detect incident radiation. However, the submm lies in the gap in between the wavelength ranges covered by these two detection methods.

Bolometery was the best technique available for performing submm astronomy when *Herschel* was designed, and is the detection method employed by SPIRE. A bolometer absorbs incoming radiation; the absorbing element will typically be a thermistor cooled to an extremely low temperature, such that even small amounts of low-energy incident radiation are sufficient to raise the temperature of the absorber enough to change the resistive properties of the thermistor to a measurable degree.

The bolometers used by SPIRE are of a spider-web design, which maximises the detector's collecting area, whilst minimising the overall bulk. This reduces the heat capacity of each element, thereby increasing both the sensitivity and response time of the detector. Spider-web architecture also has the benefit of reducing the detector cross-section to cosmic rays, which give rise to artefacts in the instrument output. Spider-web bolometers are employed for both SPIRE's photometer and spectrometer.

---

[1] `http://herschel.esac.esa.int/twiki/bin/view/Public/SpireCalibrationWeb`

The SPIRE spectrometer is a Fourier Transform Spectrometer (FTS); a mirror in the light path shifts position, causing different wavelengths of light to to undergo different modes of interference. The varying intensity of light being transmitted by the mirror as it moves encodes the spectrum of the band being observed. The SPIRE FTS observes in two overlapping bands, spanning 194–313 μm and 303–671 μm, with a spectral resolution of $\lambda/\Delta\lambda \sim$ 370–1300. Each band employs an array of bolometers to provide resolved spectroscopy of the target region.

The SPIRE photometer observes in three wavebands, each with a bandwidth $\lambda/\Delta\lambda \sim 3$. These bands have approximate central wavelengths of 250, 350, and 500 μm, observed with arrays of 139, 88, and 45 bolometers respectively. SPIRE uses dichoric (Ade et al., 2006) beam-splitters to observe in all three photometric bands simultaneously. The SPIRE photometer has a $8' \times 4'$ field of view, although a full sampling of the field requires the instrument to scan across the target area, continuously taking observations. The key parameters of each of SPIRE's photometric bands are given in Table 1.1.

The SPIRE photometer can observe in several different modes. Small map mode provides coverage of a $5'$ region of sky (plus high-noise turnaround regions to the edges), making it suitable only for individual point or slightly-extended sources; small maps are always scanned at a speed of $30''\,\mathrm{s}^{-1}$. Large map mode allows the coverage of arbitrarily-sized regions of sky; large maps can either be scanned at a normal speed of $30''\,\mathrm{s}^{-1}$, or a fast speed of $60''\,\mathrm{s}^{-1}$. The SPIRE photometer can also be operated in parallel with the PACS photometer (Section 1.1.1.3). When observing large areas of sky, parallel mode allows a given observational depth to be achieved with both instruments far more quickly than would be possible using one instrument, then the other. Mapping in parallel mode proceeds similarly to large map mode, with a slight change in scan direction to allow optimal sampling of both the PACS and SPIRE bolometer arrays. Parallel mode mapping can be conducted at fast speed of $60''\,\mathrm{s}^{-1}$, or a slow speed of $20''\,\mathrm{s}^{-1}$.

SPIRE maps are typically produced by performing orthogonal scans over the region of interest; doing so allows any time-variant noise associated with the detector to be removed from the final map.

TABLE 1.1 The key properties of the photometric bands provided by the PACS and SPIRE instruments on board *Herschel*. In each PACS band, the PSF characteristics differ depending upon mapping mode, and are stated for three cases, in the following order: slow scan mapping mode ($20'' \, \mathrm{s}^{-1}$), fast scan mapping mode ($60'' \, \mathrm{s}^{-1}$), and parallel scan mapping mode ($60'' \, \mathrm{s}^{-1}$).

Instrument	Wavelength (µm)	PSF major axis[a] (arcsec)	PSF axial ratio[a]	Pixel size (arcsec)	Calibration error (± %)
PACS	70	5.8 / 9.0 / 12.2	1.06 / 1.55 / 2.11	3.2	12
	100	6.9 / 9.7 / 12.7	1.03 / 1.41 / 1.81	3.2	12
	160	12.1 / 13.3 / 15.7	1.13 / 1.18 / 1.35	6.4	12
SPIRE	250	18.3	1.08	6	7
	350	24.7	1.06	8	7
	500	37.0	1.11	12	7

[a] Note that the PSF depends also upon the pixel size of a given reduction. The values quoted here assume the standard pixel sizes, also listed.

1.1.1.3 PACS

The Photodetector Array Camera and Spectrometer (PACS[2], Poglitsch et al., 2010) is a FIR photometer and spectrometer, that operates across the 60–210 μm wavelength range, where the emission from cold interstellar dust typically peaks; PACS can observe this emission with a resolution vastly exceeding that of any previous FIR observatory – 4 times better than that of *Spitzer* (Werner et al., 2004), and almost 6 times better than that of the InfraRed Astronomical Satellite (IRAS, Neugebauer et al., 1984).

The PACS spectrometer is an Integral Field Unit (IFU) instrument, with spectral resolution of $\lambda / \Delta\lambda \sim 1000$–$4000$. It has a $47'' \times 47''$ field of view, sampled by a 5×5 array of photoconductor spaxels.

The PACS photometer consists of two filled arrays of bolometers; a 2048 element array for observations at shorter wavelengths, and a 512 element array for longer wavelengths. Each array a has $3.5' \times 1.75'$ field of view. Despite having two bolometer arrays, the PACS photometer actually observes in three photometric bands, centred at wavelengths of 70, 100, and 160 μm respectively. The PACS photometer can therefore conduct observations at 160 μm, and either 70 *or* 100 μm at any one time; the desired shorter-wavelength band is selected by means of a filter wheel along the optical path. As such, in order to obtain coverage in all three wavebands, the PACS photometer must observe the region of interest twice (providing double the observing time at 160 μm). The PACS photometric bands have bandwidths in the range $\lambda / \Delta\lambda \sim 2$–$3$. The key parameters of each of the PACS photometric bands are given in Table 1.1.

PACS can conduct mapping in several different scanning modes. Scan mapping mode is the default way of conducting PACS observations. The standard mapping speed is $20''\,\mathrm{s}^{-1}$, with a faster mapping speed of $60''\,\mathrm{s}^{-1}$ also available. Mapping at $60''\,\mathrm{s}^{-1}$ leads to degradation in the Point Spread Function (PSF), increasing both its ellipticity and Full-Width Half-Maximum (FWHM), particularly for the shorter-wavelength band being observed. This arises in part from the 'blurring' caused by the faster scan speed; the particular degradation in the shorter-wavelength band is because adjacent bolometer elements are sampled when producing maps at the faster scanning speed, in order to achieve the necessary sensitivity. As described in Section 1.1.1.2, PACS and SPIRE photometers can conduct mapping in parallel. When operating in parallel, PACS essentially functions in its fast scan mapping mode – however, the PSF degradation is exacerbated over what

---

[2] `http://herschel.esac.esa.int/twiki/bin/view/Public/PacsCalibrationWeb`

is encountered during normal fast scan mapping mode, as the scan direction is not optimised for the orientation of the PACS bolometer arrays. The PACS photometer also has a mini-scan mapping mode, with a scan pattern designed to allow for the smallest practical map size; this produces a $3'$ diameter region of full coverage.

In common with SPIRE, mapping is typically done with orthogonal sets of scans. Not only does this permit the isolation of time-variant instrumental noise, but also reduces the PSF ellipticity that arises when carrying out scans at the faster mapping speed.

1.2 COSMIC DUST

Herschel provides an unparalleled means with which to study the the cold and dense ISM – particularly cosmic dust. Whilst the concept of 'interstellar space' dates to the renaissance (Bacon, 1626), the notion that the space beyond our Solar System might contain more than just stars is relatively recent; William Herschel was one of the first people to suggest the possibility (see the epigraph of this chapter, from Herschel, 1811). The first evidence for the existence of dust (and the ISM) was the discovery by Friedrich von Struve that star counts appear to decrease at increasing distance from the Earth (Struve, 1847). Jacobus Kapteyn posited that this effect could arise from a light-absorbing medium between the stars (Kapteyn, 1909); though he himself did not believe that to be the explanation. It was Robert Trumpler who discovered the wavelength dependence of this 'extinction', leading him to conclude that it was due to grains of solid material in interstellar space, absorbing and scattering the light that passes through it (Trumpler, 1930). For a more detailed history of the understanding of dust, see the introduction to Whittet (1992).

In the past, when all astronomy was conducted at optical wavelengths, dust was considered a nuisance; merely an obstacle to our full understanding of the Universe. To this day, optical and UltraViolet (UV) astronomers go to great lengths to account for the effects of dust on observations (Driver et al., 2007a,b). We now know that this dust is made up of grains ranging in size from $\sim 10\,\mathrm{nm}$ to $\sim 10\,\mu\mathrm{m}$ (Kim et al., 1994; Kim & Martin, 1994), although the precise size distribution is not well constrained (Jones et al., 1996). The majority of the mass of dust consists of C, N O, Mg, Si, and Fe; this is inferred from observations of the gas phase of the ISM, which is found to be highly depleted of these elements (Jenkins, 2009, 2013). The possible chemical combinations of these raw materials lead us to assume that

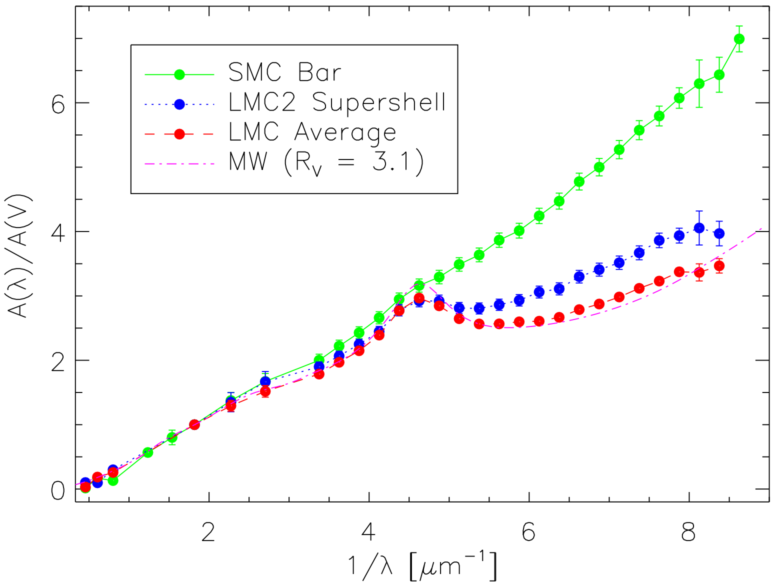

FIGURE 1.4 Extinction curves of the Milky Way and Magellanic Clouds. The term R_V, stated to be 3.1 for the Milky Way, is defined by $R_V = A_V/E(B-V)$ (ie, gives extinction in V-band, relative to the B-V reddening). Reproduced from Gordon et al. (2003), under the Creative Commons Attribution-ShareAlike 3.0 Unported license[3].

dust is fount primarily in two forms, C-rich and O-rich (Jones, 2013). The wavelength dependence of dust extinction can also inform us of the physical nature of dust. Extinction curves, such as the examples shown in Figure 1.4, suggest the presence of a range of grain sizes, similar in size to the wavelengths of UV and optical radiation. However, as can be seen, extinction curves can vary dramatically between galaxies. The 217 nm feature is strong for many galaxies, suggesting it arises from a grain species that arises from a common formation mechanism, and that is well able to survive a wide range of interstellar conditions (Fitzpatrick, 1999; Inoue et al., 2006) – that said, it is often found to be absent in observations of starburst galaxies (Gordon, 2005). Clearly, the nature of dust can vary significantly between environments. It is also important to consider that any extinction due to large dust grains (≥ 0.1 µm) would have only a very weak wavelength dependence in the commonly-studied UV and optical regimes.

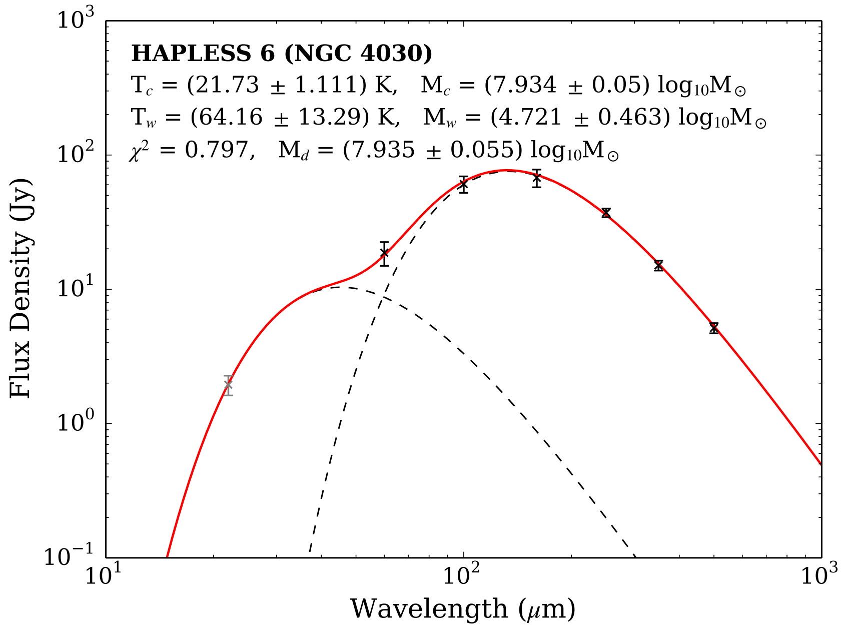

Figure 1.5 The dust SED of the massive spiral galaxy NGC 4030. The dust emission has been modelled (red line) as being the combination of two modified blackbodies (dashed black lines). Taken from Chapter 5.

1.2.1 Emission from Dust

Given the difficulties in studying dust through extinction, *Herschel*'s unparalleled ability to directly study the emission from dust is invaluable. For a blackbody emitter in radiative equilibrium with the local radiation field, the temperature T will be described by the Stefan-Boltzmann law:

$$T^4 = \frac{Uc}{4\sigma} \tag{1.1}$$

where U is the energy density of the local radiation field, c is the speed of light in a vacuum, and σ is the Stefan-Boltzmann constant. Kirchhoffs law (Kirchhoff, 1860) states that the absorptivity and emissivity of a body at a particular frequency are equal. Hence the rate of energy absorption from the local radiation field is also the rate of energy emission by the dust.

The spectrum of a blackbody emitter at a given temperature, as a function of frequency ν, is given by the Planck function:

$$B_\nu(T) = \frac{2h\nu^3}{c^2}\frac{1}{e^{\frac{h\nu}{k_BT}} - 1} \tag{1.2}$$

---

[3] `http://creativecommons.org/licenses/by-sa/3.0/deed.en`

where B_ν is the Planck function spectral radiance, h is the Planck constant, and k_B is the Boltzmann constant.

In the case of a non-ideal emitter, such as dust, the Planck function is modified by a term describing the the efficiency with which it emits. This value, Q_ν, is the ratio of the emitting power of an object at a given equilibrium temperature, to the emitting power of a perfect blackbody at the that same equilibrium temperature, at a given frequency. In the FIR and submm, the wavelength λ in question is far larger than the size of the grains; in this case, the small grain approximation (Bohren & Huffman, 1983) is valid, giving rise to a general relationship of the form:

$$Q_\nu \propto \nu^\beta \propto \lambda^{-\beta} \tag{1.3}$$

where β is the dust emissivity spectral index, dictated by the material that makes up the grain. Hence for an emitter with an efficiency Q_ν, the observed flux is described by a modified blackbody, or 'greybody' (an example of which is plotted in Figure 1.5), described by:

$$S_\nu \propto \nu^\beta B_\nu(T) \tag{1.4}$$

The value of β is generally found to be in the range 1–2 for most forms of dust. Various observational (Dunne & Eales, 2001; Clemens et al., 2013; Smith et al., 2013) and experimental (Demyk et al., 2013) evidence suggests 2 is an appropriate value for β in present-day late-type galaxies. Recent results from *Planck* suggest a typical Milky Way value of 1.65–1.90 (Planck Collaboration et al., 2014a,b). $\beta = 2$ corresponds to metallic and crystalline materials, whilst $\beta = 1$ would be expected for amorphous substances (Tielens & Allamandola, 1987). It is possible to determine the value of β by observing the dust emission SED, as it is the spectral index of the power-law slope of the Rayleigh-Jeans tail. Being a directly-observable physical property of the dust means β can be a valuable probe of dust physics; for example, it can be used study the spatial variation in dust properties in nearby galaxies (Smith et al., 2012b; Tabatabaei et al., 2014). For an equilibrium dust temperature $>25\,$K, emission in the *Herschel*-SPIRE bands is in the Rayleigh-Jeans regime, allowing estimation of β through *Herschel* observations. However, when modelling an observed dust SED, β and the dust temperature are degenerate variables (Kelly et al., 2012). Moreover, for dust temperatures $<25\,$K, or in the presence of dust emission across a range of characteristic temperatures (both of which are commonly the case), emission in *Herschel* wavelengths will not be be described by the Rayleigh-Jeans power law. In such circumstances, longer-wavelength observations are needed to constrain β.

In order to use the observed luminosity of dust emission at a given wavelength to estimate the mass of dust responsible for it, Q_ν must be considered in terms of the physical properties of dust that give rise to the efficiency. Working from the assumption of spherical grains of a constant size, the mass, M_d, of a cloud of n dust grains will be given by:

$$M_d = \frac{4}{3}\pi a^3 \rho n \tag{1.5}$$

where a is grain radius (and hence $\frac{4}{3}\pi a^3$ is the grain volume), and ρ is the mass volume density of the grain material. For grains in radiative equilibrium, the radiative transfer is described by:

$$I_\nu = (1 - e^{-\tau_\nu}) B_\nu(T) \tag{1.6}$$

where I_ν is the spectral radiance, and τ_ν is the optical depth, both at a given frequency ν. Given that dust grains are small in relation to the size of the FIR and submm wavelengths of light they typically emit, we can treat our cloud of dust grains as being optically thin ($\tau_\nu \ll 1$), in which case Equation 1.6 becomes:

$$I_\nu = \tau_\nu B_\nu(T) \tag{1.7}$$

The optical depth itself is:

$$\tau_\nu = \pi a^2 N Q_\nu \tag{1.8}$$

where πa^2 is the grain cross-sectional area, and N is the column density of grains; ie, $N = \frac{n}{A}$ where A is the cross-sectional area of the cloud. To consider the spectral radiance arising from the entire cloud, we therefore substitute Equation 1.8 into Equation 1.7, and multiply by A (thereby expressing it in terms of n), which yields:

$$I_\nu = \pi a^2 n Q_\nu B_\nu(T) \tag{1.9}$$

from which we can establish the flux density of the emission actually observed from the cloud:

$$S_\nu = \frac{\pi a^2 n Q_\nu B_\nu(T)}{D^2} \tag{1.10}$$

where D is the distance to the cloud. Rearranging this into terms of n, and then substituting it into Equation 1.5, gives the following expression for the dust mass:

$$M_d = \frac{4a\rho S_\nu D^2}{3Q_\nu B_\nu(T)} \tag{1.11}$$

Whilst Equation 1.11 allows us to calculate dust mass, it requires values for a and ρ, which as previously discussed are not well constrained. Similarly, the value of Q_ν, and its frequency dependence, are both dictated by the physical properties of a grain; surface area, heat capacity, chemical composition, size, mass, and so forth. Moreover, this derivation has assumed that grains are spherical, and all of the same size – both approximations which will break down at some point. As a matter of convenience, these various terms are grouped together into the dust mass absorption coefficient κ_ν, a single constant of proportionality that links the mass and luminosity of dust, defined as:

$$\kappa_\nu = \frac{3Q_\nu}{4a\rho} \tag{1.12}$$

which, substituted into Equation 1.11, yields:

$$M_d = \frac{S_\nu D^2}{\kappa_\nu B_\nu(T)} \tag{1.13}$$

The high uncertainty on the actual value of κ_ν is generally thought to be an order of magnitude – even without consideration for how it might vary depending upon environment (see the review in the introduction to James et al., 2002). Commonly employed values include $\kappa_{500} = 0.1\,\mathrm{m^2\,kg^{-1}}$ from Draine & Lee (1984), and $\kappa_{850} = 0.077\,\mathrm{m^2\,kg^{-1}}$ from James et al. (2002). The subscripts 500 and 850 indicate the reference wavelength, λ_0, of each model. The frequency-dependence (and hence wavelength-dependence) of κ_ν is described by:

$$\kappa_\nu = \kappa_0 \left(\frac{\nu}{\nu_0}\right)^\beta \tag{1.14}$$

where κ_0 is the dust mass absorption coefficient at frequency ν_0.

It is also important to bear in mind that, in reality, the dust in a galaxy, or even in a single cloud, will not be at a uniform temperature. Rather, it will occupy a continuum of temperatures; however, the limited photometric data generally available for FIR and submm sources limit us to modelling a finite, usually small, number of dust components, as demonstrated in Figure 1.5. In practice, the dust in galaxies is typically observed to be found in a cold ($15 < T < 25\,\mathrm{K}$) component, representing the bulk of dust dust mass in the diffuse ISM, and a warmer component ($T > 25\,\mathrm{K}$) representing the dust in stellar birth clouds.

1.3 THE ORIGINS OF DUST

Most galactic dust is classically understood to be primarily a product of the demise of low-to-intermediate-mass stars (1–8 $M_{\odot}$) as they undergo the Asymptotic Giant Branch (AGB) phase of their lives, and massive stars (>$10_{\odot}$) that have become Red SuperGiants (RSGs), enriching the ISM by means of their stellar winds (Ferrarotti & Gail, 2006; Sargent et al., 2010). Core-collapse supernovae, the endpoint in the fleeting lives of massive stars, have also been observed to produce significant quantities of dust (Dunne et al., 2003, 2009; Barlow et al., 2010; Matsuura et al., 2011). However studies of both local (Matsuura et al., 2009; Dunne et al., 2011) and high-redshift (Morgan & Edmunds, 2003; Dwek et al., 2007; Rowlands et al., 2014b) galaxies have shown a disparity between the rate at which dust is removed from the ISM (either by star formation or interstellar destruction), and the rate at which stars replenish it. As such, the origin of dust in galaxies is still very much an open question.

Dust production by supernovæ has been suggested as a solution to the dust budget shortfall (Dwek & Scalo, 1980; Clayton et al., 2001), particularly for high-redshift ($z > 5$) galaxies. Although some authors (Valiante et al., 2009; Dwek & Cherchneff, 2011) argue that some Low-to-Intermediate Mass Stars (LIMS) could reach the AGB phase rapidly enough to be a significant source of dust at high redshift, this would be highly sensitive to the Initial Mass Function (IMF), and even in extremis would be insufficient to account for all of the observed dust mass (Di Criscienzo et al., 2013). Stars with mass > 8 $M_{\odot}$, however, will end their lives as core-collapse (Type-II) supernovæ rapidly enough to occur in the time frame required.

In order to address the question of the origin of galactic dust, it is necessary to accurately determine the dust-mass injection rate contributions of supernovæ. Observations of dust associated with supernova remnants (Saken et al., 1992) have been undertaken at mid-infrared (MIR) wavelengths ever since the operation of the first infrared orbital telescopes. However, observations at FIR and submm wavelengths are required to properly constrain the dust masses associated with them; in the presence of hot dust emission, a reservoir of cold dust a 100 times more massive than the hot dust would not be detectable at shorter wavelengths, as the cold dust would emit primarily in the FIR and submm. The unprecedented resolution and sensitivity of *Herschel* means we can finally achieve this.

1.3.1 DUST CREATION IN SUPERNOVÆ

Establishing the contribution to the dust budget due to supernovæ is complicated by the fact that few are known to have occurred in recent galactic history. Dust does not form in the moment of a supernova itself, but rather condenses from the metals found in the SuperNova Remnant (SNR), the expanding cloud of debris resulting from the explosion. However, the rapid expansion of SNRs causes them to sweep up large amounts of the surrounding ISM, making it difficult to distinguish between material produced by the supernova, and that which originates from the local interstellar environment. For us to be able to determine how much dust they manufacture, SNRs must ideally be observed before they enter the Sedov phase – the point at which the mass of swept-up material exceeds of that of supernova ejecta. This window is typically less than 1,000 years. However, the available sample of sufficiently young and nearby SNRs is severely limited; fewer than a dozen galactic supernovæ are known to have occurred in the past millennium. Observations of extragalactic SNRs can provide us with only limited information. At such great distances, they will appear as point sources in the FIR and submm, making it impossible to distinguish between swept-up interstellar dust, and any dust manufactured in the supernoave; moreover, the emission from any dust in the supernova will be hard to distinguish from dust emission from the general ISM of the host galaxy.

Another complication is that, in contrast to most sources, dust is not the only significant source emission from SNRs in the FIR regime. The acceleration of charged particles (predominantly electrons) in the intense magnetic fields of SNRs gives rise to synchrotron radiation. A synchrotron spectrum can generally be described by a power law of the form:

$$S_\nu = S_0 \left(\frac{\nu}{\nu_0} \right)^{\alpha} \tag{1.15}$$

where S_ν is the synchrotron flux density at frequency ν, S_0 is the synchrotron flux density at a reference frequency ν_0, and α is the synchrotron power law spectral index. Matters are further complicated by the fact that the synchrotron spectrum of an object can exhibit 'breaks', where the spectral index abruptly changes.

Core-collapse supernovæ (Types Ib, Ic, and II) are particularly important candidates for the missing dust mass; this is especially true at high redshifts, as the greater rate of star formation in the early Universe (Heavens et al., 2004; Hopkins & Beacom, 2006; Madau & Dickinson, 2014) meant that massive stars were more prevalent. However, given the vastly greater numbers of LIMS in galaxies, Type-Ia supernovæ also bear consideration as contributors to the budget shortfall. Type-Ia supernovæ are generally understood to arise from the thermonuclear detonation of white dwarfs approaching the Chandrasekhar mass; this limits their potential dust input to more recent cosmic time due to the > 1 Gyr timescale required for white dwarf progenitors to reach the end of their lives.

It is worth noting that there are alternate scenarios for the triggering of Type-Ia supernovæ. 'Double-degenerate' supernovæ, caused by the merger of two white dwarfs, are known to occur (Schaefer & Pagnotta, 2012), but are understood to be much rarer than single-degenerate systems (Nielsen et al., 2014). An even more exotic 'single-star' origin for some Type-Ia supernovæ has also been suggested, in which super-AGB stars ($\sim$ 8 $M_{\odot}$) undergo secular thermonuclear explosions. This is believed to be possible if towards the end of its life, a star experiences asymmetric carbon shell burning, allowing material from its outer layers to fall onto a degenerate core (Tout, 2005; Denissenkov et al., 2013), therefore causing the core to exceed the Chandrasekhar mass and detonate. This would explain observations of Type-Ia remnants interacting with CircumStellar Material (CSM), a phenomenon that is difficult to explain if all Type-Ia events involve a white dwarf interacting with a companion star (Silverman et al., 2013).

Type-Ia supernovæ are of interest as the primary long-distance standard candles of modern cosmology. Phenomena with the potential to affect the luminosity of Type-Ia supernovæ, such as extinction by large masses of rapidly-produced dust, are therefore of great importance. Furthermore, Type-Ia supernovæ are believed to account for the creation of at least half the iron in the Milky Way (Acharova et al., 2012); however the gas-phase ISM is observed to suffer from significant iron depletion (Jensen & Snow, 2007; Delgado-Inglada et al., 2011). Injection of large masses of supernova-manufactured iron into the dust phase by Type-Ia supernovæ has been suggested as an explanation for this (Dwek, 1998). Large masses of dust ($\sim 0.1 M_{\odot}$) are predicted to be formed in Type-Ia supernovæ, however most of it is expected to be destroyed by the harsh environment of the remnant within 10^4 years (Nozawa et al., 2011).

In both classes of supernovæ, pre-*Herschel* mid- and far-IR observations have revealed only small quantities ($< 10^{-3}$ $M_{\odot}$) of dust present (see review in Gomez et al., 2012a). However, those detections were of hot dust, at temperatures of ~ 100 K. As this hot dust is very luminous, it would be able to out-shine any less-luminous, lower-temperature dust that may be present, and which could represent a much greater mass of material, but be indiscernible without longer wavelength coverage. However, in recent years, the submm window opened by *Herschel* has allowed us to explore the presence of cold dust in SNR.

Prior to *Herschel* the Cassiopeia A (Cas A) remnant was observed with the Submillimetre Common-User Bolometer Array (SCUBA) instrument on the James Clerk Maxwell Telescope (JCMT), and thermal emission from cold dust was detected (Dunne et al., 2003); however, it was unclear how much of this emission was due to contamination from interstellar dust clouds along the line of sight (Krause et al., 2004). *Herschel* observations of Cas A allowed warmer emission from dust in the supernova to be isolated, revealing 0.075 $M_\odot$ of cool dust at $\sim$ 35 K. This is still almost an order of magnitude less than what is needed to explain high-redshift dust observations (Barlow et al., 2010); plus contamination from large amounts of foreground cirrus make it unclear how much of this is truly associated with the remnant.

Investigation of the SN1987A remnant in the Large Magellanic Cloud (LMC) with *Herschel* (Matsuura et al., 2011), followed up by high-resolution ALMA observations (Indebetouw et al., 2014), revealed 0.2–0.7 $M_\odot$ of dust confined to the *supernova ejecta* - therefore certainly produced by the supernova itself. Although this approaches the mass per remnant necessary to account for the budget shortfall (Dunne et al., 2011), it is surprising in a remnant so young, raising questions about the processes of dust formation in SNR, and how the mass of dust changes as a remnant evolves. The fraction of the ejecta dust that will survive the harsh environment of the remnant, and go on to contribute to the galactic dust budget, remains to be seen. Indeed, this is a pressing question for supernova remnants in general. That said, before we can address the issue of how much of a supernova's dust gets destroyed in the remnant, we must first answer the question of how much gets created in the first place.

1.3.2 DUST DESTRUCTION AND DUST CREATION IN INTERSTELLAR SPACE

Classically, supernovæ were thought to interact with the dust in galaxies in only one way – as destroyers. It has long been understood that the high-energy ions that make up supernova shockwaves can 'sputter' atoms from the surface of dust grains, returning them to the gas phase (Barlow, 1978; Jones et al., 1994), and that the grain-grain collisions brought on shocks can be similarly destructive (Jones et al., 1996; Jones & Nuth, 2011). However, more recent evidence has revealed that supernovæ play a far more complex role in galactic dust budgets than previously thought. In the case of lower-energy collisions between dust grains and shock gas (for example, an interstellar cloud already swept up by a shock, and hence moving at the same bulk velocity), the impacted gas can become implanted in the grain, thereby in fact *increasing* the mass of dust present (Demyk et al., 2001). Combined with the previously-discussed evidence for large amounts of fresh dust in the ejecta of recent supernovæ, it is now unclear what the net role of supernovæ is, or how it might vary with environment and epoch.

Volatile chemicals on the surfaces of dust grains, such as ices, can be very easily desorbed (ie, 'stripped') by the UV photons (Draine & Salpeter, 1979) emitted by hot, massive stars. However, given that the supernova deaths of these same stars are known to give rise to dust injection, it is again unclear what their overall effect, on balance, might be upon the dust content of a galaxy.

Many other dust-destruction processes are known or expected to operate, such as thermal and ionising destruction by cosmic rays, high-energy photons, and free elections (see review in Jones, 2004). As a result, most models predict that the dust destruction timescale of the ISM cannot much exceed 10^8 years (Jones & Nuth, 2011). This is problematic, as the 'turnaround' time for dust manufactured in stellar deaths to be incorporated into star formation regions is $\sim 10^9$ years – which clearly occurs, given the great abundance of dust observed in protostellar systems. Therefore, it is assumed that dust growth must occur in the interstellar environment, via atoms and molecules being accreted onto the surfaces of grains, presumably in the dense molecular ISM. But whilst many mechanisms for this are suggested, most struggle to generate the mass increase needed to address the imbalance (see reviews in Draine, 2009; Jones & Nuth, 2011; Dunne et al., 2011; Rowlands et al., 2014b).

1.4 GALAXY EVOLUTION

Galaxy evolution is an area of intense investigation; how exactly galaxies develop over time, and what factors influence the process, remains unclear in many regards. It has long been known that galaxies change as they age; whilst the total number of massive disk galaxies has remained nearly constant since $z = 1$, their typical appearance has gradually shifted towards earlier morphological types (Buitrago et al., 2013). Before that time, the total number of massive galaxies was smaller, and those that are observed often appear very different to the galaxies seen today. A far higher fraction of galaxies in the early universe are observed to

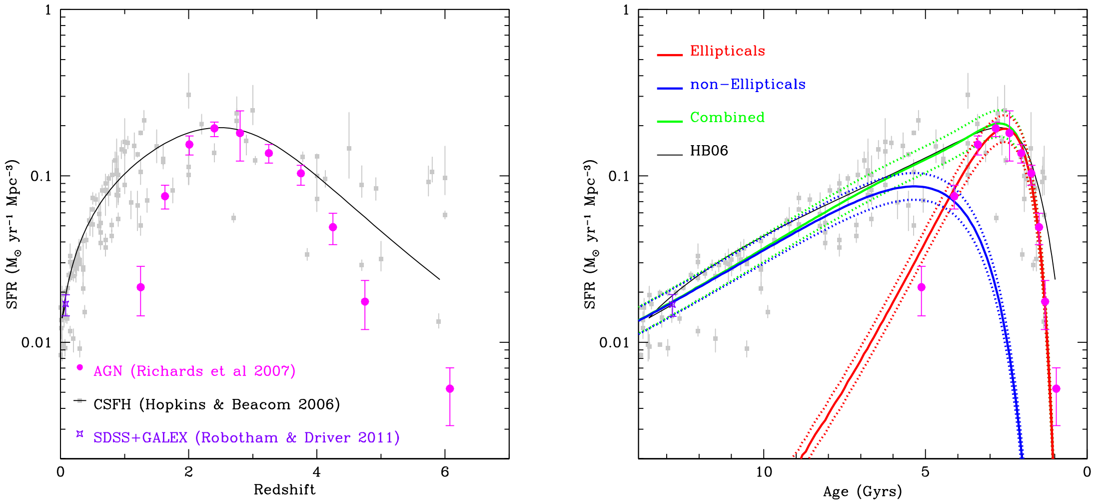

FIGURE 1.6 The star formation history of the Universe. *Left:* The star formation rate per co-moving volume, as a function of redshift, peaking at $2 \gtrsim z \gtrsim 3$, showing data from Richards et al. (2006), Hopkins & Beacom (2006), and Robotham & Driver (2011). *Right:* The star formation rate per co-moving volume, as a function of time since the Big Bang, showing the contributions of star formation in giant ellipticals (or, rather, their ancient progenitors), and in other, less-massive systems. Whilst star formation in proto-ellipticals accounts for the Universal peak at $2 \lesssim z \lesssim 3$, less massive galaxies have dominated total star formation since $z \sim 1$. Reproduced from Driver et al. (2013), with permission.

be irregular or perturbed (Bunker et al., 2000). And whilst many high-redshift systems take the form of disks, those disks are very different to the disks of modern late-type galaxies, being turbulent and highly compact; instead it is believed that they are the progenitors of modern elliptical galaxies (Conselice et al., 2005).

The evolution of galaxies is interpreted within the framework of Lambda Cold Dark Matter (ΛCDM) cosmology (see review in Liddle, 2003). In this model most of the energy density of the universe is made up of dark energy (Λ), whilst most of the mass takes the form of Cold Dark Matter (CDM). Quantum fluctuations shortly after the Big Bang were imprinted onto the structure of the Universe (Starobinskii, 1978; Linde, 1982), leading to regions of over- and under-density. Regions of over-density gravitationally attracted additional mass, taking the form of halos of dark matter, with dense regions of baryonic matter embedded within them – galaxies.

ΛCDM predicts that galaxies assemble in a ‘bottom-up’ manner – that larger galaxies are formed from the mergers of smaller systems. It appears that the massive early-type galaxies seen in the modern universe are the result of mergers involving the compact turbulent disks seen at higher redshifts (Glazebrook, 2013). The intense star formation associated with this merging process accounts for the peak in the star formation rate of the Universe seen at $2 \lesssim z \lesssim 3$ (Madau & Dickinson, 2014). It appears, however, that galaxy evolution progresses differently for high- and low- mass systems. The peak in the cosmic star formation rate (Figure 1.6, left pane) seems to correspond primarily to high-mass systems (Hopkins et al., 2007), in which most star formation appears to have been rapidly quenched thereafter. Quenching can arise from Active Galactic Nuclei (AGN) and supernovæ blowing the gas out of a galaxy (Springel et al., 2005; Croton et al., 2006); or mergers and interactions can consume the entire available gas reservoir (Mihos & Hernquist, 1994; Barnes & Hernquist, 1992). In either case, these galaxies are exhausted of their gas, leaving behind the 'red and dead' ellipticals seen today. Whereas in the case of low-mass systems, star formation appears to have evolved more steadily; such galaxies seem to have been the site of most star formation since $z \sim 1$ (Figure 1.6, right pane, see Driver et al., 2013).

This strong observed dependence between a galaxy's mass and its evolution is referred to as 'downsizing' (Cowie et al., 1996). Generally, galaxies that are more massive tend to be older (ie, in a further advanced evolutionary stage) than those that are less massive. Given that the notion of 'bottom-up' ΛCDM galaxy formation entails larger systems being formed by the merger of smaller systems, it might seem counter-intuitive that more massive galaxies look older than those that are less massive. However, many authors have pointed out that what ΛCDM predicts is that dark matter halos assemble in this manner; and that the star formation activity of the baryons ensconced with these halos should not be expected to develop in the same way (Neistein et al., 2006; Fontanot et al., 2009).

The degree to which 'nature' and 'nurture' affect the evolution of a galaxy can vary. As already described, the mass of a system has a strong influence on its evolutionary stage; however, mass is not a purely intrinsic property of a galaxy, being influenced by mergers. The morphology-density relation (Dressler, 1980; Phillipps et al., 1998; Calvi et al., 2012) demonstrates that environment can have a strong influence upon galactic development; in environments more prone to interactions, galaxies tend to be of earlier morphological types. Similarly, star-formation in a galaxy can be enhanced by interactions with other galaxies in proximity (Patton et al., 2013). But it is also evident that galaxies evolve independently, as they deplete their reservoirs of of star-forming gas whilst accreting small amounts of new gas from intergalactic space (Combes, 2007). Recent theoretical work suggests that once a spiral galaxy depletes its reservoir of star-forming material, its spiral arms will naturally disappear, leading to lenticular morphology (D'Onghia et al., 2013). And massive galaxies, independent of their environment,

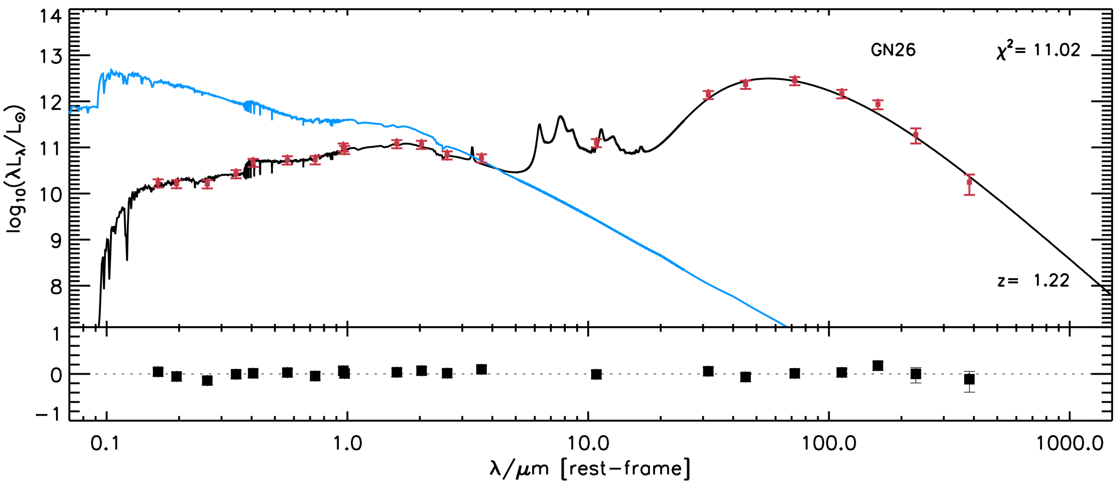

FIGURE 1.7 The observed UV–submm SED of a high-redshift dust-obscured galaxy (plotted in black), along with its unattenuated stellar emission spectrum, as it would appear if no dust were present (plotted in blue). As can be seen, the attenuation of the stellar component becomes increasingly pronounced at shorter wavelengths. Reproduced from Rowlands et al. (2014a), with permission.

are consistently found to be biased towards earlier morphological types, and lower levels of star formation (Peng et al., 2014).

1.4.1 DUST IN GALAXIES

Cosmic dust affords us a unique way of studying galaxies. Half of all the starlight ever emitted by galaxies has been absorbed by dust and thermally re-emitted in the FIR and submm (Driver et al., 2007b). This is especially the case in star-forming regions, where the high-energy photons emitted by young stars are particularly susceptible to absorption by dust grains (Fitzpatrick, 2004). Figure 1.7 illustrates the SED of a high-redshift galaxy where a large fraction of the stellar emission is being absorbed and re-radiated by dust. But whilst star formation is known to dominate the heating of the hot dust in galaxies (Kennicutt, 1998; Kennicutt et al., 2009), it is unclear if it also drives the heating of the cold dust (Law et al., 2011; Ford et al., 2013; Hughes et al., 2014), or whether the evolved stellar population is mainly responsible (Bendo et al., 2012; Boquien et al., 2011). Moreover, the dense ISM in which star-formation occurs is notoriously hard to study, as emission from molecular species tends to be faint, or entirely non-existent; on the other hand, dust is much more luminous, and also serves as a catalyst for the very formation of molecular gas, making it an invaluable way to study these regions.

Recent work also indicates that dust is a useful tracer of the molecular component (Eales et al., 2012; Smith et al., 2012b). Furthermore, dust is itself an indirect product of star formation; as discussed in Section 1.3 and explored in depth in Chapter 2, short-lived massive stars are major dust factories. By tracing the chemical and star formation history of galaxies, dust provides an invaluable avenue for the study of galaxy evolution as a whole.

As FIR and submm astronomy has matured, numerous projects have been undertaken to characterise dust in galaxies. The galaxy Dust Mass Function (DMF), the cardinal description of dust in galaxies, was first estimated by the SCUBA Local Universe Galaxy Survey (SLUGS, Dunne et al., 2000), using 450 and 850 µm observations of 104 IRAS (ie, hot dust emission) selected galaxies, and augmented by further observations of 80 optically-selected galaxies (Vlahakis et al., 2005).

This is being followed up in the *Herschel* era by the *Herschel* Reference Survey (HRS, Boselli et al., 2010) of 323 galaxies, which aims to understand the relationships between dust and galaxy evolution, interaction, and star formation; and by the Key Insights in Nearby Galaxies Far-Infrared Survey with *Herschel* (KINGFISH, Kennicutt et al., 2011), which particularly focuses upon understanding the ISM in nearby galaxies. However, these and other FIR surveys of nearby galaxies may have been hindered by the fact they are not *dust selected*, instead being dependent upon selection criteria derived from observations at other wavelengths. Large-area missions such as the InfraRed Astronomical Satellite (IRAS, Neugebauer et al., 1984) and more recently *Planck* (Planck Collaboration et al., 2011a) provide blind samples of local galaxies, including the recent sample by Clemens et al. (2013), but lack resolution and sensitivity when compared to targeted surveys.

Even with the advent of *Herschel*, many of the key questions about dust in galaxies are yet to be answered. Even the most fundamental characterisation of the dust content of the local universe, the DMF, is yet to be well constrained. As with mass and luminosity functions in other parts of the spectrum, the DMF is typically fit using a Schechter function (Schechter, 1976):

$$\phi = \phi^{\star} \left(\frac{M}{M^{\star}} \right)^{\alpha} e^{-\frac{M}{M^{\star}}} \tag{1.16}$$

where ϕ is the number volume density at a given mass M, α is the power law index of the low mass slope, $\phi^{\star}$ is the characteristic density, and $M^{\star}$ is the characteristic mass (the location of the Schechter function's 'knee').

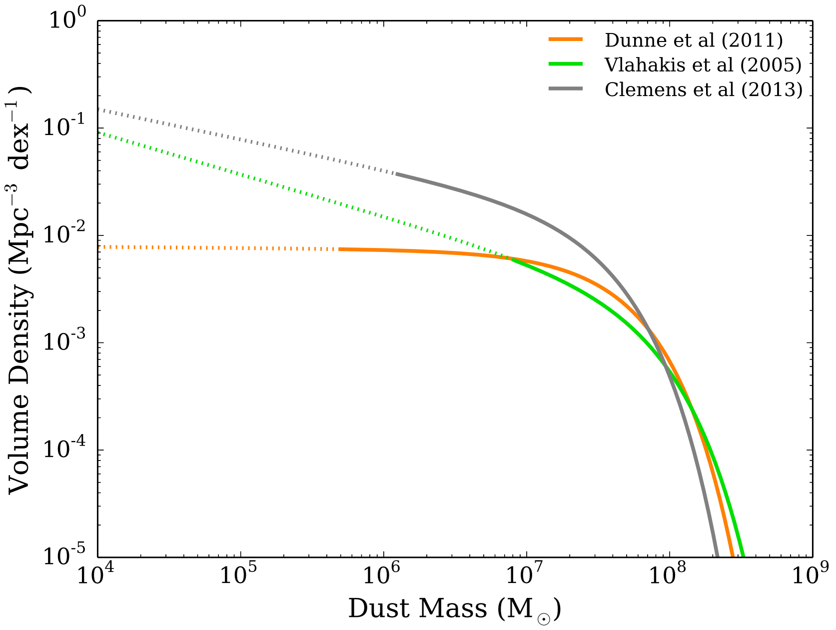

FIGURE 1.8 Estimates of the local Dust Mass Function from several recent studies using data from submm observatories; Vlahakis et al. (2005) using SCUBA, Dunne et al. (2011) using *Herschel*, and Clemens et al. (2013) using *Planck*. Each study's best-fit Schechter function is plotted as a solid line down to the minimum dust mass they sampled; below that (where they are, in effect, extrapolating) it is plotted as a dotted line. Note that all three have been scaled to the same cosmology and κ_ν to permit direct comparison. Note the significant divergence, particularly at low masses.

Determination of the DMF can only be achieved using observations in the submm, which accounts for the emission from the majority of the dust mass in galaxies. Figure 1.8 shows three estimates of the local dust mass function, by Vlahakis et al. (2005) using SCUBA, Dunne et al. (2011) using *Herschel* observations of a small (16 deg^2) patch of sky, and Clemens et al. (2013) using *Planck*. The three are in poor agreement. Their best-fit Schechter functions diverge significantly towards lower masses, suggesting values for the dust mass volume density of the local Universe that vary by a factor of 2.2; from $1.3 \times 10^5\,\mathrm{M_\odot\,Mpc^{-3}}$ for Dunne et al., 2011, to $1.2 \times 10^5\,\mathrm{M_\odot\,Mpc^{-3}}$ for Vlahakis et al., 2005 and $2.7 \times 10^5\,\mathrm{M_\odot\,Mpc^{-3}}$ for Clemens et al., 2013 (to allow direct comparison, all three have been corrected to the same cosmology and κ_ν). Despite being three of the leading estimates of the DMF, each has significant drawbacks: Vlahakis et al. (2005) only directly measured large dust masses, and used the relation between SCUBA submm luminosity and IRAS colours to extrapolate to low-mass galaxies seen with IRAS (ie, luminous hot dust, hence over-representing starbursts and major mergers); Dunne et al. (2011)

sampled only a relatively small, notoriously under-dense (Driver et al., 2011) region of sky; and Clemens et al. (2013) were only able to sample very massive (or very nearby) systems, thanks to the relatively poor resolution and sensitivity of *Planck*. This highlights the difficulties in pinning down even the most basic aspects of the dust properties of the Universe. The matter of the local DMF in particular will be addressed in detail in this work (see Chapter 6).

1.5 SURVEYS

The work in this thesis is centred around the use of observations made by *Herschel* carried out for two particular surveys – Mass-loss from Evolved StarS, and the *Herschel* Astrophysical Terahertz Large-Area Survey.

1.5.1 MESS

Mass-loss from Evolved StarS (MESS, Groenewegen et al., 2011) is a *Herschel* guaranteed time key program, the specific objective of which is to characterise the mass-loss properties of evolved stars by observing a representative sample of the full gamut of such objects; asymptotic giant branch (AGB), red supergiant (RSG), post asymptotic giant branch (P-AGB), Wolf-Rayet (WR), and luminous blue variable (LBV) stars, as well as planetary nebulæ (PNe) and supernova remnants (SNRs).

In total 150 targets were observed photometrically and spectroscopically (although not both in every case) using PACS and SPIRE. The photometric observations were conducted at 70, 100, and 160 µm in large map mode with PACS, and at 250, 350, and 500 µm in large map mode with SPIRE.

This work makes use of MESS photometric observations of the remnants of 3 historical Milky Way supernovae – Tycho's SNR (SN1572), Kepler's SNR (SN1604), and the Crab Nebula

1.5.2 *H*-ATLAS

The *Herschel* Astrophysical Terahertz Large Area Survey (*H*-ATLAS, Eales et al., 2010) is a $\sim 550\,\mathrm{deg}^2$ ($1/80^{\mathrm{th}}$ of the entire sky) survey in the FIR and submm, providing an unbiased and unrivalled view of the dusty Universe. *H*-ATLAS is the largest Open Time Key Project undertaken by *Herschel*, with a primary goal of studying, for the first time, hundreds of thousands of submm galaxies. *H*-ATLAS

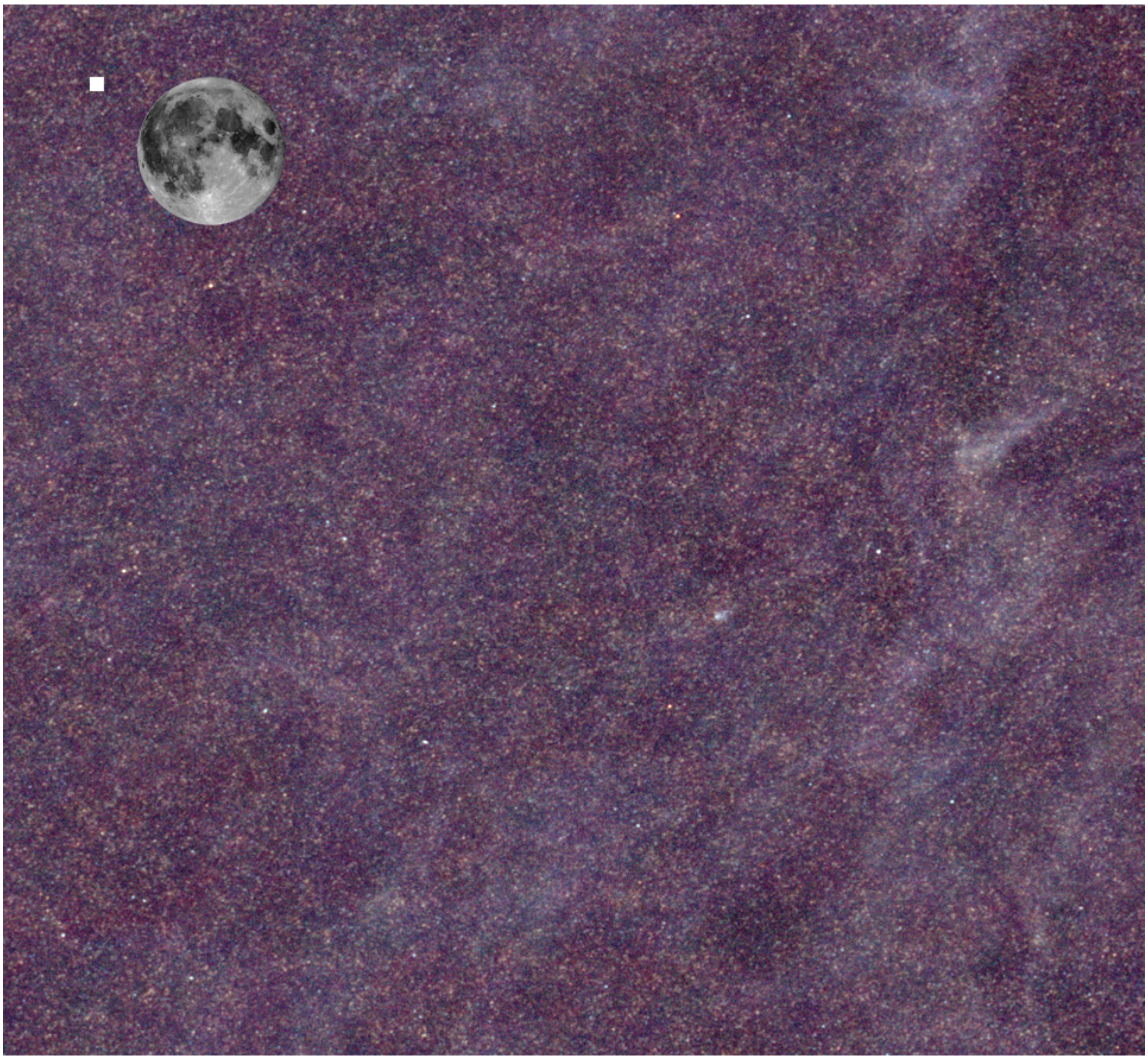

FIGURE 1.9 Three colour SPIRE 250, 350, and 500 µm image of the *H*-ATLAS Science Demonstration Phase (SDP), covering approximately 16 deg^2 of sky – representing approximately 3% of the total survey area. Shown for scale is the relative angular size of the full Moon, and a white square indicating the area (although not location) of the *Hubble* Deep Field. The region of the Hubble Deep Field was observed by SCUBA in 1998, which after 50 hours of observing had detected 5 sources in 6 arcmin^2 of sky. Compare this to the almost 10,000 galaxies detected in the 16 hours it took *Herschel* to observe this small portion of the entire *H*-ATLAS survey. Adapted from an image by Haley Gomez, with permission.

provides us with a blind, large-area sample of both nearby and high-redshift galaxies, but with the resolution and sensitivity hitherto only found in targeted dust surveys.

H-ATLAS highlights how far FIR and submm astronomy has come in a decade. Figure 1.9 depicts the $\sim 16\,\mathrm{deg}^2$ of the *H*-ATLAS Science Demonstration Phase (SDP) field. This observation took *Herschel* 16 hours to complete, and features almost 10,000 detected galaxies. Contrast this to the small white square inset in the figure; this indicates the 6 arcmin^2 area (although not location) of the *Hubble* Deep Field, which was observed using the SCUBA instrument on the JCMT for 50 hours – and in which it detected only 5 sources (Hughes et al., 1998). The *H*-ATLAS SDP therefore represents a 6,000-fold improvement in terms of observing time required per source detected, and a 30,000-fold increase in the sky area mapped in a given time, over what was achieved with SCUBA.

Photometry observations for *H*-ATLAS were carried out in fast parallel mode at 100 and 160 µm with PACS and at 250, 350 and 500 µm with SPIRE. Descriptions of the fundamental *H*-ATLAS data reduction procedures can be found in Ibar et al. (2010) for PACS, and Pascale et al. (2011) and Valiante et al., (*in prep.*) for SPIRE. Throughout this work, photometry in the SPIRE bands was performed upon the appropriate relative gain maps. The *H*-ATLAS PACS maps were reduced using the `Scanamorphos` (Roussel, 2013) pipeline, with appropriate corrections made for the relative areas of the reference pixels on the focal plane.

The source extraction algorithm MADX (Rigby et al., 2011, Maddox et al., *in prep.*) isolates $> 2.5\,\sigma$ peaks in the SPIRE 250 µm band and then measures the fluxes in all three SPIRE bands at the position determined by the 250 µm fit; the *H*-ATLAS catalogue selects those sources which have a $> 5\,\sigma$ detection in at least one band. Optical counterparts to *H*-ATLAS sources were found by direct comparison with the SDSS DR7 (Abazajian et al., 2009) by means of matching *H*-ATLAS sources to SDSS objects within a $10''$ radius using a likelihood ratio technique where reliability ≥ 0.8 (being the probability that the selected counterpart is the correct one, out of all possible counter parts within a $10''$ search radius) is required for a matched to be deemed science-quality (Smith et al., 2011).

1.5.2.1 GAMA

This work makes use of the *H*-ATLAS Phase-1 Version-3 internal data release (Valiante et al., *in prep.*), which consists of three equal-area fields along the equatorial plane, covering 161.6 deg^2 of sky. These regions were chosen as they contain low levels of contamination from Galactic cirrus, and because they are coincident with the Galaxy And Mass Assembly (GAMA, Driver et al., 2009) redshift survey. The three GAMA fields are named GAMA09, GAMA12, and GAMA15, denoting their right ascension.

The GAMA survey uses their own spectroscopy, taken at the Anglo-Australian Telescope, combined with data from previous redshift surveys such as the Sloan Digital Sky Survey (SDSS, York et al., 2000), 2 Degree Field Galaxy Redshift Survey (2dFRGS, Colless et al., 2003), and the Millenium Galaxy Catalogue (MGC, Driver et al., 2005), to provide redshift coverage complete down to a magnitude limit of $r < 19.4$.

Along with their spectroscopic data, GAMA provides supplementary reductions of imaging data, including UV GALEX (GAlaxy Evolution EXplorer, Morrissey et al., 2007), optical SDSS DR6 (Adelman-McCarthy et al., 2008), Near-InfraRed (NIR) UKIRT (United Kingdom Infrared Telescope) UKIDSS-LAS (UKIRT Infrared Deep Sky Survey Large Area Survey, Lawrence et al., 2007), NIR VISTA (Visible and Infrared Survey Telescope for Astronomy) VIKING (VISTA Kilo-degree Infrared Galaxy survey, Edge et al., 2013), and Mid-InfraRed (MIR) WISE (Wide-field Infrared Survey Explorer, Wright et al., 2010; Cluver et al., 2014) observations. By performing their own reductions, GAMA were able to ensure that their photometry was consistent between surveys (Hill et al., 2011).

1.6 THESIS OUTLINE

This thesis describes two distinct research projects concerning cosmic dust which I conducted during the course of my PhD, centred around exploiting data from the *Herschel* Space Observatory. Chapter 2 details my investigation of the remnants of three historical Milky Way supernovæ, looking for evidence of the creation of cosmic dust. Chapter 3 describes how I used *Herschel* data to assemble HAPLESS, a sample of local galaxies selected solely on the basis of the emission from their dust. Chapter 4 explains the workings of the pipeline I created to perform photometry upon this sample, and the tests I carried out to ensure the pipeline's accuracy and reliability. The properties of the HAPLESS galaxies are presented in Chapter 5. In Chapter 6, HAPLESS is compared to other surveys of dust in local galaxies. Chapter 7 explores the properties of the nearby yet immature galaxies identified in HAPLESS.

CHAPTER 2

DUST IN SUPERNOVÆ

'Dust in the air suspended,
Marks the place where a story ended.'

T. S. ELIOT

SUPERNOVÆ have been proposed as a possible solution to the dust budget crisis in galaxies – if they create large masses of dust. However, as discussed in Chapter 1, there had been no definitive detections of dust manufactured in supernovæ prior to the launch of *Herschel*. Since then, *Herschel* observations of the remnants of two recent nearby supernovæ, Cassiopeia A and SN1987A, have shown that they do indeed produce significant quantities of dust. However, two objects is a very small sample from which to draw broad conclusions. Moreover, it remains unclear whether or not this manufactured dust is actually injected into the galactic environment. In this chapter, I detail how I used *Herschel* observations to look for the presence of manufactured dust in the remnants of three recent Milky Way supernovæ; Kepler's and Tyhco's Supernovæ (SN1604 and SN1572), which were both Type-Ia explosions, and the Crab Supernova (SN1054), which is one of only two Type-II events known to have occurred in our Galaxy in the past thousand years (alongside Cassiopeia A). My investigations of these objects form a significant fraction of the work presented in Gomez et al. (2012a) and Gomez et al. (2012b).

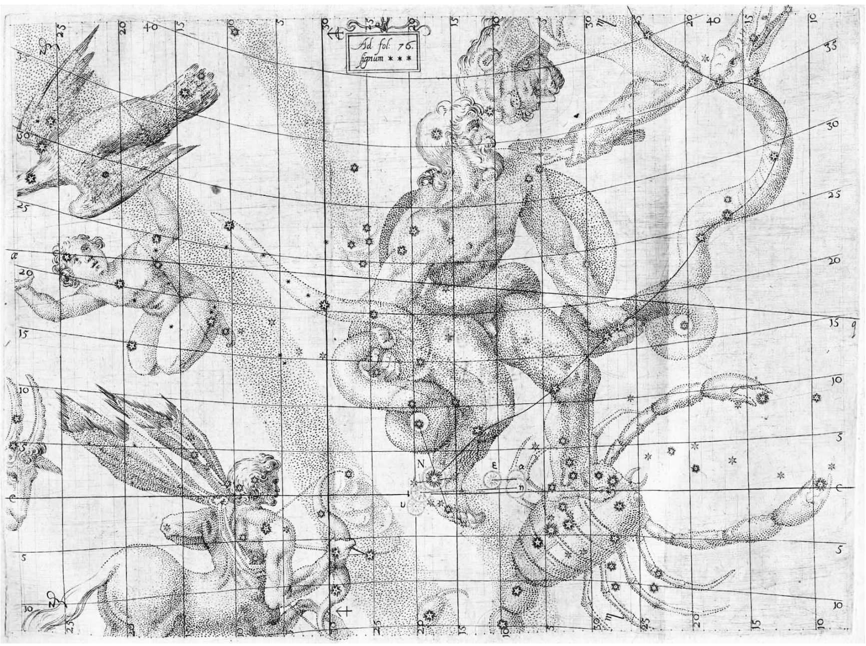

FIGURE 2.1 Optical observation of Kepler's supernova, reproduced from Kepler (1606). The supernova is the star marked 'N', on the right ankle of Ophiuchus.

2.1 KEPLER'S SUPERNOVA REMNANT

Observed most famously by German astronomer Johannes Kepler in October 1604 (Figure 2.1, Kepler, 1606), Kepler's Supernova (SN1604) is the most recent to have been observed in the Milky Way (subsequent events have only been discovered as remnants), and lies at a distance of 4 kpc (Blair et al., 2004). Views as to the type of Kepler's supernova have been conflicted, but the current consensus is that it was probably a Type-Ia event (Blair et al., 2004), albeit an idiosyncratic one; the nitrogen abundances in particular are more in line with expectations of a core-collapse origin (Hughes, 1999). MIR *Spitzer* observations indicated the presence of $5.4 \times 10^{-4}\ M_\odot$ of hot dust (Blair et al., 2007). Submm observations by SCUBA were interpreted as suggesting the presence of 0.3–3.0 $M_\odot$ of cold dust (Morgan et al., 2003); however, subsequent observations revealed that the molecular lines used to trace intervening interstellar material vastly underestimated the degree of contamination (Gomez et al., 2009). The remnant is located at coordinates $\alpha = 262.671^\circ$, $\delta = 21.4914^\circ$ (J2000), and is travelling out of the Galactic plane (Blair et al., 2004).

We sought to use *Herschel* to settle the question of the dust content of Kepler's SNR. Not only is *Herschel*'s resolution and sensitivity unmatched by other observatories, but it also able to provide self-consistent observations of the entire

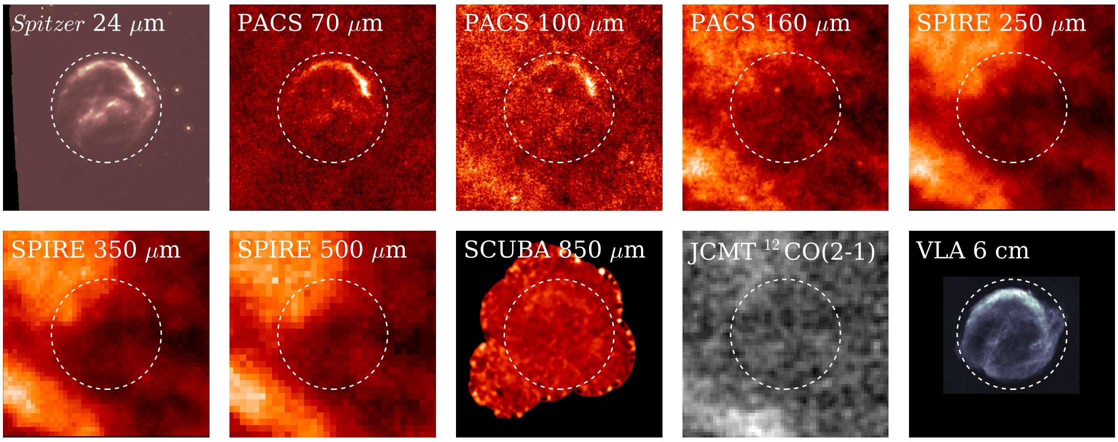

FIGURE 2.2 Multiwavelength imagery of Kepler's SNR, as seen in MIR to radio wavelengths. *Upper row: Spitzer* 24 µm; PACS 70, 100, and 160 µm; and SPIRE 250 µm. *Lower row:* SPIRE 350 and 500 µm; JCMT SCUBA 850 µm; JCMT ^{12}CO(2-1); and VLA 6 cm. The dashed circles have a radius of 120″ centred at $\alpha = 262.671°$, $\delta = 21.4914°$ (J2000), representing the photometric aperture employed. Each cutout is 550″ across (the forward shock radius being 103″, Warren et al., 2005).

dust emission spectrum.

Along with the *Herschel* observations of Kepler's SNR taken as part of the MESS survey, we also used *Spitzer* 24 µm (Blair et al., 2007), Very Large Array (VLA) 6 cm (DeLaney et al., 2002), and James Clerk Maxwell Telescope (JCMT) ^{12}CO(2-1) (Gomez et al., 2009) and Submillimetre Common-User Bolometer Array (SCUBA) 850 µm data (Morgan et al., 2003) to help identify and constrain the remnant's emission properties across the entire relevant wavelength range. These observations are shown in Figure 2.2.

There are four sources of emission in the IR and submm that are expected to originate from the SNR. The intense magnetic fields produced by the advancing shockwave will accelerate charged particles, giving rise to synchrotron radiation. Cold dust in the ISM along the line of sight to a SNR will radiate at FIR and submm wavelengths. Hot dust in the shockwave, typically at temperatures of 70–120 K, will emit in the MIR and FIR. Finally, any supernova dust at temperatures < 40 K will emit primarily in the submm, and dominate the total dust mass; however it must be disentangled from all of the previous sources of emission listed.

Visual inspection of the *Herschel* observations in Figure 2.3 clearly show the hot dust emission in blue, with the same morphology as seen in the MIR. However, they contain no indication of cold dust emission clearly associated with the remnant. Rather, the SPIRE observations broadly show the same Galactic cirrus

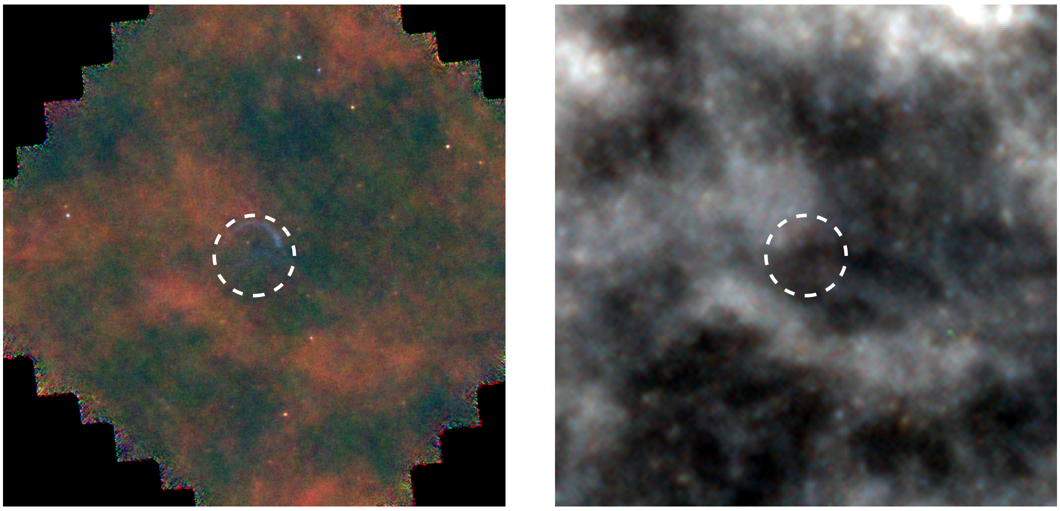

FIGURE 2.3 Three colour *Left:* PACS 70, 100, and 160 µm, and *Right:* SPIRE 250, 350, and 500 µm images of a 25′ × 25′ region centred upon Kepler's SNR. Hot dust emission from the remnant is clearly visible at the shortest *Herschel* wavelengths (PACS blue), but contamination from interstellar cirrus quickly dominates at longer wavelengths. The dashed circles have a radius of 120″ centred at $\alpha = 262.671^\circ$, $\delta = 21.4914^\circ$ (J2000), representing the photometric aperture employed.

structures visible in ^{12}CO(2-1) (Figure 2.2)

2.1.1 PHOTOMETRY AND SED FITTING

The *Spitzer*, *Herschel*, SCUBA, and VLA maps were all re-gridded to a common 1″ pixel scale, then convolved with a Gaussian so that they were all at the 36″ resolution of the SPIRE 500 µm beam. Fluxes were taken from a 120″ circular aperture centred on the remnant at $\alpha = 262.671^\circ$, $\delta = 21.4914^\circ$ (J2000); the size was chosen so as to contain the entirety of the remnant in all of the smoothed maps. Despite being well above the Galactic plane, the sky in the direction of Kepler's SNR contains vast and highly variable amounts of Galactic cirrus, which dominates the submm observations, as seen in Figure 2.3. This made it impossible to perform standard annular aperture photometry, or use a sky aperture as a representative area of background. As a result, we placed apertures over the darkest region of sky in each map, meaning no attempt was made to subtract the background flux from the measurements; rather, they represent the flux 'towards' the remnant, including that originating from the intervening ISM. The measured fluxes can be found in Table 2.1. The uncertainties in flux were estimated by adding in quadrature the

TABLE 2.1 MIR-to-submm fluxes measured in the direction of Kepler's SNR. The photometry was conducted by me, and published in Gomez et al. (2012a). Note that the flux at 100–1,000 µm is dominated by contamination from foreground Galactic cirrus. The contribution of the synchrotron component in each band was determined using Equation 1.15, with $\alpha = -0.71$, $\nu_0 = 5\,\mathrm{Ghz}$ (6 cm), and $S_0 = 6.14\,\mathrm{Jy}$.

Wavelength (µm)	Integrated Flux (Jy)	Uncertainty (Jy)	Synchrotron Flux (Jy)
24	9.5	± 1.0	0.02
70	12.3	± 2.7	0.05
100	11.2	± 2.4	0.06
160	16.5	± 2.9	0.09
250	13.0	± 2.8	0.12
350	5.8	± 1.2	0.16
500	2.7	± 0.6	0.20
850	0.7	± 0.1	0.29

pixel RMS (Root Mean Squared) within the aperture, the instrumental photometric uncertainties (Table 1.1), and the error between our maps' zero values and those of InfraRed Survey Explorer (IRAS) maps of the same region (as described in Gomez et al., 2012a).

We fit the MIR-to-submm Spectral Energy Distribution (SED) of Kepler's SNR with a three-component model; two modified blackbody ('greybody', see Section 1.2.1) components for the hot and cold dust emission, and a power law component for the non-thermal synchrotron emission. The model consists of dust components at two temperatures as any hitherto-undiscovered mass of dust in the remnant must be significantly colder than the known hot dust component, for it to have been missed by shorter-wavelength pre-*Herschel* observations.

The model takes the form:

$$S_\nu = \frac{\kappa_\nu}{D^2}\left[M_h B(\nu, T_h) + M_c B(\nu, T_c)\,\right] + S_0 \left(\frac{\nu}{\nu_0}\right)^{\alpha} \tag{2.1}$$

where S_ν is the flux at frequency ν, κ_ν is the dust mass absorption coefficient at frequency ν, M_h and M_c are the hot and cold masses, $B(\nu, T_h)$ and $B(\nu, T_c)$ are each the Planck function at frequency ν and characteristic dust temperatures T_h and T_c, D is the distance to the source, and $S_0({}^{\nu}/_{\nu_0})^{\alpha}$ is the power law describing the synchrotron component (Equation 1.15). The dust absorption coefficient κ_ν is governed by a power law described by the dust emissivity index β, such that $\kappa_\nu \propto \nu^{\beta}$.

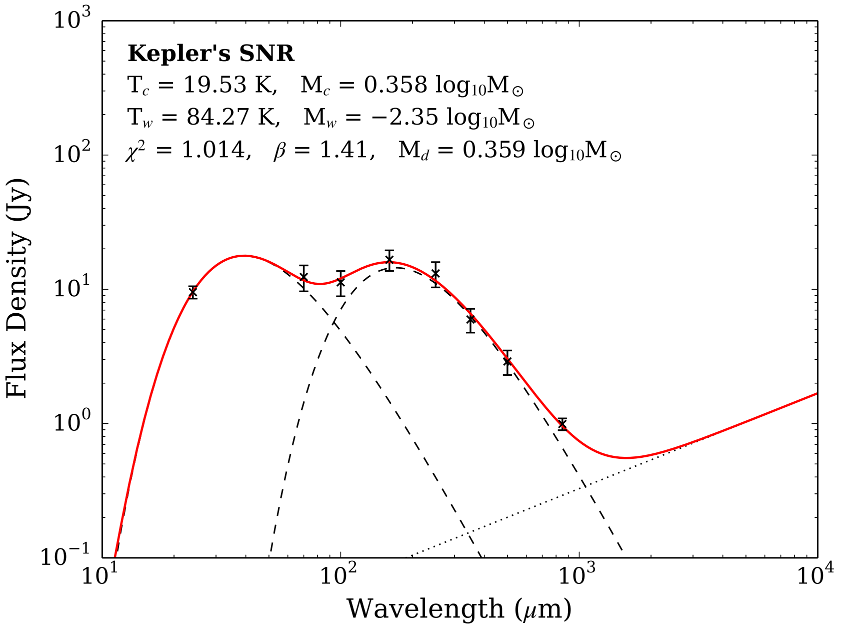

FIGURE 2.4 Spectral energy distribution of the fluxes measured towards Kepler's SNR. The SED was fit using the model described in Equation 2.1. The dashed lines indicate the best fit hot and cold dust components, whilst the dotted line is the synchrotron component; the red line shows the combined SED. Note that this represents all the flux observed in the direction of the remnant; at wavelengths 100–1,000 µm, the flux in the photometric aperture is dominated by emission from unrelated Galactic cirrus along our line of sight. Given the 5 model variables and 8 data points, the fit has 2 degrees of freedom.

To perform the SED fitting, I wrote a χ^2-minimising routine which incorporates colour-corrections for filter response function and beam area[1,2]. We employed $\kappa_{500} = 0.1\,\mathrm{m}^2\,\mathrm{kg}^{-1}$, the model of Draine & Lee (1984), which is suitable for galactic dust with $1 < \beta < 2$. For the synchrotron component, we used a value of $\alpha = -0.71$ for the remnant average spectral index, and a normalising flux of 6.1 Jy at 6.14 cm, both taken from DeLaney et al. (2002). The hot and cold dust temperatures and masses were free to vary, as was β. However the following limits were imposed: T_c and T_h must both be in the range 5–200 K; β must be > 0; and M_c and M_h must both be positive. These limits prevent nonphysical fits being returned. Both the hot and cold components have the same value of β, in order to maximise the degrees of freedom of the fit (the β value of the hot component will have minimal effect upon the properties of the cold component, for physical values of β). The resulting fitted SED can be found in Figure 2.4.

---

[1] SPIRE handbook: `http://herschel.esac.esa.int/Docs/SPIRE/spire_handbook.pdf`.

[2] PACS instrument and calibration wiki: `http://herschel.esac.esa.int/twiki/bin/view/Public/PacsCalibrationWeb`.

The best-fit SED passes within the uncertainty of every data point; assuming that the uncertainties are Gaussian, a best-fit model should be expected to pass through only two-thirds of them. Naïvely, this would suggest that either that the uncertainties are too large, or that the model is over-fitting the data. As the uncertainties only represent the standard calibration error values in each band, along with simple Poisson statistics, there is little scope for them to be any smaller.

To gauge whether the model is over-fitting the data, we can evaluate the reduced chi-squared of the fit. The reduced chi-squared statistic is defined as $\chi^2_{red} = \chi^2/k$, where k is the number of degrees of freedom in the fit. The number of degrees of freedom in a fit is defined as $k = N - n - 1$, where N is the number of data points, and n is the number of parameters. $\chi^2_{red} > 1$ indicates that the model is a poor fit to the data, whilst $\chi^2_{red} < 1$ suggests that the model is over-fitting the data; $\chi^2_{red} = 1$ is optimal. The 5 model variables and 8 data points in the fit correspond to 2 degrees of freedom. Given the best fit chi-squared of 1.014, this corresponds to $\chi^2_{red} = 0.507$, which might suggest that over-fitting is occurring. The number of degrees of freedom can be increased to 3 by fixing β; however, when fixing it to a fairly standard value of $\beta = 2$ (see Chapter 5), the chi-squared of the best-fit SED[3] increases to 4.445, giving $\chi^2_{red} = 1.48$, which is *under*-fitting the data to a similar degree. As such, the model in which β is free remains equally valid.

It should also be noted that the SED-fiting routine does not directly account for the fact the there is a ±4% correlated error the SPIRE flux calibration (incorporated into the standard ±7% photometric calibration uncertainty), shared between all three SPIRE wavebands, due to uncertainties in the model of Neptune used as the instrument calibration standard (Bendo et al., 2013). As the SPIRE wavebands trace the Rayleigh-Jeans slope of a typical cold dust SED, the effect of this correlated error will essentially be to shift the slope up or down in unison.

Parameter uncertainties were gauged by means of a Monte Carlo bootstrapping analysis, whereby the fit was repeated 5,000 times; on each occasion, the fluxes were randomly perturbed within their errors. The parameter estimates resulting from the fits were then compared; the iteratively sigma-clipped median and standard deviation of each parameter's distribution were taken to represent its uncertainty. The parameter distributions can be found in Figure 2.5. The bootstrapped medians agree well with the best-fit values for all parameters.

The best fit gives dust temperatures of $T_h = 84.3\,\mathrm{K}$ and $T_c = 19.5\,\mathrm{K}$, and

---

[3] The $\beta = 2$ fit yields $T_w = 69.7\,\mathrm{K}$, $T_c = 15.0\,\mathrm{K}$, $M_w = 3.2 \times 10^{-3}\,\mathrm{M}_\odot$ (a factor 1.38 decrease), and $M_c = 4.2\,\mathrm{M}_\odot$ (a factor 1.85 increase).

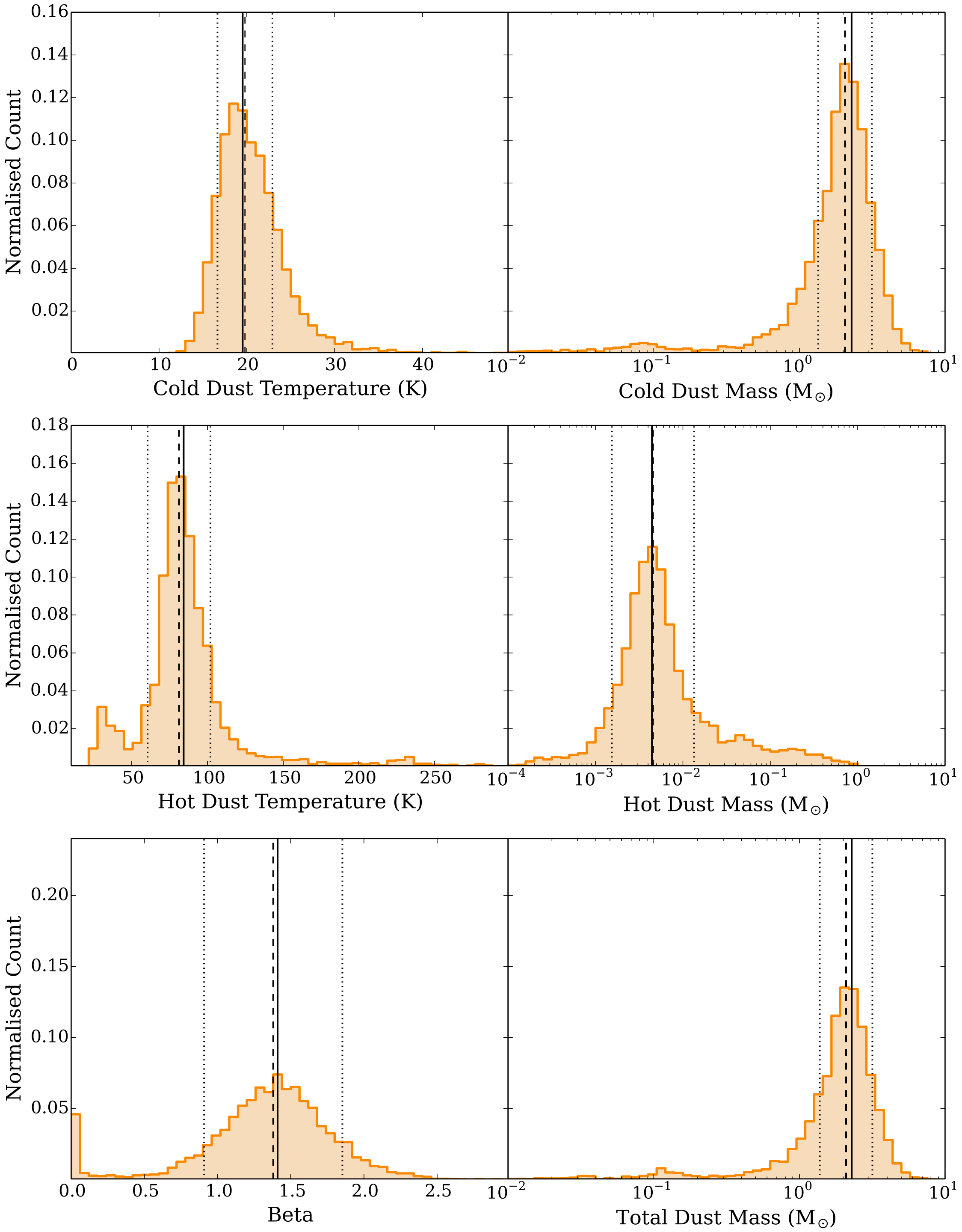

FIGURE 2.5 Distribution of parameters generated by performing 5,000 bootstrap fits to the dust SED of Kepler's SNR (Figure 2.4), using a two-greybody model described by Equation 2.1. The solid lines mark the best-fit values for each parameter; the dashed lines indicate the sigma-clipped median value from the bootstrap distribution; and the dotted lines demark 1 σ confidence intervals either side of the median, found by taking sigma-clipped standard deviation of the bootstrap distribution. The peak at $\beta \approx 0$ is because β is not permitted to vary to unphysical values of <0. Of the 5,000 bootstrap permutations, 241 (5.8%) returned fits where $\beta < 0.1$.

TABLE 2.2 Best fit and bootstrapped parameter estimates produced by fitting the SED of Kepler's SNR (Figure 2.4) with the two-greybody model described in Equation 2.1. The Bootstrapped values are the sigma-clipped median and standard deviation of the bootstrapped distribution of each parameter (Figure 2.5). The sigma-clipped standard deviations of the dust masses were calculated in logarithmic space, where the distribution is much more symmetric; as a result, the upper and lower confidence intervals are asymmetric in linear space.

Parameter	Best Fit	Bootstrapping	
		Median	Uncertainty
T_h (K)	84.3	81.3	$\pm$ 20.7
T_c (K)	19.5	19.8	$\pm$ 3.1
M_h ($10^{-3}\,\mathrm{M}_\odot$)	4.5	4.5	-3.1, +9.0
M_c ($\mathrm{M}_\odot$)	2.3	2.1	-0.7, +1.1
β	1.4	1.4	$\pm$ 0.3

dust masses of $M_h = 4.5 \times 10^{-3}\,\mathrm{M}_\odot$ and $M_c = 2.3\,\mathrm{M}_\odot$, with $\beta = 1.41$. These are all in good agreement with the median parameter values and uncertainties returned by bootstrapping, which are summarised in Table 2.2. Note that these values differ slightly (< 3%) from those we published in Gomez et al. (2012a). The fitting routine used for the published fit was normalised to the 70 μm flux, whereas mine was entirely free to fit the data. The similarity in parameter estimates is therefore reassuring. The 70 μm anchor used by Gomez et al. (2012a) also means that their bootstrapping analysis generated much smaller uncertainties than mine. Given that there is no strictly physical reason to assign the 70 μm flux a privileged position, I believe that the uncertainties presented here are more realistic.

The cold dust mass of $(2.3 \pm 1.0)\,\mathrm{M}_\odot$ is likely dominated by unrelated foreground dust. We attempted to use the JCMT ^{12}CO(2-1) observations (Figure 2.2) to account for this. At the time I conducted this analysis, the assumption was that CO emission would trace the general ISM, but not supernova ejecta – that the high-energy environment of the remnant would cause CO to disassociate. It was hoped that this would potentially make it possible to disentangle emission from dust in the foreground from any in the remnant. But since then, ALMA observations of the remnant of SN1987A have revealed that CO can survive in SNRs, at temperatures as low as $\approx$ 10 K (Kamenetzky et al., 2013). Regardless, a pixel-by-pixel comparison between the ^{12}CO(2-1) and 250 μm observations of Kepler's SNR shows that the molecular emission does a poor job of tracing the foreground cirrus. Given the cold ($\leq$ 20 K) temperature of the foreground dust, the lower-energy CO(1-0)

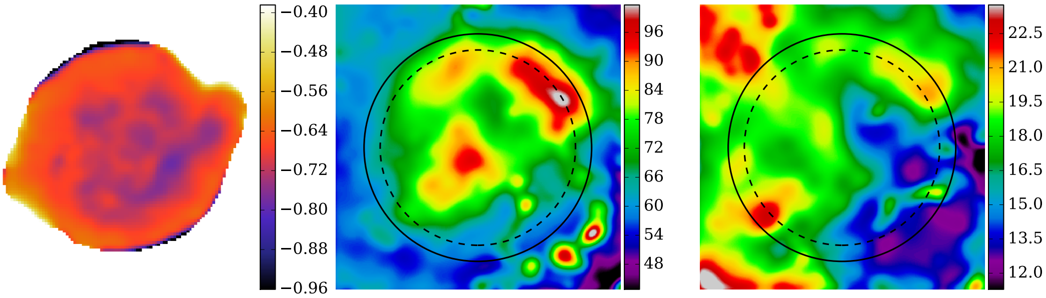

FIGURE 2.6 *Left:* Synchrotron spectral index map of Kepler's SNR, created by comparing VLA 6 and 21 cm continuum observations. *Centre:* Hot dust temperature map of the remnant, in units of kelvin. The structure of the hot dust emission, as traced by the MIR observations, is clearly visible. *Right:* Cold dust temperature map of the remnant, in units of kelvin. Clearly visible Northeast and Southeast are the prominent clouds of intervening cirrus visible in FIR and CO. Additionally, at the top right there appears to be a cold dust feature, slightly warmer than its surroundings, that traces the outer edge of the bright Northwest portion of the shockwave. Each image is 5′ across. The solid circles demark the 120″ photometric aperture. The dashed circle indicates the outer edge of the forward shock at 103″ (DeLaney et al., 2002).

transition might have been a better-suited tracer; however, such observations are not available.

2.1.2 TEMPERATURE MAPS

As an alternative approach to identifying cold dust features associated with Kepler's SNR, I created dust temperature maps of the region. As before, the 24–500 µm maps were re-gridded to a common 1″ pixel scale, then convolved with a Gaussian so that they were all at the 36″ resolution of the SPIRE 500 µm beam. The maps were then background subtracted, using the same sky apertures as previously. In order to remove the synchrotron component, I made a spectral index map of the remnant using 6 and 21 cm VLA continuum observations (shown in the left pane of Figure 2.6), which was used in conjunction with the 6 cm data to remove the synchrotron flux pixel-by-pixel in each band. The flux in each of the 24–500 µm maps was then compared pixel-by-pixel, and fit with a two-component greybody model; this returned hot and cold temperature values for every pixel. Finally, a median filter was used to remove bad pixels (typically the result of the greybody fit failing due to low signal-to-noise). The resulting temperature maps are shown in Figure 2.6

As expected, the hot temperature map traces the hot dust emission that dominates in the 24 and 70 µm images, showing dust warmed by shock heating as it is swept up by the advancing blastwave. The warmest region, peaking at $\sim$ 105 K, corresponds to the bright, dense Northeast arc of the remnant. Also as expected, the cold temperature map clearly shows the clouds of unrelated interstellar dust to the Northwest and Southwest of the remnant, as visible in the submm observations. However, the Northeast arc of the remnant also appears to be visible in the cold map. Interestingly, it lies $\sim$10–20$''$ in advance of the 103$''$ outer edge of the shockfront as visible in X-ray and radio observations (DeLaney et al., 2002), even when the low resolution (36$''$) of the temperature maps is considered.

Although our view of Kepler's SNR is obscured by large amounts of intervening Galactic cirrus, the remnant itself lies above the Galactic plane, in a region of relatively low-density ISM (Hughes, 1999); there is not enough interstellar dust in the vicinity of the remnant to account sufficient mass to correspond to a feature such as the Northwestern arc in the cold dust map.

Similarly, it is unlikely that the swept-up hot dust is merely swept-up ISM; more likely it is CSM produced by a star in the region of the supernova. And given the location of Kepler's SNR above the Galactic plane, and its high peculiar velocity moving further away from it (Borkowski et al., 1994), it would be surprising if this CSM originated from a star *not* associated with the supernova's progenitor.

If Kepler's supernova was a standard single-degenerate Type-Ia event, then it is unlikely that the CSM originates from the white dwarf progenitor itself. White dwarfs do not have stellar winds, so if the CSM originated from the progenitor, it would have to have been produced whilst it was undergoing the planetary nebula phase – immediately after which the newborn white dwarf gave rise to the supernova, which somehow didn't destroy the CSM. A more believable scenario would be that the CSM originates from a companion star to the progenitor.

Alternatively, the CSM could indicate that Kepler's supernova was of the speculative single-star type, arising from a super-AGB star thermonuclear conflagration (Miyaji et al., 1980; Denissenkov et al., 2013). Given that such events arise from stars undergoing significant mass-loss, the presence of CSM swept up by the remnant would be expected (Silverman et al., 2013). This could also explain the peculiarities in the elemental abundances observed in the remnant's spectra, not characteristic of a standard white dwarf progenitor (Hughes, 1999). Type-Ia supernovae that exhibit CSM features are preferentially found in late-type galaxies with young stellar populations (Maguire et al., 2013), suggesting that younger, more massive stars play a role in these events (Takahashi et al., 2013). An X-ray investigation with *Chandra* of Kepler's SNR by Reynolds et al. (2007) suggests that

SN1604 may have had just such an origin.

Regardless, as apparently swept-up material, that the dust associated with the Northwest feature in the hot temperature map would not have been produced by the supernova itself. As such, there is no evidence that Kepler's supernova resulted in significant dust production. This is surprising, as models of dust production in Type-Ia supernovae predict that a remnant the age of Kepler's SNR should contain ~ 0.01–$0.1\,\mathrm{M}_\odot$ of dust, depending upon the density of the local ISM (Nozawa et al., 2011).

2.2 TYCHO'S SUPERNOVA REMNANT

> *'When I had satisfied myself that no star of that kind had ever shone before, I was led into such perplexity by the unbelievability of the thing that I began to doubt the faith of my own eyes.'*
>
> TYCHO BRAHE

Observed in November 1572, and described by aristocrat-scientist Tycho Brahe (Tycho, 1573), Tycho's Supernova (SN1572) importantly served as the key counterexample to the notion of the immutability of the heavens in Renaissance Europe. Examination of the spectra of the supernova's light echo, reflected by surrounding interstellar clouds, reveals the explosion to be a standard Type-Ia event, supported by the possible detection of a binary companion to the progenitor (Krause et al., 2008). The remnant is located at coordinates $\alpha = 6.3308^\circ$, $\delta = 64.1372^\circ$ (J2000), in the Galactic plane, at a distance of 3.8 kpc, in agreement with the distance to the possible progenitor companion (Krause et al., 2008).

The study detailed here of the Tycho remnant closely follows the process described in Section 2.1 for the Kepler remnant. As with Kepler's SNR, emission from the direction of Tycho's SNR will be a combination of hot dust, synchrotron, intervening Galactic cirrus along our line of sight, and any cold dust present in the remnant itself. The remnant was observed in all 6 photometric *Herschel* bands as part of the MESS survey. We also made use of *Spitzer* 24 μm[4] and Very Large Array (VLA) 18 cm[5] data. The observations of the remnant in all these bands are

---

[4] Spitzer Heritage Archive: `http://sha.ipac.caltech.edu/applications/Spitzer/SHA/`.

[5] NRAO/VLA Archive Survey (Crossley et al., 2007): `http://archive.nrao.edu/nvas/`.

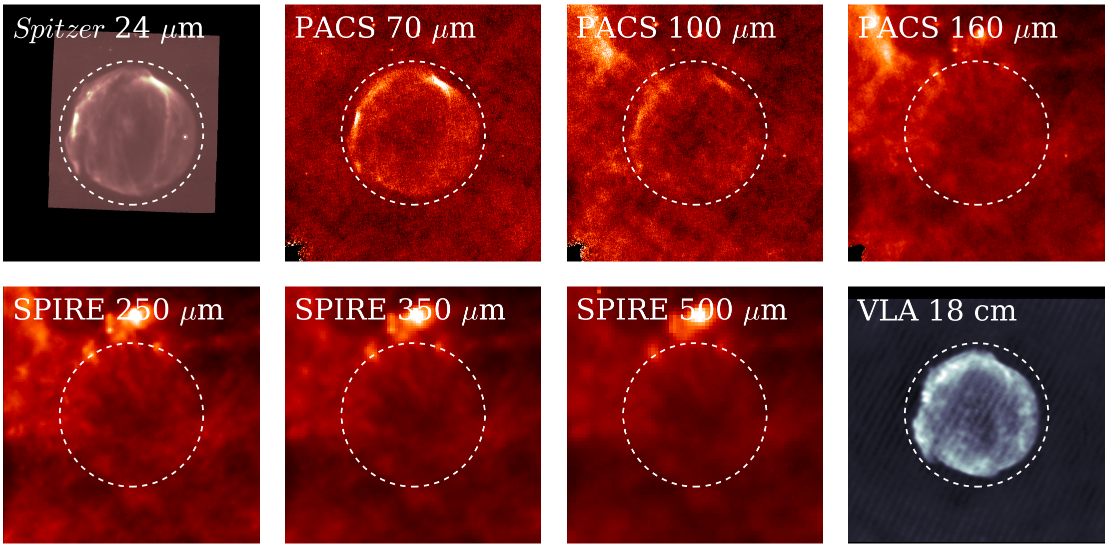

FIGURE 2.7 Multiwavelength imagery of Tycho's SNR, as seen in MIR to radio wavelengths. *Upper row: Spitzer* 24 μm; PACS 70, 100, and 160 μm. *Lower row:* SPIRE 250, 350, and 500 μm; and VLA 6 cm. The dashed circles have a radius of 280″ centred at $\alpha = 6.3308^\circ$, $\delta = 64.1372^\circ$ (J2000), representing the photometric aperture employed (the forward shock radius being 251″, Warren et al., 2005). Each cutout is 1000″ across.

displayed in Figure 2.7.

Visual inspection of the observations clearly show the emission from hot dust at $\leq 100\,\mu$m, tracing the forward shock's 251″ radius (Warren et al., 2005). At FIR and submm wavelengths Galactic cirrus along our line of sight dominates; no structures which resemble the remnant are apparent at first glance. However the regions corresponding to the edge of the remnant do show more emission than the centre; previous studies have shown that Tycho's SNR is sweeping up material from the surrounding ISM (Reynoso et al., 1999; Cai et al., 2009).

Also in the area observed by *Herschel* are regions of star formation activity, visible as the bright areas North and West of the remnant in Figure 2.8. The star-forming regions North-northeast of the remnant, which exhibit the cold temperatures characteristic of pre-stellar cores (André et al., 2009), actually intersect the position of the supernova's forward shockfront. Whilst observations of other remnants have suggested supernova shocks can serve as a means to trigger star formation (Reach & Rho, 1999), pre-stellar cores take of order 10^5 years to form; therefore these cores were already present when the supernova occurred 440 years ago.

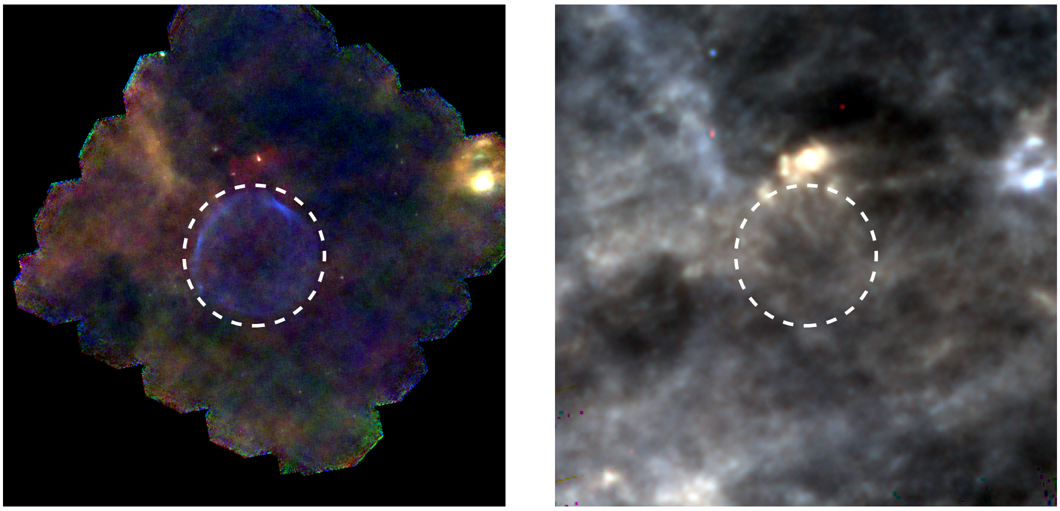

FIGURE 2.8 Three colour *Left:* PACS 70, 100, and 160 µm, and *Right:* SPIRE 250, 350, and 500 µm images of a 2,000″ × 2,000″ region centred upon Tycho's SNR. Hot dust emission from the remnant is clearly visible at the shortest *Herschel* wavelengths, but contamination from interstellar cirrus quickly dominates at longer wavelengths. The dashed circles have a radius of 280″ centred at $\alpha = 6.3308°$, $\delta = 64.1372°$ (J2000), representing the photometric aperture employed.

2.2.1 PHOTOMETRY AND SED FITTING

As with Kepler's SNR, the *Spitzer* PACS, and SPIRE maps of Tycho's SNR were re-gridded to a 1″ pixel scale and convolved to the 36″ 500 µm beam. The flux of the remnant was measured using a 280″ radius aperture, to encompass the convolved emission at all bands; sky apertures of the same size were placed upon the darkest region of each map. As with Kepler's SNR, this means that we are only measuring the total flux coming from the direction of the remnant, which is dominated by intervening Galactic cirrus; the bright and variable nature of the foreground material means there is no way to directly subtract its contribution. The measured fluxes are compiled in Table 2.3. Uncertainties were determined in the same manner as described in Section 2.1.1.

The SED of Tycho's SNR is shown in Figure 2.9. Using the same method detailed in Section 2.1.1, we fit the SED with the model described by Equation 1.15. The synchrotron component was anchored to a 18 cm flux of 43.8 Jy, with a mean spectral index of $\alpha = -0.61$, taken from Green (2001). We take account of the 0.5% per year decrease observed in the radio flux, in order for our synchrotron subtraction to be suitable for the epoch of the *Herschel* observations. We again use

TABLE 2.3 MIR-to-submm fluxes measured in the direction of Tycho's SNR. The photometry was conducted by me, and published in Gomez et al. (2012a). Note that the flux at 100–1,000 µm is dominated by contamination from foreground Galactic cirrus. The contribution of the synchrotron component in each band was determined using the power law term of Equation 1.15.

Wavelength (µm)	Integrated Flux (Jy)	Uncertainty (Jy)	Synchrotron Flux (Jy)
24	20.1	± 3.0	0.19
70	44.8	± 10.8	0.36
100	41.1	± 8.8	0.45
160	59.0	± 14.1	0.60
250	42.7	± 8.6	0.79
350	32.8	± 6.5	0.97
500	17.6	± 3.5	1.21

TABLE 2.4 Best fit and bootstrapped parameter estimates produced by fitting the SED of Tycho's SNR (Figure 2.9) with the two-greybody model described in Equation 2.1. The bootstrapped values are presented in the same manner as in Table 2.2.

Parameter	Best Fit	Bootstrapping	
		Median	Uncertainty
T_h (K)	89.9	83.9	± 23.4
T_c (K)	21.6	22.0	± 4.8
M_h ($10^{-2}\,\mathrm{M}_\odot$)	7.1	8.4	-5.6, +16.8
M_c ($\mathrm{M}_\odot$)	11.1	8.3	-4.9, +11.7
β	0.6	0.7	± 0.5

the Draine & Lee (1984) emissivity model of $\kappa_{500} = 0.1\,\mathrm{m}^2\,\mathrm{kg}^{-1}$. Uncertainties were gauged by means of a boostrapping analysis, the results of which are displayed in Figure 2.10.

The best fit gives dust temperatures of $T_h = 89.9\,\mathrm{K}$ and $T_c = 21.6\,\mathrm{K}$, and dust masses of $M_h = 7.1 \times 10^{-2}\,\mathrm{M}_\odot$ and $M_c = 11.1\,\mathrm{M}_\odot$, with $\beta = 0.60$. These are all in agreement with the median parameter values and uncertainties returned by bootstrapping, which are given in Table 2.4. As with Kepler's SNR, these results differ from those published in our analysis in Gomez et al. (2012a), which employed a fitting routine anchored to the 70 µm flux. The derived temperatures are almost identical (to within 1 K), however I find a total dust mass ~2.5 times greater

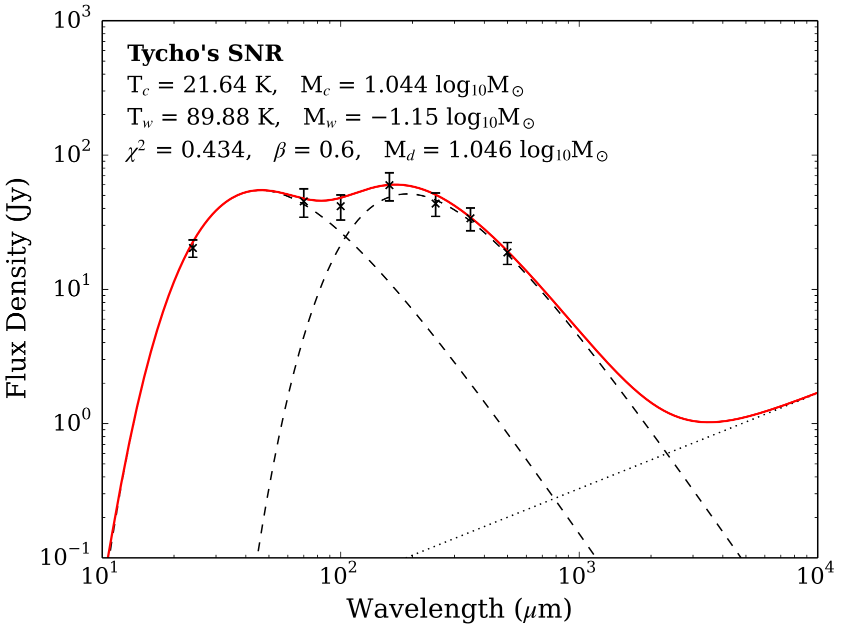

FIGURE 2.9 Spectral energy distribution of the fluxes measured towards Tycho's SNR. The SED was fit using the model described in Equation 2.1. The dashed lines indicate the best fit hot and cold dust components, whilst the dotted line is the synchrotron component; the red line shows the combined SED. Note that this represents all the flux observed in the direction of the remnant; at wavelengths 100–2,000 µm, the flux in the photometric aperture is dominated by emission from unrelated Galactic cirrus along our line of sight. Given the 5 model variables and 7 data points, the fit has 1 degree of freedom.

than the published values; this arises primarily from the fact that β is poorly constrained by my fit, as demonstrated by the bootstrapped distribution shown in Figure 2.10.

As with the SED of Kepler's SNR, the best-fit SED to the fluxes of Tycho's SNR passes within the uncertainty of every data point. Given the 5 model variables and 6 data points, the fit has 1 degree of freedom; given the best-fit chi-squared of 0.434, this yields $\chi^2_{red} = 0.434$, indicating that the model could be over-fitting the data. By fixing β to a value of 2, it is possible to examine the effect of increasing the number of degrees of freedom. Another motivation for such a test is the fact that typical measurements of β for galactic dust (along with κ_d estimates, such as the Draine & Lee, 1984 value used here) are in the range $1 < \beta < 2$; the best fit value of $\beta = 0.6$ for Tycho is therefore notably low (although the uncertainty of $\pm\,0.5$ means that it is nonetheless not incompatible with the standard range). Employing a fixed $\beta = 2$ gives a best fit chi-squared of 3.427, and hence $\chi^2_{red} = 1.718$ – therefore underfitting the data to a much greater degree than that by which the data was over-fitted when β was left free. As such, the model in which β is free remains preferred.

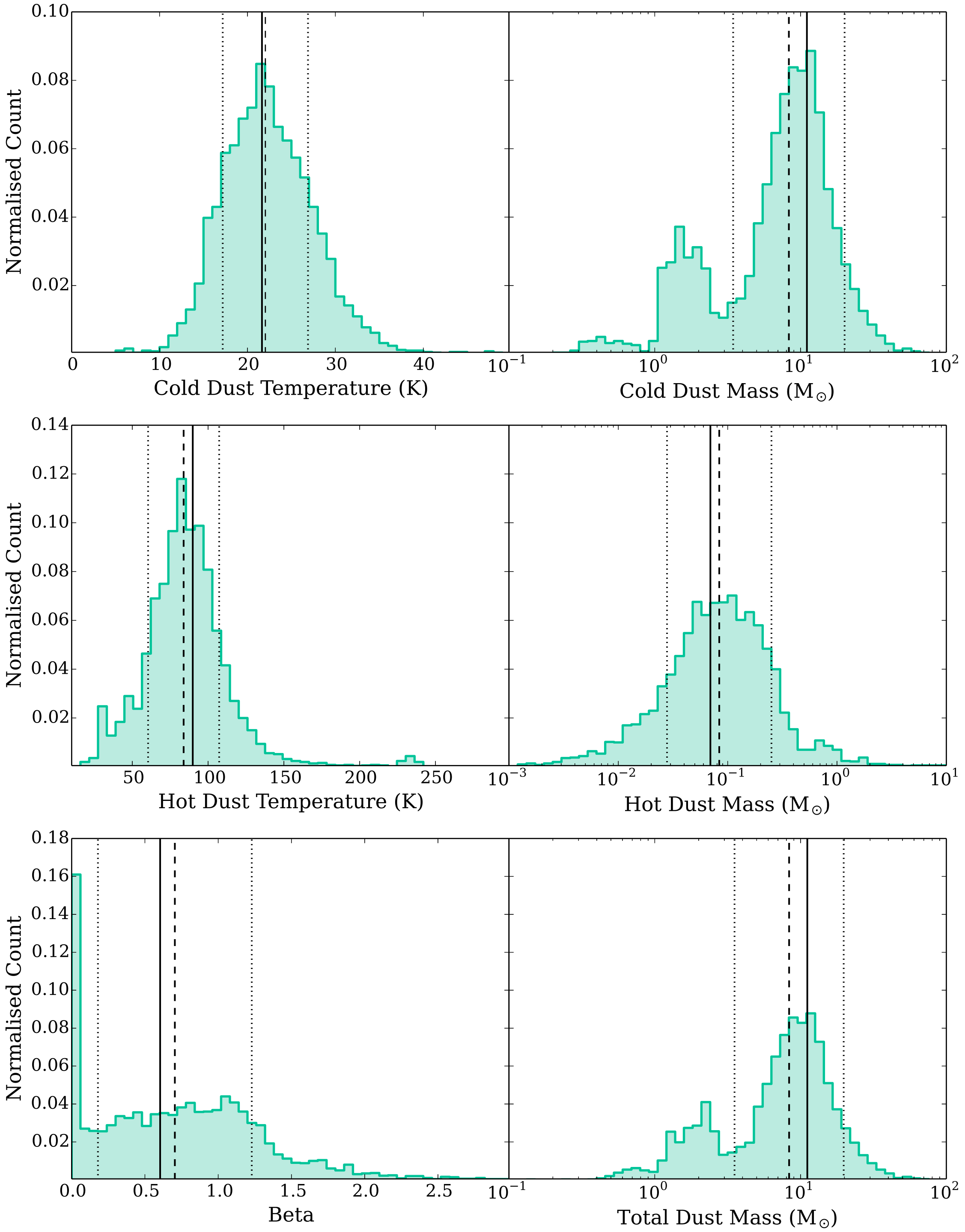

FIGURE 2.10 Distribution of parameters generated by performing 5,000 bootstrap fits to the dust SED of Tycho's SNR (Figure 2.9), using the two-greybody model described by Equation 2.1. Best-fit, bootstrapped median, and boostrapped confidence intervals are indicated in the same manner as in Figure 2.5. The peak at $\beta \approx 0$ is because β is not permitted to vary to unphysical values of <0. Of the 5,000 bootstrap permutations, 897 (17.6%) returned fits where $\beta < 0.1$. In general, β is poorly constrained, with the bootstrap fits being more-or-less equally likely to fall in the range $0 \gtrsim \beta \gtrsim 1.5$.

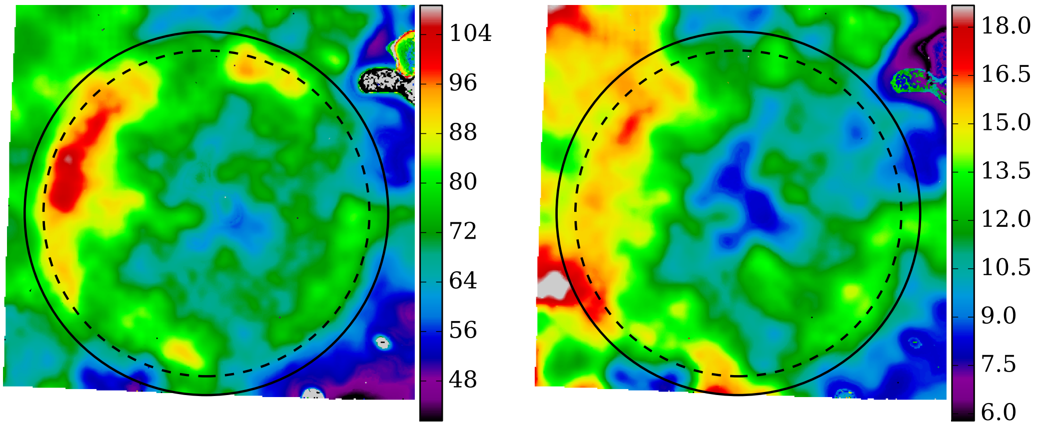

FIGURE 2.11 *Left:* Hot dust temperature map of Tycho's SNR. The hot dust morphology, as seen in MIR observations, is clearly visible. *Right:* Cold dust temperature map of the remnant. As well as the intervening Galactic cirrus, there are cold features at the Southwest and North-northwest of the remnant that spatially correspond to the hot dust structure. Each image is 640″ across. The solid circles demark the 280″ photometric aperture. The dashed circle indicates the outer edge of the forward shock at 251″. Temperatures are in units of kelvin.

Even with such a large difference in fit quality, the $\beta = 2$ model yields best-fit parameters[6] that are all within 2σ of the free-β model, given the bootstrapped uncertainties, with only a 21% difference in total dust mass.

2.2.2 TEMPERATURE MAPS

I created temperature maps of Tycho's SNR, as a potential way of identifying cold dust features associated with the remnant. As with Kepler's SNR, the 24–500 µm maps were re-gridded to a common 1″ pixel scale, then convolved with a Gaussian so that they were all at the 36″ resolution of the SPIRE 500 µm beam. The maps were then background subtracted, using the same sky apertures as for the photometry. In order to remove the synchrotron component, I also re-gridded the 18 cm VLA continuum maps to the same 1″ pixel scale, and extrapolated the flux to be subtracted using the average spectral index of $\alpha = -0.61$. The flux in each set of aligned pixels from 24–500 µm was compared, and fit with a two-component greybody; this returned hot and cold temperature values for each pixel. Finally, a median filter was used to remove bad pixels. The resulting temperature maps are

---

[6] The $\beta = 2$ fit yields $T_w = 62.6\,\mathrm{K}$, $T_c = 13.2\,\mathrm{K}$, $M_w = 1.8 \times 10^{-2}\,\mathrm{M}_\odot$ (a factor 3.99 decrease), and $M_c = 4.2\,\mathrm{M}_\odot$ (a factor 1.21 increase).

shown in Figure 2.11. The anomalous feature in the upper right of the temperature maps is due to a region of low signal-to-noise in the *Herschel* maps.

The hot dust morphology visible at MIR wavelengths is readily apparent in the hot temperature map, with particularly prominent hot features to the Northeast, North-northwest, Southwest, and South. These same features seem also seem to be present as slightly warmer regions in the cold temperature map. In Gomez et al. (2012a), we show that the hot dust of Tycho's SNR closely follows the hard X-ray emission tracing the outer edge of the shock. This emission is most prominent where the shock meets denser patches of ISM, as traced by CO observations (see Gomez et al., 2012a). Given that all the structures apparently associated with the remnant in the cold temperature map are co-incident with these collisional features, it appears that they originate from swept-up ISM.

The best-fit cold dust mass of $M_c = 11.1\,\mathrm{M}_\odot$ is extremely unlikely to represent the mass of accumulated ISM, as this would suggest that the remnant has swept up $\gtrsim 1{,}000\,\mathrm{M}_\odot$ of gas – highly unphysical for a remnant only 440 years old (therefore still in the Sedov phase). However, our line of sight to Tycho's SNR intersects ~ 500–$2{,}000\,\mathrm{M}_\odot$ of ISM (Gomez et al., 2012a), so we should expect our submm fluxes to be dominated by foreground interstellar dust. As this foreground dust we lie at a different distance than the remnant, the calculated dust mass will be misleading.

Overall, there is no evidence that significant production of dust occurred in Tycho's supernova. As with Kepler's SNR, this is surprising, as models of dust production in Type-Ia supernovae predict that a remnant the age of Tycho's SNR should contain ~ 0.01–$0.1\,\mathrm{M}_\odot$ of manufactured dust (Nozawa et al., 2011).

2.3 THE CRAB NEBULA

> *'Astronomy can be split into two studies: the Crab Nebula, and everything else.'*
>
> PHIL PLAIT

Observed on 4th July 1054 by Chinese astronomers (Yang, 1054), SN1054 is the third most recent Milky Way supernova known with confidence to have been a Type-II event. In contrast to Kepler and Tycho's Type-Ia supernovæ, this makes it particularly relevant to study with a view to explaining the potential contribution of massive-star supernovæ to the dust mass in high-redshift galaxies. The remnant of SN1054, the Crab Nebula (Messier 1), is a pulsar wind nebula located 2 kpc away (Trimble, 1968), and one of the most studied objects in the sky (see review in Hester 2008). The central Crab Pulsar is essentially the holotypical neutron star by virtue of its proximity, youth and well-constrained history. The Crab Nebula is located at coordinates $\alpha = 83.6330°$, $\delta = 22.0144°$ (J2000).

The Crab Nebula exhibits a filamentary structure in its ejecta, visible in the optical and mid- and far-IR, carved by the activity of the pulsar wind. Also visible, across almost the entire electromagnetic spectrum, is smooth synchrotron emission generated by the pulsar's magnetic field, centred on the jet and torus structure surrounding the pulsar itself. Previous IR observations of the Crab with the Infrared Space Observatory (ISO) and SCUBA suggested the presence of 0.02–0.07 $M_\odot$ of dust (Green et al., 2004), whilst studies using *Spitzer* photometry and spectra have given dust masses of 0.001–0.01 $M_\odot$ (Temim et al., 2006, 2012).

Investigation of the dust-mass properties of the Crab are complicated by several factors. Line emission is known to account for a significant fraction of the mid-IR emission, approaching 50% at 20 µm (Temim et al., 2012); however the line emission has not previously been characterised at wavelengths > 38 µm. Also, the intense magnetic fields of the pulsar wind nebula mean that synchrotron radiation dominates the emission from the Crab at most wavelengths, from UV to radio; to further complicate matters, the behaviour of the synchrotron component has not been well constrained at FIR and submm wavelengths. Moreover, previous estimates of the dust mass associated with the Crab have been derived only from observations in the MIR (excepting 850 µm SCUBA observations by Green et al., 2004, which were entirely synchrotron dominated).

The nature of the synchrotron component has been particularly heavily disputed over the past decade. It appears not to be described by a single, continuous power law, but rather experiences breaks across its wavelength range. Macías-Pérez et al. (2010) and Temim et al. (2012) suggest a single break, somewhere between 10 µm and 1,000 µm (the same range as thermal emission from any dust present), with a power law spectral index of $\alpha = 0.3$ breaking to $\alpha = 0.7$, varying by over a factor of two accross the remnant (Temim et al., 2006). Comparing 850 µm SCUBA and 20 cm VLA observations to other pre-existing measurements, Green et al. (2004) find evidence for two breaks in the spectrum, at roughly 250 µm and 10 µm respectively, but with much less variation in spectral index across the nebula. Bandiera et al. (2002) even find some justification for a fourth spectral index break in the millimetre range. Ultimately, until now there have not been

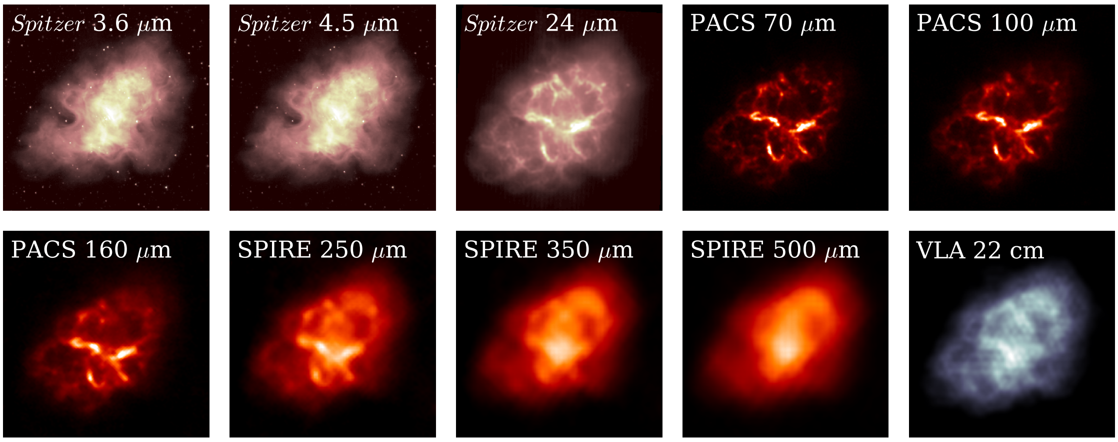

Figure 2.12 Multiwavelength imagery of the Crab Nebula, as seen in MIR to radio wavelengths. *Upper row: Spitzer* 3.6, 4.5, and 24 μm; and PACS 70 and 100 μm. *Lower row:* PACS 160 μm; SPIRE 250, 350, and 500 μm; and VLA 22 cm. Note the absence in all bands of contamination from Galactic cirrus. Each cutout is $450''$ across, centred at $\alpha = 83.6330^\circ$, $\delta = 22.0217^\circ$ (J2000).

enough precise, consistent observations over the IR-submm wavelength range to decisively settle the issue.

2.3.1 Photometry and SED Fitting

The advent of the *Herschel* era presents us with the ability to address all of the issues that have, until now, prevented a reliable estimate of the dust mass of the Crab Nebula. The Crab Nebula was observed both photometrically and spectroscopically by PACS and SPIRE. *Spitzer*, *Herschel*, and VLA imagery of the Crab Nebula can been found in Figure 2.12. The morphology differs strikingly between bands, due to variation in emission mechanisms across wavelengths. In the NIR *Spitzer* 3.6 and 4.5 μm bands, the observed emission is almost exclusively synchrotron radiation; indeed, the Crab Pulsar, along with its torus and jets, are visible in the centre of the remnant in these bands. Synchrotron also dominates the flux at 500 μm, and 22 cm, but at these longer wavelengths its structure is composed of arcs and lobes. However, from 24–350 μm the filamentary ejecta are clearly visible, superimposed upon the diffuse synchrotron emission; the flux from these filaments consists of both line emission and thermal dust emission (see below).

The combination of data from *Spitzer*, the Infrared Space Observatory (ISO), PACS Integral Field Unit (IFU), and SPIRE Fourier Transform Spectrometer (FTS) spectroscopy provide emission line coverage of the entire dust wavelength range out to beyond 600 µm, allowing for accurate photometric measurement of continuum dust emission using those same instruments, since the line emission is now constrained. The recent comprehensive study of near- and mid-IR line emission in the Crab conducted by Temim et al. (2012) using *Spitzer*-IRS spectroscopy places the contribution due to line emission in the 24 µm *Spitzer*-MIPS band (after synchrotron subtraction) at 43%; whilst Gomez et al. (2012b) find using ISO and PACS spectroscopy that line emission contributes an average of 4.9% and 9.9% in the PACS 70 and 100 µm bands respectively (again after synchrotron subtraction). Gomez et al. (2012b) find negligible contribution to the PACS 160 µm and SPIRE wavelengths. The SPIRE FTS spectra did, however, provide the first identification of a noble gas molecule in space, in the form of $^{36}\mathrm{ArH}^{+}$ in the nebula's filaments (Barlow et al., 2013).

Serendipitously, *Herschel* observations of the Crab show that it sits in a region of sky devoid of Galactic cirrus, as shown in Figure 2.13, in stark contrast to the Kepler and Tycho remnants. This greatly enhances the reliability of mass and temperature estimates of dust associated with the remnant, and our ability to analyse the FIR and submm structure of the nebula. Moreover, it means that we can be confident that any dust associated with the remnant was indeed produced by the supernova.

Herschel's sister observatory *Planck* has the most finely-calibrated millimetre-range detectors ever placed in orbit, and the two observatories were designed to make complementary observations – providing the ideal means with which to address Crab's poorly-constrained synchrotron spectrum. Furthermore, observations of the Crab by *Planck* and *Herschel* were conducted in the same epoch, thus negating any inconsistencies born of the remnant's decreasing synchrotron flux (Aller & Reynolds, 1985). In combination, *Herschel* and *Planck* observations allow for the best determination to date of the synchrotron emission over the FIR-millimetre wavelength range. Gomez et al. (2012b), using *Spitzer*, *Herschel*, and *Planck* data, find that at wavelengths 3.6–10,000 µm the Crab's synchrotron emission is fit well by *one* power law component with spectral index $\alpha = 0.417 \pm 0.006$, anchored to a flux of 1,489 Jy at a wavelength of 300 mm.

However here I opt to employ a more thorough, Monte Carlo approach to characterise the behaviour and uncertainty of the synchrotron spectrum, for two reasons. Firstly, synchrotron emission dominates the flux of the Crab across the *Spitzer* and *Herschel* wavelength ranges; therefore the uncertainty in the flux due to dust emission in these bands will be sensitive to the uncertainty in the synchrotron subtraction. Secondly, in Gomez et al. (2012b) we only consider the uncertainty in

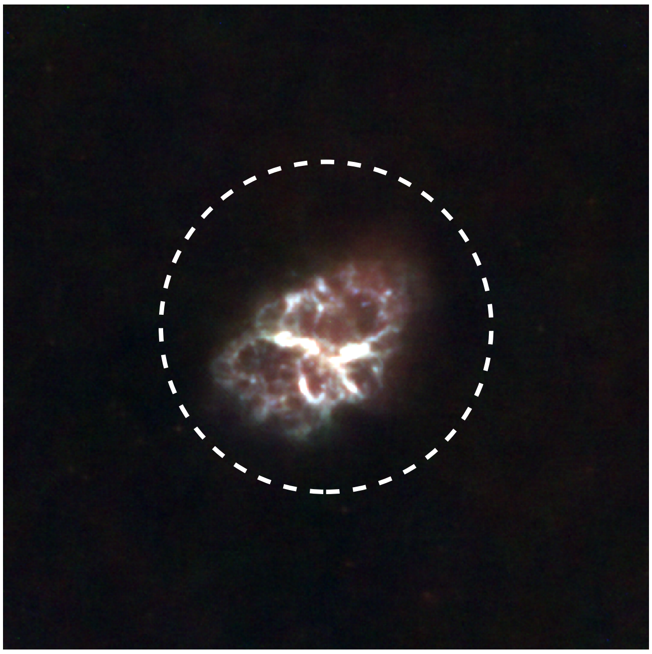

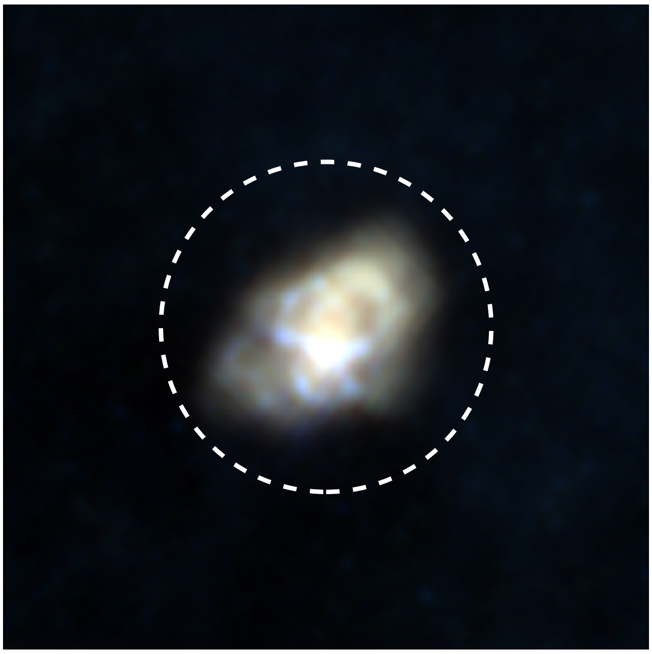

FIGURE 2.13 Three colour *Upper:* PACS 70, 100, and 160 µm, and *Lower:* SPIRE 250, 350, and 500 µm images of a 1,000″ × 1,000″ region centred upon The Crab Nebula. The diffuse redder glow in each image is the synchrotron radiation, which gets progressively brighter at longer wavelengths. The filamentary ejecta are clearly visible, arising from both line and thermal dust emission. Note the the lack of contamination from Galactic cirrus, in contrast to Kepler's and Tycho's SNRs. The dashed circles have a radius of 256″ centred at $\alpha = 83.6330^\circ$, $\delta = 22.0144^\circ$ (J2000), representing the photometric aperture employed.

the spectral index – not the anchor flux.

I performed 10,000 bootstrap fits of the model described by Equation 1.15 to the synchrotron-dominated *Spitzer* 3.6–8.0 μm and *Planck* 550–10,000 μm fluxes; the upper pane of Figure 2.14 shows the synchrotron fluxes with the bootstrapped fits over-plotted. The bootstrapped parameter distributions for the spectral index α, and anchor flux S_0, are shown in the lower panes of Figure 2.14. As a matter of convenience, I retained the choice of 300 mm as anchor wavelength.

The best fit to the unperturbed synchrotron fluxes returns parameter estimates of $\alpha = 0.4121$ and $S_0 = 1,436$ Jy. The bootstrapped parameter distributions give iteratively sigma-clipped median values of $\alpha = 0.4121 \pm 0.0041$ and $S_0 = 1,434 \pm 62$ Jy. Note that the best fit and median values are within 0.1% of one another for both parameters. For expediency, I opt to use the median values to describe the synchrotron power law, as they are not meaningfully different from the best fit values, and have the benefit of possessing well-constrained uncertainties. My spectral index estimate is within the uncertainty of the Gomez et al. (2012b) value of $\alpha = 0.417 \pm 0.006$ (but not vice-a-versa).

I used the median α and S_0 to estimate the synchrotron contribution in each photometric band, and characterised the uncertainty in these estimates by taking the sigma-clipped standard deviation of the fluxes generated at each wavelength by the bootstrapped values. The resulting values are given in Table 2.5. This additional degree of uncertainty introduced by the synchrotron subtraction is significant; it corresponds to 11% and 7% of the dust flux at 350 and 500 μm respectively.

Armed with precise determinations of the behaviour of the Crab's synchrotron radiation and line emission, it is now possible to accurately measure the contribution of dust emission to the integrated flux of the Crab Nebula. To perform photometry of the nebula, I re-gridded the *Spitzer* 24 μm and *Herschel* maps to a 1.6″ pixel scale, and convolved them to the 36″ resolution of the 500 μm beam. The flux of the remnant in each waveband was the measured using a 256″ source aperture (Figure 2.13) with an annular background aperture. Uncertainties are a combination of the aperture noise and calibration uncertainties. The measured fluxes can be found in Table 2.5, and were presented in Gomez et al. (2012b).

I used this photometry to fit the SED of the Crab Nebula following the method described in Section 2.1.1, using the model described in Equation 2.1, which consists of two greybody dust components and a power law synchrotron component. I once again used the $\kappa_{500} = 0.1\,\mathrm{m^2\,kg^{-1}}$ model of Draine & Lee (1984), appropriate for Milky Way dust grains.

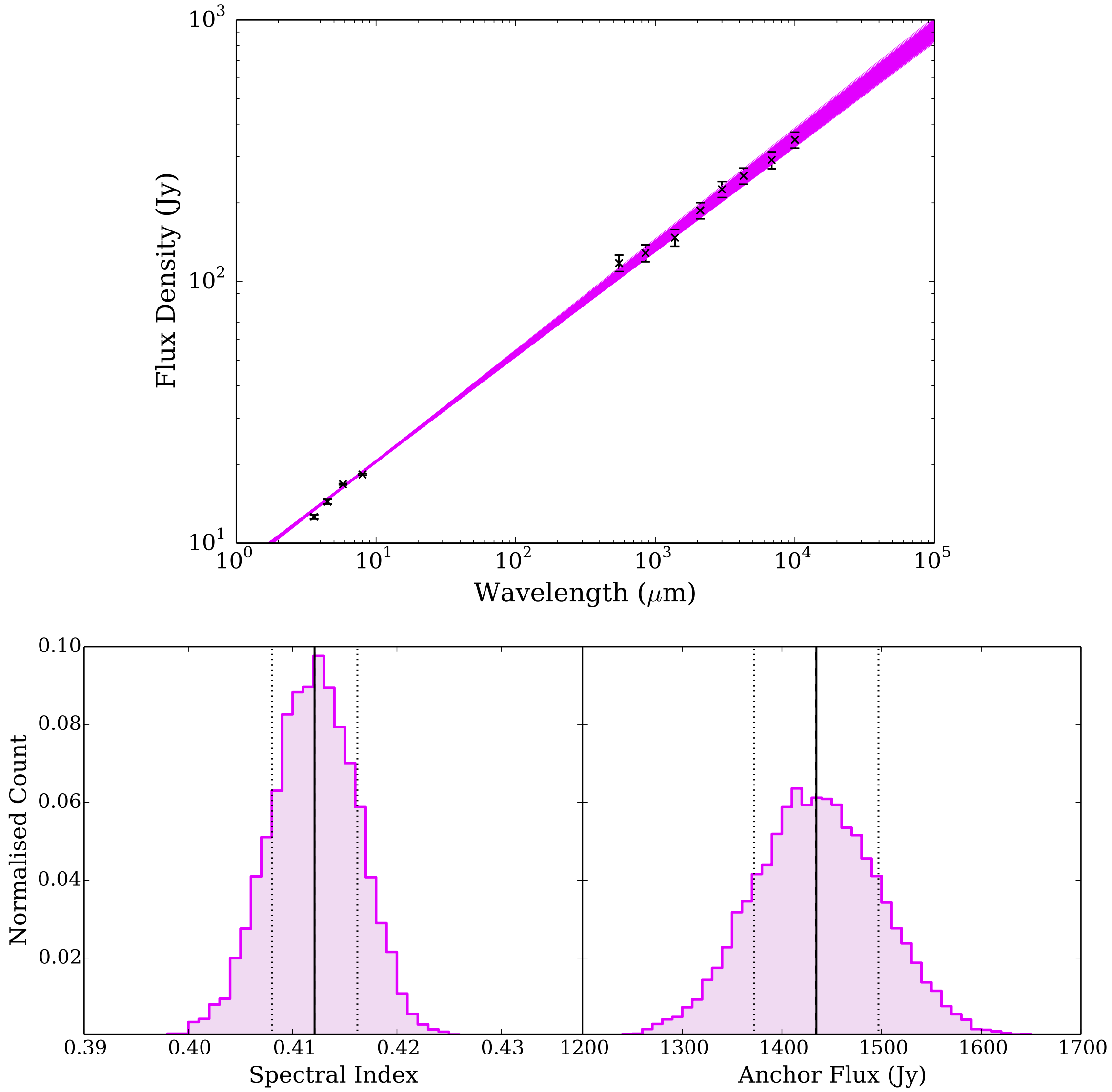

FIGURE 2.14 *Upper:* Bootstrapped synchrotron spectral energy distribution of the Crab Nebula, showing the 10,000 fits made to randomly perturbed re-samplings of the *Spitzer* 3.6–8.0 µm and *Planck* 550–10,000 µm fluxes. *Lower:* Distribution of parameters generated by performing 10,000 bootstrap fits to the synchrotron SED of the Crab Nebula, using the power law model described by Equation 1.15. Best-fit, bootstrapped median, and boostrapped confidence intervals are indicated in the same manner as in Figure 2.5. The best fit and bootstrapped median values are in excellent agreement.

TABLE 2.5 NIR-to-submm photometry of the Crab Nebula, as published in Gomez et al. (2012b). *Spitzer* 3.6–8.0 µm fluxes are from Temim et al. (2006), and *Planck* fluxes are from Planck Collaboration et al. (2011b). *Spitzer* 24 µm and *Herschel* fluxes were measured by me. Synchrotron flux density in each band was calculated using a power law described by Equation 1.15, with uncertainties estimated by means of a bootstrapping analysis (Figure 2.14). Line emission contributions determined using values from Temim et al. (2012) and Gomez et al. (2012b).

Wavelength	Integrated		Synchrotron		Line Emission
(µm)	S_{int} (Jy)	ΔS_{int} (Jy)	S_{synch} (Jy)	ΔS_{synch} (Jy)	(Jy)
3.6	12.6	± 0.2	13.5	0.1	-
4.5	14.4	± 0.3	14.7	0.1	-
5.8	16.8	± 0.1	16.4	0.1	-
8.0	18.3	± 0.1	18.7	0.1	-
24	59.3	± 5.9	29.4	0.2	13.0
70	212.8	± 21.3	45.7	0.5	8.2
100	215.2	± 21.5	52.9	0.6	16.1
160	141.8	± 14.2	64.2	0.9	-
250	103.4	± 7.8	77.2	1.2	-
350	102.4	± 7.7	88.7	1.4	-
500	129.0	± 9.7	102.8	1.8	-
550	117.7	± 8.5	106.9	1.9	-
850	128.6	± 9.5	127.9	2.5	-
1,382	147.2	± 10.8	156.2	3.4	-
2,098	187.1	± 13.3	185.6	4.4	-
3,000	225.4	± 15.8	215.0	5.4	-
4,286	253.6	± 17.9	249.1	6.6	-
6,818	291.6	± 21.6	301.6	8.5	-
10,000	348.2	± 24.4	353.2	10.5	-

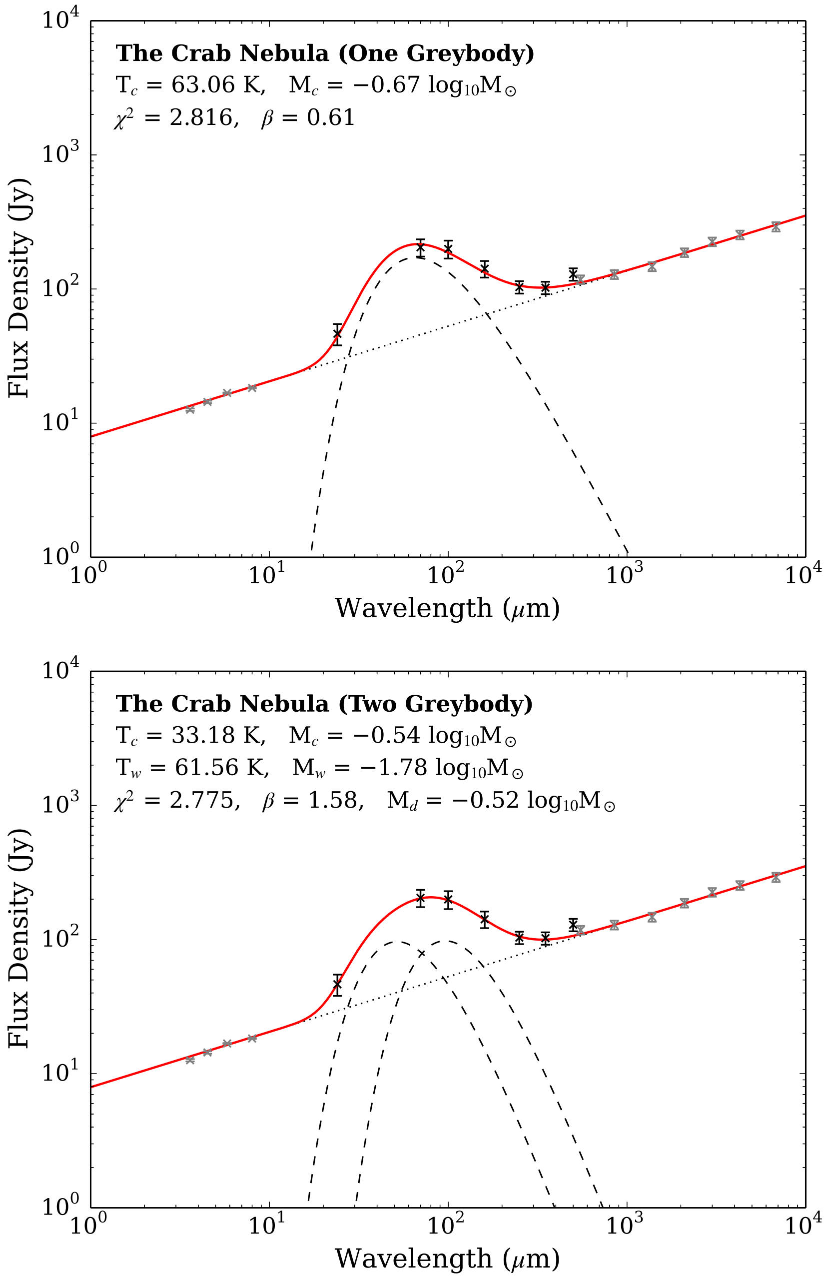

FIGURE 2.15 Spectral energy distributions of The Crab Nebula, using the photometry given in Table 2.5, with flux due to line emission at 24, 100, and 160 µm removed. *Upper:* SED fit using a two-component model, with one dust greybody and a synchrotron power law, as described by Equation 2.2. Black data points show the fluxes to which dust SED fitting was performed, whereas the grey points are the *Spitzer* and *Planck* fluxes used to constrain the synchrotron emission. The dashed lines indicate the best fit dust components, whilst the dotted lines are the synchrotron component; the red lines show the combined SEDs. The plotted fluxes in both graphs represent the continuum flux only; the line emission contribution is omitted. Given the 7 data points, the 3 model variables in the one-greybody fit give it 3 degrees of freedom, whilst the 5 model variables in the two-greybody fit give it 1 degree of freedom.

I also attempted an SED fit that employed the synchrotron power law alongside only one greybody component. This model is described by:

$$S_\nu = \frac{\kappa_\nu \, M_d B(\nu, T_d)}{D^2} + S_0 \left(\frac{\nu}{\nu_0}\right)^\alpha \tag{2.2}$$

The resulting SEDs are shown in Figure 2.15. In order to determine which SED fit was the most suitable, I compared their chi-squared values and degrees of freedom to determine the reduced chi-squared value for each. The one-greybody fit has $\chi^2 = 2.82$ and $k = 3$, giving $\chi^2_{red} = 0.94$. The two-greybody fit has $\chi^2 = 2.78$ and $k = 1$, giving $\chi^2_{red} = 2.78$. Therefore the one-greybody model is the preferred fit. This is in contrast to the two-greybody fit favoured in Gomez et al. (2012b). The one-greybody best fit returns a dust temperature of $T_d = 63.1\,\mathrm{K}$, dust mass of $M_d = 0.21\,\mathrm{M}_\odot$, and $\beta = 0.61$.

Uncertainties for both the one- and two-greybody fits were gauged by means of a bootstrapping analysis. The best fit values, along with the bootstrapped median and uncertainty values, for both the one- and two-greybody fits are listed in Table 2.6. The bootstrapped distributions for each parameter are shown in Figures 2.16 and 2.17.

Interestingly, several of the two-greybody best-fit values are not in good agreement with the median values derived from the bootstrapped fits. The best fit M_h, M_c, and M_d barely lie within the $1\,\sigma$ confidence intervals of their respective bootstrapped medians. Moreover, the best-fit dust temperatures of $T_h = 61.6\,\mathrm{K}$ and $T_c = 33.2\,\mathrm{K}$ are actually lie outside the confidence intervals. The best-fit value for T_h lies at the 69th percentile away from the median along the bootstrapped distribution, just outside the confidence interval; however the best-fit T_c outlies by 2.6σ, at the 83rd percentile. This difference is important; using the median value of T_c (17 K) instead of the best-fit (33 K) would result in a significantly higher dust mass, as $M_d \propto T^{4+\beta}$. Figure 2.18 compares the χ^2 of each of the two-greybody bootstrap fits to the corresponding values of T_c. This reveals that whilst most of the bootstrap iterations gave rise to $T_c < 20\,\mathrm{K}$, these low-temperature outcomes tended to be the worst fits. The bin encompassing the median bootstrapped T_c (16.5 K) has an average value of χ^2 that is ~ 3 times greater than that of the bin encompassing the best-fit T_c (33.2 K).

In contrast, the bootstrapping of the one-greybody fit gave median values that agree well with the best fit results, and produced parameter distributions that are nearly Gaussian (with the exception of minor bimodality in temperature).

The best-fit one-greybody model value of $\beta = 0.61$ is a low value. However

TABLE 2.6 Best fit and bootstrapped parameter estimates produced by fitting the SED of the Crab Nebula (Figure 2.15) with the two-greybody model described in Equation 2.1, and the one-greybody model given in Equation 2.2; the one-greybody model is the preferred fit. The bootstrapped values are presented in the same manner as in Table 2.2. Note that the total dust mass M_d of the two-greybody fit is not a parameter of the model, but rather the result of summing M_h and M_c; as fits that return a larger cold mass typically result in a smaller hot mass (and vice-a-versa), the uncertainty in M_d is not a simple combination of the uncertainties in M_h and M_c. The best-fit values of T_h and T_c from the two-greybody fit are not within one standard deviation of their bootstrapped medians; rather, they lie at the 69th and 83rd percentiles away from the median along the bootstrapped distributions.

Parameter	Best Fit	Bootstrapping	
		Median	Uncertainty
One-Greybody			
T_d (K)	63.1	61.7	± 7.1
M_d ($M_\odot$)	0.21	0.21	-0.05, +0.07
β	0.61	0.68	± 0.32
Two-Greybody			
T_h (K)	61.6	47.1	± 13.5
T_c (K)	33.2	16.5	± 6.4
M_h ($10^{-2}\,M_\odot$)	1.7	7.1	-5.9, +35.7
M_c ($M_\odot$)	0.28	0.60	-0.37, +0.95
β	1.58	1.78	± 0.85
M_d ($M_\odot$)	0.30	0.75	-0.46, +1.20

even if the SED fit is repeated with a fixed value of $\beta = 1$, the one-greybody fit exhibits a reduced chi-squared of $\chi^2_{red} = 1.51$ – still superior to the two-greybody model – with $T_d = 57.2\,\mathrm{K}$ and $M_d = 0.15\,M_\odot$. Repeating both the one- and two-greybody model fits using a more standard interstellar value of $\beta = 2$ produces best-fit chi-squared values of 11.05 for the one-greybody fit[7], and 2.95 for the two-greybody fit[8] – corresponding to $\chi^2_{red} = 2.48$ and $\chi^2_{red} = 1.48$ respectively. Therefore both of these are also inferior to the free-beta one-greybody fit. Indeed, for the 4 degrees of freedom in the one-greybody fixed $\beta = 2$ model, the critical value of chi-squared is 9.49 – as such, the best-fit chi-squared of 11.05 indicates that this is in

---

[7] The best-fit one-greybody model with a fixed $\beta = 2$ (for which $k = 4$) gives $T_d = 44.2\,\mathrm{K}$ and $M_d = 0.07\,M_\odot$.

[8] The best-fit two-greybody model with a fixed $\beta = 2$ (for which $k = 2$) gives $T_h = 54.0\,\mathrm{K}$, $T_c = 26.0\,\mathrm{K}$, $M_h = 1.8 \times 10^{-2}\,M_\odot$, and $M_c = 0.36\,M_\odot$.

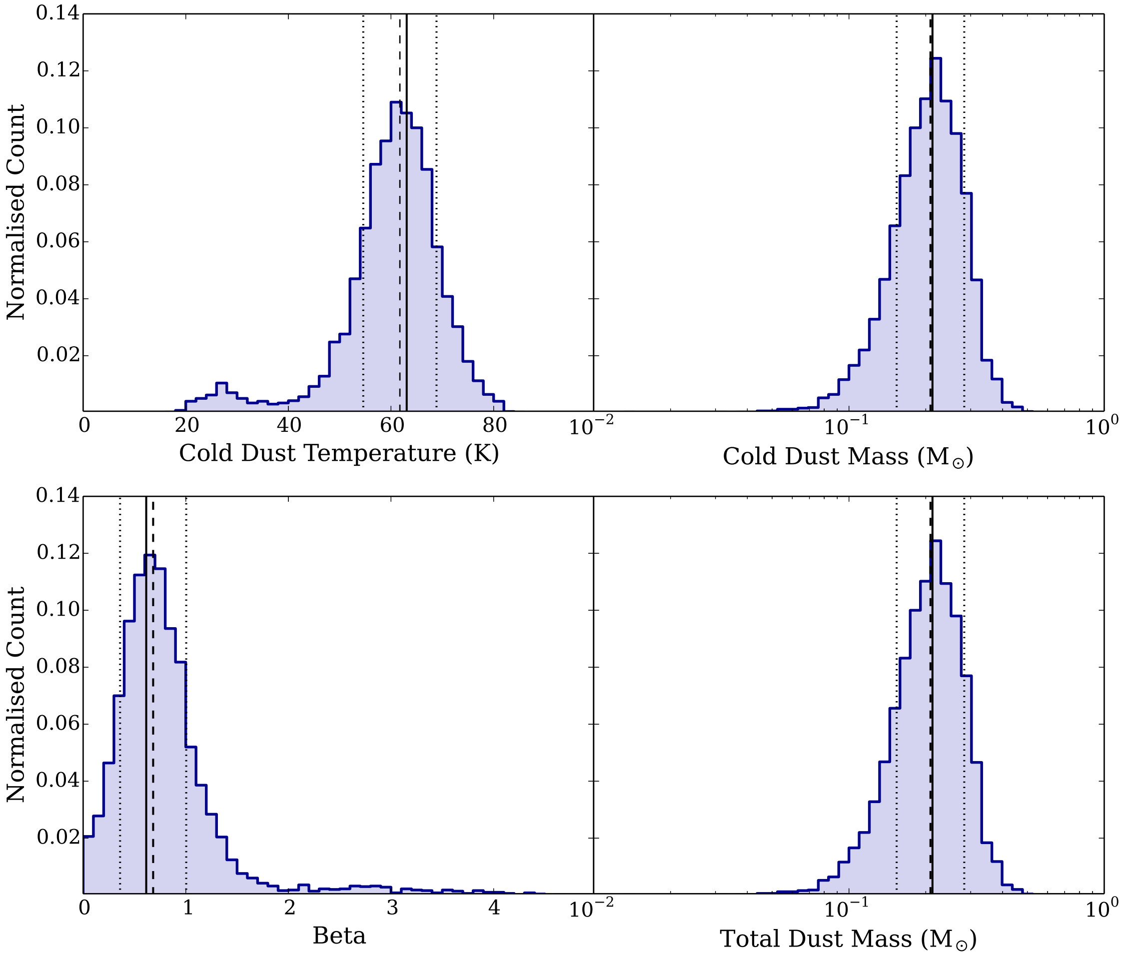

FIGURE 2.16 Distribution of parameters generated by performing 5,000 bootstrap fits to the dust SED of the Crab Nebula (Figure 2.15), using the one-greybody model described by Equation 2.2. This model yields the preferred fit. Best-fit, bootstrapped median, and boostrapped confidence intervals are indicated in the same manner as in Figure 2.5.

fact a failed fit. Whilst for the best-fit two-greybody $\beta = 2$, the returned parameters are within the boostrapped uncertainties, despite the far poorer fit quality.

My photometry was used in Gomez et al. (2012b) to fit the Crab's SED, anchored to the 70 μm flux. Also, instead of modelling dust emissivity as varying according to ν^{β}, they used optical constants appropriate to carbon grains, as carbon-rich ejecta are indicated by the *Herschel* spectroscopy. Specifically, they use the 'BE' amorphous carbon model of Zubko et al. (1996) for the dust emissivity, with the grain density taken from Rouleau & Martin (1991). Using this model, Gomez et al. (2012b) found the SED to be well fit by a two-greybody model, with a warm dust component at temperature $T_w = 63.4^{+5.1}_{-2.7}$ K, cold dust component at temperature $T_c = 34^{+2.3}_{-1.8}$ K, and a total dust mass of $M_d = 0.12 \pm 0.01$ $M_{\odot}$ (using a model with

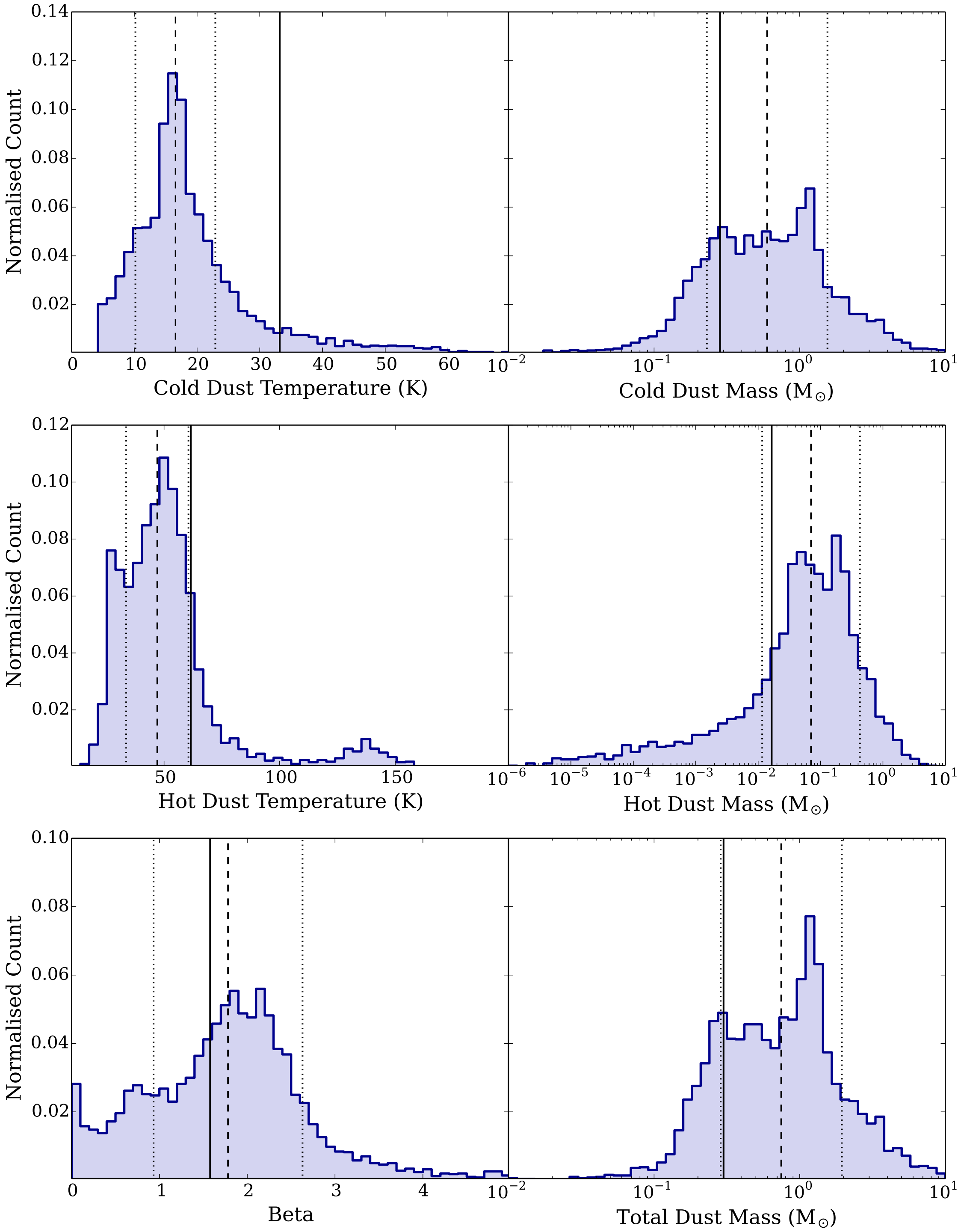

FIGURE 2.17 Distribution of parameters generated by performing 5,000 bootstrap fits to the dust SED of the Crab Nebula (Figure 2.15), using the two-greybody model described by Equation 2.1. This model does not yield the preferred fit. Best-fit, bootstrapped median, and boostrapped confidence intervals are indicated in the same manner as in Figure 2.5. The peak at $\beta \approx 0$ is because β is not permitted to vary to unphysical values of <0. Of the 5,000 bootstrap permutations, 141 (2.8%) returned fits where $\beta < 0.1$.

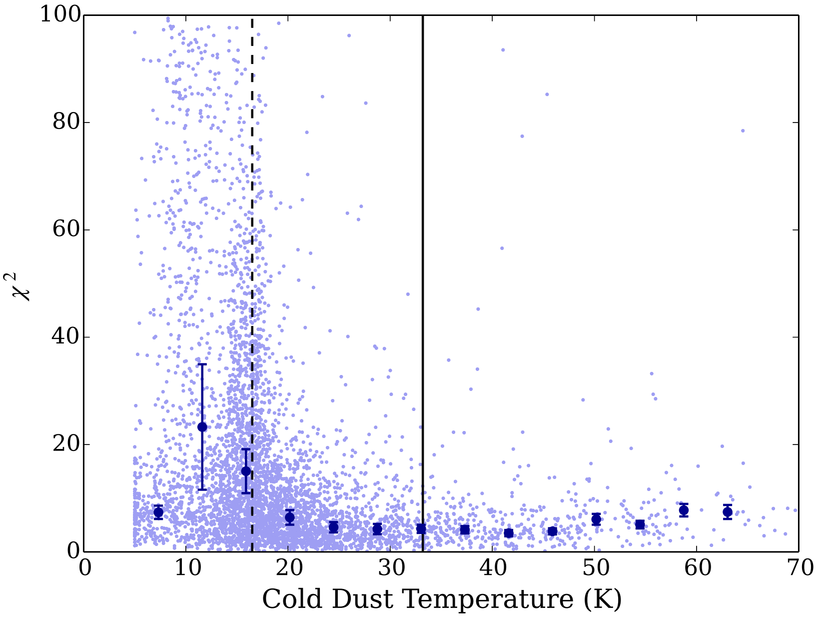

FIGURE 2.18 Plot of the cold dust temperature and χ^2 of the bootstrap fits found in Figure 2.17, performed by fitting the model given in Equation 2.1 to the SED of the Crab Nebula (Figure 2.15). The darker points show the average χ^2 value in each bin of temperature, with error bars showing the standard error on the mean of each. The solid line marks the best-fit value (33.2 K), whilst the dashed line indicates the sigma-clipped median value from the bootstrap distribution (16.5 K). This demonstrates that the fits which returned temperatures similar to the best fit tended to have much better χ^2 values than the fits in the region of the median temperature

silicate instead of carbon grains results in a mass of $M_d = 0.24^{+0.3}_{-0.1}\,\mathrm{M}_\odot$). Uncertainties were estimates by finding the range of fits which could adequately fit the data. A one-component fit was not found to be suitable. The Gomez et al. (2012b) best-fit dust masses are not in agreement with my own; however we ascribe this to the different dust emissivity models used.

All of the dust mass estimates we derived with *Herschel* data are well in excess of pre-*Herschel* values (Green et al., 2004; Temim et al., 2006), by more than an order of magnitude. Given the lack of unrelated Galactic cirrus surrounding the remnant, or along our line of sight, we can be confident that this dust has indeed been manufactured in the supernova. Moreover, the fact that the Crab is a pulsar wind nebula, apparently in a region of low-density ISM, means that there is no reverse shock threatening to destroy the dust in the future. We can therefore be reasonably confident that this dust will survive in the long term, and contribute to the galactic dust budget – a statement we cannot make about the dust reservoirs of Cas A or SN1987A, as their reverse shocks are expected to cause dust destruction in the future. If the Crab does indeed harbour 0.22 $M_\odot$ of dust, this would mean that almost all of the metals that were present in the Crab's progenitor, and those which were nucleosynthesised in SN1054, have been processed into dust grains (Woosley & Weaver, 1995; Nomoto et al., 2006; Woosley & Heger, 2007).

2.3.2 RESOLVED COMPONENT SEPARATION

The lack of significant contamination from Galactic cirrus, as well as our ability to constrain the various components of emission in the Crab, combined with *Herschel*'s unparalleled FIR and submm resolution, mean that I was able to perform the first ever resolved component separation of the synchrotron, warm dust and cold dust emission in a supernova remnant. The distribution of the massive cold dust component is of particular interest; if it truly is manufactured supernova dust, then we should expect it to be confined primarily to the filamentary ejecta. This work was carried out for inclusion in Gomez et al. (2012a), and so used a two-temperature greybody model for the dust.

Firstly, I created a spectral index map of the Crab by performing a pixel-by-pixel comparison between the *Spitzer* 4.5 μm and SPIRE 500 μm maps, both of which are dominated by the synchrotron component. To make the maps suitable for direct comparison, I re-gridded each to a 1.6″ pixel scale, and background subtracted them with the same sky annulus used for the global photometry. I applied an extinction correction factor of 1.08 (Temim et al., 2012) to the 4.5 μm map, then convolved it to the 36″ 500 μm beam. To avoid the comparison returning spurious spectral indices in pixels with low signal-to-noise, the spectral index was only calculated for pixels where the the 4.5 μm surface brightness was $> 2.3\ \mu\mathrm{Jy\ arcsec}^{-2}$ (6 μJy per pixel). The resulting spectral index map, having been deconvolved back to the resolution of the 4.5 μm image, is displayed in the left panel of Figure 2.19.

In broad agreement with previous studies, I find the spectral index to be relatively flat ($\alpha \approx 0.3$) in the central region surrounding the pulsar, whilst it steepens ($\alpha \approx 0.7$) in the outer reaches of the nebula. However, whereas Temim et al. (2012) meaure the spectral index to be much shallower in the South of the remnant (~ 0.3) than the North (~ 0.8), my map contains no such dichotomy. Instead, I generally find the spectral index to be shallowest in the regions of the nebula dominated by the pulsar jets. The Temim et al. (2012) spectral index map was created by comparison of *Spitzer* 3.6 and 4.5 μm observations, meaning that it has far superior spatial resolution to my own. However, using two such closely adjacent wavebands will result in a much larger uncertainty on the derived synchrotron slope. Whereas by

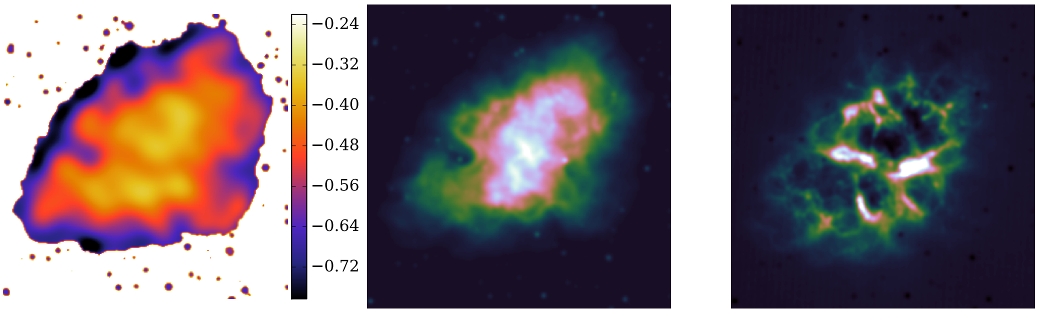

FIGURE 2.19 *Left:* Spectral index map of the Crab Nebula, created by comparison between the synchrotron-dominated *Spitzer* 4.5 and SPIRE 500 μm observations of the remnant. The 'spots' are due to stars visible in the 4.5 μm data. *Centre:* Map of synchrotron emission from the Crab at 24 μm, created using the spectral index map and 4.5 μm *Spitzer* data. *Right:* Map of warm dust emission from the Crab at 24 μm.

using bands separated by two orders of magnitude, my map sacrifices resolution in exchange for a vastly lower uncertainty in spectral index.

In order to extract the warm dust component, the *Spitzer* 24 μm data was used. I made a map of the synchrotron emission at by comparing the spectral index map to the synchrotron-dominated 4.5 μm data to extrapolate the synchrotron flux expected in each pixel at 24 μm. This image was then convolved to the $7''$ resolution of the *Spitzer* 24 μm beam; the resulting synchrotron emission map is shown in the central panel of Figure 2.19. I used this map to remove the synchrotron flux from the emission-line-subtracted 24 μm image. After that, the 43% flux correction due to line emission was applied; this was done globally, as the Temim et al. (2012) determination of the 24 μm line emission contamination used spectra taken of only a few small regions of the nebula. This left behind only the flux due to the warm dust in the remnant, as shown in the right panel of Figure 2.19. The 24 μm synchrotron map of the Crab is generally similar to the NIR synchrotron-dominated morphology, with the jet and torus structure in the remnant core clearly visible. In the synchrotron- and line-subtracted 24 μm map, the diffuse emission is entirely removed, showing that the thermal emission from the warm dust component follows the filamentary structure of the optical ejecta.

With the synchrotron-subtracted 24 μm map serving as a tracer of its location, the warm dust component can be disentangled from the cold dust at FIR wavelengths. This was done using the 160 μm PACS data, as this wavelength features both significant emission from the cold component, as well as a relatively

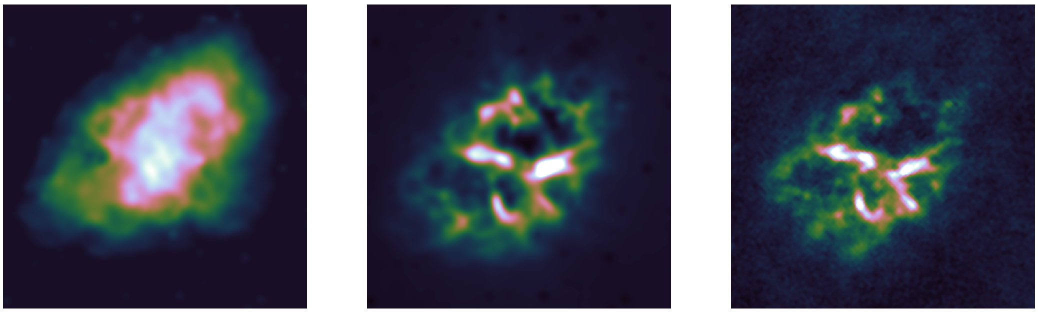

FIGURE 2.20 *Left:* Map of synchrotron emission from the Crab at 160 µm. *Centre:* Map of warm dust emission from the Crab at 160 µm. *Right:* Map of cold dust emission from the Crab at 160 µm.

high resolution of 12″. Firstly, the synchrotron component at 160 µm was extrapolated using the spectral index map. The resulting image of the synchrotron emission at 160 µm is shown in the left panel of Figure 2.20. The synchrotron emission in the Crab at 160 µm bears morphological similarities to both the NIR synchrotron, with bright areas in the location of the jets and torus, and arc features like those visible at radio wavelengths.

The distribution of warm dust emission at 160 µm was found by assuming that the flux traced by the 24 µm warm dust map is at a characteristic temperature of $T_w = 59\,\mathrm{K}$; the corresponding flux at 160 µm in each pixel due to this warm dust emission was then calculated. The resulting image of the warm dust emission in the remnant at 160 µm is shown in the centre panel of Figure 2.20. It was then possible to subtract both the synchrotron and warm dust emission from the 160 µm PACS map, revealing for the first time the spatial distribution of the newly discovered cold dust component in the Crab Nebula, shown in the right panel of Figure 2.20.

The cold dust, like the warm dust, appears to be confined mainly in the filaments in the nebula. However, relative to the warm dust, it appears to be noticeably more concentrated in the Southeast of the remnant. Also, it is not distributed amongst the filaments in the same manner as the warm dust; some filaments with less warm dust possess more cold dust (and vice-a-versa) relative to their overall distributions. This is most easily seen in the West of the remnant. The reasons for this are unclear, but it is worth considering that in such a hostile environment as a pulsar wind nebula, dust grains will only be able to survive under certain conditions; for example, in the sheltered environment of the denser filaments. Also the Crab's pronounced oblate spheroid shape suggests that SN1054 was somewhat asymmetrical, potentially distributing different types of material in different directions, as is observed in Cas A, another core-collapse supernova (Fesen et al., 2006). Of course, this apparent effect could also be due to flaws in how the component separation was carried out. In particular, the approximation that all of the Crab's warm dust has a characteristic temperature of 59 K is naïve, and will break down at some point. Nonetheless, the flux contained in the synchrotron, warm dust, and cold dust maps are compatible with the flux ascribed to each component in the global SED fit; the agreement is to within 4% at 24 µm, and to within 11% at 160 µm; less than the photometric uncertainty in each band. This is interesting, as resolved component separation of dust emission from nearby galaxies does not produce values that agree with global measurements (Smith et al., 2012b).

2.3.3 ADDRESSING A COUNTER-CLAIM REGARDING THE DUST MASS OF THE CRAB NEBULA

> *'Those people who think they know everything are a great annoyance to those of us who do.'*
>
> ISAAC ASIMOV

After our work on the Crab Nebula was published in Gomez et al. (2012b), Temim & Dwek (2013) claimed that a 'physical' model of dust heating in the remnant yields a lower, and more plausible, dust mass than our own. They find a dust mass of 0.019 $M_\odot$ assuming carbon grains (as carbon grain composition is supported by the spectra) – a factor of $\approx$ 6 less than the mass we find in Gomez et al. (2012b), and a factor of 11 less than the mass I derive here. Alternatively, assuming silicate grains, they find a dust mass of 0.13 $M_\odot$.

Temim & Dwek model the heating of the dust by a source located at the centre of the pulsar wind nebula. They calculate the resulting dust temperatures of a continuum of grain sizes, at a range of distances from the centre of the nebula. From this they then calculate the corresponding dust mass using optical constants.

However, their model is not quantitatively better than ours. They state that their best fit has $\chi^2_{red} = 0.06$, compared to $\chi^2_{red} = 0.94$ for my single-greybody preferred fit, indicating that their model significantly over-fits the data in comparison to mine.

We also have questions regarding other aspects of their methodology. Temim & Dwek impose an upper limit of 5 µm upon the size of the dust grains in the remnant, despite the fact their own model *requires* grains larger than this to properly fit the FIR fluxes. Such grains would be larger than the maximum grain size predicted by models of dust condensation in core-collapse supernovæ (Todini & Ferrara, 2001). But if grains this large are present, as the large-grain portion of the Temim & Dwek model (which they chose to ignore) suggests, then their low temperatures mean that their mass-to-luminosity ratio would be high indeed, and contribute significantly to the total dust mass of the Crab.

It appears that much of the difference between the dust mass estimates of the Crab discussed here arises from differing assumptions about the emissivity properties of the dust. Whereas here I assume a simple model where $\kappa_\nu \propto \nu^\beta$, Gomez et al. (2012b) and Temim & Dwek (2013) use optical constants. But whilst Gomez et al. uses the 'BE' amorphous carbon model of Zubko et al. (1996), Temim & Dwek uses the 'AC' amorphous carbon model of Rouleau & Martin (1991). When Temim & Dwek use the BE model instead, they arrive at a dust mass of $0.04\,\mathrm{M}_\odot$, which more than halves the factor by which their mass estimate differs from that of Gomez et al..

There are reasons to suspect that the choice of the AC optical constants by Temim & Dwek was not the correct one. They opt for the AC model as it is complete down to wavelengths of less than 0.1 μm, where much of the dust absorption occurs; this permits them to more reliably compute grain temperatures. However, emission beyond a wavelength of 300 μm is not constrained by the AC model. Given that the grain size distribution of Temim & Dwek suggests that there are large, cold grains present in the Crab – a fact they nonetheless disregard – it is important to accurately account for the longer-wavelength emission. In order to deal with emission at wavelengths > 300 μm, Temim & Dwek use a power law to extrapolate the AC model. However they provide no physical justification for this approach – nor do they even even state the power law used. Note that Temim & Dwek identify the longer wavelengths as being where their model fits the observed fluxes least well. The BE model employed by Gomez et al., however, covers the entire 0.1–1,000 μm wavelength range. Moreover, only by using the BE optical constants can a fair, direct comparison to the Gomez et al. masses truly be made.

Also, whilst Temim & Dwek find the BE fit has a larger χ^2 value than the AC fit, this is actually a point in its favour. Given that Temim & Dwek report that the AC fit has $\chi^2 = 1.86$, we can infer that the model has 31 degrees of freedom. As the BE model has the same number of variables, it should also have 31 degrees of freedom; we can therefore infer that its fit exhibits a reduced chi-squared of $\chi^2_{red} = 0.10$, which means that this fit should generally be preferred over the $\chi^2_{red} = 0.06$

of the AC fit.

Finally, **?** have performed a full radiative-transfer modelling of the Crab Nebula, which suggests a dust mass of ≈ 0.3–$0.7\,\mathrm{M}_\odot$; larger than the best-fit masses derived by myself, Temim & Dwek, or Gomez et al.. I note, however, that 0.3 and $0.7\,\mathrm{M}_\odot$ are the best-fit and median dust masses suggested by my two-greybody model – and are in line with the dust mass observed in SN1987A (Matsuura et al., 2011; Indebetouw et al., 2014).

It may well be the case that the 'physical' approach followed by Temim & Dwek is superior to simple greybody fitting – both methods involve numerous assumptions and simplifications. But we feel that the issues described here make it impossible to say that their approach provides a more accurate or reliable dust mass estimate for the Crab Nebula.

2.4 CONCLUSION

Using observations taken by *Herschel* as part of the MESS survey of evolved stars, along with supplementary multiwavelength data, I have carried out photometry and modelling of the NIR-radio emission of the remnants of supernovæ SN1604 (Kepler's), SN1572 (Tycho's), and SN1054 (the Crab); this work was published in Gomez et al. (2012a) and Gomez et al. (2012b).

The remnants of Kepler's and Tycho's supernovæ, both Type-Ia events, show no evidence of dust manufactured by the supernovae. Observations of both remnants suffer from severe contamination from unrelated Galactic cirrus along our of line of sight. The MIR-submm SEDs of both remnants are well-fit by a three-component model – two modified greybodies representing hot and cold dust components, and a power law for the contribution of synchrotron radiation. The contributions of the unrelated cold interstellar dust along our line of sight, and any cold dust in the remnants, could not be disentangled. The best-fit parameter estimates for both remnants, along with bootstrapped medians and uncertainties, can be found in Table 2.7.

I produced temperature maps of the hot and cold dust components of Kepler's and Tycho's SNRs. The hot temperature maps traced the hot dust structures visible in MIR observations. But in both cases, the cold temperature maps also show evidence of structures associated with the remnants. In the case of Tycho's SNR, these coincide with regions where the expanding remnant is observed to be colliding with surrounding ISM, suggesting that the structures correspond to

TABLE 2.7 Best fit and bootstrapped parameter estimates produced by fitting the dust SEDs of the remnants of Kepler's, Tycho's, and the Crab supernovæ. Kepler's and Tycho's SNRs were best fit using the two-greybody model described in Equation 2.1, whilst the Crab Nebula was best fit using the one-greybody model described by Equation 2.2. The Bootstrapped values are the sigma-clipped median and standard deviation of the bootstrapped distribution of each parameter. The sigma-clipped standard deviations of the dust masses were calculated in logarithmic space, where the distribution is much more symmetric; as a result, the upper and lower confidence intervals are asymmetric in linear space.

Parameter	Best Fit	Bootstrapping	
		Median	Uncertainty
Kepler's SNR			
T_h (K)	84.3	81.3	± 20.7
T_c (K)	19.5	19.8	± 3.1
M_h ($10^{-3}\,M_\odot$)	4.5	4.5	-3.1, +9.0
M_c ($M_\odot$)	2.3	2.1	-0.7, +1.1
β	1.4	1.4	± 0.3
Tycho's SNR			
T_h (K)	89.9	83.9	± 23.4
T_c (K)	21.6	22.0	± 4.8
M_h ($10^{-2}\,M_\odot$)	7.1	8.4	-5.6, +16.8
M_c ($M_\odot$)	11.1	8.3	-4.9, +11.7
β	0.6	0.7	± 0.5
The Crab Nebula			
T_d (K)	63.1	61.7	± 7.1
M_d ($M_\odot$)	0.21	0.21	-0.05, +0.07
β	0.61	0.68	± 0.32

swept-up interstellar dust. Kepler's SNR, on the other hand, lies out of the Galactic plane in an area of low-density ISM, making it unlikely that the temperature map structures correspond to swept-up interstellar dust; rather, it appears to be circumstellar material. Such circumstellar material may have originated from a stellar companion of the supernova progenitor, or could suggest that Kepler's supernova may have been of an exotic variety, with a lone super-AGB progenitor star.

The lack of evidence for dust manufacture in either supernova is surprising, as models predict that Type-Ia supernovæ should produce large quantities of dust. It is thought that such dust is eventually destroyed by the harsh conditions of the remnant, but not in remnants as young as Kepler's and Tycho's.

Observations of the Crab Nebula, the remnant of a Type-II supernova, are not contaminated by unrelated Galactic cirrus. However the remnant's pulsar wind nebula gives rise to a complex synchrotron component, which had to be accounted for before the dust emission could be characterised. Fitting the flux in the synchrotron-dominated 3.6–8 μm *Spitzer* and 550–10,000 μm *Planck* bands indicated that the synchrotron emission is well-described by a power law (described by Equation 1.15), with a spectral index of $\alpha = 0.4121 \pm 0.0041$, and an anchor flux of $S_0 = 1,434 \pm 62$ Jy at a wavelength of 300 mm; uncertainties were estimated by means of a bootstrapping analysis.

With the synchrotron component subtracted, and line emission contribution accounted for using ISO, *Spitzer*, and *Herschel* spectroscopy, it was possible to disentangle the flux emission due to dust emission. I found that the Crab's dust SED was well-fit by a one-greybody model, with $T_d = 63.1\,\mathrm{K}$, dust mass of $M_d = 0.21\,\mathrm{M}_\odot$, and $\beta = 0.61$. Bootstrapped medians and uncertainties for these parameters can be found in Table 2.7. I created the first ever map of the distribution of cold dust in a supernova remnant by means of a resolved component separation, which revealed that the dust is found primarily in the filamentary ejecta. Combined with the minimal amount of interstellar material in the region of the Crab Nebula, this means that we can be confident that the dust was manufactured by the supernova. The remnant's lack of a reverse shock strongly suggests that this dust will survive long-term, and be injected into the galactic dust budget; this is the first – and to date, only – detection of dust in a supernova remnant for which this can be said.

CHAPTER 3

HAPLESS: ASSEMBLING A BLIND, DUST-SELECTED GALAXY SAMPLE

> *'Choose well. A choice is brief, and yet endless.'*
>
> JOHANN WOLFGANG VON GOETHE

WITH the launch of *Herschel*, we truly entered the era of multiwavelength astronomy. The submillimetre was the last part of the electromagnetic spectrum to be fully exploited in the study of celestial objects. Many surveys have been undertaken by *Herschel*, and other observatories, with the aim of understanding dust in nearby galaxies. However, there has never previously been a large-area submillimetre-selected survey of local galaxies – despite the fact that the majority of the dust mass in a galaxy emits primarily in this wavelength regime. In this chapter, I detail how I assembled HAPLESS: the *Herschel*-ATLAS Phase-1 Limited Extent Spatial Survey. HAPLESS is a blind, volume-limited survey, and represents the first ever sample of galaxies in the local volume selected purely on the basis of their submillimetre luminosity. The work presented in this chapter is published in Clark et al. (*submitted*).

Throughout, I adopt the cosmology of Planck Collaboration et al. (2013), specifically $\mathrm{H}_0 = 67.30\,\mathrm{km\,s^{-1}\,Mpc^{-1}}$, $\Omega_m = 0.315$, and $\Omega_\Lambda = 0.685$.

3.1 SAMPLE SELECTION

I assembled a volume-limited, submm-selected sample of local galaxies using the catalogue of the *H*-ATLAS Phase-1 Version-3 internal data release, which is described in Section 1.5.2. *H*-ATLAS Phase-1 consists of three fields coincident with the fields of the GAMA survey, which is itself described in Section 1.5.2.1, and which supplies spectroscopic redshifts for the majority of the sources.

I selected sources from a distance range of $15 < D < 46\,\mathrm{Mpc}$. The lower distance limit of 15 Mpc was put in place for two reasons. Firstly, a number of sources in the *H*-ATLAS catalogue were found to have very low redshifts to which they had been incorrectly matched. This happened when a foreground Milky Way star lay in front of a distant, submm-bright background galaxy, which resulted in the *H*-ATLAS source being erroneously associated with the low (often negative) recessional velocity of the star; imposing a requirement of $D > 15\,\mathrm{Mpc}$ excluded the bulk of these mismatched objects. Secondly, the peculiar motions of galaxies renders recessional velocity an unreliable estimator of distance below $\sim 15\,\mathrm{Mpc}$.

Of the 109,231 sources contained in the *H*-ATLAS Phase-1 Version-3 catalogue, 86,036 (79%) are matched to optical counterparts, determined via a radially-dependant likelihood ratio technique, where reliability ≥ 0.8 (being the probability that the selected counterpart is the correct one, out of all possible counterparts within a $10''$ search radius) is required for a matched to be deemed science-quality (Smith et al., 2011). Of the sources with counterparts, 44 were in the distance range $15 < D < 46\,\mathrm{Mpc}$; all possess redshifts classed as science-quality by GAMA (Driver et al., 2011). Of these, 39 have reliable SDSS counterparts; the 5 sources excluded were revealed by inspection to all be due to the incorrect association of foreground Milky Way stars with background galaxies.

To ensure that we were not missing sources from our sample, we compared the position of every galaxy in our volume found in the NASA/IPAC Extragalactic Database (NED[1]) to the *H*-ATLAS maps and catalogues. This lead to the inclusion of 3 additional galaxies; 1 which lay outside the GAMA spectroscopic footprint, 1 which had an incorrect redshift in the preliminary GAMA data used for source-matching, and 1 which lay too close to a foreground star to allow for a reliable automated match (visual inspection reveals that the resolved submm source clearly corresponds to the galaxy in question, not the foreground star). Note that because NED includes redshifts from a wide range of sources, the depth to which it is spectroscopically complete varies across the sky.

The final 42 galaxies form the *Herschel*-ATLAS Phase-1 Limited-Extent Spatial Survey, hereafter referred to as HAPLESS. Multiwavelength imagery of the galaxies that make up the sample can be found in Figure 3.1. The basic properties of the HAPLESS galaxies, such as their common names, coordinates, redshifts,

---

[1] `http://ned.ipac.caltech.edu/`

distances, and morphologies, can be found in Table 3.1; the location of each in the *H*-ATLAS GAMA fields is shown in Figure 3.5.

Distances were calculated using spectroscopic redshifts, velocity corrected by GAMA (Baldry et al., 2012) to account for bulk deviations from Hubble flow determined according to the method of (Tonry et al., 2000), which accounts for the motion of the Local Group relative to the CMB due to the gravitational influence of the Virgo Cluster and the Great Attractor. In the nearby regions of the GAMA fields, this correction is dominated by the influence of the Virgo Cluster – especially in the case of GAMA12, which lies in close proximity to Virgo. The velocity correction for every GAMA source at $D < 180\,\mathrm{Mpc}$ is shown in Figure 3.2. For $\mathrm{H}_0 = 67.30\,\mathrm{km\,s^{-1}\,Mpc^{-1}}$, the distance limits we impose correspond to a (flow corrected) redshift range of $0.0035 \lesssim z \lesssim 0.01$. Reliable redshift-independent distances were used for the two sources for which they were available; the distance to UGC 06877 has been determined using surface brightness fluctuations (Tonry et al., 2001), and the distance to NGC 5584 is known from measurements of Cepheid variables (Riess et al., 2011).

I obtained morphology information from the EFIGI catalogue of Baillard et al. (2011), which includes 76% of the HAPLESS galaxies; I visually classified the remainder (all of which were compact dwarf galaxies) using their prescription.

Comparing *r*-band absolute magnitude (listed in Table 3.2, with photometry and radial profiling conducted according to the process laid out in Chapter 4) to distance, as shown in the upper pane of Figure 3.3, shows that there does not seem to be any bias against the inclusion of less optically-luminous galaxies that lie further away. However, there appears to be fewer galaxies located at greater distances, despite the larger volume sampled. The equally-sized GAMA09, GAMA12, and GAMA15 fields, from which this sample is drawn, contain 1, 16, and 25 of the HAPLESS galaxies respectively (lower pane of Figure 3.3); the statistical likelihood of any field containing no more than 1 of the 42 galaxies, by chance, is less than 0.01%. This difference, and the lack of sources sampled in the higher redshift bins, could arise from strong variations in density due to large scale structure. The distribution in right ascension and redshift of the submm-selected HAPLESS and optically-selected GAMA galaxies are displayed in Figure 3.4 to illustrate the large scale structure present in the sampled volume. The position of each of the HAPLESS sources within the GAMA fields is shown in Figure 3.5; even within each field, the galaxies of the sample appear to be clustered.

In order identify a complete sample (necessary for Section 6.4), I further isolated the portion of our sample which is limited by intrinsic submm luminosity.

TABLE 3.1 Basic properties of the galaxies of the HAPLESS sample.

HAPLESS	Common name	*H*-ATLAS IAU ID	SDSS RA (J2000 deg)	SDSS DEC (J2000 deg)	z (helio)	Velocity[c] ($\mathrm{km\,s^{-1}}$)	Distance (Mpc)	Morphology[d] (T)	Flocculence[d]
1[a]	UGC 06877	HATLAS J115412.1+000812	178.55114	0.13663	0.00379	1336	18.3[e]	-1	0.25
2	PGC 037392	HATLAS J115504.7+014310	178.77044	1.71981	0.00421	1796	26.7	8	0.75
3	UGC 09215	HATLAS J142327.2+014335	215.86297	1.72630	0.00457	1726	25.6	6	0.75
4	UM 452	HATLAS J114700.5-001737	176.75303	-0.29422	0.00470	1970	29.3	11	0.25
5[b]	PGC 052652	HATLAS J144430.6+013120	221.12828	1.52201	0.00475	1728	25.7	10	0.25
6	NGC 4030	HATLAS J120023.7-010553	180.09843	-1.10008	0.00477	1978	29.4	3	0.75
7	NGC 5496	HATLAS J141137.7-010928	212.90774	-1.15908	0.00488	1840	27.4	6	0.75
8	UGC 07000	HATLAS J120110.4-011750	180.29502	-1.29751	0.00489	2016	30.0	9	0.50
9	UGC 09299	HATLAS J142934.8-000105	217.39416	-0.01823	0.00516	1904	28.3	9	1.00
10	NGC 5740	HATLAS J144424.3+014046	221.10186	1.67977	0.00520	1890	28.0	3	0.50
11	UGC 07394	HATLAS J122027.6+012812	185.11526	1.46974	0.00526	2197	32.7	7	0.25
12	PGC 051719	HATLAS J142837.8+003311	217.15652	0.55280	0.00527	1952	29.0	7	0.50
13[b]	LEDA 1241857	HATLAS J145022.9+025729	222.59524	2.95853	0.00533	1928	28.6	10	0.50
14	NGC 5584	HATLAS J142223.4-002313	215.59903	-0.38766	0.00548	2033	22.1[f]	6	1.00
15[b]	MGC 0068525	HATLAS J144515.7-000936	221.31587	-0.15953	0.00548	1964	29.2	10	0.25
16	UGC 09348	HATLAS J143228.6+001739	218.11878	0.29402	0.00558	2044	30.4	8	0.50
17	UM 456	HATLAS J115036.2-003406	177.65119	-0.56866	0.00561	2250	33.4	10	0.75
18	NGC 5733	HATLAS J144245.8-002104	220.69130	-0.35108	0.00565	2028	30.1	9	0.75
19	UGC 06780	HATLAS J114850.4-020156	177.21002	-2.03224	0.00569	2261	33.6	8	0.75
20	NGC 5719	HATLAS J144056.2-001906	220.23484	-0.31821	0.00575	2067	30.7	1	0.25
21	NGC 5746	HATLAS J144455.9+015719	221.23300	1.95495	0.00575	2077	30.9	1	0.25

[a] HAPLESS 1 (UGC 06877) is an AGN (Osterbrock & Dahari, 1983) known to exhibit UV continuum emission (Markaryan et al., 1979).

[b] HAPLESS 5, 13, 15, 22, 24, 41, and 42 are not included in the luminosity-limited sub-sample.

[c] Velocity is corrected to account for bulk deviations from Hubble flow (Baldry et al., 2012).

[d] From EFIGI catalogue of detailed morphologies (Baillard et al., 2011).

[e] HAPLESS 1 (UGC 06877) redshift-independent distance from surface brightness fluctuations measurement (Tonry et al., 2001).

[f] HAPLESS 14 (NGC 5584) redshift-independent distance from Cepheid variable measurement (Riess et al., 2011).

TABLE 3.1 – *Continued*

HAPLESS	Common name	*H*-ATLAS IAU ID	SDSS RA (J2000 deg)	SDSS DEC (J2000 deg)	z (helio)	Velocity[c] ($\mathrm{km\,s^{-1}}$)	Distance (Mpc)	Morphology[d] (T)	Flocculence[d]
22[b]	NGC 5738	HATLAS J144356.1+013615	220.98488	1.60418	0.00582	2100	31.2	-2	0.00
23	NGC 5690	HATLAS J143740.9+021729	219.42114	2.29082	0.00583	2130	31.6	3	0.75
24[b]	UM 456A	HATLAS J115033.8-003213	177.64179	-0.53782	0.00585	2391	31.6	10	0.50
25	NGC 5750	HATLAS J144611.2-001324	221.54635	-0.22294	0.00588	2094	31.1	1	0.25
26	NGC 5705	HATLAS J143949.5-004305	219.95704	-0.71846	0.00591	2097	31.2	9	0.75
27	UGC 09482	HATLAS J144247.1+003942	220.69560	0.66173	0.00607	2177	32.3	8	0.50
28	NGC 5691	HATLAS J143753.3-002354	219.47225	-0.39888	0.00626	2244	33.4	3	0.50
29	NGC 5713	HATLAS J144011.1-001725	220.04794	-0.28897	0.00633	2261	33.6	3	0.50
30	UGC 09470	HATLAS J144148.7+004121	220.45287	0.68697	0.00633	2265	33.6	9	0.75
31	UGC 06903	HATLAS J115536.9+011417	178.90395	1.23717	0.00635	2535	37.7	6	0.75
32	CGCG 019-084	HATLAS J144229.4+013006	220.62338	1.50040	0.00652	2330	34.6	10	0.75
33	UM 491	HATLAS J121953.0+014623	184.97165	1.77347	0.00671	2673	39.7	10	0.50
34	UGC 07531	HATLAS J122611.1-011813	186.54927	-1.30475	0.00675	2654	39.4	9	0.75
35	UGC 07396	HATLAS J122033.9+004719	185.14066	0.78806	0.00706	2779	41.3	8	0.50
36	CGCG 014-014	HATLAS J122106.0+003306	185.27385	0.55283	0.00719	2820	41.9	8	0.25
37	UGC 6879	HATLAS J115425.2-021910	178.60434	-2.31955	0.00803	2774	45.6	4	0.75
38	CGCG 019-003	HATLAS J141919.9+010952	214.83417	1.16516	0.00806	2893	43.0	9	0.50
39	UGC 04684	HATLAS J085640.5+002229	134.16946	0.37500	0.00859	2796	41.5	7	1.00
40	NGC 5725	HATLAS J144058.3+021110	220.24298	2.18626	0.00543	2035	30.2	9	0.75
41[b]	UGC 06578	HATLAS J113636.7+004901	174.15315	0.81543	0.00375	1164	17.3	10	1.00
42[b]	MGC 0066574	HATLASJ143959.9-001113	219.99950	-0.18609	0.00620	2246	33.4	11	0.25

[b] HAPLESS 5, 13, 15, 22, 24, 41, and 42 are not included in the luminosity-limited sub-sample.
[c] Velocity is corrected to account for bulk deviations from Hubble flow (Baldry et al., 2012).
[d] From EFIGI catalogue of detailed morphologies (Baillard et al., 2011).

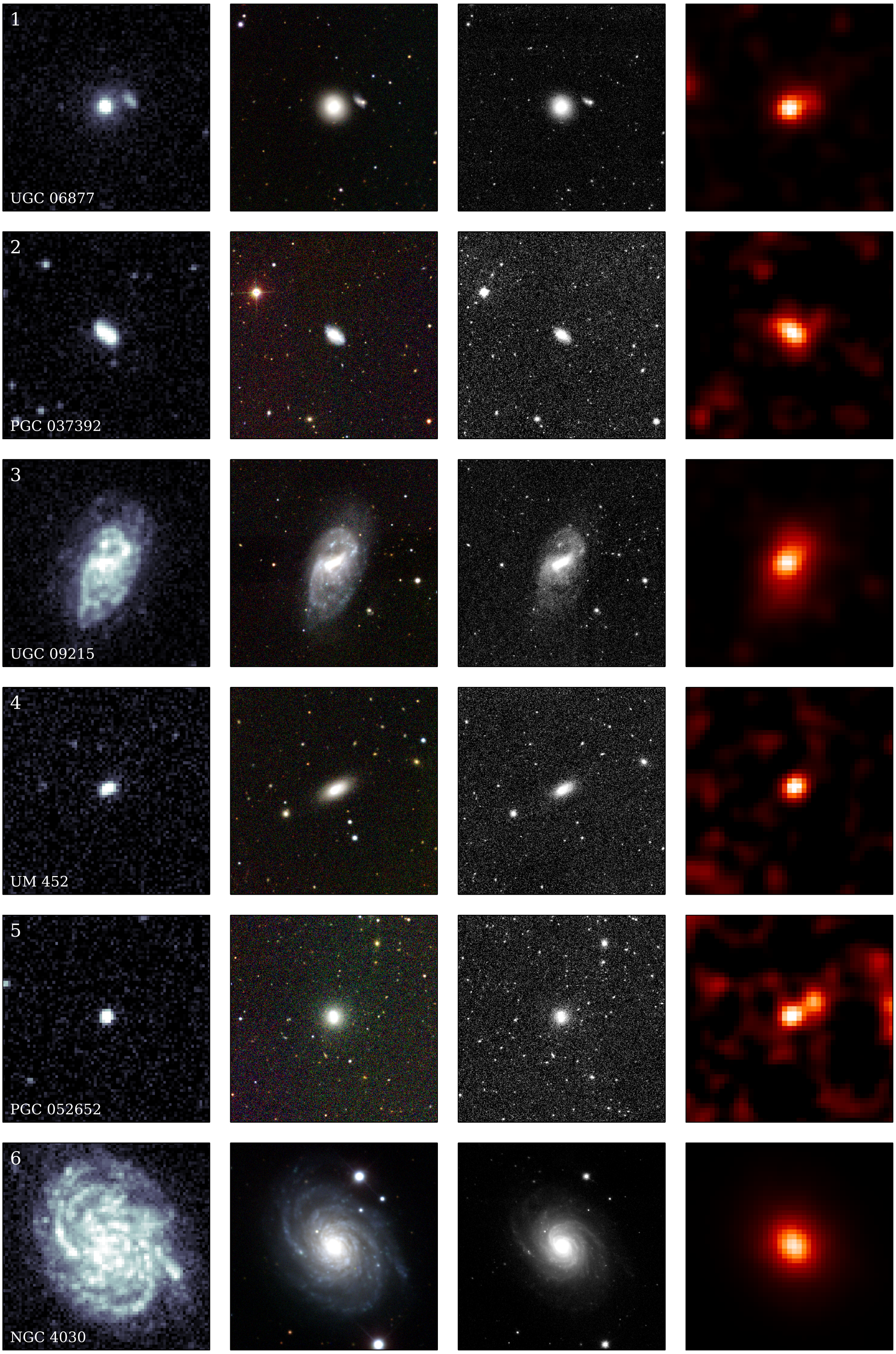

FIGURE 3.1 Multiwavelength imagery of each of the HAPLESS galaxies. The bands displayed, from left-to-right, are: GALEX FUV, SDSS *gri* three-colour, VIKING K_S-band, and *Herschel* 250 μm. Each cutout is 250″on a side. Two sources do not have GALEX coverage.

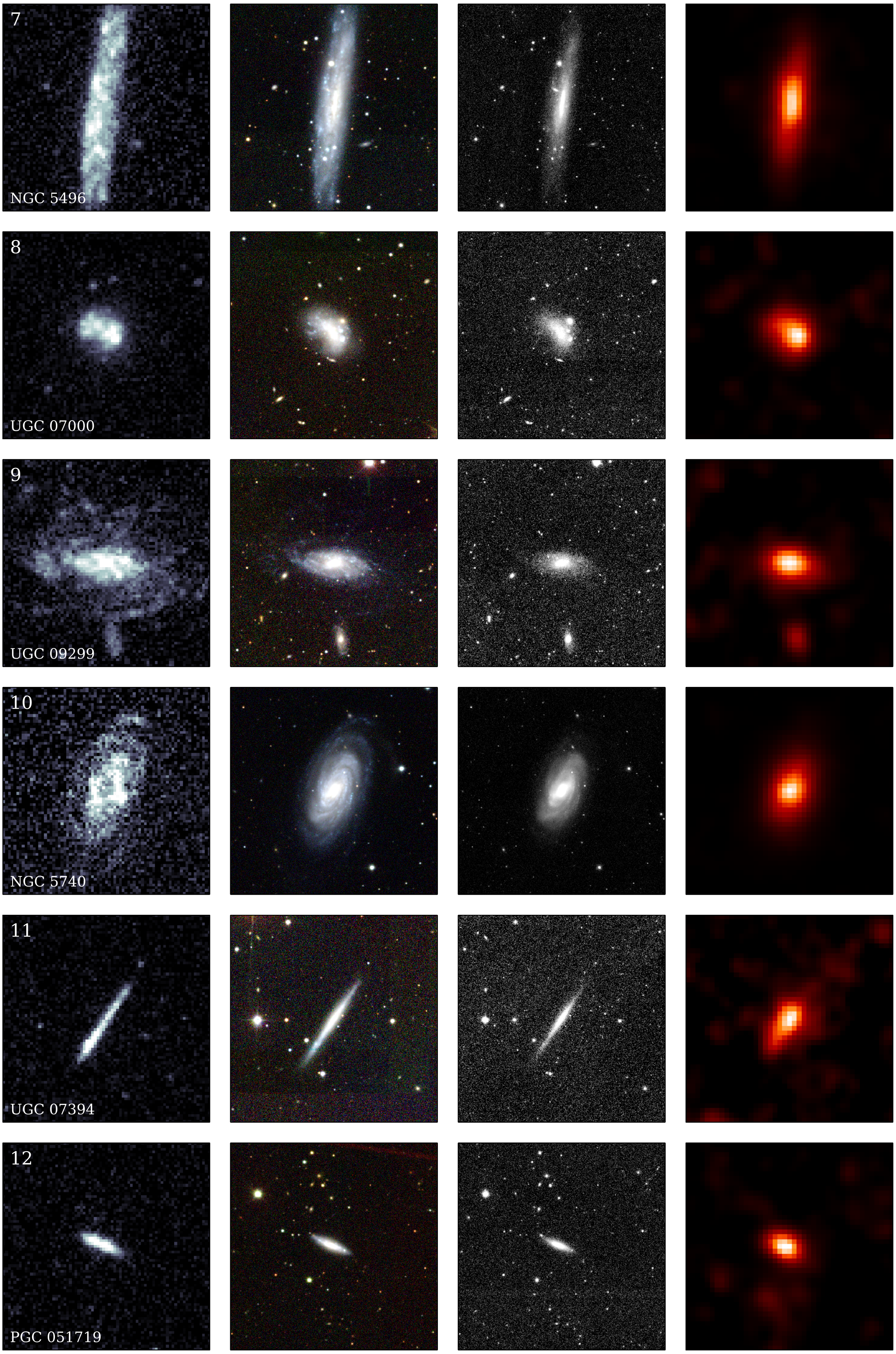

FIGURE 3.1 – *Continued*

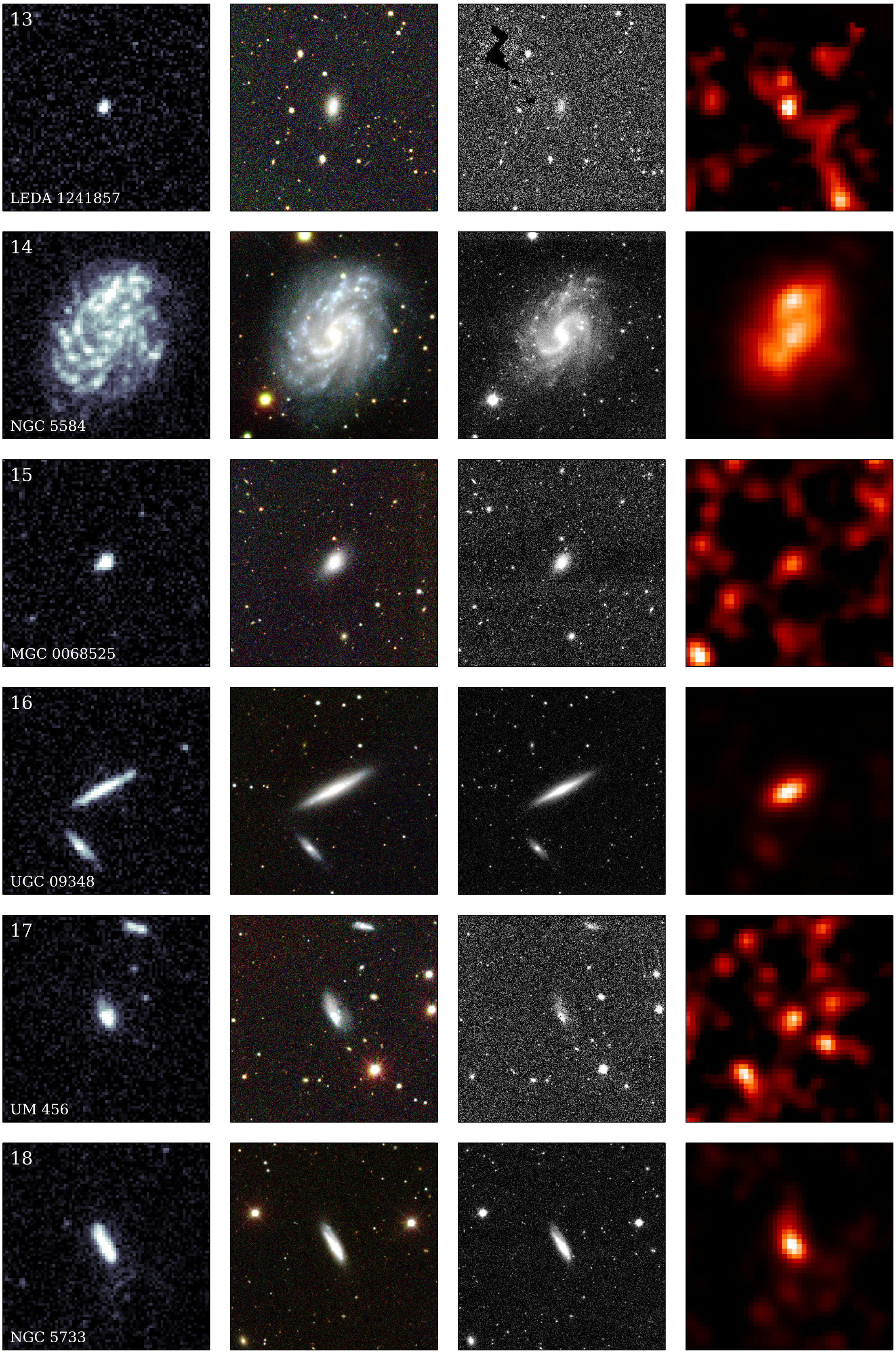

FIGURE 3.1 – *Continued*

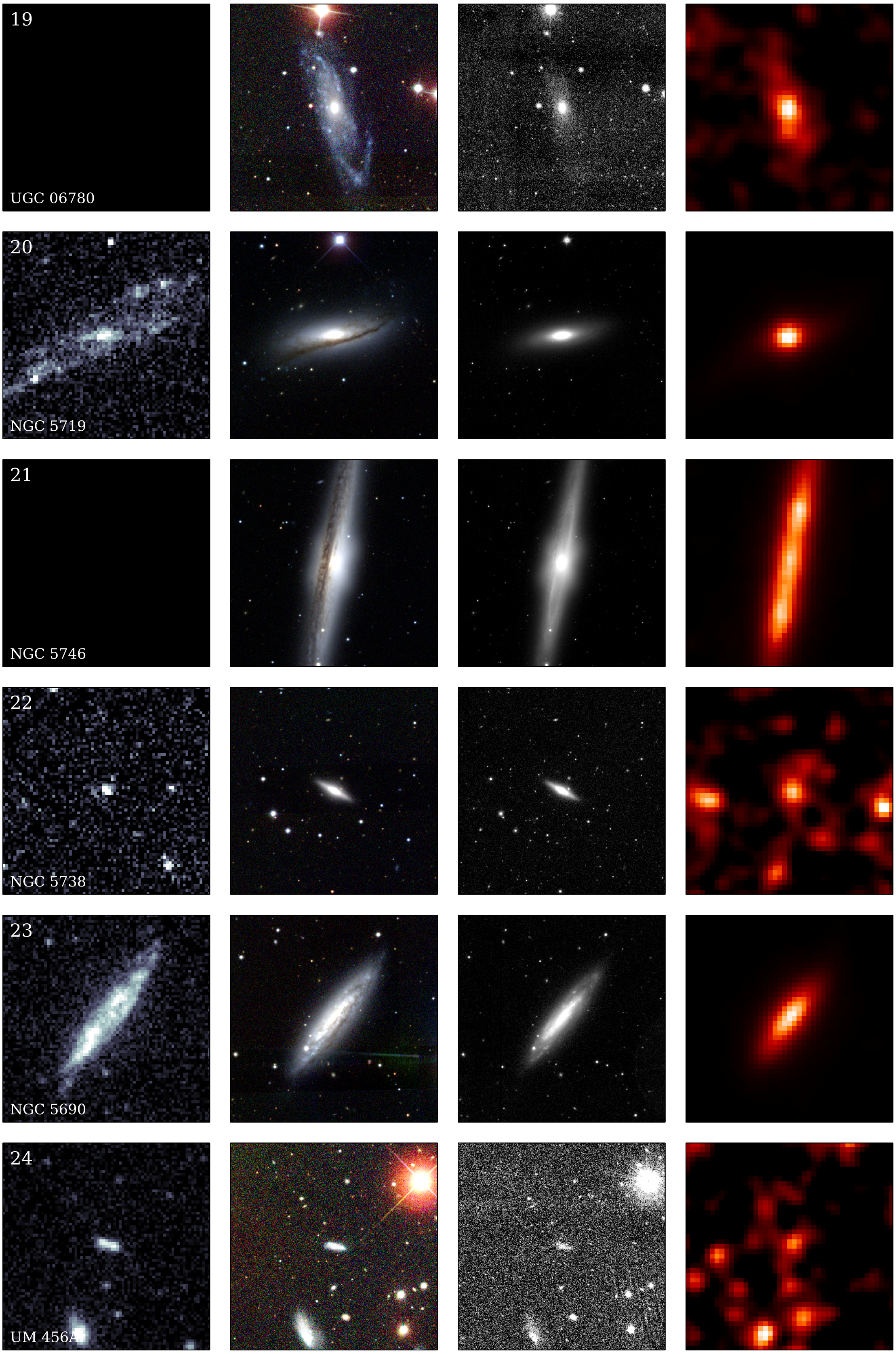

FIGURE 3.1 – *Continued*

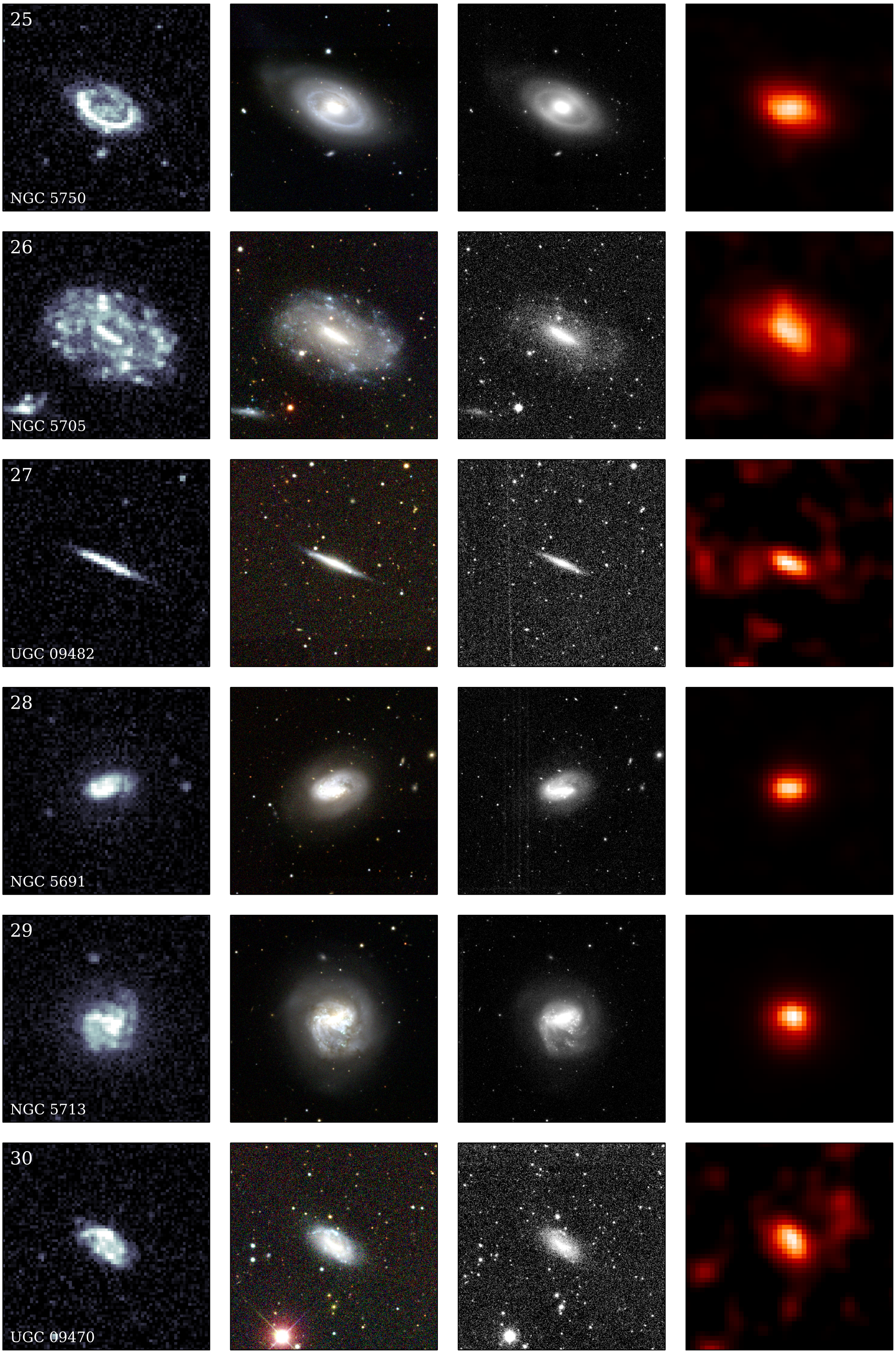

FIGURE 3.1 – *Continued*

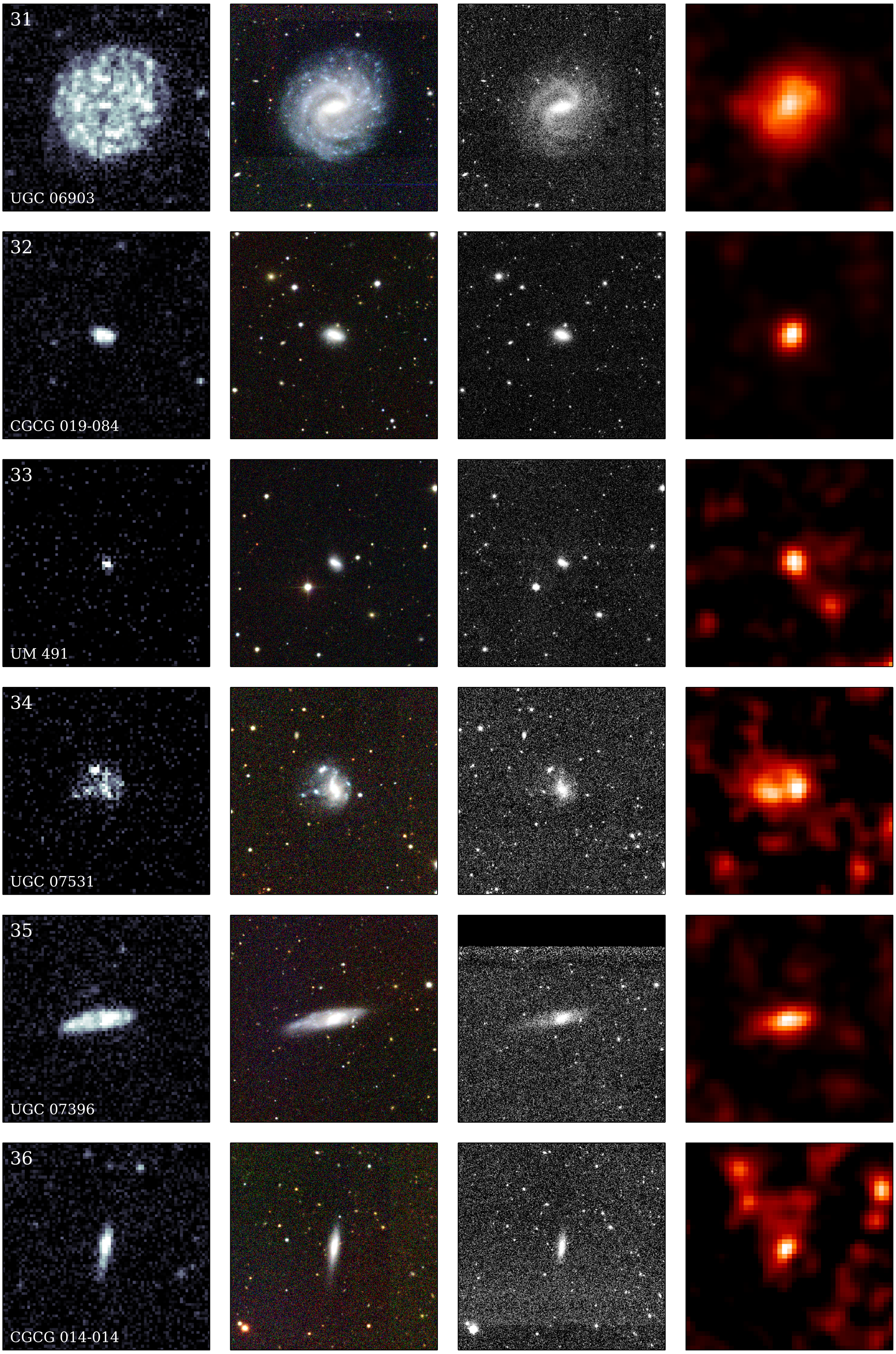

FIGURE 3.1 – *Continued*

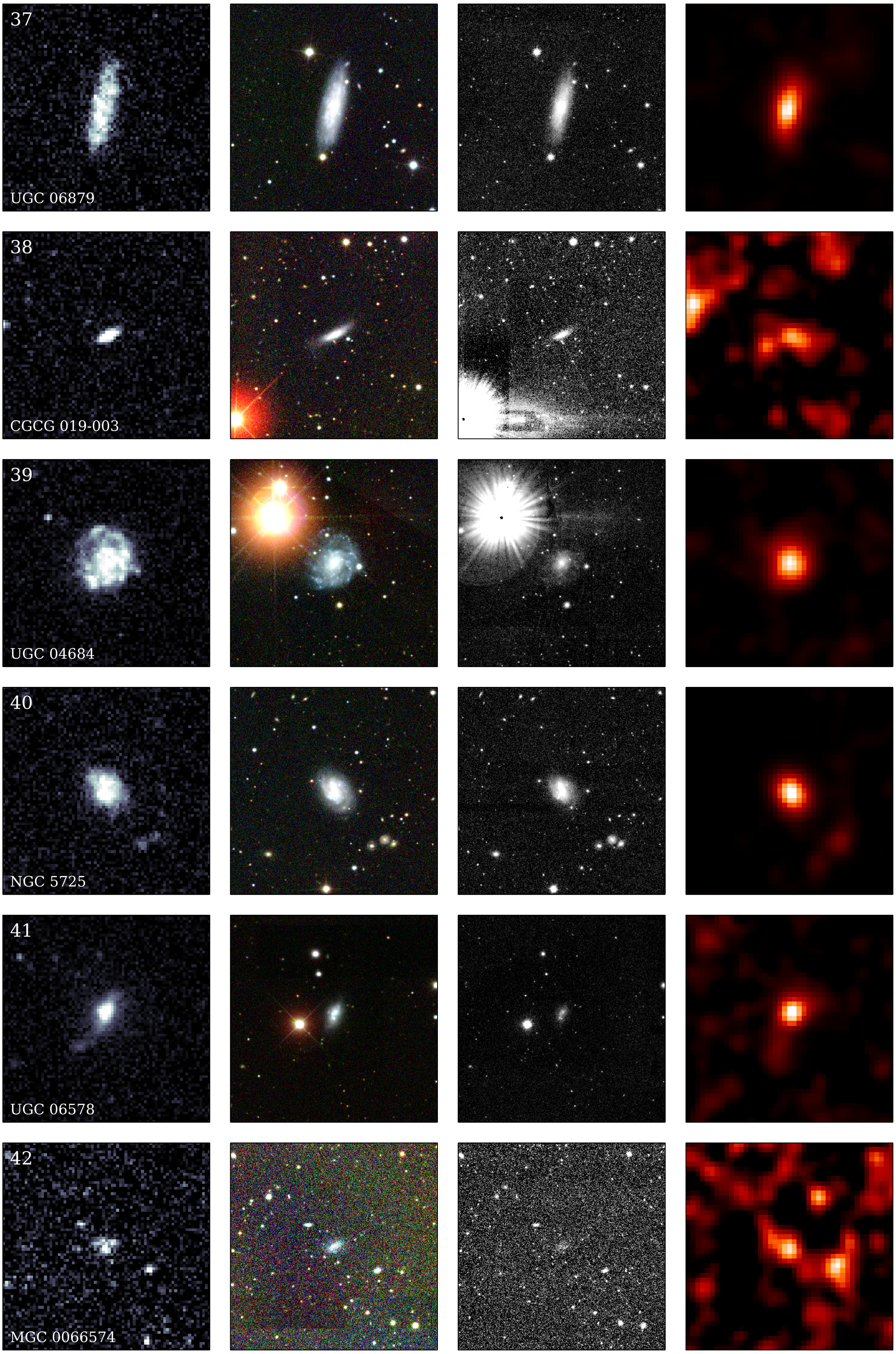

FIGURE 3.1 – *Continued*

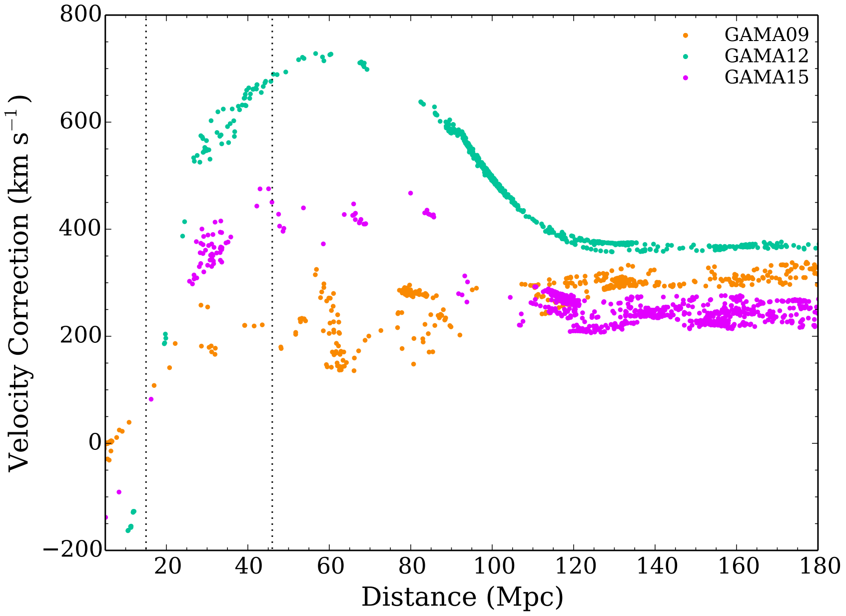

FIGURE 3.2 The velocity correction applied to each source in the GAMA fields out to $D = 180$ Mpc, determined according to the method of Tonry et al. (2000), which accounts for the motion of the Local Group relative to the CMB due to the gravitational influence of the Virgo Cluster and the Great Attractor. The particularly pronounced velocity corrections required in the GAMA12 field are due to its proximity to the Virgo Cluster. The dotted lines indicate the 15 and 46 Mpc distance limits of the HAPLESS sample.

Of the 42 HAPLESS galaxies, 35 would still be detected were they located at the furthest distance of the volume sampled (46 Mpc). This 250 μm luminosity limit is 2.8×10^7 L$_\odot$ (corresponding to a 250 μm flux of 35 mJy at a source distance of 46 Mpc). Following the assumptions detailed in Section 5.1, this is equivalent to a dust mass limit of 7.4×10^5 M$_\odot$ for a dust temperature of 14.6 K (the average cold dust temperature of the sample – see Chapter 6). The 7 sources fainter than this limit are HAPLESS 5, 13, 15, 22, 24, 41, and 42.

This is a 250 μm-selected sample; whether or not a galaxy is bright enough to be detected depends upon both the mass and temperature of its dust. A very large mass of cold dust will be much fainter than a smaller mass of warm dust. Whereas 9.2×10^4 M$_\odot$ of 25 K dust would be detected at 46 Mpc, 6.2×10^5 M$_\odot$ of 15 K dust would not. Although we caution that even hot galaxies can be missed if they posses too little dust; I revisit this issue in Section 6.4.1.

Finally, UGC 06877 (HAPLESS 1) is an AGN (Osterbrock & Dahari, 1983), with a significant contribution from non-thermal continuum emission in the UV (Markaryan et al., 1979). This contaminates our star formation rate estimate for

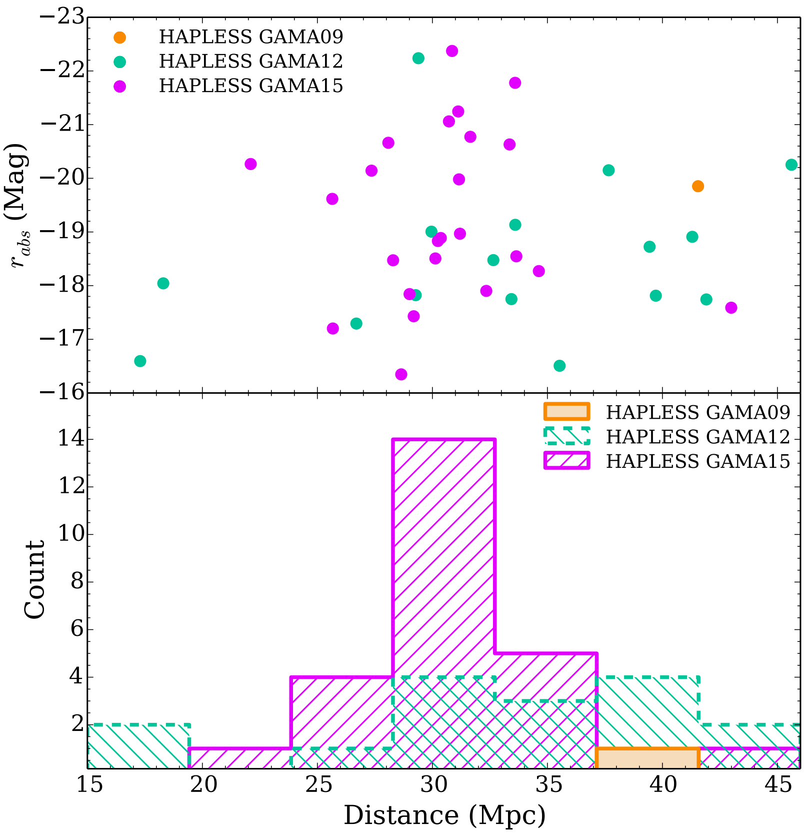

FIGURE 3.3 *Upper:* Heliocentric redshift against absolute r-band magnitude for the galaxies of the HAPLESS sample. The different colours denote whether the galaxy lies in the GAMA09, GAMA12, or GAMA15 fields sampled as part of the H-ATLAS Phase 1 data release. *Lower:* The redshift distribution of HAPLESS sources in the different fields.

this galaxy, rendering it unreliable.

In order to quantify the influence of cosmic variance upon the number of galaxies present in the sample, we use the formula of Driver & Robotham (2010), whereby the percentage cosmic variance ζ_{cv} of a survey is given by:

$$\zeta_{cv} = (1.00 - 0.03\sqrt{X-1}) \times \frac{219.7 - 52.4\log_{10}[V] + 3.21(\log_{10}[V])^2}{\sqrt{N}} \tag{3.1}$$

where X is the aspect ratio of the survey fields; V is the sampling volume of each of the survey's independent volumes; and N is the number of independent volumes in the survey. H-ATLAS GAMA consists of $N = 3$ fields, all with aspect ratios of $X = 4$, in each of which HAPLESS samples a volume of $V = 514\,\mathrm{Mpc}^3$. This therefore yields a cosmic variance for HAPLESS of $\zeta_{cv} = 166\%$. This high

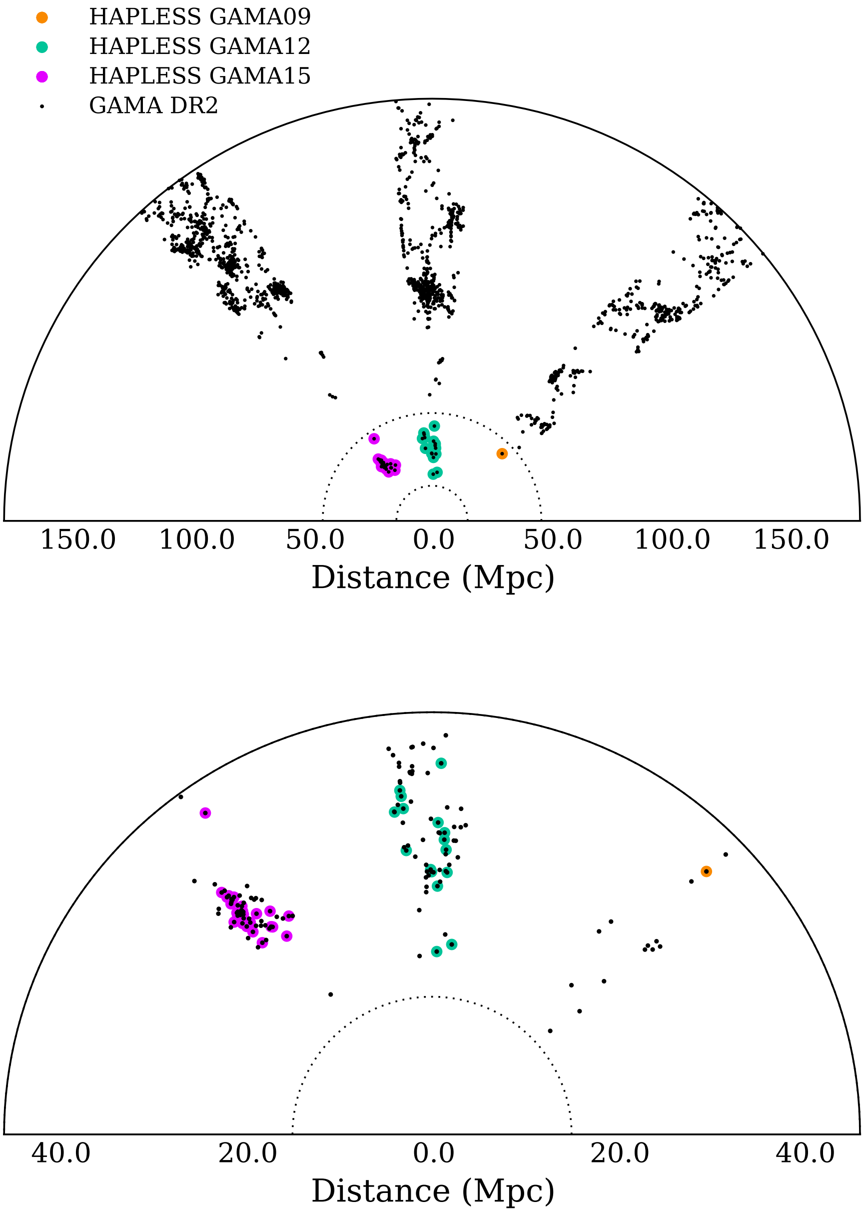

FIGURE 3.4 The large scale structure in the GAMA09, GAMA12, and GAMA15 fields. Black points show the (flow-corrected) positions of optical sources, with the HAPLESS galaxies highlighted in colour. The HAPLESS distance limits of $15 < D < 46$ Mpc are demarked by dotted black lines. *Upper:* The GAMA survey fields out to a distance of 180 Mpc, showing the large-scale structure present in this region. All GAMA DR2 galaxies brighter than $r_{abs} = -16.5$ (the r_{abs} of the faintest HAPLESS galaxy in the luminosity-complete sub-sample) in the $46 < D < 180$ Mpc distance range are shown. *Lower:* Detailed view of the HAPLESS volume, showing all NED sources present in our distance range.

TABLE 3.2 Miscellaneous measured and derived properties of the HAPLESS galaxies. Photometry and radial profiling conducted according to the process laid out in Chapter 4

HAPLESS	r_{abs} (Mag)	$R25_r$ (arcsec)	$R28_{FUV}$ (arcsec)	FUV-K_S (mag)
1	-18.0	32	33	3.07[a]
2	-17.2	11	17	2.03
3	-19.6	67	80	2.13
4	-17.8	21	14	3.16
5	-17.2	28	13	3.58
6	-22.2	131	124	4.51
7	-20.1	124	125	2.66
8	-19.0	36	37	2.41
9	-18.4	39	81	1.35
10	-20.6	89	10	4.39
11	-18.4	54	56	3.74
12	-17.8	21	26	3.08
13	-16.3	13	8	3.14
14	-20.2	96	92	2.72
15	-17.4	19	10	3.74
16	-18.8	43	36	4.26
17	-17.7	21	21	1.55
18	-18.5	25	28	2.21
19	-19.1	102	-	<3.5[b]
20	-21.0	115	34	7.00
21	-22.3	210	-	>3.5[b]
22	-18.9	24	34	7.12
23	-20.7	86	87	4.96
24	-16.5	10	15	1.82
25	-21.2	97	51	5.85
26	-19.9	75	82	2.39
27	-17.9	37	36	2.90
28	-20.6	68	39	3.99
29	-21.7	93	53	4.55
30	-18.5	33	35	2.24
31	-20.1	65	74	2.94
32	-18.2	18	15	3.60
33	-17.8	13	15	1.58
34	-18.7	35	15	1.16
35	-18.9	36	46	2.78
36	-17.7	21	23	2.32
37	-20.2	61	56	4.09
38	-17.5	14	13	2.70
39	-19.8	36	42	2.34
40	-18.8	32	29	2.60
41	-16.5	26	35	0.64
42	-15.2	4	9	2.47

[a] Note that UGC 06877 (HAPLESS 1) is an AGN (Osterbrock & Dahari, 1983), with a contribution from non-thermal continuum emission in the UV (Markaryan et al., 1979).

[b] Sources UGC 06780 (HAPLESS 19) and NGC 5746 (HAPLESS 21) do not have GALEX coverage, so there is not a FUV magnitude with which to determine their FUV-K_S colour. I predict what side of the FUV-$K_S < 3.5$ colour criterion they lie upon using Figure 3.7 (Section 3.1.1).

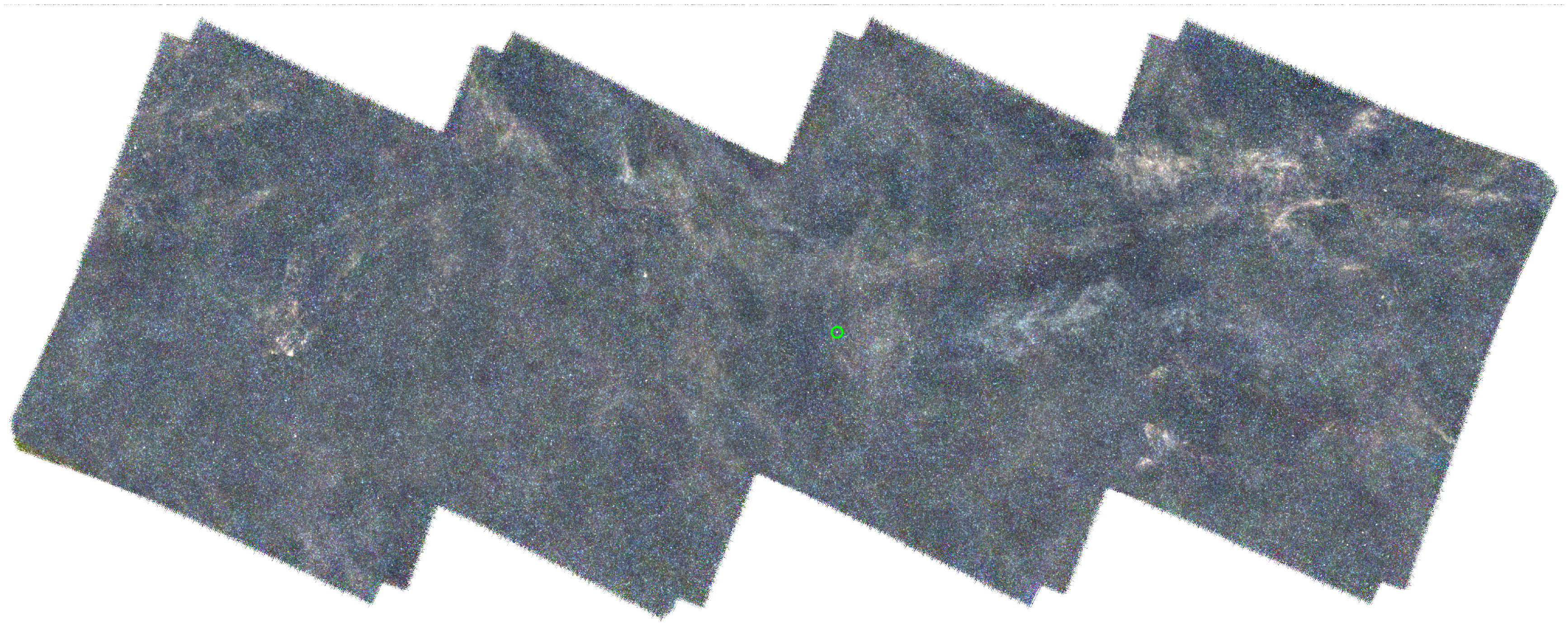

FIGURE 3.5 Three-colour SPIRE (250, 250, and 500 µm) images of the *H*-ATLAS GAMA fields, with the locations of the HAPLESS galaxies indicated by the green circles. *This Page:* The *H*-ATLAS GAMA09 field.

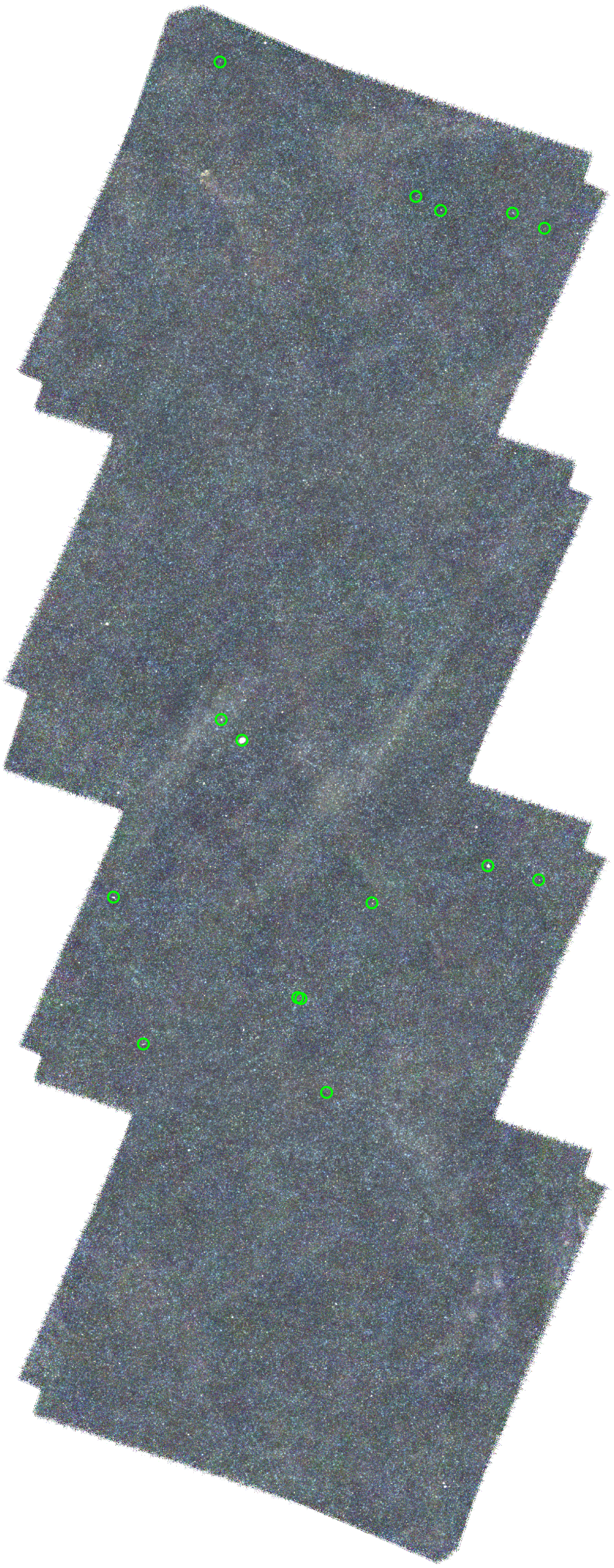

FIGURE 3.5 – *Continued – This Page:* The *H*-ATLAS GAMA12 field.

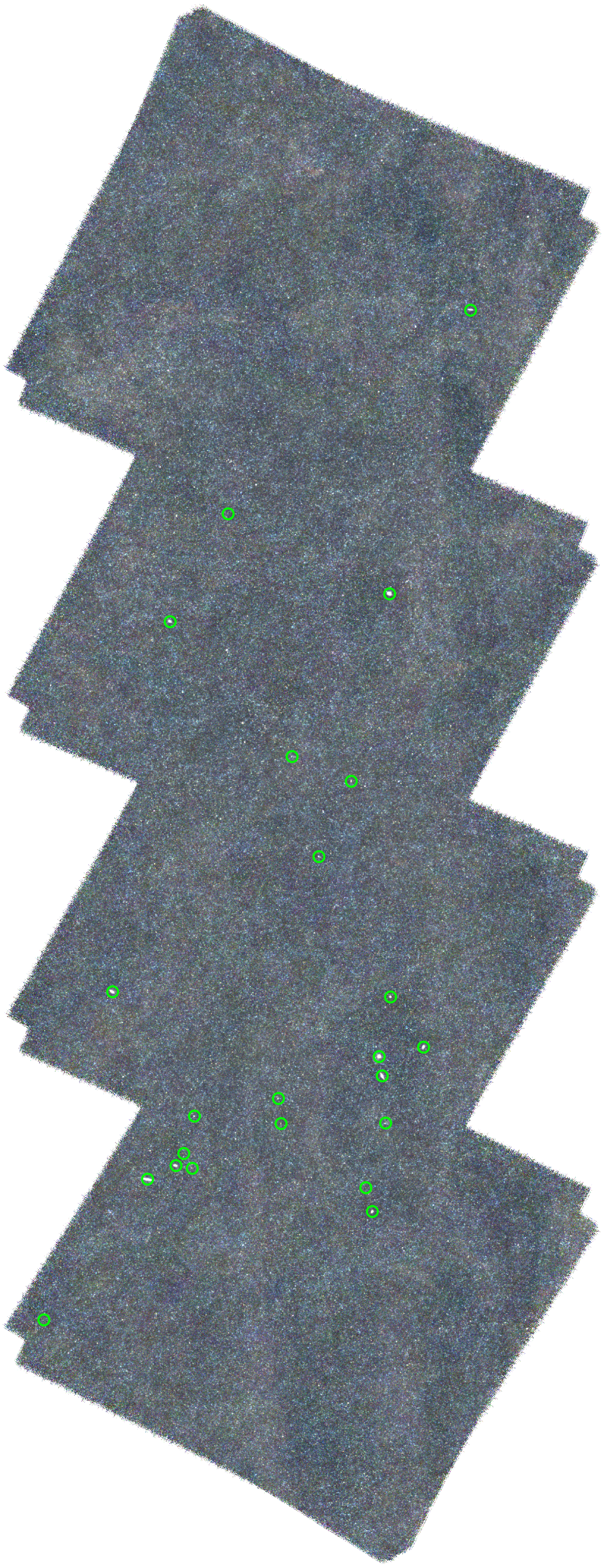

FIGURE 3.5 – *Continued – This Page:* The *H*-ATLAS GAMA15 field.

value is in keeping with the stark differences between the numbers and distributions of galaxies in the three fields, clearly seen in Figure 3.4. The total number of sources listed in the NASA/IPAC Extragalactic Database (NED[2]) in the same volume as our sample is 141, therefore we detect 30% of this population. The GAMA09, GAMA12, and GAMA15 fields contain 1, 16, and 25 HAPLESS sources respectively, representing detection rates of 7%, 24%, and 42%.

3.1.1 CURIOUS BLUE GALAXIES

The majority of the galaxies in our sample possess very late-type, irregular morphology (Hubble stage $T \geq 8$), although there are two early types (HAPLESS 1 and 22). Furthermore, a large fraction of the sample exhibit a high degree of flocculence (as defined by the EFIGI catalogue). In all, 24 of our sample are classed as irregular, and 19 as highly flocculent; 31 are one or the other, whilst 11 are both (Table 3.1). These galaxies are bright in the submm and UV, indicating significant dust mass and high Specific Star Formation Rates (SSFRs). They are optically blue, and exhibit extremely blue UV-NIR colours, arising from the fact that, along with being UV-bright, they are NIR-faint; examples of this can be seen in Figure 3.6. We find a UV-NIR colour-cut of FUV-$K_S < 3.5$ to be an effective criterion for identifying such galaxies – the systems selected by this cut consistently display the interesting properties in question, whilst redder systems consistently do not. This approach is supported by the work of Gil de Paz et al. (2007), who found FUV-K_S colour to be a powerful diagnostic for discriminating morphological type.

GALEX coverage is not available for 2 of the HAPLESS galaxies, therefore there is no FUV-K_S colour with which to classify them. However, the colour u-K_S is well correlated with FUV-K_S, as can be seen in Figure 3.7. The ratio of FUV-K_S to u-K_S across this sample is well fit by a Gaussian distribution with $\mu = 1.75$ and $\sigma = 0.21$. Therefore it can be stated with $3\,\sigma$ confidence that a source with u-$K_S < 1.76$ will have FUV-$K_S < 3.5$. This indicates that of the 2 HAPLESS galaxies without GALEX coverage, 1 is a member of our curious blue population; visual inspection confirms that it exhibits irregular and extremely flocculent morphology. The FUV-K_S colours of the HAPLESS galaxies can be found in Table 3.2, whilst the photometry used to acquire the requisite magnitudes is described in detail in Chapter 4.

These curious blue galaxies (those with FUV-$K_S < 3.5$) span a wide range of sizes, from 1.3 to 33.3 kpc, with a median major axis of 9.3 kpc (derived from

---

[2] `http://ned.ipac.caltech.edu/`

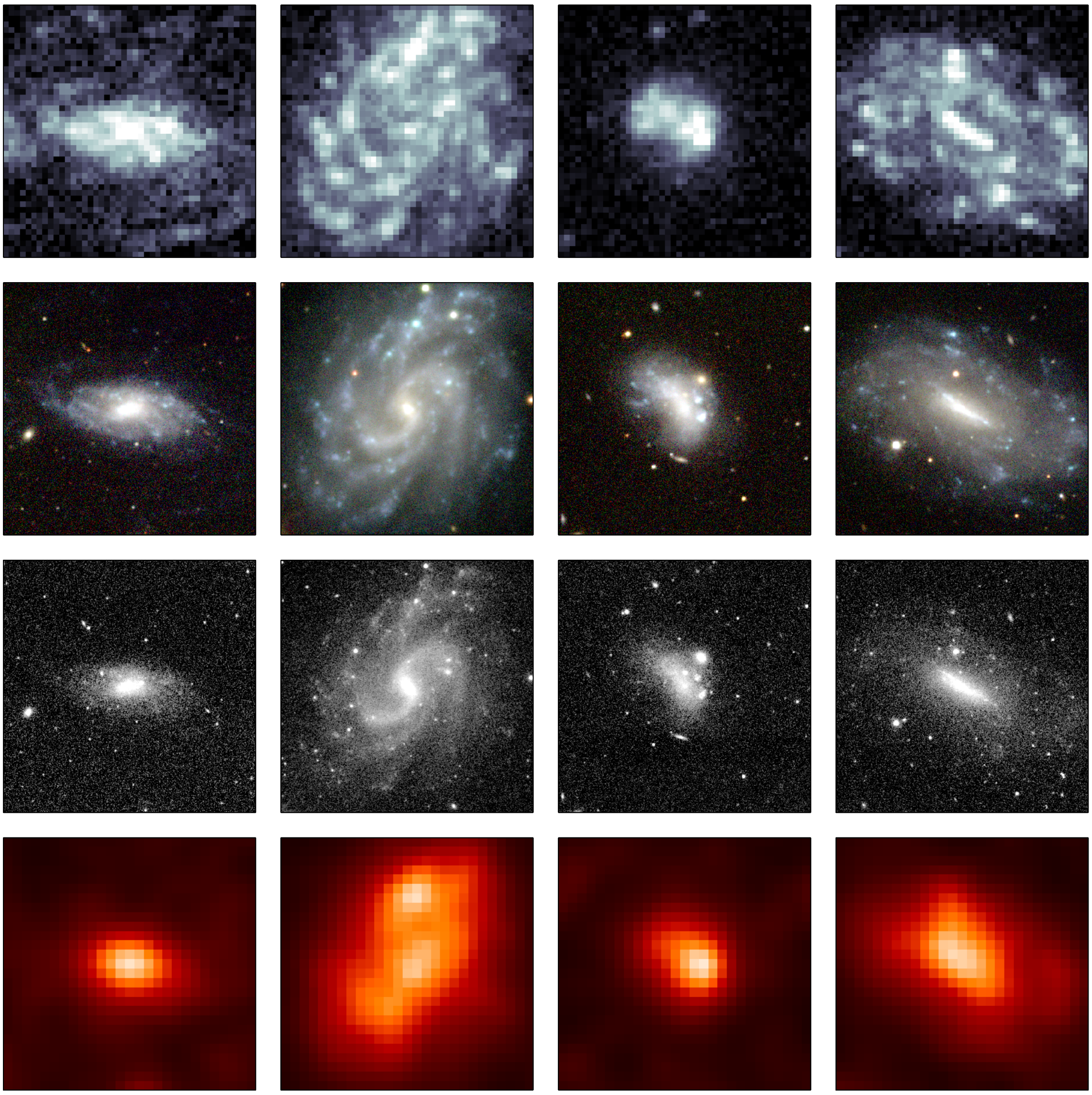

FIGURE 3.6 Multiwavelength imagery of four examples of the curious very blue galaxies found in the HAPLESS sample. From left-to-right they are, UGC 09299, NGC 5584, NGC 5733, and NGC 5705 (HAPLESS 9, 14, 8, and 26). The bands displayed, from top-to-bottom, are: GALEX FUV, SDSS *gri* three-colour, VIKING K_S-band, and PSF-filtered *Herschel* 250 μm. Each image is $150'' \times 150''$. Note the blue optical colours, flocculent morphologies, NIR faintness, and bright extended UV emission.

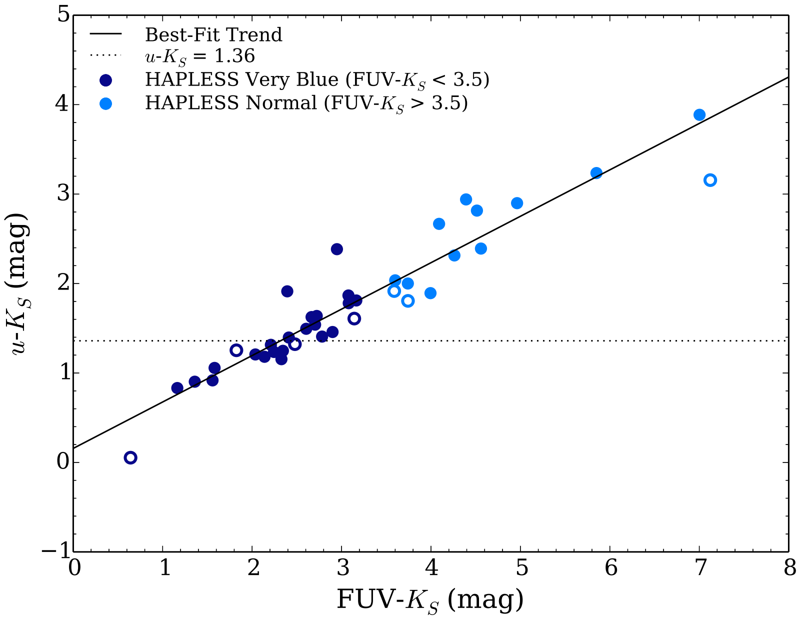

FIGURE 3.7 FUV-K_S colour against u-K_S colour for the HAPLESS galaxies. The two colours are well correlated. A colour criterion of FUV-$K_S < 3.5$ is used to classify galaxies as belonging to the curious very blue population described in Section 3.1.1. Whether a point is blue or cyan denotes the FUV-K_S colour of the source, as separated by the FUV-$K_S = 3.5$ criterion, with hollow circles indicating galaxies not in our luminosity-limited sub-sample; this colour scheme will be used throughout subsequent plots. FUV data is not available for all HAPLESS galaxies, but the correlation in this plot allows us to state with $3\,\sigma$ confidence that a source with u-$K_S < 1.34$ (as demarked by the dotted line) will have FUV-$K_S < 3.5$.

the r-band R25, as measured in Chapter 4). Whilst many of them, particularly the larger examples, possess disks, they often lack defined spiral structure, and show only a weak bulge contribution. Of the 42 HAPLESS galaxies, 27 (64%) satisfy the very blue FUV-$K_S < 3.5$ criterion; 25 (93%) of these exhibit irregular and/or highly flocculent morphology. Of the 15 HAPLESS galaxies with FUV-$K_S > 3.5$, irregular and/or highly flocculent morphology is exhibited by only 7 (47%).

3.2 CONCLUSION

In this chapter, I have described how I used the *Herschel*-ATLAS Phase-1 Version-3 internal data release to assemble HAPLESS: the *Herschel*-ATLAS Phase-1 Limited Extent Spatial Sample – a blind, volume-limited, dust-selected sample of 42 nearby galaxies.

This sample appears to be strongly affected by large scale structure, with a large variation in number counts between the survey fields, and an estimated cosmic variance of 166%.

Noticeable amongst HAPLESS are a subset of curious very blue galaxies. Often irregular and/or flocculent in morphology, these galaxies appear to be prominent in the local dusty universe. Exhibiting extremely blue UV-NIR colours, I found a colour criterion of FUV-$K_S < 3.5$ to be an effective way of identifying these interesting systems.

CHAPTER 4

CAAPR: BESPOKE PHOTOMETRY FOR THE HAPLESS GALAXIES

> *'Make not, when you work a deed of shame,*
> *The scoundrel's plea, "My forbears did the same!"'*
>
> ABU AL-'ALA' A'MAD IBN 'ABD ALLAH IBN SULAIMAN AL-TANU'I AL-MA'ARRI

WHILST the HAPLESS sample, the assembly of which was described in Chapter 3, provides us with a new way to study dusty galaxies, it also presents a panoply of challenges. Foremost amongst these was finding a way to perform accurate and consistent aperture photometry, using a diverse multiwavelength dataset, upon galaxies that display a wide range of characteristics. To that end, this chapter describes CAAPR: Chris' Adequate Aperture Photometry Routine. This chapter also describes the tests I performed upon CAAPR to ensure its reliability and stability. The work presented in this chapter is published in Clark et al. (*submitted*).

4.1 MOTIVATION

The *H*-ATLAS Phase-1 Version-3 catalogue includes UV, optical, and NIR photometry for the counterpart of each *H*-ATLAS source (thus including the HAPLESS sources), performed by GAMA. As described in Section 1.5.2.1, GAMA carry out their own reductions of GALEX, SDSS, UKIDSS-LAS, VIKING, and WISE observations, to ensure that the photometry they perform across surveys is consistent

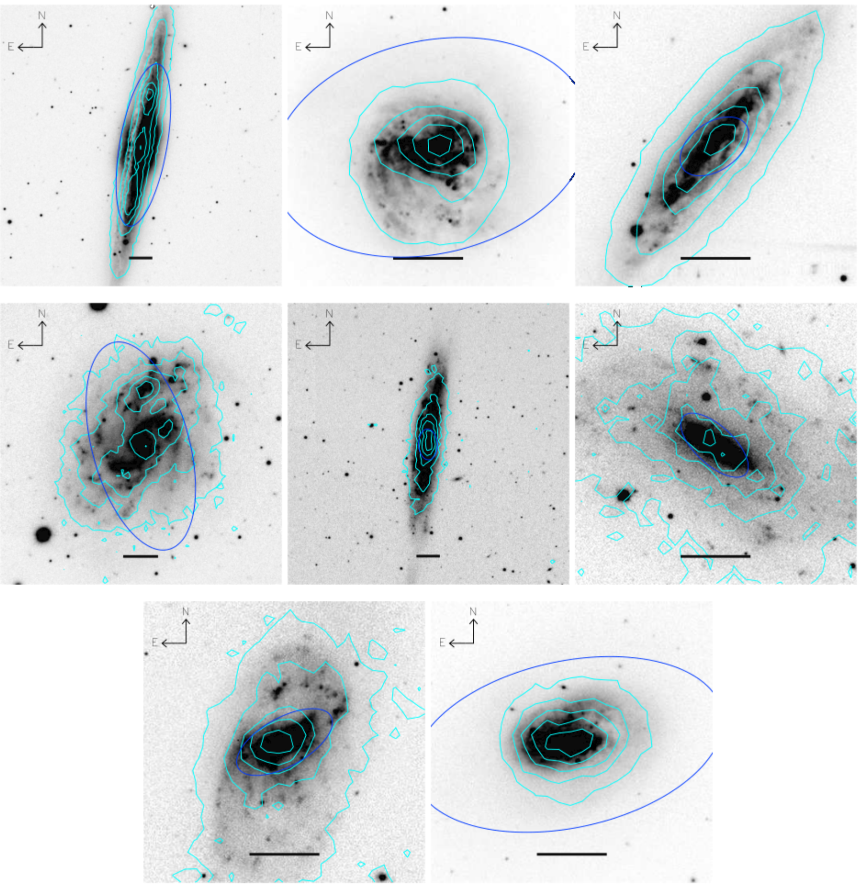

FIGURE 4.1 Examples of apertures used by GAMA to perform photometry upon galaxies in the HAPLESS sample, demonstrating the inability of their pipeline to cope with nearby galaxies, especially those that are highly flocculent. The images are SDSS r-band; the cyan contours show the distribution of the 250 µm emission, whilst the dark blue ellipses show the photometric aperture GAMA used for each source. The white scale bar is 30″ across in each case. Image provided by Nathan Bourne.

(see Section 1.5.2.1). Their *fnugrizYJHK* photometric pipeline is described in Hill et al. (2011), and uses `SExtractor` (Bertin & Arnouts, 1996) to produce apertures for the photometry of each source.

As was made clear in Chapter 3, HAPLESS consists of a diverse set of systems. It represents nearly the full gamut of galaxy morphologies (although is dominated by late types), and spans well over an order of magnitude in both physical and apparent source size. Many of the HAPLESS objects exhibit a high degree of irregularity and flocculence, especially members of the curious very blue population described in Section 3.1.1. Indeed, in the EFIGI morphological catalogue of 4,458 nearby galaxies (Baillard et al., 2011), HAPLESS 14 (NGC 5584) is used as the archetype of a maximally flocculent galaxy. The process used to acquire photometry for the HAPLESS galaxies needs to be able to cope with this diversity.

The primary scientific interests of the *H*-ATLAS and GAMA consortia involve studying galaxies well beyond the local volume. Of the 20,464 galaxies in the *H*-ATLAS Phase-1 Version-3 catalogue matched to optical counterparts with reliable GAMA spectroscopic redshifts, 16,836 (82%) lie at redshifts $z > 0.1$. Moreover, the majority of the remaining 82,676 sources without reliable spectroscopic redshifts possess photometric redshift estimates of $z > 0.3$. Likewise, the SDSS, VIKING, and other supplementary surveys exploited by GAMA are similarly focused on objects beyond the nearby Universe. Consequently, the photometry pipelines of *H*-ATLAS, GAMA, SDSS, and similar surveys are concerned primarily with making accurate measurements of distant galaxies, which tend to be of small angular size; therefore not well resolved in the optical, and unresolved in the submm. In contrast, the majority of the HAPLESS galaxies have angular sizes in excess of $1'$. This compounds with the flocculent nature of many of the HAPLESS galaxies, with the result that they are prone to getting 'shredded' – misinterpreted as several separate sources of emission – by the source-extraction routine employed by GAMA. Even in the cases of less flocculent HAPLESS galaxies, their sheer angular size confounds the standard GAMA pipeline. Figure 4.1 shows the photometric apertures fit by GAMA to several of the HAPLESS galaxies; the dimensions of the GAMA apertures (in dark blue) bear little relation to the shape and size of these galaxies. The UV–MIR photometry provided by GAMA is completely inappropriate for sources in the local volume. Furthermore, the *H*-ATLAS Phase-1 Version-3 catalogue only includes approximate 'by hand' photometry for extended SPIRE sources, and no photometry at all for extended PACS sources.

It was clear that HAPLESS required a bespoke multiwavelength photometry pipeline. This in fact presented an opportunity; HAPLESS would be furnished with a truly cross-comparable, aperture-matched photometric dataset – a valuable resource in this era of multiwavelength astronomy, especially in light of the increasing use of panchromatic SED-fitting tools such as MAGPHYS (da Cunha et al., 2008). To that end, I created CAAPR: Chris' Adequate Aperture Photometry Routine. For the HAPLESS sample, CAAPR carries out photometry in 20 wavebands, spanning over 3 orders of magnitude in wavelength, from GALEX FUV to *Herschel* 500 μm. The properties of each waveband are detailed in Table 4.1.

In panchromatic astronomy, making directly-comparable measurements of

TABLE 4.1 Details of the wavebands used in CAAPR photometry of the HAPLESS galaxies.

Band	Instrument	Survey	Wavelength (m)	Resolution (arcsec)
FUV	GALEX	GALEX-GAMA	1.52×10^{-7}	4.0
NUV	GALEX	GALEX-GAMA	2.27×10^{-7}	5.6
u	SDSS	-	3.54×10^{-7}	1.3[a]
g	SDSS	-	4.77×10^{-7}	1.3[a]
r	SDSS	-	6.23×10^{-7}	1.3[a]
i	SDSS	-	7.63×10^{-7}	1.3[a]
Z	VISTA	VIKING	8.78×10^{-7}	1.0[b]
Y	VISTA	VIKING	1.02×10^{-6}	1.0[b]
J	VISTA	VIKING	1.25×10^{-6}	1.0[b]
H	VISTA	VIKING	1.65×10^{-6}	1.0[b]
K_S	VISTA	VIKING	2.15×10^{-6}	1.0[b]
3.4 µm	WISE	-	3.37×10^{-6}	6.1
4.6 µm	WISE	-	1.21×10^{-5}	6.4
12 µm	WISE	-	1.21×10^{-5}	6.5
22 µm	WISE	-	2.22×10^{-5}	12
100 µm	*Herschel*-PACS	*H*-ATLAS	1.0×10^{-5}	7
160 µm	*Herschel*-PACS	*H*-ATLAS	1.6×10^{-4}	12
250 µm	*Herschel*-SPIRE	*H*-ATLAS	2.5×10^{-4}	18
350 µm	*Herschel*-SPIRE	*H*-ATLAS	3.5×10^{-4}	25
500 µm	*Herschel*-SPIRE	*H*-ATLAS	5.0×10^{-4}	36

[a] Quoted SDSS imaging resolution represents maximum typical seeing (Pier et al., 2003).

[b] Quoted VISTA imaging resolution represents maximum typical seeing (Andrews et al., 2014).

a source's flux at a range of wavelengths is often a far less complex task than making directly-comparable estimates of the uncertainties on those fluxes. But obtaining meaningful derived properties of galaxies from tools such as MAGPHYS (or other, less complex SED-fitting routines) is equally dependant upon them being provided with accurate fluxes *and accurate uncertainties*. Consider the wide range of noise environments present in the different wavebands of imaging data listed in Table 4.1; GALEX is dominated by pure photon arrival statistics, VISTA suffers significantly from sky brightness, and SPIRE experiences a large contribution from confusion noise. The uncertainty estimation process in CAAPR would have to be able to produce reliable flux uncertainty estimates in this full range of situations.

TABLE 4.2 Comparison of the resolution and sensitivity of the various NIR imaging surveys covering the *H*-ATLAS GAMA fields, for which GAMA provides supplementary reductions.

Survey	Resolution	Depth (mag)				
	(arcsec)	z / Z	Y	J	H	K / K_S
SDSS	$< 1.3^a$	20.5	-	-	-	-
UKIDSS-LAS	$< 1.2^b$	-	20.5	20.0	18.8	18.4
VIKING	$< 1.0^c$	23.1	22.3	22.1	21.5	21.2

[a] Quoted SDSS imaging resolution represents maximum typical seeing (Pier et al., 2003).

[b] Quoted UKIDSS-LAS imaging resolution represents maximum typical seeing (Lawrence et al., 2007).

[c] Quoted VIKING imaging resolution represents maximum typical seeing (Lawrence et al., 2007).

4.1.1 EXCLUDING UKIDSS-LAS

The supplementary imaging data reductions carried out by GAMA include both UKIRT UKIDSS-LAS and VISTA VIKING, which feature almost identical NIR wavelength coverage. Similarly, VIKING has an overlap of one waveband with the SDSS. In this work, I opt to use the VIKING data, for several reasons.

The first and foremost reason is that VIKING is significantly more sensitive in all bands (see Table 4.2). VIKING is 2.6 magnitudes (a factor of 11) deeper in Z-band than SDSS is in z-band (the filters of which differ slightly, having effective wavelengths separated by 25 nm). Likewise, VIKING is 2.1–2.8 magnitudes (a factor of 5–13) deeper than UKIDSS-LAS in the bands that they share. Enhanced NIR sensitivity is valuable, given the NIR faintness displayed by many of the HAPLESS galaxies. (see Section 3.1.1).

Secondly, VIKING consistently benefits from better seeing conditions than either UKIDSS-LAS or the SDSS (see Table 4.2). Even in K-band, the diffraction limit for UKIRT is $0.15''$, smaller than the detector pixel size; hence seeing completely dominates the resolution achieved.

Thirdly, whilst UKIDSS-LAS uses a K-band filter[1], VIKING employs a K_S-band filter[2]; whilst the two have similar effective wavelengths, the K-band filter has a wider overall passband. The VIKING K_S-band filter is almost identical to

---

[1] `http://www.jach.hawaii.edu/UKIRT/instruments/wfcam/user_guide/description.html.`

[2] `http://www.vista.ac.uk/Files/vts_rds/VIS-PRO-ATC-06032-0003.pdf.`

the K_S-band filter of 2MASS, making it straightforward to perform direct comparisons of their photometry (typically requiring a correction of ~ 0.001 mag[3]). This becomes useful when comparing HAPLESS to other samples in Chapter 6.

4.2 THE CAAPR PIPELINE

This section describes the process followed by CAAPR in performing photometry. The pipeline consists of three distinct stages: fitting a source aperture, measuring the source's flux, and estimating the uncertainty on that flux. CAAPR is, in essence, a 'simple' aperture photometry routine. It employs ellipses as source apertures, elliptical annuli as background apertures, and randomly-placed sky apertures to estimate noise. The procedure took initial inspiration from the method devised by Auld et al. (2013) for SPIRE photometry of the *Herschel* Virgo Cluster Survey (HeViCS). CAAPR is written in Python 2.7.

What follows is a step-by-step description of the operation of CAAPR for a given source. The main steps (1, 2, 3, etc) give an outline of the fundamentals of the process, whilst the substeps (a, b, c, etc) provide further details of the workings of the pipeline. The key stages of the process are illustrated by Figure 4.2.

Tests carried out to determine the validity of the pipeline can be found in Sections 4.4, 4.5, and 4.6. The results of these tests motivated many of the stages in the pipeline.

4.2.1 APERTURE FITTING

The initial stage of CAAPR involves defining for each source the aperture which will be used to perform the photometry. This aperture fitting procedure is conducted in the following manner.

1 Centred on the SDSS coordinates given in the *H*-ATLAS Phase-1 Version-3 catalogue for the source, a $2000'' \times 2000''$ cutout is produced for each band in which coverage is available[4]. From this point onwards each cutout, in sequence, undergoes the aperture-fitting process in its entirety.

---

[3] `http://casu.ast.cam.ac.uk/surveys-projects/vista/technical/photometric-properties`.

[4] GAMA-GALEX coverage does not include 4 of the HAPLESS galaxies (HAPLESS 19, 21, 33, and 34). However for two of them (HAPLESS 33 and 34), I was able to locate shallow observations in the GALEX archive: `http://galex.stsci.edu/GR6/`.

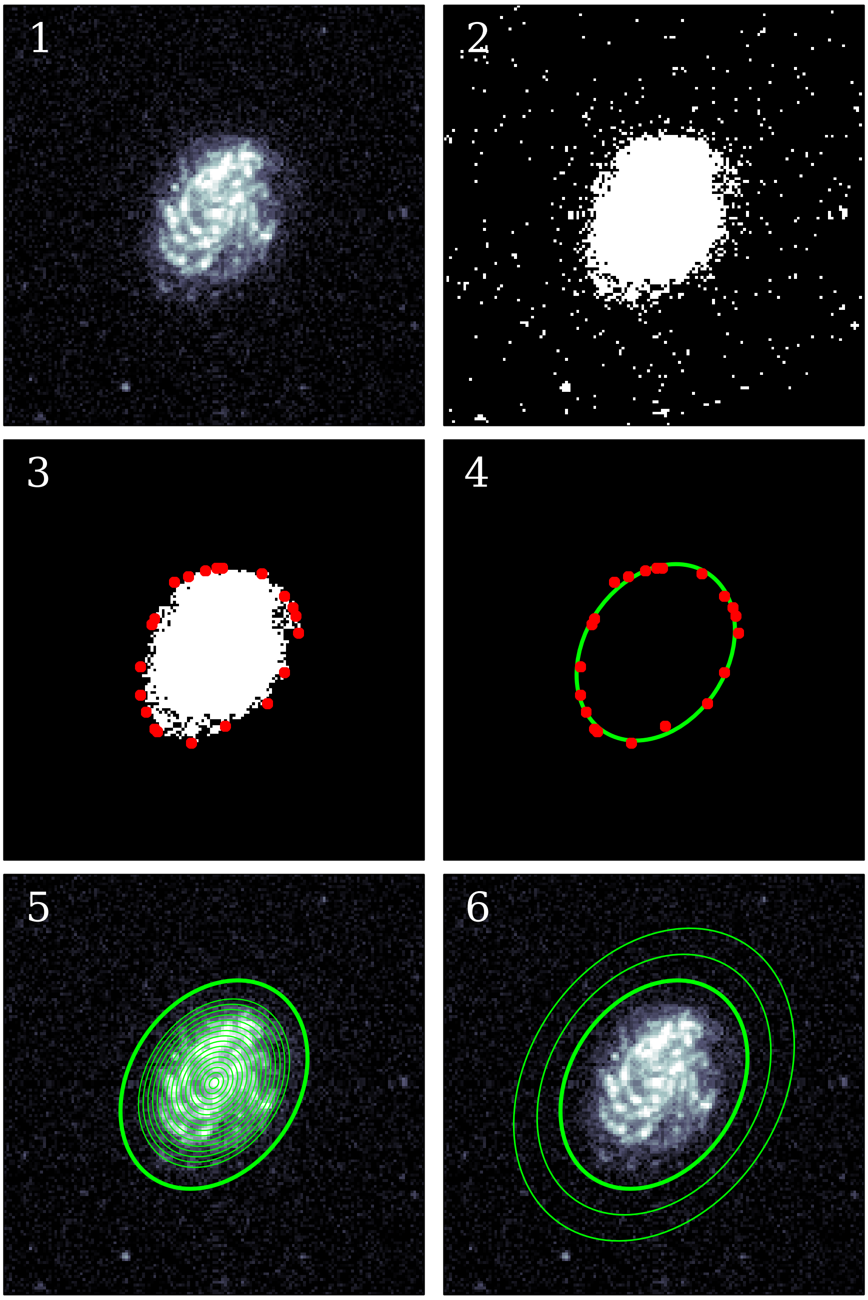

FIGURE 4.2 Illustration of the stages of the CAAPR aperture-fitting process, using GALEX FUV imagery of galaxy NGC 5584 (HAPLESS 14) as an example. Pane 1 shows the inner 500″ × 500″ portion of the full cutout, centred upon the target source. Pane 2 shows all of the pixels in the cutout with SNR > 3 (based on the cutout pixel noise, estimated according to Step 4). Pane 3 shows the significant pixels associated with the target source, contained within their convex hull (red points). Pane 4 shows an ellipse fitted to the convex hull; this ellipse provides the position angle and axial ratio of the source aperture. Pane 5 depicts the incremental annuli used to establish the semi-major axis at which the annular mean per-pixel SNR < 2 (thin concentric lines); 1.2 times this distance is then used as the semi-major axis of the source aperture (thick line). Pane 6 displays the final source aperture (thick line) and sky annulus (thin lines). The apertures at all bands for a given sources are then compared to select the largest, which is then employed for all bands.

  a The choice of $2000'' \times 2000''$ as the cutout size was made as this size is sufficient to contain the largest galaxy present in *H*-ATLAS, NGC 5746 (HAPLESS 21), with sufficient additional space for background and sky apertures.

2 The cutout is checked for large contiguous regions where a lack of coverage is represented by pixel values of 0; if found, such regions have their pixels values changed to be NaN (Not a Number).

  a Typically, map regions without coverage are represented by pixel values of NaN. However, this is not the case for the GALEX data. In the case of any of the other instruments, it would be trivial to simply replace pixels containing a value of 0 to instead contain a value of NaN. However, GALEX observations are based upon pure photon counting – meaning it is possible for a pixel to *genuinely* have received no photons during the course of an exposure. Therefore there will be many 0-value pixels in areas of actual coverage; these pixels cannot simply be converted to NaNs, as their presence conveys important information about the noise characteristics of the map. However, it is also important that the 0-value pixels that represent regions of no coverage are converted to NaN pixels; otherwise, these regions will be interpreted as being 'noiseless', resulting in an underestimate of the sky noise. Consequently, additional steps have to be taken when processing GALEX imagery.

  b GALEX cutouts where more than 10% of the pixels contain a value of 0 are deemed to be 'at risk' of having large areas without coverage filled with 0-value pixels. If a GALEX cutout is found to not be 'at risk', then it undergoes no further processing in this regard. Otherwise, it is treated to remove any large contiguous regions of 0-value pixels.

  c An 'at risk' GALEX cutout is convolved with a boxcar kernel with a diameter of 10 pixels. In map regions with actual coverage, this has the effect of 'washing out' any 0-value pixels. But large contiguous regions of 0-value pixels remain unchanged.

  d Any remaining 0-value pixels in the convolved GALEX cutout can now be safely assumed to trace areas without coverage. These pixels in the unconvolved cutout are converted to NaNs.

3 In UV-NIR bands, bright foreground stars were removed from the cutout, in order to prevent aperture contamination.

   a The SDSS DR9 (Ahn et al., 2012) catalogue was queried to identify the locations of the brightest 20% of stars in the cutout. For *ugriZ*-bands, the brightest 20% of stars were selected using the corresponding *ugriz* columns of the SDSS DR9 catalogue. Locations for stars in the non-SDSS bands were also taken from the SDSS DR9 catalogue; using SDSS *u*-band for GALEX, and SDSS *z*-band for VIKING and WISE. This was because the SDSS was still found to provide the most complete and robust identification of the stars present – particularly in the cases of the very brightest stars, the artefacts associated with which often resulted in them being missed by the catalogues of other surveys (such as UKIDSS-LAS).

   b Each star is profiled using a curve-of-growth technique, which defines the stellar-contaminated region to be masked. Starting at a radius dictated by the resolution of the current band (so as not be effected by saturated stars), concentric circular annular apertures are placed around the star. Each annulus has a width of 1 pixel, and a radius 1 pixel greater than than the annulus interior to it. The mean per-pixel flux of each annulus is compared to that of the annulus immediately preceding it. The edge of the region to be masked is defined by the annulus for which the mean per-pixel flux is $>80\%$ that of the annulus immediately preceding it.

   c Each pixel inside the masked region is replaced by means of a random sampling of the pixels immediately adjacent to the edge of the mask.

4 A preliminary estimate is made of the per-pixel noise and the average pixel value in the cutout. This is done by iteratively-sigma-clipping the cutout pixel values (with a $5\,\sigma$ clipping threshold).

   a Iterative sigma clipping is a tool used frequently throughout CAAPR, as it provides an invaluable way of estimating both the average and the scatter in a given set of values, whilst accounting for outliers in a well-controlled and consistent manner. For the set of values in question, the average (by default the median) and standard deviation are calculated. All values that lie more than a certain threshold away from the average (by default 3 times the standard deviation, although 5 standard deviations are used for Step 4) are deleted from the set of values. The average and standard deviation are then re-calculated for the clipped set of values. This process repeats until the calculated average varies by less than

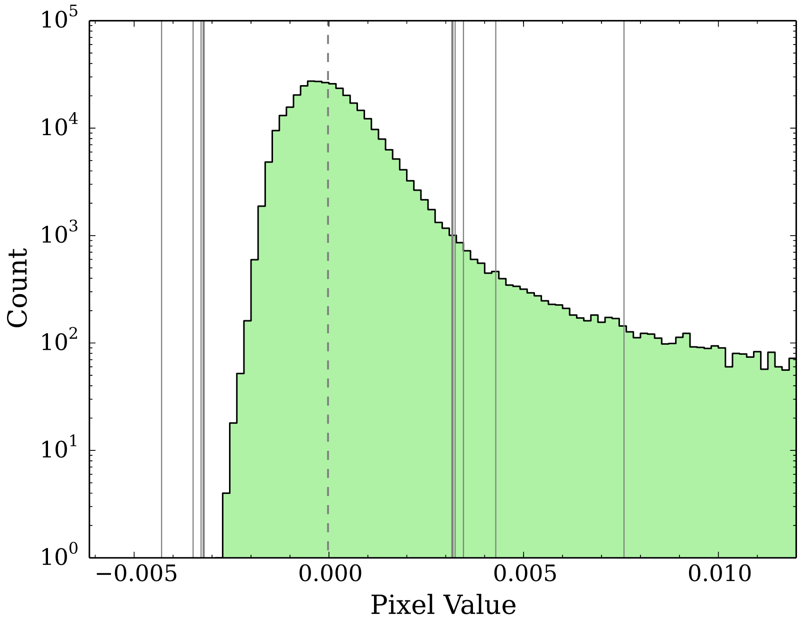

FIGURE 4.3 Histogram illustrating the process of iterative sigma-clipping, using the example of making an initial estimate of the per-pixel noise in a cutout, as per Step 4. Plotted in green is the distribution of pixel values of the $2000'' \times 2000''$ GALEX FUV photometry cutout of NGC 5584 (HAPLESS 14). The solid grey lines indicate the bounties of the clipped region (at 5 standard deviations away from the median), moving progressively inwards with each clip iteration, until converging. The dashed grey line indicates the median pixel value after the final iteration. Note that the y-axis scale is logarithmic; of the full set of 346,921 pixel values that underwent the iterative-sigma-clipping process, 337,438 (97.3%) remain inside the $5\,\sigma$ boundies of the final clip.

a given factor (by default 0.001) between iterations. This process is illustrated in Figure 4.3.

5 CAAPR isolates the region of the cutout that contains emission from the target source

a Using the estimates from Step 4 for the average pixel value and per-pixel noise, CAAPR identifies the significant pixels, defined as those pixels where $\mathrm{SNR} > 3$. This is illustrated in Pane 2 of Figure 4.2.

b Every contiguous group of significant pixels in the cutout is catalogued, and assigned a unique identifier.

c A circular aperture (with a radius equal to the beam-width in the current band) is placed in the centre of the cutout. In the vast majority of cases, all of the significant pixels found in this aperture will belong to a single contiguous feature, corresponding to the target source. This feature is thereupon isolated, and assumed to be representative the shape (though not necessarily the *size* of the target source.

d However, if no significant pixels are found inside the circular aperture, or if significant pixels belong to two separate contiguous features are present, then Step 6 goes on to assume that the source is circular in shape.

6 An ellipse is fitted to the contiguous feature of significant pixels isolated in Step 5; this ellipse provides the position angle and axial ratio (ie, the *shape*, but not the *size*) of the ellipse which will serve as the source's best-fit photometric aperture in the current band.

a CAAPR finds the vertices of the convex hull of the shape made by the significant pixels associated with the source, as illustrated in Pane 3 of Figure 4.2. The convex hull of a shape is the tightest possible polygon which will enclose that shape. In two dimensions, it can be thought of as the outline traced by an elastic band made to snap around the edge of an object.

b An ellipse is least-squares fit to the vertices of the convex hull; this is illustrated in Pane 4 of Figure 4.2. The position angle and axial ratio of this ellipse will be used for the source's photometric aperture in the current band.

7 The semi-major axis of the source aperture is determined by placing concentric elliptical annuli (with the position angle and axial ratio determined in Step 4) around the source in increments of 1 pixel-width, centred upon the optical position. The annuli are increased in size until the mean per-pixel $\mathrm{SNR} < 2$; the semi-major axis of this annulus is then multiplied by a factor of 1.2 to provide the semi-major axis of the source annulus aperture. This is illustrated in Pane 5 of Figure 4.2.

a The reason for this extension factor of 1.2 is that some flux associated with any source with a Sersic profile (ie, the vast majority of galaxies) will fall beyond the edge of any practical SNR cutoff. This is true not only for this SNR technique, but also a curve-of-growth approach (Overcast, 2010), and the SDSS Petrosian method (Blanton et al., 2001). An extension factor of 1.2 is large enough to be confident of encompassing nearly all the flux, whilst small enough to minimise aperture noise.

8 The process laid out in this subsection is repeated with each available band for a given source. The semi-major and -minor axes determined for each band are corrected for the size of the beam (see Table 4.1), by subtracting half the beam width in quadrature. The corrected semi-major axes are compared, and the largest is chosen to be the semi-major axis of the final source aperture; likewise for the semi-minor axes. Similarly, the position angle corresponding to the largest corrected semi-major axis is selected as the position angle of the final source aperture. For the vast majority of the HAPLESS galaxies (73%), it was the GALEX FUV or NUV band which defined the size of the aperture. The instances when this was not the case were typically earlier-type galaxies, where a NIR band defined the aperture size – typically VIKING *Z*-band. The selected aperture was used to perform photometry for all bands, with the exception of PACS (see Section 4.2.1.1).

9 As a by-product of the aperture-fitting process, the radial profile of each source is recorded. Using this information, the *r*-band R25 and FUV R28 for each source was determined; these values are given in Table 3.2.

4.2.1.1 PACS APERTURE FITTING

For standard *H*-ATLAS PACS 100 and 160 μm data reduction, `Nebuliser` (Irwin, 2010) was used to flatten the maps before they were run through `Scanamorphos` (Roussel, 2013). For sources with apertures $>2.5'$, I used the raw `Scanamorphos` maps instead, as `Nebuliser` removes some emission at these larger scales. Nonetheless, I still find that using the same apertures for PACS as for the other bands can result in poor-quality 100 and 160 μm photometry. Flux at 100 and 160 μm tends to be concentrated towards the centres of galaxies, often resulting in a small patch of flux at the centre of a needlessly large aperture. Examples are shown in Figure 4.4. The high amount of noise in the PACS maps means that when apertures are too large, the aperture noise will be large compared to the flux, potentially yielding an uncertainty that suggests a non-detection – even when emission associated with the source is clearly visible at the centre of the aperture. As a result, CAAPR defines the PACS apertures separately, using the 250 μm SPIRE maps, as these are reliable indicators of where detectable dust emission is present.

For 100 μm sources with SNR >1 (according to photometry with the new apertures), the improvements are modest; the median change in flux is by a negligible factor of 0.998, the median SNR increases from 7.3 to 8.0, and the number of sources with SNR >1 increases from 26 to 27.

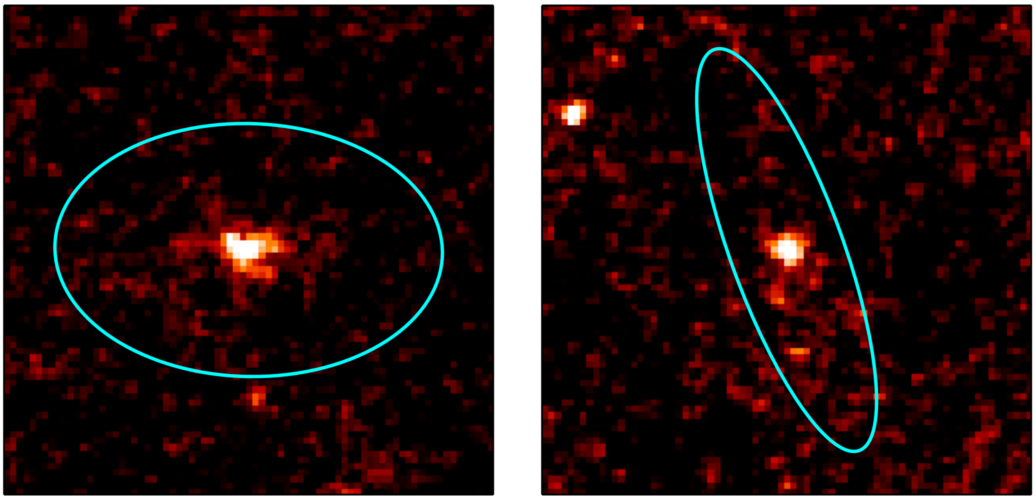

FIGURE 4.4 Examples of instances where the standard aperture generated by CAAPR for a given source is far larger than the region containing detectable emission in the PACS bands. These images, each 300″ across, show UGC 09299 (HAPLESS 9, *left*) and UGC 06780 (HAPLESS 19, *right*) as they appear at 160 µm, in comparison to the size of the standard aperture (shown in cyan). In the case of UGC 09299, the standard aperture was defined by NUV observations; in the case of UGC 06780, the standard aperture was defined by g-band observations.

However, for 160 µm sources with SNR > 1 (with the new apertures), the improvements are much more marked; the median change in flux is by a similarly insignificant factor of 1.002, but the median SNR increases from 7.3 to 9.2, whilst the number of sources with SNR > 1 increases from 30 to 36.

By employing different apertures in the PACS bands, the uncertainty in the flux is drastically reduced, and the number of detections increased – but with essentially no change in the measured fluxes. Apart from using a different band to define the apertures, PACS photometry otherwise proceeds in the same manner as described in this chapter.

4.2.2 APERTURE PHOTOMETRY

The fluxes of the HAPLESS galaxies, as given in Table 4.6, were measured by means of the method described here.

1 An elliptical source aperture, with the semi-major axis, position angle, and axial ratio determined by the method described in Section 4.2.1, and centred on the optical position of the source, is placed upon the 2000″ × 2000″ cutout

of whichever band is in question (with bright foregound stars already removed as per Section 4.2.1, Step 3). To correct for the size of the beam, the semi-major and -minor axes of the aperture are each added in quadrature to half the beam width in the current band.

2 The sum of the flux contained within the source aperture is calculated. Given the large pixel sizes in the SPIRE bands, each individual pixel is divided into a 10×10 grid of 100 sub-pixels (in a manner which preserves the integrated flux of the pixel); whenever the border of the source aperture ellipse passes through a pixel, the flux from the sub-pixels which lie inside the aperture is counted.

3 To serve as a background aperture, an elliptical annulus is placed around the source aperture, likewise centred upon the optical position of the source, and with the same position angle and axial ratio as the ellipse of the source aperture. For FUV–MIR bands, the annulus has inner and outer semi-major axes that are 1.25 and 1.5 times that of the source aperture. This is illustrated in Pane 6 of Figure 4.2. However for the *Herschel* bands, the inner and outer semi-major axes of the annulus are 1.5 and 2.5 times that of the source aperture.

a For the FUV-MIR bands, the smaller 1.25–1.5 background annulus was employed due to the manner in which GAMA mosaicked the maps together from individual observations, resulting in a variation in coverage levels across the fields. The coverage level of a given region of these maps has a strong effect upon its average sky flux. Therefore keeping the background annulus close to the source aperture ensures that the sky being sampled is representative of the sky the target source is sat upon.

b For the *Herschel* bands, there is no variation in sky flux due to different coverage levels; although there are regions of the *H*-ATLAS GAMA fields that have double coverage due to the observing strategy, the average sky flux is not affected. This makes the larger 1.5–2.5 background annulus preferable. Placing the inner edge of the background annulus further from the source aperture ensures that the annulus does not inadvertently sample actual source flux, arising from the large *Herschel* beam size. Moreover, the larger pixel size in the *Herschel* bands means that a larger background annulus is necessary simply to be confident of including a large enough number of pixels to get a reliable sampling of the local background.

c In addition to the standard reduction, the *H*-ATLAS consortium also produced background-subtracted versions of the SPIRE maps. These were produced to aid in point-source photometry, removing the need for local background subtraction of the kind performed here. In Section 4.4, I describe tests which show that for extended sources such as the HAPLESS galaxies, it is *still* necessary to perform additional background subtraction when using the background-subtracted maps.

4 To estimate the local background, CAAPR finds the iteratively sigma-clipped mean (see Section 4.2.1, Step 4) of the pixel values contained within the sky annulus.

a A number of methods of estimating the average sky value within the background annulus were compared; the regular mean, the regular, median, the iteratively-sigma-clipped mean, and the iteratively-sigma-clipped median. The regular mean and median were found to be highly unstable; in many cases one or both would radically disagree with the values given by other estimates. However the iteratively-sigma-clipped median and mean are both reasonably stable; the latter slightly more so than the former, hence this is the method used by CAAPR.

b In Section 4.6, I use the difference in calculated source flux arising from using the sigma-clipped median as opposed to the sigma-clipped mean to quantify the limit of CAAPR's ability to accurately estimate the background.

5 The calculated average local background value is then subtracted from the flux measured in the source aperture, pro rata to the number of pixels present.

6 The photometry in the GALEX, SDSS, and VIKING bands was corrected for galactic extinction in line with the GAMA method described in Hill et al. (2011), which is performed relative to SDSS measurements of *r*-band extinction (Stoughton et al., 2002), calibrated using the Schlegel et al. (1998) dust maps created using IRAS data.

7 The photometry in the PACS and SPIRE bands had aperture corrections applied, to account for flux lost due to the size of the *Herschel* beam. The necessary corrections in the SPIRE bands were computed using the SPIRE Point Spread Function (PSF) model of Griffin et al. (2013), whilst the PACS corrections were taken from the PACS instrument and calibration wiki[5].

4.2.2.1 IRAS SCANPI PHOTOMETRY

Whilst the datasets available for HAPLESS span a very wide range of wavelengths, there is nonetheless a sizeable gap in the wavelength coverage between the WISE 22 µm and PACS 100 µm bands. To constrain the emission in this regime, I used 60 µm data from IRAS (InfraRed Astronomical Satellite, Neugebauer et al., 1984). However, performing photometry with IRAS observations is notoriously difficult, not least due to its extremely poor resolution – $2.5'$at 60 µm.

Therefore to acquire IRAS 60 µm photometry of the HAPLESS galaxies I used the Scan Processing and Integration Tool (SCANPI[6]), following the procedure laid out by Sanders et al. (2003). The SCANPI tool is unable to process non-detections where the estimated background is greater than the measured flux; in those cases I recorded a flux of 0, with an uncertainty equal to the IRAS 60 µm $1\,\sigma$ sensitivity limit of 56 mJy (Riaz et al., 2006).

4.2.2.2 PHOTOMETRY OF NGC 5738

NGC 5738 (HAPLESS 22) presents an exceptional case for photometry. NGC 5738 is an edge-on dwarf lenticular galaxy, and whilst a $\sim 1'$ stellar disc is visible in the optical and NIR, its emission in the UV and in the *Herschel* bands is limited to a point-source at the centre of the optical disk. Because of the extremely different emission scales at different wavelengths, the resulting FIR and submm photometry is very poor when using CAAPR to define the appropriate aperture (which automatically fits to the optical disk). Consequently, fitting the SED of this source (Chapter 5) using the fluxes returned by CAAPR fails (χ^2 of 11.97). Therefore in this one case, I opt to make use of the *Herschel* point-source photometry. NGC 5738 is unlike any of the other HAPLESS galaxies; whilst many of the sources in my sample are compact, and present point-sources in the the *Herschel* (and UV) bands, they are usually compact across the spectrum. NGC 5738 is the only galaxy

---

[5] `http://herschel.esac.esa.int/twiki/bin/view/Public/PacsCalibrationWeb#Photometer_calibration_in_scan_m`

[6] Provided by the NASA/IPAC Infrared Science Archive: `http://irsa.ipac.caltech.edu/applications/Scanpi/`

to present a point-source in the UV and *Herschel* bands, but have its photometric aperture defined by a far more extended optical and NIR stellar disk.

4.2.3 UNCERTAINTY ESTIMATION

The uncertainty in the measured fluxes of the HAPLESS galaxies, as given in Table 4.6, were estimated as follows.

1 The aperture noise for each source is estimated. Section 4.5 details why such a convoluted process was adopted for estimating the aperture noise. It transpires that more straightforward (and widely-used) methods for estimating the aperture noise are often highly unstable – there is potentially a great deal of noise upon the noise.

  a The median and standard deviation of the pixel values in the cutout in question are calculated, and the corresponding upper and lower $3\,\sigma$ limits are determined; pixels which have values outside these $3\,\sigma$ are identified, and are deemed to be rejected pixels.

  b Random apertures are placed across the cutout. The apertures are circular, with the same area as the source aperture used for the actual photometry of the current target object. Each random aperture is background-subtracted using its own background aperture, in the same manner as for the source aperture (detailed in Section 4.2.2). The location at which each random aperture is placed upon the cutout is randomly generated, with the exception that both it, and its corresponding background annulus, must lie wholly within the cutout, and must not intersect with the source aperture of the target object.

  c Pixels within each random aperture are inspected. Every rejected pixel, as identified in Step 1.a, is removed. If more than 20% of the pixels in an aperture are removed, then the whole aperture is rejected entirely, and is no longer considered. If an aperture is accepted, the values of the non-rejected pixels it contains are summed; this summed total is then scaled up to account for that aperture's removed pixels. In essence, the rejected pixels within an aperture have their individual values each replaced by the mean of the values of that aperture's non-rejected pixels. For example, if the sum measured (excluding rejected pixels) within such an aperture were 3.5, but only 85% of its pixels had been accepted, then the

TABLE 4.3 The uncertainty contributions, as a fraction of measured flux, arising from the various sources of uncertainty discussed in this chapter, along with the total uncertainty (from summing those contributions in quadrature). The Calibration column gives the calibration uncertainty in that band. The Aperture Size column gives the uncertainty due to the variation in aperture size, as detailed in Section 4.6. The Sky Estimation column gives the uncertainty arising from the limitations on how accurately the background flux can be estimated, as described in Section 4.6.

Band	Uncertainty (%)			
	Calibration	Aperture Size	Sky Estimation	Total
FUV	4.5[a]	1.8	1.9	5.2
NUV	2.7[a]	1.4	0.6	3.1
u	1.3[b]	7.8	3.3	8.7
g	0.8[b]	4.0	0.7	4.2
r	0.8[b]	4.5	0.6	4.7
i	0.7[b]	5.6	0.9	5.8
Z	2.7[c]	5.9	0.7	6.5
Y	2.7[c]	6.3	0.7	6.9
J	2.7[c]	6.8	2.0	7.6
H	2.7[c]	6.1	1.2	6.8
K_S	2.7[c]	4.8	2.0	5.8
3.4 µm	2.9[d]	4.9	1.5	5.9
4.6 µm	3.4[d]	6.7	2.1	7.8
12 µm	4.6[d]	9.6	1.8	10.8
22 µm	5.6[d]	14.2	4.4	15.9
100 µm	12.0[e]	8.8	2.3	15.1
160 µm	12.0[e]	9.3	1.4	15.2
250 µm	7.0[f]	2.9	0.2	7.6
350 µm	7.0[f]	5.2	0.3	8.7
500 µm	7.0[f]	5.2	0.5	8.8

[a] From Morrissey et al. (2007).

[b] From the SDSS DR10 Data Release Supplement: `https://www.sdss3.org/dr10/scope.php`

[c] From Edge & Sutherland (2013).

[d] From the WISE All-Sky Release Explanatory Supplement: `http://wise2.ipac.caltech.edu/docs/release/allsky/expsup/sec4_4h.html`

[e] From the PACS insturment and calibration wiki: `http://herschel.esac.esa.int/twiki/bin/view/Public/PacsCalibrationWeb`

[f] From the SPIRE instrument and calibration wiki: `http://herschel.esac.esa.int/twiki/bin/view/Public/SpireCalibrationWeb`

final sum would be scaled up to 3.5/0.85 = 4.12. This process is repeated until 100 random apertures have been accepted.

d The standard deviation is taken of the (appropriately scaled) summed totals returned from the 100 accepted random apertures. This standard deviation is taken as the estimate of the aperture noise of the associated source flux. This process fully incorporates the contribution of confusion noise in the SPIRE bands (as confusion noise is the origin of some of the variation between the flux measured in the random apertures).

2 Each band also has a corresponding calibration uncertainty, typically expressed as a fraction of the observed flux; the calibration uncertainty for each band is listed in Table 4.3.

3 The uncertainty values of CAAPR's flux measurements need to be representative not only of the aperture noise and photometric uncertainty, but also of the limits to our ability to *truly* measure the flux of a galaxy. The tests I performed the quantify this are given in Section 4.6

4 The uncertainties from Steps 2 and 3 are added in quadrature to produce the base uncertainty for that band. This is in turn added in quadrature to the aperture noise estimate calculated Step 1.d to yield the final uncertainty for given source in a particular band.

4.3 COMPARISON OF CAAPR AND GAMA PHOTOMETRY

Figure 4.5 compares the photometry produced by the GAMA pipeline (from Hill et al., 2011, and provided for each source in the *H*-ATLAS Phase-1 Version-3 catalogue), and by CAAPR, for the HAPLESS galaxies in the FUV and *r*-band. This demonstrates that CAAPR finds a large fraction of the HAPLESS sources to be significantly brighter than indicated by the GAMA pipeline. Note that the curious very blue HAPLESS galaxies, identified in Section 3.1.1, are particularly susceptible to having their fluxes underestimated by GAMA. As discussed in Section 4.1, these sources tend to have flocculent and/or irregular morphologies, which prove especially problematic for photometric pipelines designed for sources with small angular sizes and smooth profiles.

Approximately half the HAPLESS galaxies are measured as being significantly brighter with CAAPR. Across the sample, the recorded flux increases by an

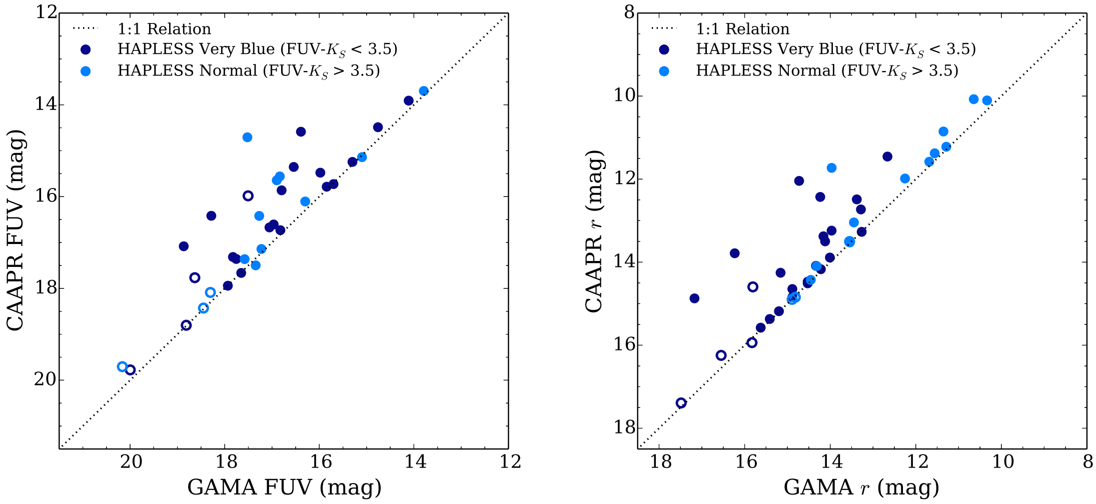

FIGURE 4.5 Comparison of photometry of the HAPLESS galaxies provided by the GAMA pipeline of Hill et al. (2011), to the photometry produced by CAAPR, in the FUV (*left*) and r-band (*right*). Note the large fraction of galaxies for which CAAPR returns significantly brighter magnitudes; this is particularly prone to happening in the case of the very blue HAPLESS galaxies. Whether a point is blue or cyan denotes the FUV-K_S colour of the source, as separated by the FUV-$K_S = 3.5$ criterion, with hollow circles indicating galaxies not in the luminosity-limited sub-sample.

average factor of 1.4 in the FUV, and 2.6 in r-band. For the very blue HAPLESS galaxies in particular, the increases in FUV and r-band are 2.1 and 2.9 respectively. This clearly demonstrates that not only did GAMA dramatically underestimate the flux of a large fraction of the HAPLESS sample, but that this effect was biased towards a particular subset. Moreover, the degree of underestimation varies noticeably between bands. Employing the GAMA photometry would have resulted in systematic errors throughout.

4.4 TESTING THE USE OF BACKGROUND-SUBTRACTED SPIRE MAPS

Aperture photometry generally entails placing a source aperture around the target object to measure its flux, then placing a sky aperture around a nearby region of the map (often an annulus around the source aperture) to measure and subtract the background contribution. When doing this, we are including the noise from both the source aperture and the sky aperture. Aperture noise increases with $\sqrt{N_{pix}}$. Not requiring a sky aperture would reduce N_{pix}, leading to a significant reduction in the uncertainty on the flux.

To this end, background-subtracted *H*-ATLAS SPIRE maps were created by Matt Smith. These maps were processed to remove the contribution of emission over scales larger than 30 pixels (3′, 4′, and 6′ at 250, 350, and 500 µm respectively), such as instrumental noise, cirrus, or large-scale background clustering. Then the pixel values were scaled such that a pixel at the peak of the pixel value distribution is set to zero. The result of this should be that the sum of the contents of an aperture placed over a source in these maps should give the flux of just that source, since any background contribution would already have been removed. The software used to achieve this was `Nebuliser`, produced by the Cambridge Astronomy Survey Unit[7].

For the purposes of clarity, from here onwards the background-subtracted maps are referred to as the nebulised maps.

For the HAPLESS galaxies, the reduction in aperture noise when using the nebulised maps, compared to the raw maps, is by a median factor of 2 (although once calibration errors are accounted for, the total reduction in uncertainty is only by a median factor of 1.4). However, the nebulised maps were created with point-source photometry in mind; it was not immediately clear whether they would also remove the need to carry out further local sky subtraction when performing aperture photometry. But even *with* further local sky subtraction (ie, using a sky annulus), there is still an average reduction in aperture noise of 2% when the nebulised maps are used.

Therefore, there are two issues that need addressing. Firstly, what is the correct way of performing aperture photometry with the nebulised maps – do they truly remove the need to carry out further local sky subtraction? This is answered in Section 4.4.1.

Secondly, how does the photometry produced using the nebulised maps compare to that from the raw maps? We are unable to assume *a priori* that the raw maps are more accurate than the nebulised ones (therefore, it is not possible to establish whether or not further background subtraction is necessary with the nebulised maps by simply comparing their fluxes to those from the raw maps). However, once it has been determined what is the correct way to perform photometry with the nebulised maps, the resulting fluxes can then be compared to those from the raw maps, to establish if there are any systematic differences. This is done in Section 4.4.2.

There was also an additional concern we wished to examine – whether or

---

[7] `http://casu.ast.cam.ac.uk/surveys-projects/software-release/background-filtering`

not distant background sources in the maps significantly affect the photometry. High-redshift sources are brighter at the longer SPIRE wavelengths. This is due to negative *k*-correction; although sources become fainter at greater distance, redshift causes increasingly bright parts of the rest-wavelength dust emission spectrum to be sampled by the SPIRE passbands. An aperture devoid of background sources at 250 μm might be dominated by them at 500 μm (despite the fact that 250 μm is the more sensitive band), potentially making extended-source photometry increasingly unreliable at longer wavelengths due to interloping red sources. Usefully, the various tests performed upon the nebulised maps in this section also provide a way to gauge the effect of these red sources. This is addressed in Section 4.4.1.4.

4.4.1 TESTING THE EFFECTS OF FURTHER SKY SUBTRACTION

Ultimately, when measuring the brightness of a source, we are interested in the amount of light we detect from it that is in excess of the local background. Thus generally speaking, it should always be 'correct', when performing aperture photometry, to perform a local sky subtraction – even on nebulised maps. Obviously, performing further sky subtraction drastically limits the reduction in aperture noise that is the main motivation for attempting to use the nebulised maps.

To test the effect of performing local sky subtraction on sources in the nebulised maps, and to test whether background sources (both resolved and unresolved) impact the photometry, I ran the SPIRE data of the HAPLESS sources though CAAPR three times; performing the photometry differently each run:

1. A source aperture was placed upon the target source, without any further sky subtraction.
2. A source aperture was placed upon the target source, then a sky annulus was placed around the source aperture (with annular inner and outer semi-major and -minor axes of 1.5 and 2.5 those of the source aperture) to estimate and subtract the background flux.
3. A source aperture was placed upon the target source, then 100 random sky apertures were placed across the photometry cutout to estimate and subtract the background flux (similar to the random apertures used by CAAPR to estimate the aperture noise).

For later comparison, I also ran the raw SPIRE maps through CAAPR twice; once with further subtraction using annuli, and once with further subtraction using sky apertures.

I adopt the following nomenclature for referring to fluxes measured via different methods of sky subtraction. Subscripts indicate what kind of further sky subtraction, if any, was carried out: $_{ann}$ for sky annuli, $_{aps}$ for sky apertures, and $_{sans}$ for cases without further sky subtraction. Superscripts convey what type of map the photometry was performed upon: $^{(R)}$ for raw maps, and $^{(N)}$ for nebulised (ie, background-subtracted) maps. So for example, $S_{aps}^{(N)}$ would denote flux measured from the nebulised map, with further sky subtraction conducted using sky apertures.

4.4.1.1 ADDITIONAL SKY SUBTRACTION WITH SKY ANNULI

Figure 4.6 shows, for all three SPIRE bands, the absolute offset in janskys between the source fluxes obtained with and without additional annular sky subtraction, plotted against source flux. Or put algebraically:

$$\text{x-axis: } S_{sans}^{(N)} \qquad \text{y-axis: } S_{ann}^{(N)} - S_{sans}^{(N)}. \tag{4.1}$$

The uncertainty in the offsets was found by adding in quadrature the aperture noise for both $S_{ann}^{(N)}$ and $S_{sans}^{(N)}$. Across all three bands there appears to be a systematic bias: fainter source fluxes tend to be measured when additional sky subtraction is employed with the nebulised maps. The size of this offset seems to become greater for brighter source flux. For some of the brightest sources at 250 and 350 µm, the offset is greater than the uncertainty in their flux. Overall, 37 of the 39 sources in the 250 µm plot were measured to be fainter when further sky subtraction was performed; at 350 µm the number is 35, and at 500 µm the number is 23.

Figure 4.7 shows the offset as a fraction of source flux, plotted against source flux. Or put symbolically:

$$\text{x-axis: } S_{sans}^{(N)} \qquad \text{y-axis: } \frac{S_{ann}^{(N)} - S_{sans}^{(N)}}{S_{sans}^{(N)}}. \tag{4.2}$$

This is essentially the same as plotting the ratio between the flux obtained with sky subtraction using sky annuli and the flux obtained without further sky subtraction (but in more straightforward units). These plots show a trend where further sky subtraction tends to cause a large relative reduction in the measured source flux of fainter sources, albeit well within their uncertainties. Whilst the brightest sources have offsets that are larger than their uncertainties, these offsets

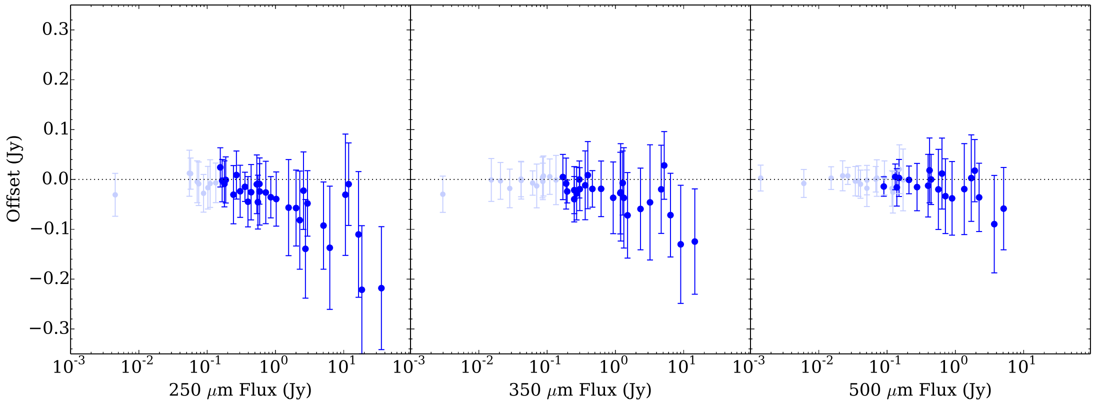

FIGURE 4.6 Source flux versus offset due to sky annuli, as described in Equation 4.1, for the HAPLESS sources in all three SPIRE bands. Full-colour data points are $> 5\,\sigma$ detections, whilst faint data points are not.

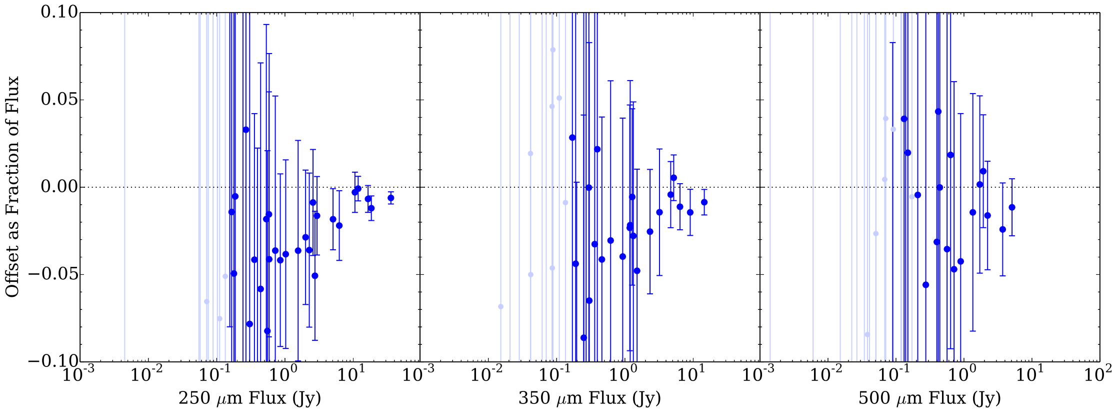

FIGURE 4.7 Source flux versus offset due to sky annuli as a fraction of source flux, as described in Equation 4.2, for the HAPLESS sources in all three SPIRE bands. Full-colour data points are $> 5\,\sigma$ detections, whilst faint data points are not.

are only a very small fraction of the source flux. The mean offset as a fraction of the source flux for $> 5\,\sigma$ detections is -2.5%, -2.5 %, and -1.4%; at 250, 350, and 500 µm respectively.

In the case of the 7 sources 250 µm which have offsets larger than their uncertainties, the mean offset is on average -1.9% of their total source flux. The reason why the offset is significant in the case of these galaxies is not because of how *large* the offset is, but instead due to how *small* their fluxes' uncertainties are (relative to the actual flux). For example, the brightest source at 250 µm has aperture noise of 80 mJy, but a flux of 35 Jy. The variation in the flux contained in randomly-placed apertures, even large randomly-placed apertures, is inevitably going to be small relative to a flux of 35 Jy. As sources this bright have such small uncertainties proportional to their flux, it is possible for a relatively small offset to nonetheless be significant.

4.4.1.2 ADDITIONAL SKY SUBTRACTION WITH SKY APERTURES

As a further check I repeated the analysis above, but employing 100 random sky apertures (used to estimate the aperture noise) to perform the additional background subtraction, instead of the annuli. In practice, CAAPR requires that sky annuli be used for background subtraction, in order to take account of map features in the region of the target source, such as cirrus, variation in coverage depth, or the highly clustered confused background (Maddox et al., 2010). However for the purposes of the current analysis, using a large number of sky apertures for background subtraction will negate the sensitivity of these tests to the localised quirks of contents of the sky annuli (such as bright background sources, etc), making it easier to identify systematic effects.

Figure 4.8 is the same as Figure 4.6, but instead using sky apertures for the additional background subtraction, ie:

$$\text{x-axis: } S_{sans}^{(N)} \qquad \text{y-axis: } S_{aps}^{(N)} - S_{sans}^{(N)}. \tag{4.3}$$

The same trend is apparent, this time with less scatter: source fluxes are consistently returned as fainter when performing additional sky subtraction, compared to source-aperture-only measurements on the nebulised maps. At 250 and 350 µm, this is the case for every source; at 500 µm, it's the case for all but 4. This offset increases with source flux, and is larger than the uncertainty for the brightest sources.

Likewise, Figure 4.9 is a repeat of Figure 4.7 (but using sky apertures instead

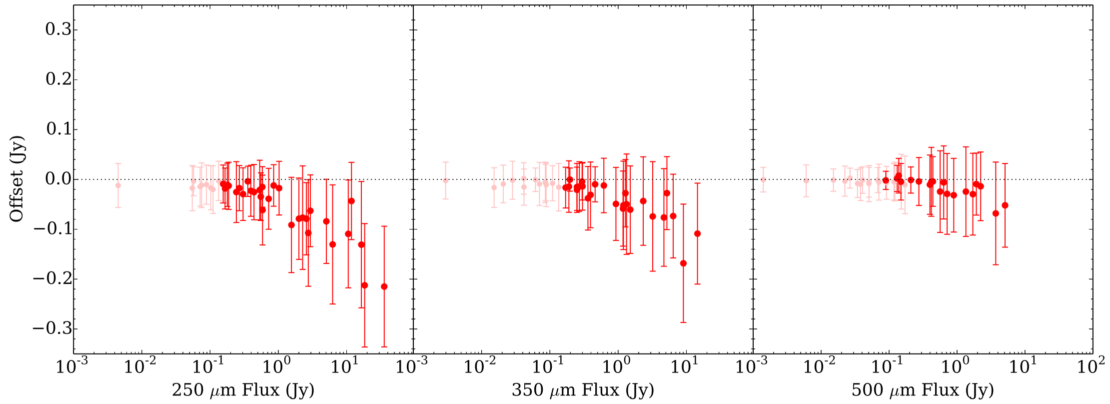

FIGURE 4.8 Source flux versus offset due to sky apertures, as described in Equation 4.3, for the HAPLESS sources in all three SPIRE bands. Full-colour data points are $> 5\,\sigma$ detections, whilst faint data points are not.

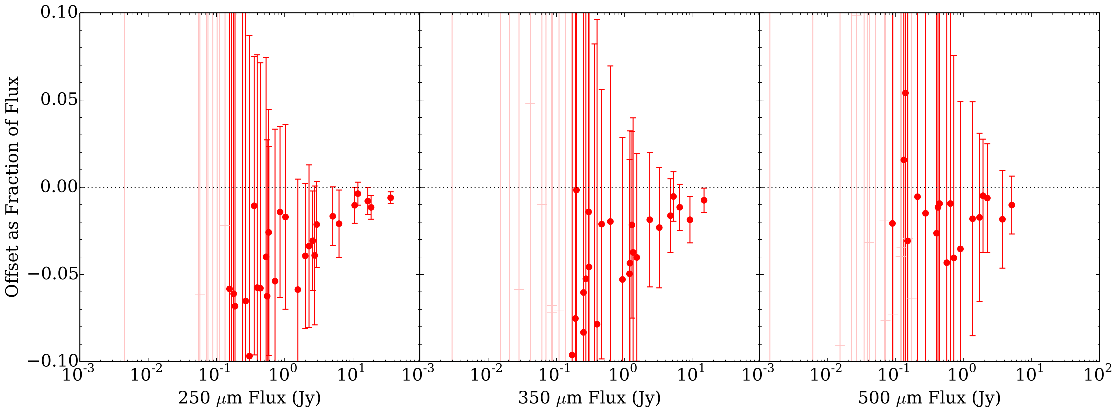

FIGURE 4.9 Source flux versus offset due to sky apertures as a fraction of source flux, as described in Equation 4.4, for the HAPLESS sources in all three SPIRE bands. Full-colour data points are $> 5\,\sigma$ detections, whilst faint data points are not.

of sky annuli) showing the offset as a fraction of source flux, as given by:

$$\text{x-axis: } S_{sans}^{(N)} \qquad \text{y-axis: } \frac{S_{aps}^{(N)} - S_{sans}^{(N)}}{S_{sans}^{(N)}}. \tag{4.4}$$

The mean offset as a fraction of the source flux for $> 5\,\sigma$ detections is -3.9%, -3.7%, and -1.5%; at 250, 350, and 500 µm respectively – all larger than was the case when using sky annuli. In the cases where the difference in source flux measured between the two methods is larger than the uncertainty, the actual offset represents $\lesssim$ 2% of the total source flux. The standard SPIRE calibration uncertainty is 7%. For comparison, the number of $> 5\,\sigma$-detected sources for which the offset is greater than this 7% limit is 4, 4, and 2; at 250, 350, and 500 µm respectively.

4.4.1.3 ORIGIN OF THE OFFSET CAUSED BY ADDITIONAL SKY SUBTRACTION

A consistent decrease in flux measured from nebulised maps is observed when further local sky subtraction is carried out. This means that the sky level being subtracted *consistently contains a positive amount of flux*. In creating the background-subtracted maps, `Nebuliser` essentially attempts to filter out the large-scale background. However, when performing photometry upon the nearby HAPLESS galaxies, the necessary apertures are large enough that they also include a 'background' of more distant galaxies, both detected and undetected. `Nebuliser` cannot remove the flux of smaller features such as these, so they could be the origin of the flux causing the offset.

The *H*-ATLAS Phase-1 Version-3 catalogue contains 109,231 at $> 5\,\sigma$ across the equatorial fields, and these fields have a combined area of 161.6 deg^2. That corresponds to one source per 5.3 arcmin^2 of sky. Compare this to the mean source aperture size for the HAPLESS sources of 8.9 arcmin^2 at 250 µm (and the mean sky annulus size of 35.6 arcmin^2). We should therefore clearly expect to find these detected background sources in most of the HAPLESS photometric apertures.

Moreover, Figures 4.6 and 4.8 demonstrate that the flux offsets due to further sky subtraction are greatest for the brightest sources. The brightest sources also tend to be the largest in angular size, with correspondingly large apertures, therefore making them exactly the sources which we would expect to be the most affected by detected background sources falling into the apertures.

These detected background sources are therefore plausible candidates to be the origin on the positive flux being removed by further sky subtraction. To examine this, Figure 4.10 shows the offset due to sky subtraction, per arcmin^2 of

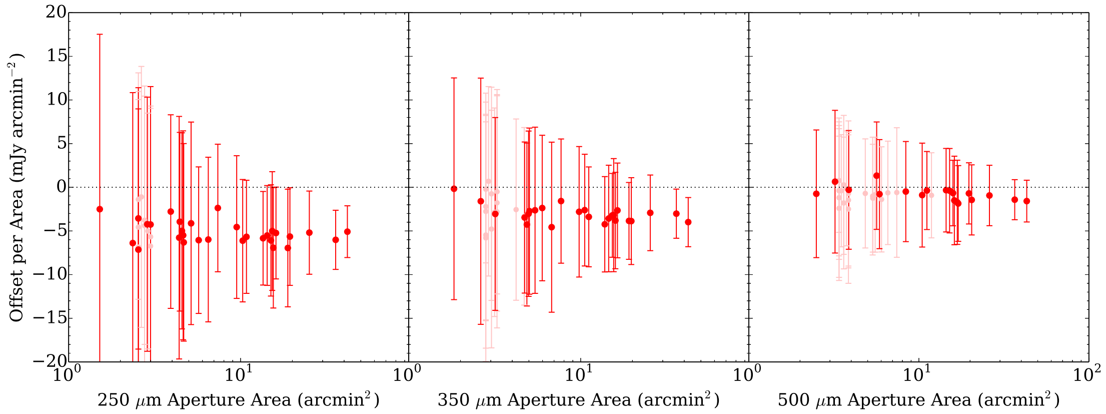

FIGURE 4.10 Source aperture area versus offset per area of sky aperture, as described in Equation 4.5, for the HAPLESS sources in all three SPIRE bands. Full-colour data points are $> 5\,\sigma$ detections, whilst faint data points are not.

sky aperture. Using A_{aps} to represent sky aperture area, this is given explicitly by:

$$\text{x-axis: } S_{sans}^{(N)} \qquad \text{y-axis: } \frac{S_{aps}^{(N)} - S_{sans}^{(N)}}{A_{aps}}. \tag{4.5}$$

This shows a near-constant flux offset due to further sky subtraction in each band, per unit area of aperture. The offset per aperture area does seem to decrease in the case of some of the smaller sources. The offset per aperture area also decreases at increasing wavelength. The median offset due to further sky subtraction is (-5.01 ± 1.47), (-2.86 ± 1.38), and $(-0.81 \pm 0.78)\,\text{mJy}\,\text{arcmin}^{-2}$ at 250, 350, and 500 μm respectively (with standard deviations as errors). The fact that these values are roughly constant per unit aperture area indicates that the offsets are due to a near constant level of positive flux being present across the nebulised maps, which further sky subtraction is removing from the measured source fluxes. This is what is giving rise to the difference between the fluxes measured with and without further sky subtraction on the nebulised maps in Section 4.4.1.

To test whether this is what would be expected due to the detected background sources in the maps, we can compare these values to the average levels of flux that would be due to sources found in the *H*-ATLAS catalogues, and to the total flux present in the nebulised maps themselves.

The 109,231 $5\,\sigma$ sources of the *H*-ATLAS Phase-1 Version-3 catalogue represent a combined 250 μm flux of $(5,737 \pm 758)$ Jy (uncertainty derived from linearly summing the uncertainties of all sources), across 161.6 deg^2 of sky. This corresponds to a mean flux level across the maps of $(9.86 \pm 1.31\,\mathrm{mJy\,arcmin})^{-2}$, incompatible with the $(5.01 \pm 1.47)\,\mathrm{mJy\,arcmin}^{-2}$ level of sky flux that leads to the offset observed when performing further sky subtraction.

The *H*-ATLAS consortium has also produced provisional matched-filter source catalogues, which contain many more sources, 172,926 at $>5\,\sigma$. With their combined flux of $(6,399 \pm 850)$ y at 250 μm, the resulting mean map surface brightness level due to these sources would be $(11.00 \pm 1.46)\,\mathrm{mJy\ arcmin}^{-2}$. If the threshold for inclusion is reduced to $>3\sigma$ sources (of which there are 452,040 with a total flux of $(11,442 \pm 2,250)$ Jy), the mean surface brightness due to sources at 250 μm would increase to $(19.67 \pm 3.81)\,\mathrm{mJy\,arcmin}^{-2}$. In both cases, the value is far in excess of the sky flux level giving rise to the observed offset. Counter-intuitively, the offset caused by performing further sky subtraction on the nebulised maps is significantly *less* than the offset that the detected background sources in the maps would be *expected* to cause.

Setting the nebulised maps to be zero mean when performing photometry without further sky subtraction would not account for the observed offsets. The total flux contained in the nebulised maps (found by simply summing the flux contained in all map pixels) is 5,004, 2,730, and 842 Jy, at 250, 350, and 500 μm respectively. This corresponds to a mean flux level of (8.6 ± 0.8), (4.7 ± 0.4), and $(1.5 \pm 0.4)\,\mathrm{mJy\,arcmin}^{-2}$ at each band (uncertainties from maximum variation in mean pixel level between maps), which are greater than, and incompatible with, the sky flux levels that correspond to the offset observed in the photometry.

Table 4.4 summarises the sky flux levels that would be predicted due to the causes detailed above, and the level actually measured as giving rise to the photometry offset in the nebulised maps.

4.4.1.4 RED SPIRE INTERLOPERS

As previously mentioned, there is a concern that due to the negative *k*-correction in SPIRE bands, red submm sources not in the 250 μm maps, but present at longer wavelengths, could interfere with the photometry; particularly at 500 μm. However Figures 4.6 to 4.10 demonstrate clearly that the offsets in flux due to further sky subtraction always become less significant at longer wavelengths.

Figure 4.10 in particular allows us to gauge the effects of background

TABLE 4.4 The levels of flux per unit area of sky observed in an offset in each SPIRE band when performing further sky subtraction upon the nebulised maps, along with the flux levels that would be expected for different potential origins. As the *H*-ATLAS catalogues are 250 µm-selected, no catalogue estimates are provided for them at 350 and 500 µm, as these would not be representative.

Origin of Offset Values	Sky Flux Level (mJy arcmin^{-2})		
	250 µm	350 µm	500 µm
Measured by CAAPR	5.0 ± 1.5	2.9 ± 1.4	0.8 ± 0.8
Phase-1 Version-3 catalogue prediction	9.9 ± 1.3	-	-
Matched-filter 5σ catalogue prediction	11.0 ± 1.5	-	-
Matched-filter 3σ catalogue prediction	19.7 ± 3.8	-	-
Map mean level prediction	8.6 ± 0.8	4.7 ± 0.4	1.5 ± 0.4

sources upon the photometry. If red interlopers are present in the 500 µm SPIRE maps, we can expect them to contribute some extra amount of flux per map area. Were they significantly influencing the photometry, we would expect to see a noticeable negative offset per area in the 500 µm pane of Figure 4.10. However this plot in fact shows the lowest level of offset per area of all the SPIRE wavelengths. Indeed, from this plot it is not clear that there is any systematic flux offset at all at 500 µm. In light of this, we can safely conclude that if interloping sources do have an effect upon the photometry, it is insignificant across the HAPLESS sample.

4.4.2 COMPARING FLUXES OBTAINED FROM BACKGROUND SUBTRACTED AND RAW MAPS

Another way of assessing the nebulised maps is by simply comparing the fluxes measured using them to the fluxes measured using the raw maps. Ideally, if the fluxes obtained from the nebulised maps are correct, they should not differ systematically from those obtained from the raw maps using the necessary further background subtraction.

Figure 4.11 shows the offset between the the fluxes from nebulised maps (with no further sky subtraction), and the fluxes measured using the raw maps (with standard local sky subtraction using sky annuli), which stated algebraically is:

$$\text{x-axis: } S_{ann}^{(R)} \qquad \text{y-axis: } S_{sans}^{(N)} - S_{ann}^{(R)}. \tag{4.6}$$

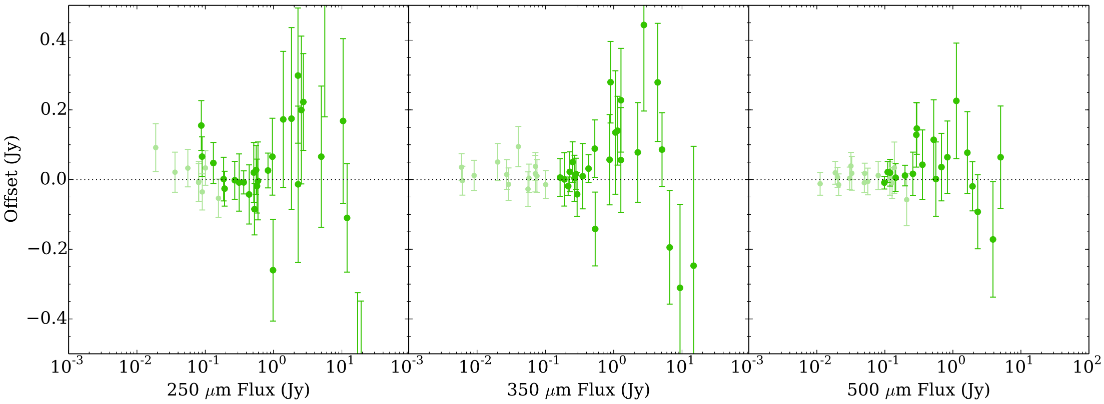

FIGURE 4.11 Source flux versus the offset between fluxes measured from raw maps and fluxes measured from nebulised maps without further sky-subtraction, as described in Equation 4.6, for the HAPLESS sources in all three SPIRE bands. Full-colour data points are $> 5\,\sigma$ detections, whilst faint data points are not.

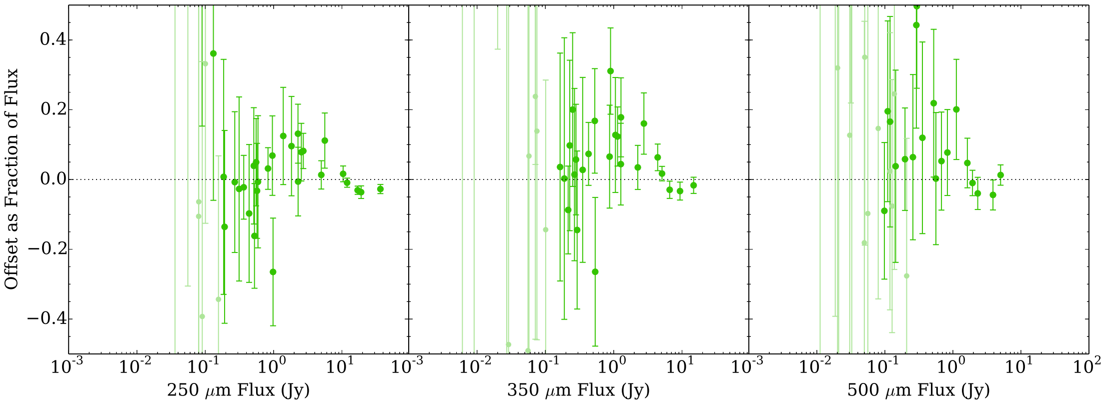

FIGURE 4.12 Source flux versus the offset as a fraction of source flux between fluxes measured from raw maps and fluxes measured from nebulised maps without further sky-subtraction, as described in Equation 4.7, for the HAPLESS sources in all three SPIRE bands. Full-colour data points are $> 5\,\sigma$ detections, whilst faint data points are not.

The uncertainty in the offsets was found by adding in quadrature the aperture noise of each. There does not appear to be any systematic trend between offset and source flux, although there is a lot of scatter. The number of $> 5\,\sigma$ sources for which the offset is greater than the uncertainty is 10, 9, and 4; at 250, 350, and 500 µm respectively.

Figure 4.12 shows the offset in Figure 4.11 as a fraction of the flux obtained from the raw maps, as given by:

$$\text{x-axis: } S_{ann}^{(R)} \qquad \text{y-axis: } \frac{S_{sans}^{(N)} - S_{ann}^{(R)}}{S_{ann}^{(R)}}. \tag{4.7}$$

This shows that brighter sources are more to likely suffer from an offset greater than their uncertainty. The median offset as a fraction of the source flux for $> 5\,\sigma$ sources is 1.0%, 4.2%, and 5.5%; and the number of sources offset by more than their uncertainty is 10, 9, and 4; at 250, 350, and 500 µm respectively. Whilst this suggests that sources fluxes measured for the HAPLESS galaxies with the nebulised maps tend to be lower than those from the raw maps, there is again no obvious trend of this depending upon source brightness.

Figure 4.13 is a repeat of Figure 4.11, except that the photometry obtained from the nebulised maps now use further local annular sky subtraction, as described by:

$$\text{x-axis: } S_{ann}^{(R)} \qquad \text{y-axis: } S_{ann}^{(N)} - S_{ann}^{(R)} \tag{4.8}$$

Likewise, Figure 4.14 is a repeat of Figure 4.12 but with the annular sky-subtracted fluxes from the nebulised maps, as stated by:

$$\text{x-axis: } S_{ann}^{(R)} \qquad \text{y-axis: } \frac{S_{ann}^{(N)} - S_{ann}^{(R)}}{S_{ann}^{(R)}} \tag{4.9}$$

The median offset as a fraction of the source flux for $> 5\,\sigma$ detections is 0.2%, -2.2%, and -3.1%; at 250, 350, and 500 µm respectively – smaller than for Figure 4.12. However, the number of sources offset by more than their uncertainty is 11, 12, and 7, at 250, 350, and 500 µm respectively – more than was the case in Figure 4.12. This suggests that the scatter between the fluxes measured from the raw and nebulised maps is enough to overwhelm any difference in flux due to performing further sky subtraction on the nebulised maps.

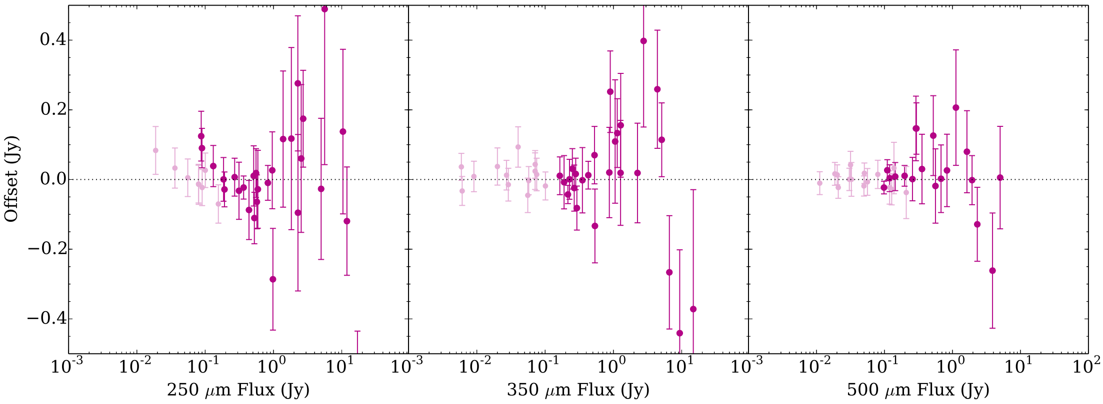

FIGURE 4.13 Source flux versus the offset between fluxes measured from raw maps and fluxes measured from nebulised maps with further sky-subtraction using sky annuli, as described in Equation 4.8, for the HAPLESS sources in all three SPIRE bands. Full-colour data points are $> 5\,\sigma$ detections, whilst faint data points are not.

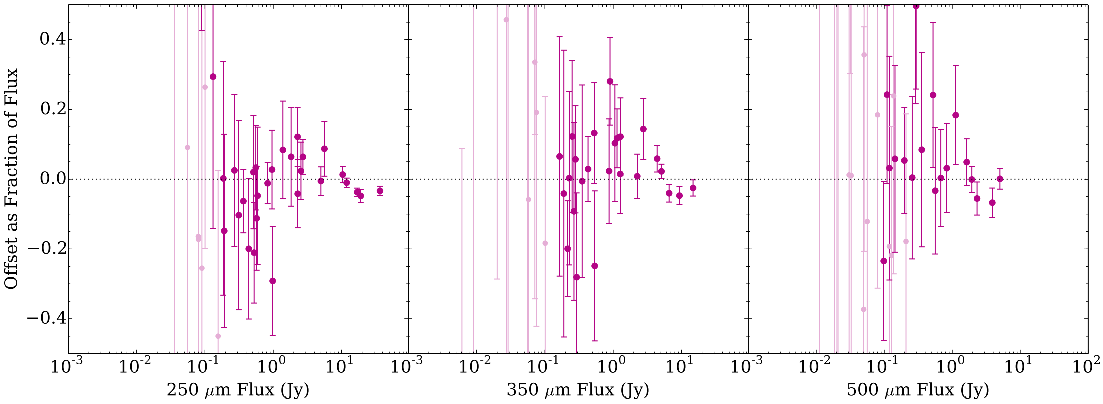

FIGURE 4.14 Source flux versus the offset as a fraction of source flux between fluxes measured from raw maps and fluxes measured from nebulised maps with further sky-subtraction using sky annuli, as described in Equation 4.9, for the HAPLESS sources in all three SPIRE bands. Full-colour data points are $> 5\,\sigma$ detections, whilst faint data points are not.

4.4.2 CONCLUSIONS FROM TESTING THE USE OF BACKGROUND-SUBTRACTED SPIRE MAPS

Ideally, background-subtracted maps produced using `Nebuliser` should allow the flux of a source to be measured without the need for further sky subtraction with annuli or apertures. As a test of the nebulised maps, photometry of the HAPLESS sources was performed on these maps by CAAPR, both without further local sky subtraction, and with sky subtraction performed using sky annuli, and sky apertures. With further local sky subtraction, the measured fluxes are found to change at 250, 350, and 500 µm by an average of -2.5%, -2.5 %, and -1.4% when using sky annuli, and by -3.9%, -3.7%, and -1.5%, when using sky apertures.

The process of creating the nebulised maps does not remove the flux of detected background sources. The sky density of sources detected in the *H*-ATLAS Phase-1 Version-3 catalogue is one source per 5.3 arcmin^2 of sky, compared to the mean HAPLESS source aperture size of 8.9 arcmin^2. Therefore, we would expect these background sources, and their flux, to be present in the photometric apertures of the HAPLESS source.

The flux offset due to further sky subtraction on the nebulised maps is found to be roughly constant per unit area of aperture. However the offsets encountered are incompatible with the offsets that would arise from the maps not being set to have a zero mean. Nor can the flux of the detected sources in the *H*-ATLAS source catalogues explain the flux levels causing the offsets (Section 4.4.1.3).

All of this evidence suggests that it is necessary to perform further sky subtraction on the nebulised maps. The confused background of these maps is highly clustered (Maddox et al., 2010), so this further sky subtraction should employ sky annuli, in order to properly sample the sky at the particular location of each target source. Even though this means performing photometry with the nebulised maps in exactly the same way as with the raw maps, using the nebulised maps provides a median 2% reduction in aperture noise. This is therefore the method CAAPR employs for SPIRE photometry. Note that the average *systematic* offsets caused by further sky subtracting the background subtracted maps are smaller than the average *random* offsets between the fluxes obtained from the raw and nebulised maps (Section 4.4.2).

The offset per aperture area is found to be insignificant at 500 µm, which suggests that red sources (brighter at longer wavelengths due to negative *k*-correction) do not noticeably affect photometry (Section 4.4.1.4).

4.5 TESTING METHODS OF RELIABLY ESTIMATING APERTURE NOISE

Originally, CAAPR calculated aperture noise by placing 100 apertures at random positions across the photometry cutout of a given source (excluding the location of the target source itself). Each aperture was circular, with the same area as the target source aperture. The flux in each random aperture was summed, and background subtracted in the same manner as the target source aperture had been (to reflect the additional noise introduced by carrying out sky subtraction). The resulting 100 summed values were then sigma-clipped, and the final clipped standard deviation was taken to represent the aperture noise.

However, upon repeating this same process multiple times for any given source, it was noticed that significantly different values for the aperture noise would be returned each time. This is due to the use of randomly positioned apertures. Depending upon whether the random apertures were placed on bright background sources, or unusually empty patches of sky, a different estimate of the aperture noise would be calculated each time. In the cases of some bands, particularly the WISE 3.4 and 3.6 µm bands, the aperture noise values returned could vary by a factor of several. Therefore the aperture noise estimates generated by any individual run were not reliable, which was not acceptable.

Steve Maddox devised an improved method of estimating aperture noise, described in Steps 1.a–1.d of Section 4.2.3, designed to curtail the potential for severe variation in the returned aperture noise values.

4.5.1 COMPARISON OF OLD AND NEW APERTURE NOISE ESTIMATIONS

To characterise the behaviour of this new technique, and establish whether or not this new approach succeeds in limiting the variation in noise values, I ran CAAPR 20 times for all of the HAPLESS galaxies; 10 times using the original aperture noise estimation method, then 10 times using the new technique. Each run was performed for the GALEX NUV, WISE 3.4 µm, and SPIRE 250 µm bands; these bands provide a good range of noise environments, whilst also being quick to run.

With the runs completed, each of the sources had 10 aperture noise values calculated with the old method, and 10 with the new. The upper left pane of Figure 4.15 shows all of the old and new aperture noise values returned for each

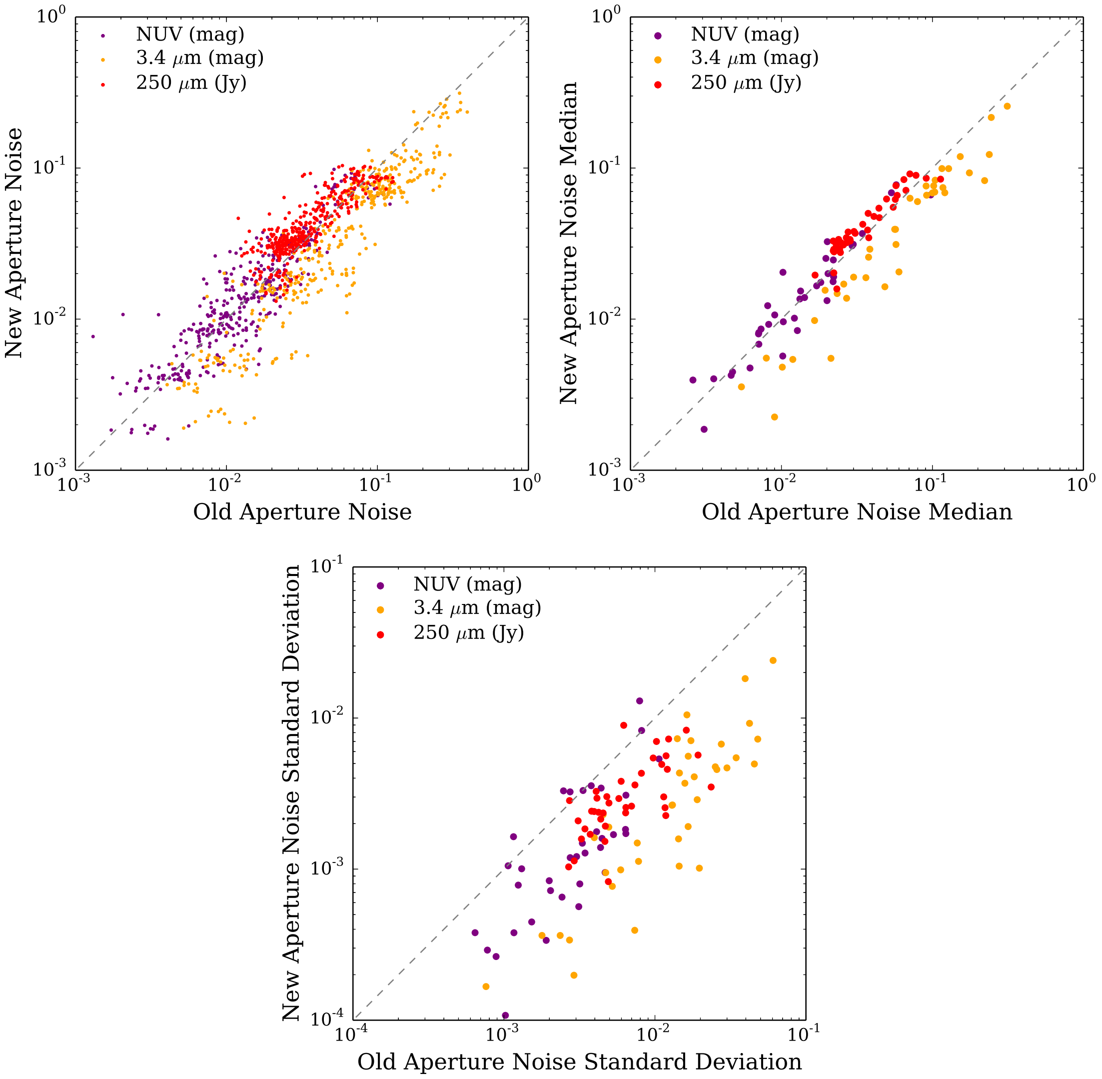

FIGURE 4.15 *Upper Left:* Plot comparing all of the aperture noise values returned for each of the HAPLESS sources in the GALEX NUV, WISE 3.4 µm, and SPIRE 250 µm bands, using the old and new methods. *Upper Right:* Plot comparing the medians of the aperture noise values returned for each source. *Lower:* Plot comparing the standard deviation of the 10 aperture noise values returned for each source with the old and new methods, showing the marked increase in stability with the new approach.

TABLE 4.5 The median standard deviations, $\sigma_{\sigma_{ap}}$, of the aperture noise values, σ_{ap}, for the HAPLESS sources, using the old and new aperture noise estimation techniques.

Band	Old Median $\sigma_{\sigma_{ap}}$	New Median $\sigma_{\sigma_{ap}}$
NUV (mag)	0.0027	0.0012
3.4 µm (mag)	0.0145	0.0027
250 µm (Jy)	0.0058	0.0027

source. The horizontal 'strata' visible in the scatter, particularly for the 3.4 µm values, show the wide range of aperture noise values produced by the old method. The range of values generated by the new technique is noticeably reduced in all three bands, indicating that it is much more stable.

The upper right pane of Figure 4.15 compares the medians of the noise values returned for each source, between the two methods. As would be expected, the WISE 3.4 µm values exhibit the largest difference; on average, the new aperture noise is 68% of the old value. Unexpectedly, the NUV and 250 µm values show, on average, an increase in their noise values returned with the new technique. In the NUV case this increase is small (median increase of 9%), the scatter of which in Figure 4.15 encompasses the 1:1 relationship. However, the median increase in the new average noise values at 250 µm is 18%; this is most pronounced for sources with smaller noise values. The potential origins of this increase are addressed in Section 4.5.2.

To quantify how successful the new technique is at reducing the range of noise values returned, the standard deviation was taken of the old and new sets of noise estimates for each HAPLESS source. These are plotted against one another in the lower pane of Figure 4.15. This clearly demonstrates a large reduction in the variation in noise values returned using the new method. The standard deviation is lower in all but five cases at NUV, and one at 250 µm. The median standard deviations in all three bands for both the old and new methods are given in Table 4.5.

The WISE 3.4 µm band, previously the worst offender, has shown a dramatic reduction in median standard deviation, 5.0 times smaller than it was with the old method. Sizeable reductions are also seen in NUV and 250 µm, which now exhibit median standard deviations 2.3 and 2.0 times smaller then what they were previously. The average standard deviation reduction is by a factor of 2.7, across all bands. It seems that the new technique has succeeded in the providing much more stable estimates of the aperture noise.

4.5.2 INCREASES IN APERTURE NOISE ESTIMATES WHEN USING THE NEW TECHNIQUE

As can be seen in Figure 4.15, estimates of the aperture noise using the new technique are found to slightly increase compared to the old for NUV (average 9%), and more noticeably for 250 μm (average 18%). Naïvely, one would expect the new method to result in consistently lower noise estimates, as it is designed to curtail the influence of outlier pixels; which, in most cases, will be bright background sources such as stars and galaxies.

The increase in the noise in the NUV band is within its own scatter, and seems negligible. However at 250 μm, there is an interplay between the effects of confusion, and effects of the differing clipping methods employed by the old and new techniques.

For most bands, observations consist of 'empty' sky, punctuated by sources. When randomly placing noise apertures across such a map, the variation in the flux contained within each such aperture simply reflects how much flux is present due to sources on top of the background. The old technique would sigma-clip these 100 values, removing the outliers: it would exclude those apertures which contained an above- or below-average amount of flux from these resolved background sources. However, *H*-ATLAS 250 μm observations approach the confusion limit. There is no such thing as 'empty' sky. Some patches of sky will contain more flux from confused sources, some less. Moreover, this confused background is highly clustered (Maddox et al., 2010), and so varies considerably depending upon location.

The result of this is that random apertures placed upon the 250 μm maps are far less likely to contain sum values which can be considered particularly extreme, given the inherently wider range of likely background values. This can be seen in Figure 4.16, which contains histograms of the distribution of random aperture values returned by the old and new methods. The stepped black line shows the sums in aperture returned by the old method (so without any of the exclusions made using the new technique). The NUV and 3.4 μm distributions show a steep ascent from the faintest values ('empty' sky) to most-common values (sky with an average amount of flux from background sources), followed by a long tail out to steadily larger values (sky containing increasingly brighter background sources). Whereas the 250 μm distribution is much more symmetrical – the wide range of confused sky values is sufficient to subsume the values of sky apertures which contain particularly large or small amounts of flux from resolved background sources.

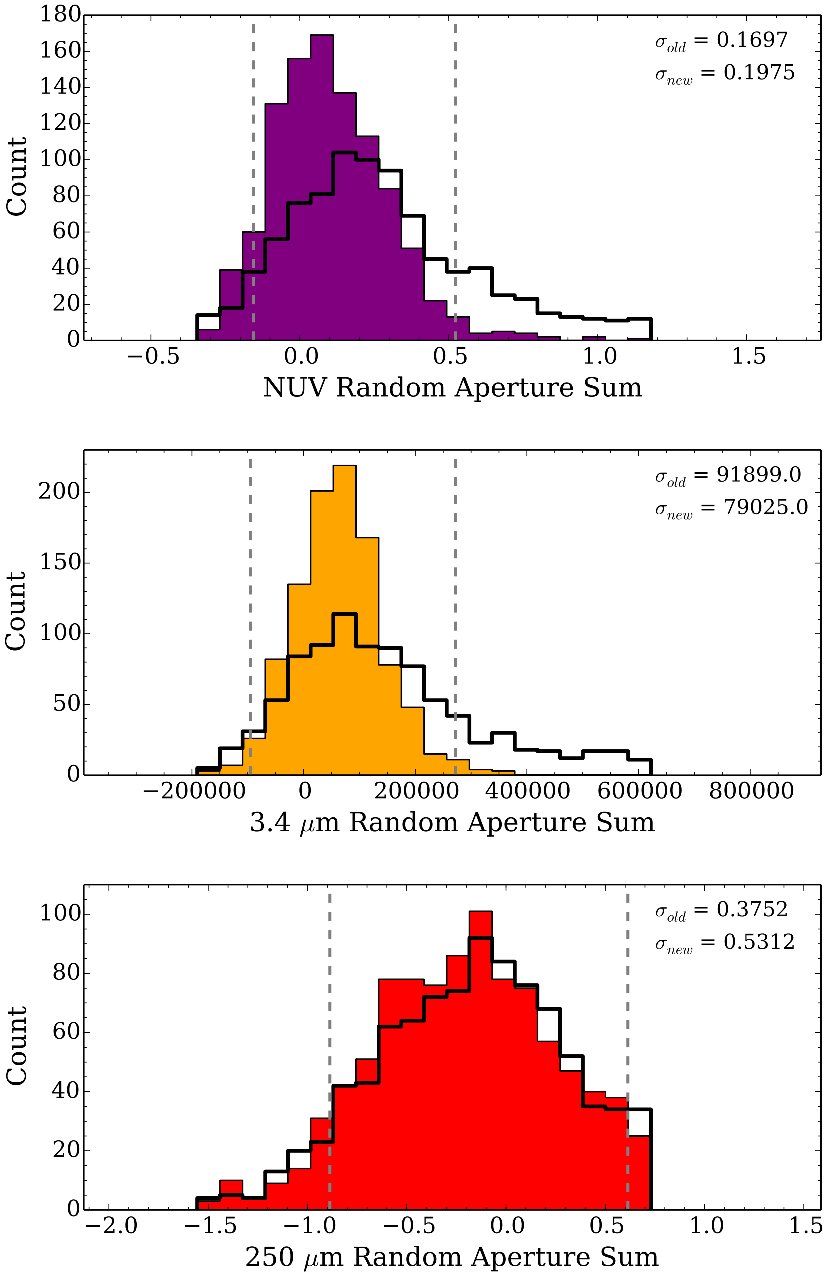

FIGURE 4.16 Histograms of the pixel sums contained within random apertures positioned across 2000″ × 2000″ photometry cutouts of an arbitrary patch of sky at NUV (*upper*), 3.4 µm (*centre*), and 250 µm (*lower*). Sum values are in the pixel units of their respective maps (which are arbitrary). The coloured bars show the distributions of aperture sums returned by the new technique, whilst the stepped black lines show the distributions produced by the old. The calculated aperture noise values for both are stated in the upper right corner of each plot. The dashed vertical lines demark the converged 2σ clipping limits outside which all values were discarded by the old method. Note that, whilst both aperture noise estimation procedures only involve using 100 random apertures per cutout, these histograms were created by using 1000 apertures apiece; this was to make the nature of the underlying distributions clear in each case.

This prevents the 250 µm distribution forming tails like those seen in the NUV and 3.4 µm distributions.

The difference in these distributions mean that the bands are differently affected by the clipping methods employed by the old and new aperture noise techniques.

In the old technique, the sums from 100 randomly placed apertures were collected, shown by the stepped black line in Figure 4.16. These values were then iteratively sigma-clipped with a $2\,\sigma$ threshold. The dashed vertical lines show the upper and lower converged $2\,\sigma$ limits produced by this method. The final standard deviation only counted the values contained within these limits. In the NUV and 3.4 µm plots, this has the effect of clipping out all of the values contained within their bright tails.

The coloured bars in Figure 4.16 show the distribution of random aperture sums produced by the new technique for each band. As detailed in Section 4.5, the new technique excludes random apertures containing extreme sums; this therefore excludes in the first instance the aperture sums which would have otherwise made up the bright tail of the distribution. The apertures that are not excluded have the values of their extreme pixels replaced by the mean value of the non-extreme pixels; this causes the aperture sums that are included in the distribution to be biased towards being located closer to the peak.

For the NUV and 3.4 µm bands, the point brighter than which the old method clips extreme apertures is very similar to the point brighter than which the new method does not return apertures. However, the new method returns a more centrally concentrated distribution than is exhibited by the old values that survive the clip at 3.4 µm; this is why the new technique generally returns a smaller value for aperture noise than the old. For NUV, the distribution with the clip boundaries of the old technique is no less smooth than the new distribution, hence the negligible change in noise value returned.

In the 250 µm case, the distributions returned by the old and new techniques are essentially identical; very few get rejected, or have their sum significantly altered by excluded pixels. But the old method clips this distribution, whilst the new does not. As a result, the final standard deviation measured by the old technique includes a broader range of values, and so generally returns a larger aperture noise estimate.

4.5.2 CONCLUSIONS FROM TESTING METHODS OF RELIABLY ESTIMATING APERTURE NOISE

The old aperture noise estimation technique employed by CAAPR was found to return significantly varying output between runs; therefore new technique was suggested by Steve Maddox to limit the effect of extremal values upon the process, to make it more stable. I find that this new technique reduces the standard deviation of the values generated between runs by an average factor of 2.7 compared to the old method. The actual noise values produced by the two techniques are compatible, and generally within the scatter of their 1:1 relation. However in the case of the 250 µm band in particular, the aperture noise estimates returned were on average greater by 18%. This transpires to be due the interplay between the clipping procedures employed and the noise environments involved. Both sets of results seem reasonable, and it is not necessarily possible to identify one aperture noise estimate to be the 'more correct'. However, given that the new technique is much more stable, it is the one utilised for CAAPR.

4.6 TESTING THE LIMITS OF CAAPR'S ABILITY TO DETERMINE FLUXES

As explained in Section 4.2.3, calibration uncertainty and aperture noise alone do not fully quantify the limit of our ability to measure the flux of astronomical sources – despite the fact that it is common practice in much of the literature to use only these two measures to define photometric uncertainties. To quantify the limit of CAAPR's ability to measure the true flux of a source, I performed two tests.

Firstly, I repeated the photometry for the HAPLESS sample in all bands, but with a source aperture size 20% larger for each source. Ideally, the fluxes obtained using these larger apertures would be identical to those obtained from the normal apertures; the amount of deviation between the two lets us gauge the effectiveness of both our aperture-fitting and our background-subtraction. The distribution of deviations for each band is shown in Figure 4.17. In the case of every band, the mean deviation is within the standard error of a deviation 0, suggesting that no systematic difference in flux is caused by the larger aperture. I took the root median squared deviation to represent the uncertainty in each band arising from this effect; the values are given in Table 4.3.

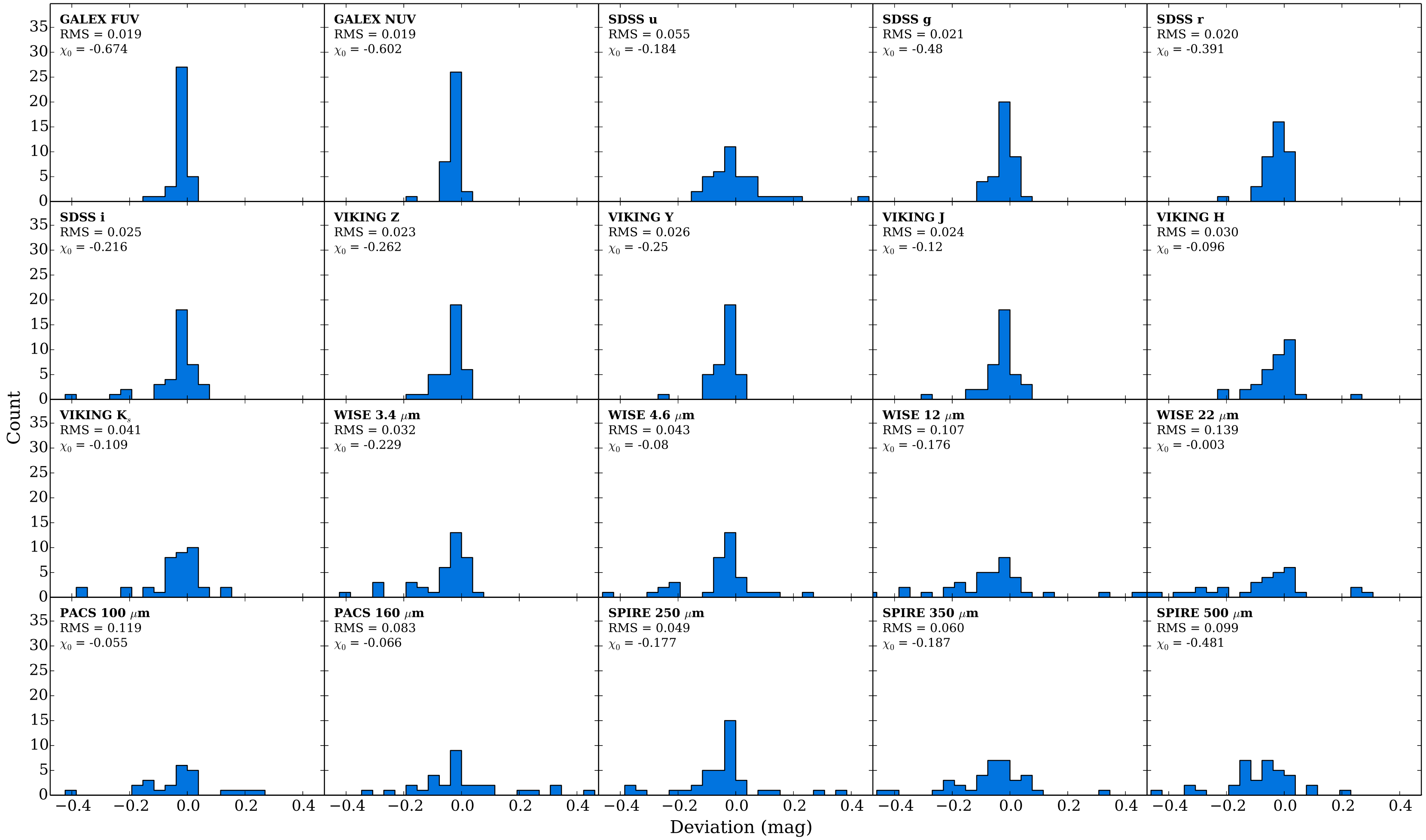

FIGURE 4.17 Histograms of the deviation between the standard CAAPR fluxes measured for the HAPLESS sources in each band, and the fluxes measured using apertures with semi-major axes 20% larger. For each band, the root median squared deviation is given. Also stated is χ_0: the difference between the median deviation and a deviation of 0, expressed as a fraction of the standard deviation (meaning that $-1 > \chi_0 > 1$ is compatible with an average deviation of 0).

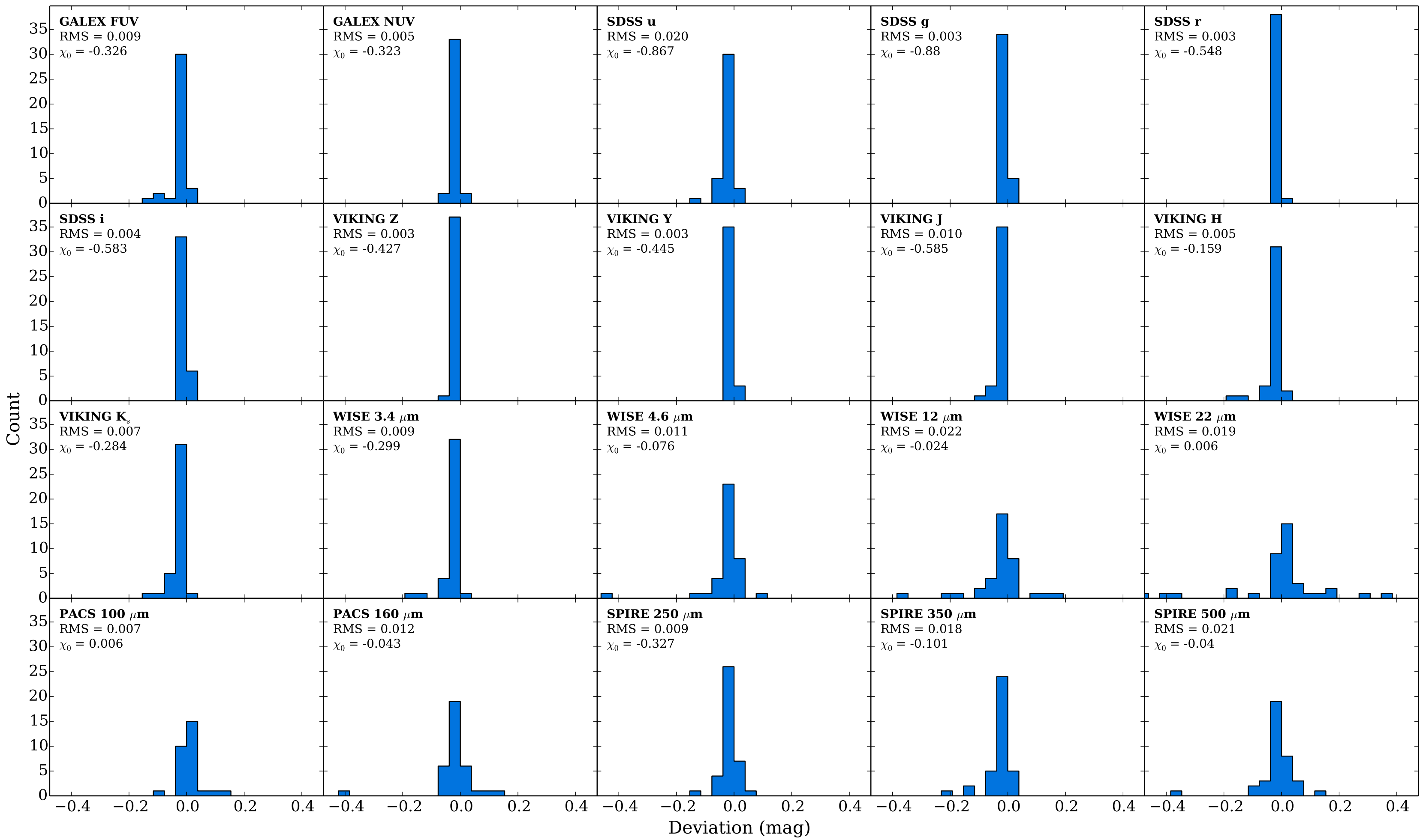

FIGURE 4.18 Histograms of the deviation between the standard CAAPR fluxes measured for the HAPLESS sources in each band, and the fluxes measured When estimating the background using the iteratively sigma-clipped median (as opposed to the usual iteratively sigma-clipped mean). For each band, the root median squared deviation is given. Also stated is χ_0: the difference between the median deviation and a deviation of 0, expressed as a fraction of the standard deviation (meaning that $-1 > \chi_0 > 1$ is compatible with an average deviation of 0).

The second test I performed involved repeating the photometry, this time estimating the average pixel value in the sky annuli using the iteratively sigma-clipped median, instead of the iteratively sigma-clipped mean. In an ideal world, these would both be equally valid methods, and so the deviation between the final fluxes returned by them allows us to gauge the limits of our ability to accurately determine the background. The deviation values within each band are plotted in Figure 4.18. The mean deviation in each band is compatible with zero, implying that no systematic bias is caused by the difference in background estimation technique. To quantify the uncertainty due to this limitation in background estimation, I once again took the root median squared of the deviations for each band; Table 4.3 lists the resulting values.

4.7 PHOTON NOISE CONTRIBUTION

Given this chapter's extensive efforts to precisely quantify flux uncertainties (particularly for *Herschel* observations), I have here, for completeness, also considered the contribution of photon noise to the uncertainty of submm photometry.

As described in Chapter 1, the submm wavelength regime lies in the 'no-man's land' between the detection methods generally used at shorter and longer wavelengths. In the submm, photons possess too little energy for photoconductors to be useful as detectors; however, the wavelengths in question are nonetheless too short for antennae to be used.

This 'no-man's land' status remains when considering photon noise in the submm. At shorter wavelengths, where $h\nu \gg kT$, photon noise is dominated by shot noise – simple Poissonian uncertainty arising from photon arrival statistics. At lower energies, where $h\nu \ll kT$, the wave-like behaviour of light takes over, and the random arrival of individual photons is replaced by the highly correlated arrival of consecutive peaks in the wave (Ade, Griffin, & Tucker, *in prep.*), and interference becomes a source of noise. However, in the submm, $h\nu \approx kT$. Consider a typical *Herschel* observation, being made at a frequency of 1.2×10^{12} Hz (250 μm), of an object at a temperature of 20 K – in which case, $h\nu = 2.88\,kT$. As such, it is necessary to consider both the shot noise and wave noise aspects of photon noise in the submm.

The flux of a fainter source will consist of fewer photons, increasing the uncertainty due to photon noise (which scales with $\sqrt{N}$ for both shot and wave noise, where N is the number of photons detected). However, for a brighter source, aperture noise can be rendered negligible, potentially increasing the photon noise as a fraction of the total uncertainty. Hence, I determined the shot noise and wave noise at 250 µm for both the brightest HAPLESS source, NGC 4030 (HAPLESS 6), and the faintest, LEDA 1241857 (HAPLESS 13).

To determine the photon noise, it is necessary to work out the total number of detected photons that corresponds to a given flux. By definition, 1 Jy = $10^{-26}\,\mathrm{J\,s^{-1}\,Hz^{-1}\,m^{-2}}$. At a wavelengths of 250 µm, the photon energy $h\nu = 7.956 \times 10^{-22}\,\mathrm{J}$; given *Herschel*'s effective collecting area of $8.50\,\mathrm{m^2}$ (Pilbratt et al., 2010), a flux of 1 Jy therefore corresponds to an incident photon rate of $n = 1.068 \times 10^{-4}\,\mathrm{s^{-1}\,hz^{-1}}$. The SPIRE 250 µm filter has a bandwidth of $\lambda/3$ (Griffin et al., 2010), corresponding to $\Delta\nu = 4.11 \times 10^{11}\,\mathrm{Hz}$; therefore we can approximate the incident photon rate from a source with a flux of 1 Jy at 250 µm to be $4.39 \times 10^{7}\,\mathrm{s^{-1}}$.

Because *Herschel* observes by continually scanning the sky, an observation of a given source does not have a straightforward 'integration time' to combine with the incident photon rate to provide the total number of photons detected. However, the coverage maps created as part of the *H*-ATLAS SPIRE data reduction can be used to determine the average effective integration time per sky area. At 250 µm this is $0.7\,\mathrm{s\,arcsec^{-2}}$. This value allows us to calculate the effective integration time for a source, using the area of its photometric aperture.

At 250 µm, the photometric aperture of NGC 4030 has an area of $19.3\,\mathrm{arcmin^2}$, which yields an effective integration time of $\tau = 13.51\,\mathrm{s}$. Given its flux of 36.8 Jy (see Table 4.6), the 250 µm detection of NGC 4030 represents 8.72×10^{10} incident photons. However, account also needs to be taken of the quantum efficiency (η) of the SPIRE detectors, and the overall throughput efficiency (f) of instrumentation as a whole – which have values of $\eta = 0.66$ and $f = 0.38$ at 250 µm (Griffin et al., 2008). Incorporating these factors gives a total number of photons detected from NGC 4030 of 2.19×10^{10}. This entails a Poissonian photon shot noise of 1.48×10^{5} photons – 0.00066 % of the total. Or, put in terms of the source flux, 0.25 mJy.

Similarly, LEDA 1241857 has an aperture area of $0.45\,\mathrm{arcmin^2}$, giving an effective integration time of $\tau = 0.32\,\mathrm{s}$ at 250 µm. Combined with its 250 µm flux of 45 mJy, and following the same process as above, this gives a total of 6.16×10^{5} detected photons, and hence a photon shot noise of 785 photons – 0.12 % of the total, equating to 57 µJy.

The photon wave noise is more complex to consider. The root-mean-squared fluctuation in the number of photons detected is described by Bose-Einstein statistics, and is given by:

$$\sigma_{wave} = \sqrt{n\tau\Delta\nu\left(1 + \frac{f\eta}{e^{\frac{h\nu}{kT}} - 1}\right)} \tag{4.10}$$

taken from Ade, Griffin, & Tucker (*in prep.*). Assuming a source temperature of 20 K, and using all other values as above, this yields photon wave noise for NGC 4030 of 1.49×10^5 photons; this is 0.00068 % of the total, or 0.25 mJy. For LEDA 1241857, the photon wave noise corresponds to 790 photons – 0.13 % of the total, or 58 µJy.

The shot noise and wave noise estimates are extremely similar, serving to illustrate the position of the submm at the crossover between the two domains. Regardless, in the case of both the brightest and faintest HAPLESS sources, photon noise is utterly negligible.

4.8 CONCLUSION

In this chapter, I have described the process of acquiring high-quality photometry of the HAPLESS galaxies. There was no existing reliable photometry for the galaxies of the HAPLESS sample, so I designed, created, and tested a purpose-built photometric pipeline – CAAPR: Chris' Adequate Aperture Photometry Routine. The emphasis for CAAPR was that it not only produce reliable fluxes, but also reliable uncertainties; an aspect of photometry often neglected in the literature, but of growing importance as SED-fitting becomes a tool increasingly relied upon by astronomers. The extensive testing detailed in Sections 4.4, 4.5, and 4.6 suggests that CAAPR is able to consistently produce the accurate, reliable photometry required.

The photometry conducted using CAAPR demonstrated that the GAMA pipeline severely underestimated the brightness of many of the HAPLESS galaxies. With CAAPR, the average increase in observed flux is by a factor of 1.6 in the FUV and 1.4 in r-band, relative to the GAMA photometry.

The full photometry of the HAPLESS galaxies, carried out by CAAPR as per the process laid out in this chapter, is given in Table 4.6.

TABLE 4.6 CAAPR photometry of the HAPLESS galaxies. The dimensions of the elliptical apertures used are also provided – the semi-major axis is denoted by a, the position angle by θ, and the axial ratio (the semi-major axis divided by the semi-minor axis) by a/b. Coverage was not available for all sources in all bands. Supplemented by IRAS 60 µm photometry acquired using SCANPI, as described in Section 4.2.2.1.

HAPLESS	Aperture dimensions			GALEX (mag)			
	a (arcsec)	θ (deg)	a/b	FUV	Δ FUV	NUV	Δ NUV
1	28.4	158.2	1.075	15.78	0.05	15.23	0.03
2	36.5	23.8	1.064	16.67	0.05	16.36	0.03
3	122.0	72.8	1.477	14.48	0.05	14.18	0.03
4	36.6	28.0	1.437	17.31	0.05	16.94	0.03
5	36.5	0.7	1.381	18.08	0.10	17.41	0.03
6	178.9	117.2	1.455	13.69	0.05	12.99	0.03
7	178.9	85.3	3.424	14.58	0.05	14.08	0.03
8	65.0	141.2	1.292	15.47	0.05	15.14	0.03
9	122.0	178.5	1.533	15.35	0.05	15.08	0.03
10	126.0	62.1	2.058	15.14	0.07	14.61	0.03
11	85.3	50.2	3.665	17.36	0.05	16.75	0.03
12	44.6	147.2	1.568	17.08	0.05	16.65	0.03
13	24.3	67.3	1.347	18.80	0.05	18.38	0.03
14	134.2	63.9	1.205	13.90	0.06	13.52	0.03
15	32.5	46.2	1.289	18.42	0.05	17.79	0.03
16	69.1	32.2	2.122	17.14	0.05	16.50	0.03
17	44.7	139.4	1.156	16.41	0.05	16.16	0.03
18	52.8	96.6	1.274	15.86	0.05	15.51	0.03
19	134.2	109.9	3.776	-	-	-	-
20	142.3	30.3	2.096	17.01	0.10	16.27	0.04
21	276.6	78.5	4.490	-	-	-	-
22	40.6	151.1	1.638	19.70	0.08	18.50	0.05
23	117.9	60.0	2.317	15.64	0.05	14.91	0.03
24	36.5	152.8	1.729	17.76	0.05	17.59	0.03
25	126.1	151.5	1.811	16.10	0.05	15.42	0.03
26	113.8	162.3	1.366	14.83	0.05	14.52	0.03
27	65.0	157.4	3.380	17.35	0.05	16.80	0.03
28	85.3	28.8	1.394	15.56	0.05	15.03	0.03
29	117.9	85.0	1.197	14.70	0.05	13.87	0.03
30	60.9	143.7	1.439	16.19	0.05	15.86	0.03
31	101.6	47.4	1.123	15.24	0.05	15.16	0.03
32	37.9	46.3	1.391	17.49	0.07	17.00	0.03
33	28.4	136.9	1.540	16.60	0.05	16.36	0.03
34	65.0	178.7	1.338	15.55	0.06	15.46	0.04
35	73.1	8.1	1.846	16.73	0.05	16.25	0.03
36	48.7	76.6	2.341	17.66	0.05	17.24	0.03
37	89.4	76.2	2.711	16.42	0.05	16.01	0.03
38	32.4	30.8	1.650	17.94	0.05	17.53	0.03
39	48.8	131.0	1.110	15.72	0.05	15.34	0.03
40	52.8	117.6	1.161	15.89	0.05	15.47	0.03
41	48.7	50.5	1.619	15.98	0.05	15.83	0.03
42	24.3	3.6	1.471	19.77	0.10	19.53	0.08

TABLE 4.6 – *continued*

HAPLESS	SDSS (mag)							
	u	$\Delta\,u$	g	$\Delta\,g$	r	$\Delta\,r$	i	$\Delta\,i$
1	14.57	0.10	13.72	0.04	13.26	0.05	13.06	0.06
2	15.84	0.33	15.08	0.06	14.83	0.07	14.72	0.10
3	13.53	0.22	12.72	0.06	12.42	0.06	12.23	0.08
4	15.96	0.13	15.00	0.05	14.51	0.06	14.28	0.07
5	16.41	0.37	15.29	0.06	14.84	0.07	14.61	0.09
6	11.99	0.11	10.68	0.04	10.10	0.05	9.76	0.06
7	13.54	0.30	12.41	0.04	12.04	0.05	11.82	0.06
8	14.46	0.19	13.67	0.05	13.37	0.06	13.15	0.07
9	14.89	0.39	13.82	0.08	13.78	0.12	13.53	0.12
10	13.68	0.20	12.20	0.05	11.58	0.05	11.26	0.06
11	15.62	0.38	14.53	0.05	14.09	0.06	13.90	0.07
12	15.78	0.17	14.88	0.06	14.47	0.06	14.29	0.08
13	17.26	0.42	16.39	0.08	15.93	0.07	15.75	0.11
14	12.82	0.13	11.87	0.05	11.45	0.05	11.33	0.06
15	16.49	0.24	15.37	0.06	14.89	0.06	14.62	0.09
16	15.19	0.20	14.02	0.05	13.52	0.05	13.23	0.07
17	15.77	0.28	15.08	0.06	14.87	0.08	14.88	0.12
18	14.96	0.22	14.20	0.05	13.88	0.05	13.74	0.08
19	14.64	0.20	13.71	0.06	13.49	0.07	13.15	0.07
20	13.90	0.39	12.29	0.05	11.37	0.05	10.91	0.06
21	12.54	0.16	10.94	0.04	10.07	0.05	9.61	0.06
22	15.73	0.24	14.22	0.05	13.50	0.05	13.11	0.06
23	13.58	0.18	12.29	0.05	11.72	0.05	11.38	0.06
24	17.19	0.47	16.43	0.10	16.24	0.12	16.20	0.25
25	13.49	0.15	11.95	0.04	11.22	0.05	10.83	0.06
26	14.35	0.53	12.83	0.06	12.48	0.06	12.25	0.08
27	15.91	0.34	15.01	0.06	14.64	0.06	14.47	0.08
28	13.45	0.12	12.43	0.05	11.98	0.05	11.75	0.06
29	12.53	0.15	11.40	0.04	10.85	0.05	10.58	0.06
30	15.18	0.26	14.43	0.06	14.08	0.06	13.94	0.09
31	14.67	0.72	13.14	0.07	12.73	0.07	12.51	0.08
32	15.93	0.30	14.84	0.05	14.42	0.06	14.19	0.10
33	16.08	0.14	15.41	0.05	15.18	0.07	15.07	0.07
34	15.22	0.36	14.39	0.07	14.25	0.08	14.16	0.15
35	15.35	0.34	14.55	0.07	14.17	0.06	13.97	0.09
36	16.49	0.42	15.64	0.07	15.36	0.08	15.22	0.14
37	14.99	0.19	13.70	0.05	13.04	0.05	12.73	0.06
38	16.77	0.35	15.83	0.06	15.57	0.08	15.39	0.09
39	14.63	0.13	13.58	0.05	13.24	0.05	13.06	0.06
40	14.78	0.24	13.94	0.05	13.57	0.06	13.40	0.08
41	15.39	0.14	14.75	0.04	14.59	0.05	14.57	0.07
42	18.62	1.31	17.70	0.33	17.39	0.36	17.28	1.11

TABLE 4.6 – *continued*

HAPLESS	VIKING (mag)									
	Z	ΔZ	Y	ΔY	J	ΔJ	H	ΔH	K_S	ΔK_S
1	12.83	0.07	12.70	0.07	12.62	0.08	12.50	0.07	12.70	0.06
2	14.59	0.08	14.56	0.09	14.57	0.10	14.48	0.10	14.63	0.12
3	12.14	0.07	12.05	0.08	12.00	0.10	12.03	0.10	12.34	0.10
4	14.18	0.07	14.05	0.08	13.97	0.09	13.93	0.16	14.15	0.09
5	14.47	0.07	14.36	0.08	14.32	0.09	14.24	0.09	14.49	0.10
6	9.54	0.07	9.32	0.07	9.18	0.08	8.96	0.07	9.18	0.06
7	-	-	-	-	11.66	0.09	11.48	0.08	11.92	0.06
8	13.08	0.07	13.00	0.08	12.93	0.10	12.82	0.08	13.06	0.10
9	13.63	0.22	13.53	0.14	13.49	0.25	14.26	6.85	13.99	0.35
10	10.99	0.07	10.79	0.07	10.65	0.08	10.49	0.07	10.74	0.06
11	13.72	0.07	13.63	0.08	13.56	0.10	12.88	0.27	13.62	0.17
12	14.07	0.07	13.98	0.08	13.90	0.10	13.80	0.10	14.00	0.09
13	15.60	0.09	15.45	0.09	15.53	0.12	15.54	0.19	15.66	0.16
14	11.16	0.07	11.09	0.07	11.09	0.08	11.08	0.09	11.18	0.07
15	14.57	0.07	14.48	0.08	14.46	0.09	14.40	0.11	14.68	0.12
16	13.03	0.07	12.89	0.07	12.82	0.08	12.72	0.08	12.87	0.06
17	14.73	0.08	14.66	0.11	14.64	0.15	14.65	0.20	14.86	0.35
18	13.62	0.07	13.54	0.08	13.49	0.09	13.43	0.09	13.65	0.16
19	13.34	0.08	13.46	0.11	13.15	0.12	13.18	0.15	13.62	0.17
20	10.62	0.07	10.33	0.07	10.10	0.08	9.84	0.07	10.01	0.06
21	9.27	0.07	8.95	0.07	8.73	0.08	8.50	0.07	8.66	0.06
22	12.85	0.07	12.65	0.07	12.53	0.08	12.36	0.07	12.58	0.06
23	11.12	0.07	10.90	0.07	10.75	0.08	10.49	0.07	10.68	0.06
24	16.09	0.10	16.13	0.16	16.01	0.31	16.01	0.36	15.94	0.36
25	10.59	0.07	10.36	0.07	10.22	0.08	10.12	0.07	10.25	0.06
26	12.22	0.07	12.18	0.08	12.20	0.09	12.09	0.08	12.44	0.17
27	14.35	0.08	14.27	0.09	14.24	0.11	14.19	0.19	14.45	0.12
28	11.61	0.07	11.48	0.07	11.40	0.08	11.28	0.07	11.56	0.07
29	10.38	0.07	10.19	0.07	10.07	0.08	9.94	0.07	10.14	0.08
30	13.83	0.08	13.79	0.11	13.80	0.11	13.81	0.26	13.95	0.13
31	12.24	0.07	12.17	0.08	12.11	0.10	12.05	0.09	12.29	0.13
32	13.99	0.07	13.86	0.08	13.82	0.09	13.71	0.08	13.89	0.09
33	14.97	0.07	14.92	0.10	14.97	0.11	13.97	0.11	15.02	0.11
34	14.20	0.09	14.19	0.20	14.09	0.16	14.19	0.18	14.38	0.24
35	13.90	0.08	13.83	0.09	13.78	0.12	-	-	13.94	0.38
36	15.14	0.09	15.11	0.10	14.99	0.14	14.88	0.34	15.33	0.83
37	12.45	0.07	12.26	0.08	12.25	0.08	12.22	0.09	12.33	0.08
38	15.15	0.08	15.09	0.11	15.08	0.14	15.19	0.20	15.23	0.19
39	12.70	0.07	12.71	0.08	12.83	0.09	12.84	0.08	13.38	0.13
40	13.25	0.07	13.15	0.08	13.08	0.08	12.92	0.09	13.29	0.08
41	14.39	0.08	14.51	0.12	14.46	0.11	15.09	0.23	15.34	0.26
42	17.11	0.28	17.06	0.59	17.07	0.35	16.91	1.05	17.29	0.59

TABLE 4.6 – *continued*

HAPLESS	WISE (mJy)							
	3.4 µm	Δ 3.4 µm	4.6 µm	Δ 4.6 µm	12 µm	Δ 12 µm	22 µm	Δ 22 µm
1	14.91	0.86	9.52	0.75	32.61	3.71	98.06	16.53
2	2.62	0.21	1.36	0.20	2.57	0.46	-	-
3	30.03	1.93	18.25	1.62	52.02	6.26	124.94	21.41
4	3.54	0.24	2.26	0.24	2.55	0.46	7.68	1.75
5	2.80	0.19	1.65	0.18	1.65	0.33	3.81	1.57
6	463.11	26.73	287.13	22.43	1287.59	146.06	1945.55	326.94
7	39.32	2.36	24.25	2.01	43.01	5.18	71.70	13.16
8	11.70	0.78	7.12	0.71	15.21	2.10	26.63	6.63
9	7.59	0.86	4.26	0.93	9.68	1.99	15.94	6.29
10	102.86	5.96	59.48	4.67	182.60	20.72	327.67	55.13
11	6.01	0.41	3.39	0.41	4.97	2.05	8.35	3.51
12	4.86	0.32	2.66	0.26	7.34	0.89	9.95	2.00
13	0.88	0.08	0.54	0.08	0.60	0.19	0.94	1.23
14	77.59	4.57	46.95	3.79	158.51	18.05	331.32	55.87
15	3.02	0.21	1.66	0.20	0.85	0.62	3.57	1.17
16	13.89	0.82	8.28	0.69	17.15	1.99	23.12	4.25
17	2.23	0.25	1.60	0.27	2.14	0.67	19.54	3.86
18	6.85	0.45	3.93	0.40	7.02	0.89	21.33	4.03
19	10.21	0.70	5.20	0.57	4.54	1.02	18.33	4.18
20	203.06	11.75	122.99	9.62	378.25	42.99	683.62	114.96
21	641.00	36.97	358.08	27.95	390.83	44.48	429.46	72.33
22	15.94	0.92	8.86	0.70	3.15	0.48	1.81	1.48
23	122.38	7.07	78.87	6.17	397.79	45.15	609.66	102.47
24	0.60	0.11	0.19	0.26	0.25	0.06	4.03	1.29
25	143.77	8.32	78.92	6.21	64.70	7.74	49.72	9.06
26	28.30	1.75	16.15	1.41	26.79	3.19	34.04	6.42
27	2.72	0.22	1.57	0.21	1.58	0.44	4.67	1.46
28	52.03	3.04	33.82	2.68	134.25	15.25	308.95	52.01
29	200.25	11.59	134.95	10.57	947.13	107.46	2427.67	408.04
30	5.53	0.40	2.95	0.40	2.56	0.53	13.02	2.79
31	25.93	1.71	15.75	1.45	31.86	5.48	28.27	7.75
32	5.42	0.35	3.38	0.30	10.59	1.26	16.55	2.94
33	1.85	0.13	0.84	0.14	2.00	0.53	5.94	1.72
34	3.61	0.41	1.96	0.44	4.44	0.86	4.37	4.64
35	5.32	0.44	2.23	0.46	4.13	2.48	4.84	10.47
36	1.43	0.16	0.51	0.28	0.73	0.69	-	-
37	21.91	1.28	12.13	1.02	21.03	2.47	22.77	4.68
38	1.15	0.15	0.81	0.13	0.71	0.60	3.08	1.11
39	19.89	1.18	12.19	1.00	11.35	1.59	19.43	3.88
40	10.86	0.70	6.41	0.62	17.66	2.13	25.36	5.13
41	2.80	0.32	1.98	0.29	7.57	1.02	41.26	6.42
42	0.20	0.12	0.13	0.38	-	-	-	-

TABLE 4.6 – *continued*

HAPLESS	IRAS SCANPI (mJy)		*Herschel*-PACS (mJy)			
	60 µm	Δ 60 µm	100 µm	Δ 100 µm	160 µm	Δ 160 µm
1	1310.00	266.45	1387.15	219.81	1602.08	238.71
2	120.00	76.14	84.28	79.95	421.45	89.68
3	1270.00	256.58	3331.62	631.78	3502.96	705.72
4	80.00	52.70	184.36	49.68	164.46	45.74
5	170.00	191.88	64.41	51.71	40.66	48.09
6	18780.00	3756.40	61020.59	8519.13	69358.11	10198.06
7	550.00	123.30	2900.78	616.31	3236.56	688.95
8	350.00	81.51	814.95	153.08	1433.18	214.11
9	210.00	55.48	374.73	103.74	784.69	138.80
10	2730.00	548.10	8166.43	1360.14	8316.84	1295.71
11	0.00	56.00	33.36	96.72	161.65	90.14
12	200.00	51.21	473.04	102.40	602.62	109.52
13	100.0	45.56	-33.8	44.50	74.30	37.55
14	2340.00	469.96	7941.90	1494.84	9091.88	1587.11
15	30.00	36.08	27.00	42.92	28.34	36.07
16	460.00	98.60	1011.81	185.56	1684.40	260.50
17	240.00	64.17	141.94	42.77	120.14	44.53
18	350.00	76.69	696.79	128.00	617.64	112.90
19	80.00	49.83	264.56	101.85	358.95	88.39
20	8090.00	1618.42	19549.90	2770.41	19867.75	2939.29
21	2350.00	471.67	14624.22	2392.07	24916.23	3807.53
22	0.00	56.00	99.52	19.26	38.62	15.17
23	7250.00	1450.64	19264.58	2772.15	22023.09	3249.34
24	0.00	56.00	-2.0	46.68	97.51	41.24
25	550.00	117.20	4222.31	840.95	4005.41	766.60
26	500.00	122.91	1333.25	588.14	2116.58	594.26
27	110.00	145.24	-8.7	68.14	137.46	53.35
28	3770.00	760.63	7735.75	1066.90	7023.54	972.91
29	19560.00	3912.25	44031.71	6054.90	38567.82	5528.44
30	170.00	45.89	323.81	98.58	307.54	81.30
31	340.00	82.77	1028.02	499.16	2740.92	638.74
32	430.00	93.31	1154.40	192.59	817.59	152.62
33	80.00	52.75	-	-	-	-
34	0.00	56.00	247.96	108.46	103.19	93.55
35	150.00	57.75	41.46	86.88	341.33	79.16
36	120.00	66.55	-36.4	42.24	51.08	37.62
37	260.00	66.55	686.97	289.21	1864.80	348.26
38	0.00	56.00	35.23	41.20	77.68	41.36
39	350.00	88.46	1026.31	189.93	896.63	160.63
40	430.00	92.28	-	-	-	-
41	370.00	90.46	251.76	82.52	324.24	79.87
42	0.00	56.00	-36.1	36.09	63.73	37.65

Table 4.6 – *continued*

HAPLESS	*Herschel*-SPIRE (mJy)					
	250 μm	Δ 250 μm	350 μm	Δ 350 μm	500 μm	Δ 500 μm
1	427.94	34.84	161.96	20.96	54.96	9.87
2	204.11	30.24	111.00	23.39	57.35	17.70
3	2351.96	205.46	1279.07	136.93	560.28	79.40
4	102.47	21.44	56.53	16.18	13.81	12.36
5	99.70	23.01	46.14	17.04	26.92	12.48
6	36792.35	2775.40	14854.21	1276.14	5134.39	448.21
7	2657.91	243.22	1453.49	158.95	683.97	80.92
8	675.04	82.80	327.31	62.87	128.52	34.82
9	625.65	108.22	402.94	80.91	184.27	54.10
10	5199.65	395.95	2337.76	209.50	882.87	91.98
11	249.67	40.45	182.15	33.64	99.09	19.22
12	391.55	35.79	211.30	26.93	83.64	13.75
13	45.34	13.72	21.34	11.57	13.22	9.69
14	6340.79	533.89	3256.95	309.99	1350.70	139.03
15	53.25	20.23	19.20	17.34	1.02	12.42
16	874.30	71.99	470.14	48.91	213.04	29.09
17	69.67	33.30	11.91	30.21	4.34	19.00
18	418.04	45.76	228.25	34.23	109.71	21.17
19	480.02	72.13	286.89	54.87	161.44	33.59
20	10656.58	807.11	4569.69	400.61	1629.31	147.40
21	18567.37	1415.15	8892.77	773.69	3516.77	317.25
22	51.10	6.92	20.30	8.30	11.48	8.83
23	11932.25	887.39	5139.88	436.57	1896.64	164.87
24	51.84	19.90	25.41	16.99	10.15	10.59
25	2637.02	223.50	1198.41	128.49	428.35	61.84
26	2015.23	215.48	1147.87	151.78	589.46	82.07
27	151.16	26.04	75.29	18.44	37.06	15.27
28	3008.62	230.80	1254.65	115.44	447.29	52.58
29	17142.52	1272.60	6536.57	559.94	2158.08	191.51
30	274.88	44.08	160.90	34.82	85.20	24.36
31	1588.00	157.54	922.73	101.27	413.94	76.84
32	516.41	43.37	253.84	25.62	93.09	13.21
33	115.18	15.51	45.39	12.74	20.12	8.59
34	198.34	54.04	122.85	34.92	81.44	24.24
35	267.19	47.46	148.84	39.72	78.26	25.40
36	104.39	23.32	72.53	21.47	35.06	12.11
37	1060.72	93.62	608.12	63.30	283.41	35.29
38	66.09	18.69	32.65	15.85	19.91	9.95
39	619.56	74.65	321.32	46.29	151.88	30.18
40	691.09	64.53	324.21	45.35	127.06	22.43
41	209.03	39.02	121.31	31.74	64.60	17.37
42	48.98	12.64	42.76	11.38	27.75	10.86

CHAPTER 5

HAPLESS: THE PROPERTIES OF A DUST-SELECTED GALAXY SAMPLE

> *'Love not too well the works of thy hands*
> *and the devices of thy heart.'*
>
> J. R. R. TOLKIEN

In Chapter 3, I described how I used *H*-ATLAS to create HAPLESS, a blind galaxy sample selected solely on the basis of submillimetre luminosity; in Chapter 4 I detailed the custom photometric pipeline I created to perform reliable measurements of those galaxies, from the UV to the submm. In this chapter, I use this multiwavelength dataset to determine the properties of the HAPLESS galaxies, including dust temperature, dust mass, stellar mass, and star formation rate. The work presented in this chapter is published in Clark et al. (*submitted*).

5.1 MODIFIED BLACKBODY SED FITTING

To estimate the dust masses and temperatures of the HAPLESS galaxies, I fit modified blackbodies ('greybodies', see Section 1.2.1) to the dust Spectral Energy Distributions (SEDs). I used the same χ^2-minimisation routine used in Chapter 2. I first tried to fit the photometry using a single temperature greybody model, which took the form:

$$S_\nu = \frac{\kappa_\nu \, M_d B(\nu, T_d)}{D^2} \tag{5.1}$$

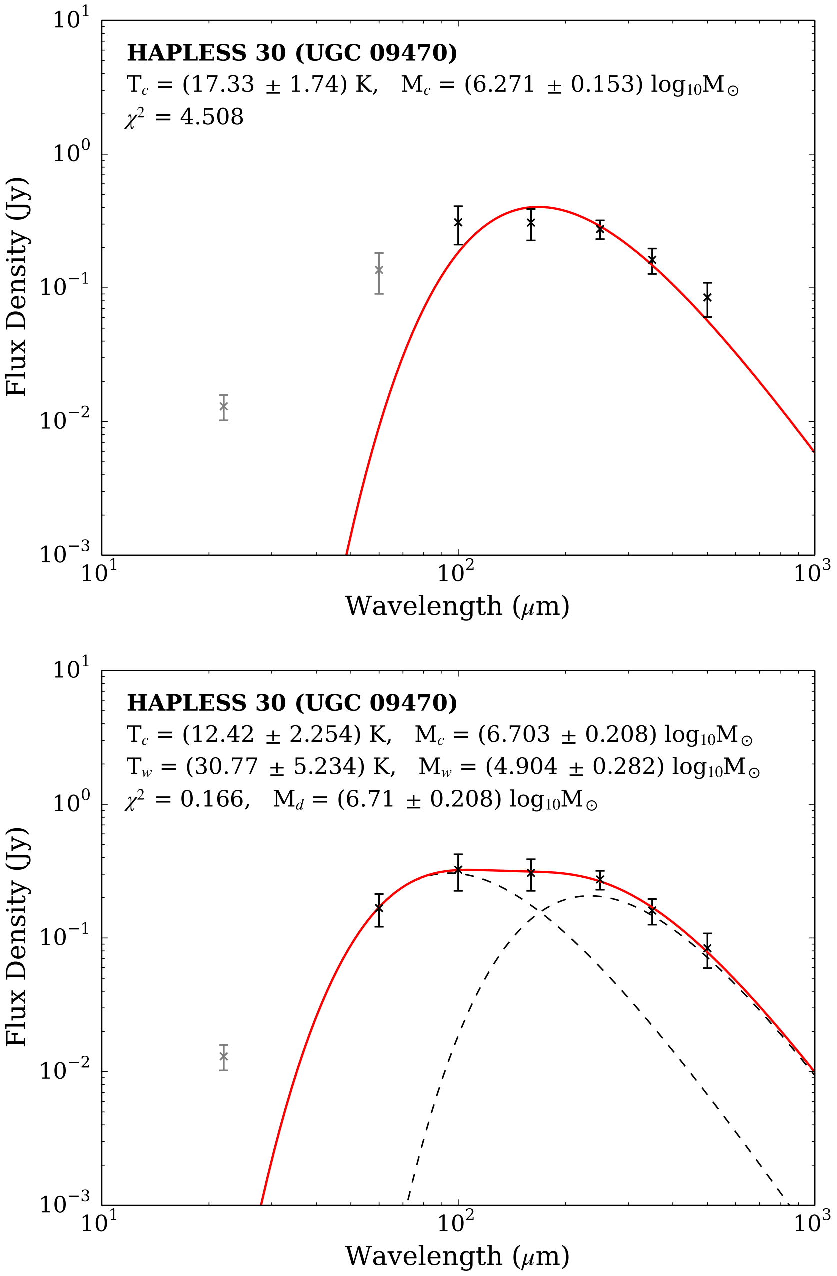

FIGURE 5.1 Example dust SED of UGC 09470 (HAPLESS 30), with one- and two-temperature component modified blackbody fits attempted (upper and lower panes respectively). Grey points represent upper limits. This is an example of a galaxy for which a one-component dust model systematically underestimates the flux at both 100 and 500 µm, whilst overestimating it at 160 µm. The 5 data points and 2 model variables in the one-greybody fit give it 2 degrees of freedom, whilst the 6 data points and 4 model variables in the two-greybody fit give it 1 degree of freedom.

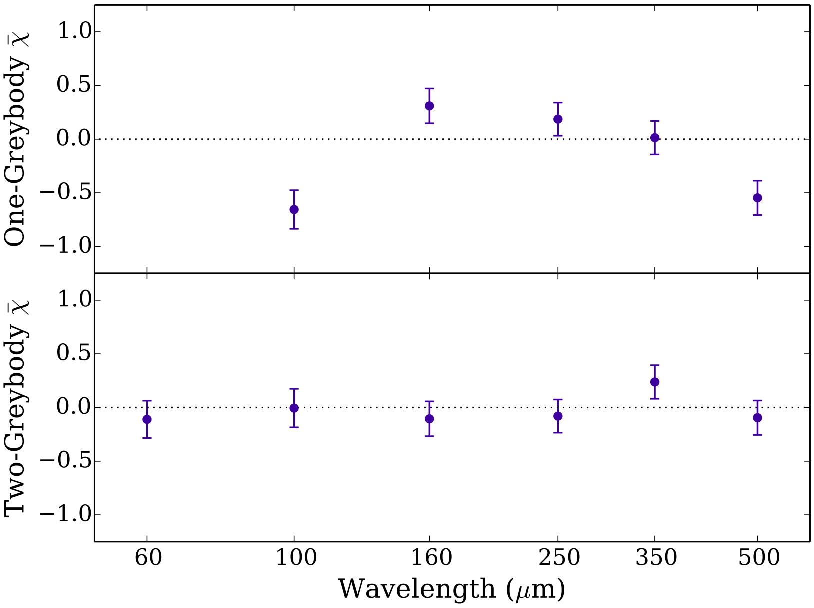

FIGURE 5.2 The mean (ie, stacked) residuals between the model and the fit as a fraction of the uncertainty, $\bar{\chi}$, for the entire sample, in each band, for the one- and two-temperature component modified blackbody fits (example in Figure 5.1). Across the sample as a whole, the one-greybody approach systematically overestimates the flux at 160 µm whilst systematically underestimating it at 100 and 500 µm.

where S_ν is the flux at frequency ν, κ_ν is the dust mass absorption coefficient at frequency ν, M_d is the dust mass, $B(\nu, T_d)$ is the Planck function at frequency ν and characteristic dust temperature T_d, and D is the distance to the source. An example of such an SED fit is shown in the upper pane of Figure 5.1.

However, we found that the one-greybody method did not provide suitable fits; rather, this approach systematically underestimated the fluxes at 100 and 500 µm, whilst overestimating them at 160 µm. This can be demonstrated using the residuals between the model and the data. If we assume the uncertainties are Gaussian, then so too should be the residuals; if the residuals show a bias towards being non-zero, we can determine how likely this would be to occur by chance. We calculated χ (the residual as a fraction of the uncertainty) in a given band band for each source, and then found $\bar{\chi}$, the mean across the sample – essentially stacking the residuals (note that in doing this, we only included measurements for which the uncertainty on the flux was less than the flux itself). The χ of any one data point has, by definition, an uncertainty of $\sigma = 1$; the mean residual $\bar{\chi}$ of N data points has an uncertainty of $\sigma = N^{-\frac{1}{2}}$. The values of $\bar{\chi}$ in each band for the one-greybody fit are shown in the upper pane of Figure 5.2; the average residuals of

$\bar{\chi}_{100} = -0.656$, $\bar{\chi}_{160} = 0.310$, and $\bar{\chi}_{500} = -0.547$, are significant to $3.6\,\sigma$, $1.9\,\sigma$ and $3.4\,\sigma$ respectively.

This approach assumes, however, that the photometric uncertainties are Gaussian. In reality, they also incorporate systematic error. For PACS, the systematic calibration uncertainty corresponds to ±5% of the measured flux at each wavelength[1]. Given that the mean HAPLESS 100 µm uncertainty is 26% of the measured flux, this could in the extremal case negate enough of the mean residual to decrease it by 0.126; this would reduce it to $\bar{\chi}_{100} = -0.530$, which is still significant at the $3.0\,\sigma$ level. For SPIRE, there are two sources of systematic calibration uncertainty[2]: ±4% correlated between all three wavebands, and ±4% which is band-independent. The band-independent ±4% systematic could contribute to the 500 µm flux underestimation. Nonetheless, given that the mean HAPLESS 500 µm uncertainty is 22% of the measured flux, the remaining mean residual could be reduced by no more than 0.099, to $\bar{\chi}_{500} = -0.448$, which is significant to $2.8\,\sigma$. We conclude therefore that a one-temperature fit to the HAPLESS SEDs is not a suitable model.

The residuals suggest that a 'flatter' SED, produced either by a lower value of β or by having dust at a range of temperatures (Dunne & Eales, 2001; Shetty et al., 2009), would be more suitable. At first, we left β as a free variable, and found a wide range of dust emissivity values (0–4) could adequately fit the HAPLESS sources, with a median of 1.72. However, Kelly et al. (2012) recently demonstrated that χ^2 SED fitting routines can return a wide range of fitted values for β for a given 'true' value of β. Furthermore, Galametz et al. (2012) demonstrated that using a variable β will produce less accurate results than a fixed value. We therefore used a fixed β of 2, as both observational (Dunne & Eales, 2001; Clemens et al., 2013; Smith et al., 2013; Planck Collaboration et al., 2014a) and experimental (Demyk et al., 2013) evidence suggest this is an appropriate value for nearby late-type galaxies (we use this same value of β for all dust components). As a single-temperature greybody only provides a useful approximation if the large grains are in a narrow range of temperatures, it is not surprising that there are galaxies in HAPLESS for which this approximation breaks down. We therefore opted to use an SED model which incorporates two temperature components:

---

[1] PACS instrument and calibration wiki: `http://herschel.esac.esa.int/twiki/bin/view/Public/PacsCalibrationWeb`

[2] SPIRE instrument and calibration wiki: `http://herschel.esac.esa.int/twiki/bin/view/Public/SpireCalibrationWeb`

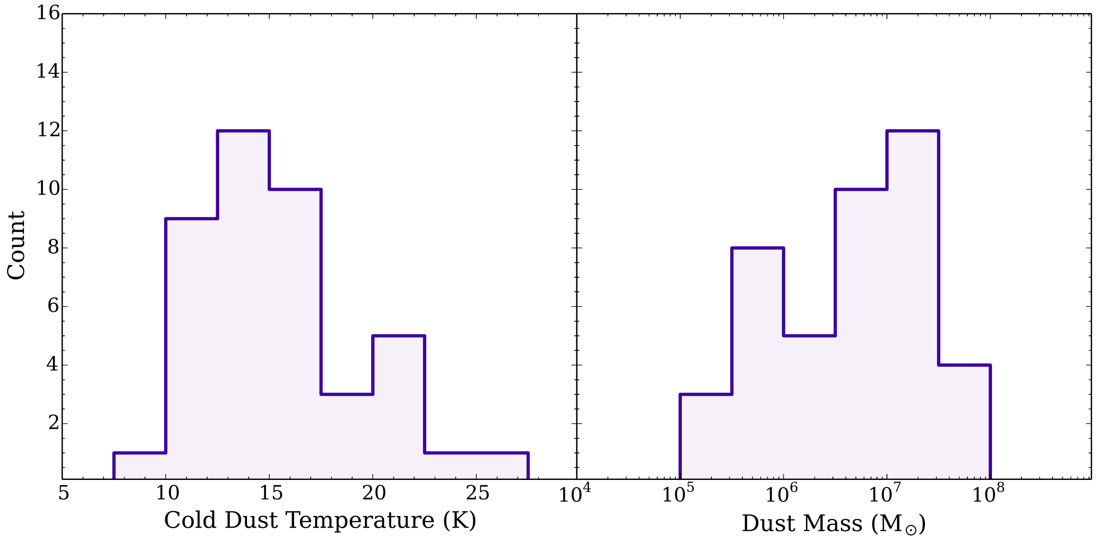

FIGURE 5.3 The distributions of (*left*) cold dust temperatures (*right*) dust masses derived for the 42 HAPLESS galaxies using using an adaptation of the method followed by Ibar et al. (2013)

$$S_\nu = \frac{\kappa_\nu}{D^2}\left[\, M_w B(\nu, T_w) + M_c B(\nu, T_c) \,\right] \tag{5.2}$$

where subscripts $_w$ and $_c$ indicate the warm and cold dust components respectively.

We performed the SED fitting from 60–500 µm; the 22 µm point is used as an upper limit to prevent unconstrained warm components from being fitted. Both temperature components were kept within the 5–200 K range, but were otherwise entirely free. Note that for a galaxy with an SED that is well-fit by a single-component model, this method is free to assign negligible mass to the warm dust component. In keeping with other *H*-ATLAS works, we used a value for the dust absorption coefficient of $\kappa_{850} = 0.077\,\mathrm{m^2\,kg^{-1}}$ from James et al. (2002); for a given β, we can then determine the appropriate κ_ν at *Herschel* wavelengths. As before, the fitting routine incorporates colour-corrections to account for filter response function and beam area[3,4,5]. The median colour-corrections in each band across the entire sample are given in Table 5.1. The larger scatter in the PACS bands is because at these wavelengths some SEDs are still ascending, some are flat, and some are

---

[3] LAMBDA IRAS explanatory supplement: `http://lambda.gsfc.nasa.gov/product/iras/colorcorr.cfm`.

[4] PACS instrument and calibration wiki: `http://herschel.esac.esa.int/twiki/bin/view/Public/PacsCalibrationWeb`.

[5] SPIRE handbook: `http://herschel.esac.esa.int/Docs/SPIRE/spire_handbook.pdf`.

TABLE 5.1 Median colour-corrections in each band (C_λ) found when fitting the dust SEDs of the HAPLESS galaxies, along with the standard deviations across the sample (σ_{C_λ}).

Instrument	Wavelength (µm)	C_λ	σ_{C_λ}
IRAS[a]	60	0.957	0.040
PACS[b]	100	0.995	0.212
PACS[b]	160	0.990	0.211
SPIRE[c]	250	1.000	0.006
SPIRE[c]	350	1.004	0.007
SPIRE[c]	500	0.992	0.008

[a] LAMBDA IRAS explanatory supplement: `http://lambda.gsfc.nasa.gov/product/iras/colorcorr.cfm`.

[b] SPIRE handbook: `http://herschel.esac.esa.int/Docs/SPIRE/spire_handbook.pdf`.

[c] PACS instrument and calibration wiki: `http://herschel.esac.esa.int/twiki/bin/view/Public/PacsCalibrationWeb`.

already descending; hence the range of possible gradients (and therefore colour-corrections) is larger than in other bands.

Using the two-temperature SED fitting, we no longer encountered any systematic biases in our model fits to the data, as can be seen in the lower pane of Figure 5.2. Figure 5.1 shows an example of both one- and two-temperature fits to the SED of HAPLESS 30; the two-temperature fits of all the sources are displayed in Figure 5.4. Given the 6 data points (the 22 µm point typically does not contribute to the χ^2 of a fit) and 4 model variables in the two-greybody fits, they have 1 degree of freedom; therefore the χ^2 of each fit also serves as the χ^2_{red}.

Note that whilst comparing the results from the one- and two-temperature fits to the SEDs, and using fixed versus variable β values, we saw that relatively small methodological differences in SED fitting can lead to an apparent 'excess' submm emission at 500 µm (the top panel in Figure 5.1 shows an example of this). This agrees with the recent findings of Kirkpatrick et al. (2013) regarding the susceptibility of apparent submm excess to subtle changes in the SED fitting routine. The two-temperature SED fitting model with the requirements listed above removed any indication of excess submm emission or the need for additional ultra cold dust temperatures in the galaxies of our sample, such as the < 10 K component suggested by Grossi et al. (2010).

Dust masses and temperatures for the HAPLESS galaxies are listed in Table 5.2, and the distributions of cold dust temperatures and dust masses are displayed in Figure 5.3. The cold dust temperatures range from 9.2 to 25.6 K, with

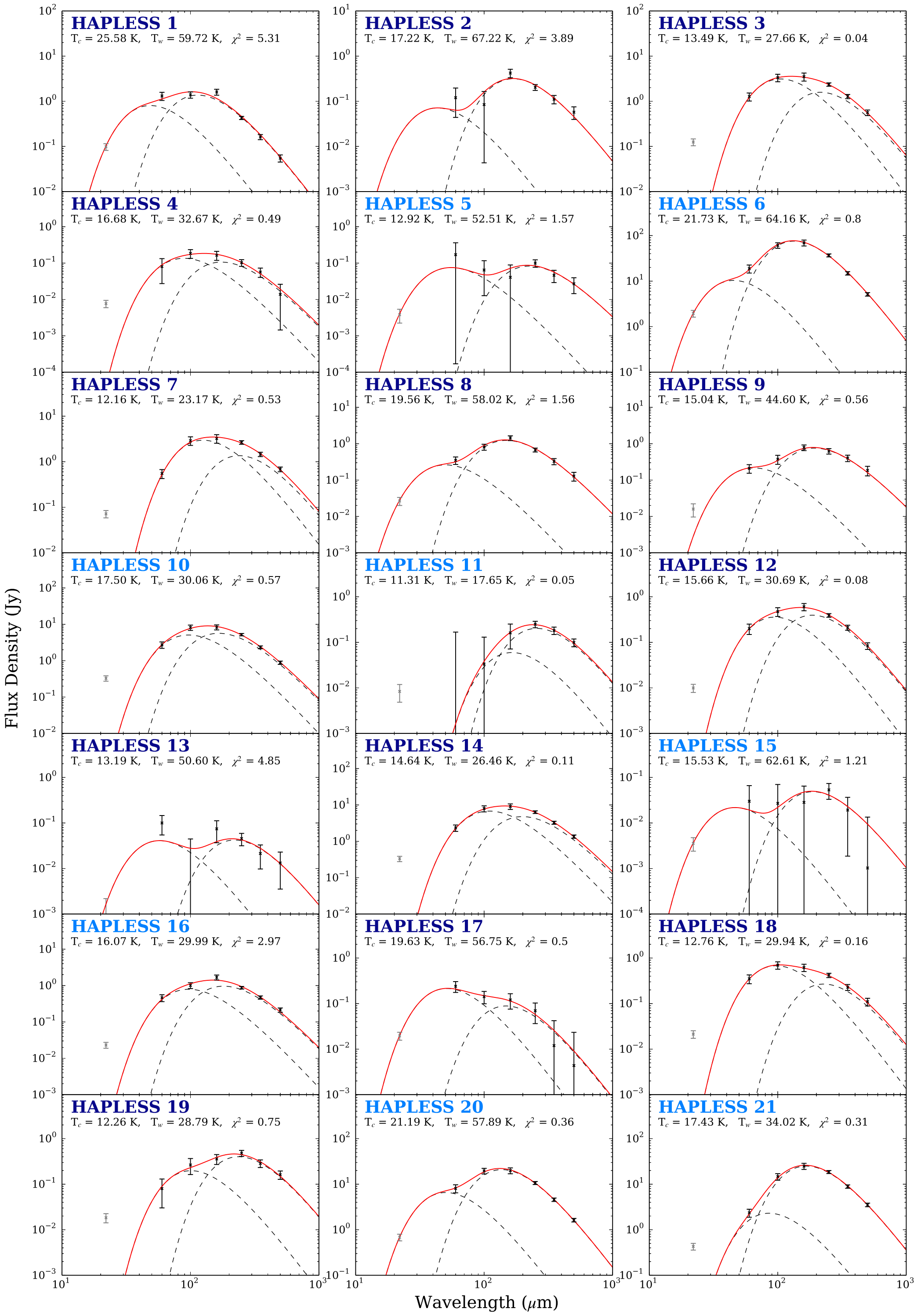

FIGURE 5.4 Spectral energy distributions for the HAPLESS sample. The two-temperature modified blackbody fits are shown in red; the warm and cold dust components shown by the dashed curves. The grey 22 µm point was treated as an upper limit. Sources with dark blue names satisfied the FUV-$K_S < 3.5$ colour criterion necessary to be counted amongst the curious blue sub-population; sources with light blue names did not. Given the 6 data points and 4 model variables in these fits, they have 1 degree of freedom; therefore the χ^2 of each fit also serves as the χ^2_{red}.

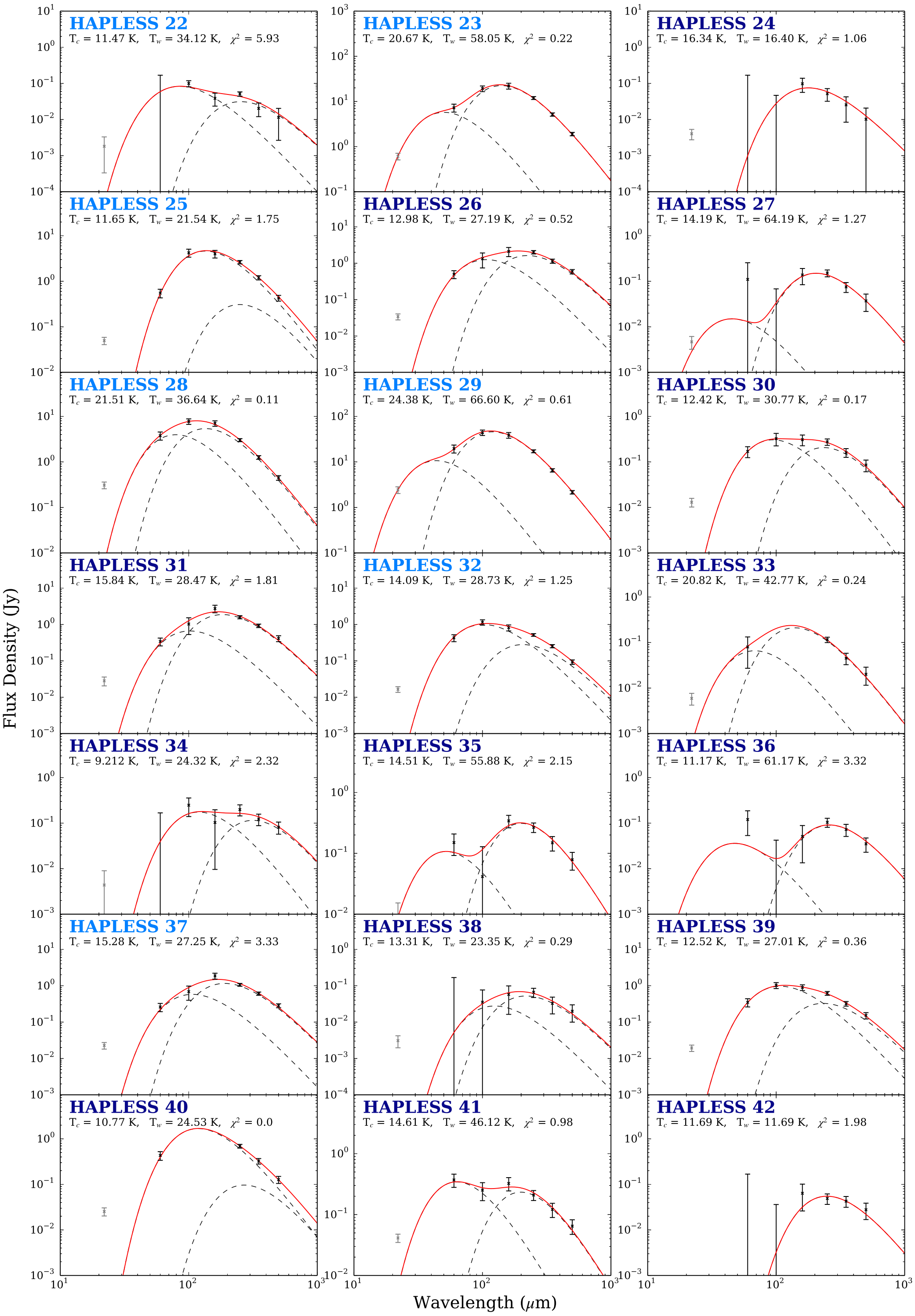

FIGURE 5.4 – *Continued*

TABLE 5.2 Dust properties of the HAPLESS galaxies. Dust masses (M) and temperatures (T) were derived using a χ^2-minimising fit to a two-component modified blackbody SED model, given by Equation 5.2. Uncertainties were determined by means of a bootstrapping analysis. L_{TIR} was estimated using an adaptation of the method followed by Ibar et al. (2013), as described in Section 5.1.1.

HAPLESS	T_c (K)	ΔT_c (K)	T_w (K)	ΔT_w (K)	M_c ($\log_{10}$ M$_\odot$)	ΔM_c (dex)	M_w ($\log_{10}$ M$_\odot$)	ΔM_w (dex)	M_d ($\log_{10}$ M$_\odot$)	ΔM_d (dex)	L_{TIR} ($\log_{10}$ L$_\odot$)
1	25.5	1.9	59.7	11.3	5.42	0.07	3.35	0.68	5.43	0.07	9.0
2	17.2	1.5	67.2	19.3	5.97	0.15	2.37	1.69	5.97	0.15	8.4
3	13.4	2.3	27.6	2.9	7.17	0.18	5.90	0.34	7.19	0.18	9.5
4	16.6	4.8	32.6	14.2	5.65	0.40	4.29	0.94	5.67	0.40	8.3
5	12.9	2.5	52.5	6.8	5.98	0.29	2.90	1.45	5.98	0.29	8.1
6	21.7	1.0	64.1	16.4	7.93	0.05	4.72	1.33	7.93	0.06	10.9
7	12.1	2.8	23.1	2.3	7.38	0.21	6.32	0.37	7.42	0.21	9.4
8	19.5	1.3	58.0	13.8	6.39	0.10	3.35	0.89	6.39	0.10	9.1
9	15.0	1.6	44.6	12.0	6.70	0.18	3.79	0.78	6.70	0.18	8.8
10	17.5	2.5	30.0	14.0	7.24	0.10	6.01	0.92	7.26	0.11	9.9
11	11.3	1.4	17.6	15.5	6.87	0.20	5.37	1.91	6.88	0.20	8.4
12	15.6	2.4	30.7	9.8	6.35	0.17	4.85	0.78	6.36	0.18	8.7
13	13.1	3.0	50.6	6.4	5.74	0.33	2.81	1.26	5.74	0.33	7.9
14	14.6	2.4	26.4	2.8	7.34	0.14	6.21	0.44	7.37	0.14	9.7
15	15.5	4.2	62.6	9.0	5.46	0.53	2.09	1.76	5.46	0.53	7.9
16	16.0	3.1	29.9	11.1	6.72	0.18	5.28	0.89	6.73	0.19	9.1
17	19.6	6.0	56.7	7.9	5.33	0.58	3.41	0.39	5.34	0.57	8.7
18	12.7	2.4	29.9	3.0	6.66	0.23	5.21	0.31	6.67	0.23	8.9
19	12.2	1.5	28.7	6.2	7.01	0.19	4.85	0.91	7.02	0.19	8.8
20	21.1	2.3	57.9	14.1	7.47	0.07	4.78	0.94	7.47	0.09	10.4
21	17.4	0.9	34.0	18.6	7.97	0.06	5.48	1.31	7.97	0.06	10.3

TABLE 5.2 – *Continued*

HAPLESS	T_c (K)	ΔT_c (K)	T_w (K)	ΔT_w (K)	M_c ($\log_{10}$ M$_\odot$)	ΔM_c (dex)	M_w ($\log_{10}$ M$_\odot$)	ΔM_w (dex)	M_d ($\log_{10}$ M$_\odot$)	ΔM_d (dex)	L_{TIR} ($\log_{10}$ L$_\odot$)
22	11.4	2.0	34.1	6.8	5.99	0.35	4.04	0.38	5.99	0.35	8.1
23	20.6	1.8	58.0	14.8	7.58	0.07	4.74	1.01	7.58	0.08	10.4
24	16.3	3.9	16.4	4.5	5.71	0.32	-0.0	1.17	5.71	0.32	8.1
25	11.6	1.1	21.5	4.2	6.94	0.08	6.78	2.08	7.17	0.09	9.6
26	12.9	1.7	27.2	10.1	7.43	0.17	5.72	0.89	7.44	0.17	9.3
27	14.2	1.6	64.2	5.2	6.24	0.18	1.96	1.64	6.24	0.18	8.1
28	21.5	4.1	36.6	14.8	6.92	0.10	5.62	0.96	6.94	0.12	10.1
29	24.3	1.5	66.6	16.8	7.58	0.06	4.76	1.44	7.58	0.06	10.9
30	12.4	2.4	30.7	3.9	6.70	0.27	4.90	0.55	6.71	0.27	8.7
31	15.8	3.2	28.4	15.8	7.23	0.18	5.50	1.31	7.24	0.19	9.4
32	14.1	2.9	28.7	2.5	6.58	0.18	5.59	0.28	6.62	0.18	9.2
33	20.8	8.2	42.7	13.7	5.73	0.84	3.66	2.51	5.73	0.84	8.6
34	9.2	2.6	24.3	4.6	7.23	0.50	5.31	0.54	7.24	0.50	8.5
35	14.5	1.4	55.8	12.3	6.72	0.18	3.33	0.57	6.72	0.19	8.8
36	11.1	1.0	61.1	18.6	6.76	0.18	2.67	1.15	6.76	0.18	8.3
37	15.2	2.8	27.2	15.4	7.26	0.15	5.71	1.22	7.27	0.16	9.4
38	13.3	4.0	23.3	15.9	6.16	0.56	4.67	2.11	6.18	0.56	8.2
39	12.5	2.8	27.0	2.4	7.06	0.30	5.87	0.31	7.09	0.29	9.3
40	10.7	6.2	24.5	14.4	6.59	0.59	6.04	1.67	6.69	0.59	9.2
41	14.6	2.4	46.1	10.8	5.82	0.25	3.49	0.54	5.82	0.25	8.4
42	11.7	2.5	11.7	14.8	6.25	0.37	3.08	2.03	6.25	0.37	7.4

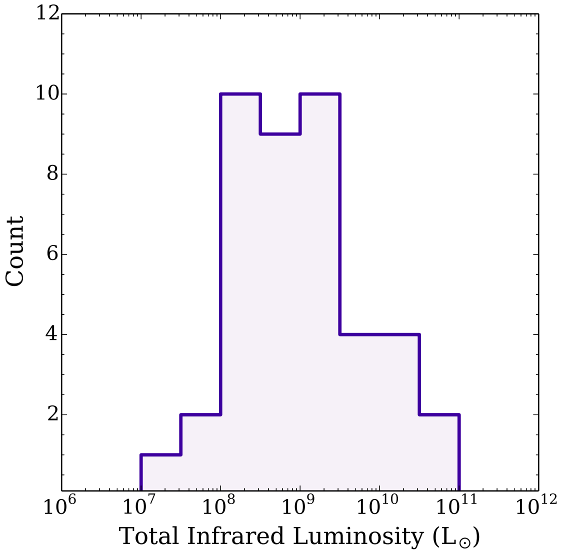

FIGURE 5.5 The distribution of total infrared luminosities, L_{TIR}, of the HAPLESS galaxies.

a median temperature of 14.6 K. The total dust masses range from 2.2×10^5 to $9.5 \times 10^7\,M_\odot$, with a median mass of $5.3 \times 10^6\,M_\odot$. All quoted dust masses are the sum of the cold and warm components. Uncertainties in the derived dust masses and temperatures were estimated by means of a bootstrapping analysis, whereby the fluxes were randomly re-sampled according to a Gaussian distribution defined by the flux uncertainties, and a best fit was made to the re-sampled SED; this was repeated 1,000 times. For each parameter, the distribution of absolute deviations between the bootstrapped best-fit values the actual best-fit value were determined, and the 66.6th percentile level of the deviation distribution was taken to represent the parameter's uncertainty.

5.1.1 TOTAL INFRARED LUMINOSITIES

Total infrared luminosities, L_{TIR}, were estimated following the method of Ibar et al. (2013). A power law was derived using the existing SEDs of the sources, anchored to the observed WISE 22 μm flux (or the WISE 12 μm flux, if a 22 μm value was not available), and to the flux at the peak of the best-fit SED. At wavelengths shorter than the best-fit SED peak, the flux corresponding the the Wien slope of the existing best-fit SED was replaced with the flux from the power law, if the power law flux was the larger of the two. This new SED was then integrated in the 8–1000 μm range to produce an estimate of L_{TIR}. This provides an estimate of

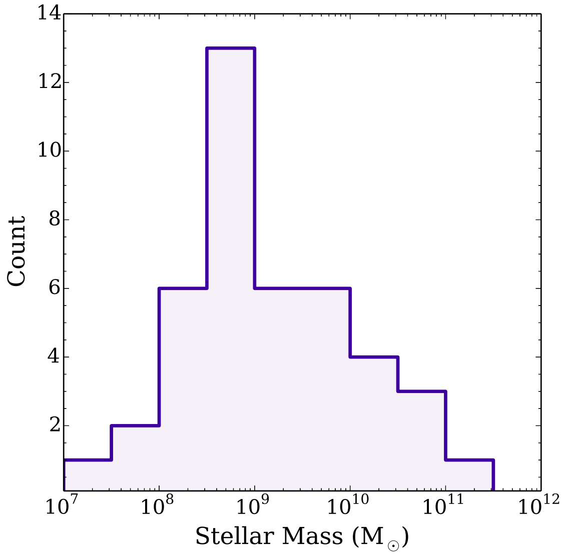

FIGURE 5.6 The distribution of stellar masses derived for the 42 HAPLESS galaxies using Equation 5.3.

L_{TIR} that is, on average, 14% greater than arrived at by just integrating the two-greybody SED with no MIR extrapolation.

The values determined using this method are in good agreement with those determined by De Vis et al. (*in prep.*) by performing energy-balance modelling of the full UV–submm SED with MAGPHYS (da Cunha et al., 2008). We note that the monochromatic L_{TIR} estimation prescription of Galametz et al. (2013) suggests values that are, on average, 1.7 times greater than those derived here, or by MAGPHYS.

The resulting L_{TIR} values are listed in Table 5.2. The L_{TIR} distribution for the HAPLESS sample is shown in Figure 5.5.

5.2 STELLAR MASSES

To determine the stellar masses of the HAPLESS galaxies, we followed the method of Zibetti et al. (2009), which assumes a Chabrier (Chabrier, 2003) Initial Mass Function (IMF) and uses *i*-band luminosity along with a stellar mass-to-light ratio defined by *g*-*i* colour. Stellar masses arrived at by this method have a typical uncertainty of 0.15 dex (Cortese et al., 2012b). The full formula we employed to calculate stellar mass is:

$$M_\star = L_i 10^{-0.963+1.032(g-i)} \tag{5.3}$$

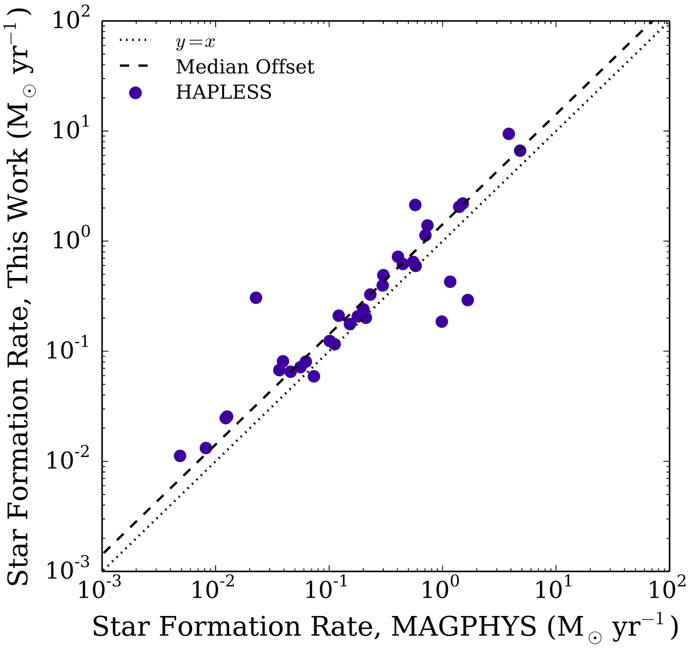

FIGURE 5.7 The SFRs calculated using Equation 5.4 compared to those derived by De Vis et al., (*in prep.*) by fitting the full UV-submm SEDs of our sample using MAGPHYS. The offset between the two prescriptions is by a factor of 1.42, as indicated by the dashed line.

where $M_\star$ is stellar mass and L_i is i-band luminosity, both in Solar units. Stellar masses are listed in Table 5.3.

A histogram of the stellar mass distribution of the HAPLESS galaxies can be found in Figure 5.6. The stellar masses range from 5.6×10^7 to $2.2 \times 10^{11}\,M_\odot$, with a median mass of $9.8 \times 10^8\,M_\odot$.

5.3 STAR FORMATION RATES

To estimate star formation rate (SFR), use the Hirashita et al. (2003) method of combining UV and IR tracers, specifically following Jarrett et al. (2013) to combine GALEX FUV and WISE 22 μm measurements to give the total SFR as:

$$SFR = SFR_{FUV} + SFR_{22} \tag{5.4}$$

where SFR is the total star formation rate, SFR_{FUV} is the FUV-derived SFR (calculated using Equation 5.5), and SFR_{22} is the 22 μm-derived SFR (calculated using Equation 5.6). All SFR values are in units of $M_\odot$ yr^{-1}.

UV emission traces unobscured high-mass stars, indicating star formation on timescales of $\sim$ 100 Myr (Kennicutt, 1998; Calzetti et al., 2005). SFRs derived from the FUV have been demonstrated to be a much more reliable estimator for normal- and low-SFR galaxies, compared to other proxies for unobscured star formation, such as Hα (Lee et al., 2009; Kennicutt et al., 2009). For SFR_{FUV}, we follow Jarrett et al. (2013) and use the prescription of Buat et al. (2008, 2011):

$$SFR_{FUV} = 10^{-9.69} \nu_{FUV} L_{FUV} \tag{5.5}$$

where $\nu_{FUV} L_{FUV}$ is the νL_{ν} luminosity in the GALEX FUV waveband[6] in units of bolometric Solar luminosity. Buat et al. (2012) find the uncertainty in this relation to be 0.13 dex. It was calibrated using 656 local galaxies (described in Buat et al. 2007) with stellar masses greater than $10^{10}\,M_{\odot}$, and extends down to SFRs of $0.07\,M_{\odot}\,yr^{-1}$; as such it includes a range of actively star-forming and quiescent systems. The stellar masses of our sample extend to lower values than the Buat et al. (2007) sample, however, the Buat et al. (2007) sample does cover the full luminosity, SSFR, and colour range (specifically NUV-*r* against FUV-NUV) exhibited by the HAPLESS galaxies. Note that their SFR prescription assumes a Kroupa (2001) IMF; we convert it to the Chabrier IMF (which we use to derive stellar masses) using a correction factor of 0.94.

MIR emission comes primarily from hot dust, heated by short-wavelength photons emitted from newborn stars, and traces star formation on time scales $< 10\,$Myr (Calzetti et al., 2005; Kennicutt & Evans, 2012a). The WISE 22 μm SFR relation of Jarrett et al. (2013) was calibrated by bootstrapping to the *Spitzer* 24 μm SFR relation of Rieke et al. (2009), and is given by:

$$SFR_{22} = (1 - \eta) 10^{-9.125} \nu_{22} L_{22} \tag{5.6}$$

where η (discussed below) is the fraction of MIR emission originating from heating by the evolved stellar population, and $\nu_{22} L_{22}$ is the νL_{ν} luminosity in the WISE 22 μm waveband[7] in units of bolometric Solar luminosity. Rieke et al. (2009) estimate the uncertainty in their *Spitzer* 24 μm SFR relation to be 0.25 dex, and find it to be accurate at gauging the star formation giving rise to thermal dust emission in IR-selected galaxies. Jarrett et al. (2013) find the scatter in their WISE 22 μm bootstrap to this relation to be negligible ($\sim$1%), thanks to the close similarity between the *Spitzer* 24 μm and WISE 22 μm passbands.

The value of η will vary from galaxy to galaxy depending on its current star

---

[6] $\nu_{FUV} = 1.987\,$PHz

[7] $\nu_{22} = 13.64\,$THz

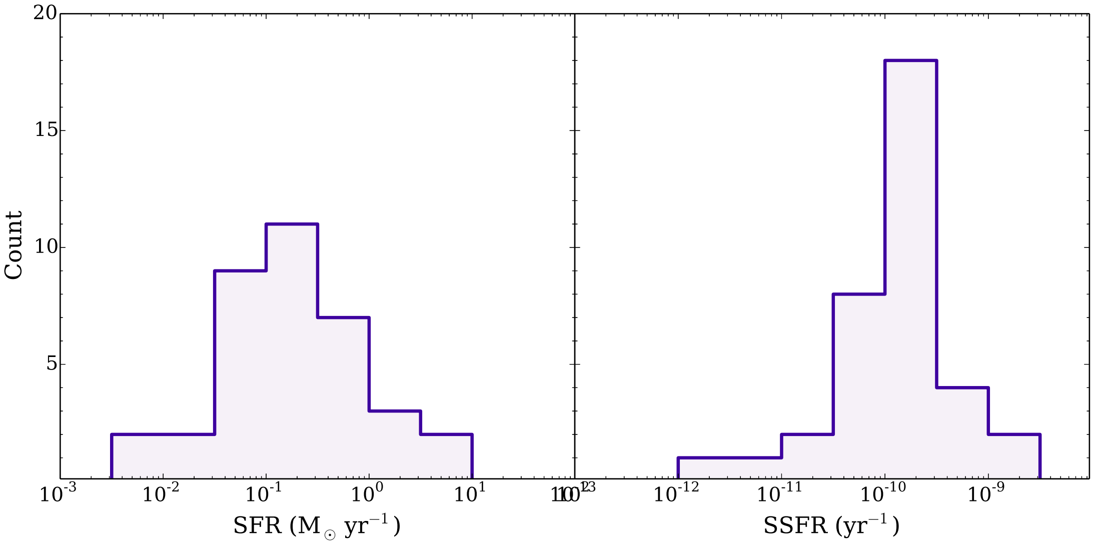

FIGURE 5.8 The distributions of SFRs (*left*) and SSFRs (*right*) derived for the HAPLESS galaxies, using Equation 5.4.

formation activity and dust geometry. η may be calculated theoretically, or calibrated independently if other tracers of dust-corrected SFR are available. Values in the literature for star forming samples range from $0.17 \leq \eta \leq 0.55$ (Buat et al., 2011; Hao et al., 2011; Smith et al., 2011; Kennicutt & Evans, 2012a). Here we follow Buat et al. (2011) and employ $\eta = 0.17$.

Comparing our total SFRs from Equation 5.4 with those derived from MAGPHYS (da Cunha et al., 2008) energy balance modelling of the full UV–submm SED, performed by De Vis et al., (*in prep.*), shows that our values are offset from theirs by a median factor of 1.42; this is demonstrated in Figure 5.7. Modulo the offset, the correlation between the two SFR estimates is very tight, with the exception of 4 outliers[8]. We therefore opt to reduce our calculated SFRs by this factor to allow for better direct comparison to De Vis et al., (*in prep.*), and to the *Planck* sample of Clemens et al. (2013) in Chapter 6. Note that this rescaling factor is well within the usual variation found between different SFR prescriptions; for example, the oft-used Kennicutt (1998) method yields SFR estimates for our sample that are a median factor of 1.45 less than those suggested by MAGPHYS.

Having calculated SFRs of the HAPLESS galaxies with these relations,

---

[8] The 3 galaxies below the scatter are UGC 09299, UM 491, and UGC 07531 (HAPLESS 9, 33, and 34), three of the four bluest HAPLESS galaxies (in terms of FUV-K_S colour) for which SFR estimates are available. Similarly, the galaxy above the scatter is NGC 5750 (HAPLESS 25), which has the third reddest FUV-K_S colour found in the sample. This suggests that the agreement between the SFR estimates only struggles in systems with extremes of FUV-K_S colour.

TABLE 5.3 Stellar properties of the HAPLESS galaxies. Stellar masses were calculated using Equation 5.3. GALEX FUV (unobscured) and WISE 22 μm (obscured) star formation rates, SFR_{FUV} and SFR_{22}, were determined via Equations 5.5 and 5.6, and combined as per Equation 5.4 to yield the total SFR (only for sources with both FUV and 22 μm coverage).

HAPLESS	$M_\star$	SFR_{FUV}	SFR_{22}	SFR	$SSFR$
	($\log_{10}$ M$_\odot$)	($\log_{10}$ M$_\odot$ yr^{-1})			($\log_{10}$ yr^{-1})
1[a]	8.8	-	-1.1	-	-
2	8.1	-1.4	-	-	-
3	9.2	-0.5	-0.7	-0.2	-9.5
4	8.8	-1.5	-1.8	-1.3	-10.1
5	8.5	-2.0	-2.2	-1.7	-10.2
6	10.8	-0.1	0.6	0.7	-10.1
7	9.5	-0.5	-0.8	-0.3	-9.9
8	9.0	-0.8	-1.2	-0.6	-9.6
9	8.6	-0.8	-1.5	-0.6	-9.3
10	10.1	-0.7	-0.2	-0.0	-10.2
11	8.9	-1.5	-1.6	-1.2	-10.1
12	8.6	-1.5	-1.6	-1.2	-9.8
13	8.1	-2.2	-2.7	-2.0	-10.1
14	9.5	-0.4	-0.4	-0.1	-9.6
15	8.6	-2.0	-2.1	-1.7	-10.4
16	9.3	-1.4	-1.2	-1.0	-10.3
17	8.1	-1.1	-1.2	-0.8	-8.9
18	8.7	-0.9	-1.3	-0.7	-9.5
19	9.2	-	-1.3	-	-
20	10.8	-1.4	0.2	0.2	-10.6
21	11.3	-	-0.0	-	-
22	9.7	-2.4	-2.3	-2.0	-11.8
23	10.2	-0.8	0.1	0.2	-9.9
24	7.6	-1.6	-1.9	-1.3	-9.0
25	10.6	-1.0	-0.9	-0.6	-11.2
26	9.5	-0.5	-1.0	-0.3	-9.8
27	8.6	-1.5	-1.9	-1.3	-9.9
28	9.8	-0.7	-0.0	0.0	-9.8
29	10.4	-0.4	0.8	0.8	-9.6
30	8.8	-1.0	-1.4	-0.8	-9.6
31	9.6	-0.5	-1.0	-0.3	-9.9
32	8.9	-1.5	-1.3	-1.0	-9.9
33	8.3	-1.0	-1.6	-0.8	-9.2
34	8.6	-0.6	-1.7	-0.5	-9.1
35	9.0	-1.0	-1.7	-0.9	-9.9
36	8.4	-1.4	-	-	-
37	10.0	-0.8	-0.9	-0.5	-10.6
38	8.4	-1.5	-1.8	-1.2	-9.6
39	9.3	-0.6	-1.0	-0.4	-9.8
40	8.9	-0.9	-1.2	-0.7	-9.7
41	7.6	-1.5	-1.5	-1.1	-8.8
42	7.4	-2.4	-	-	-

[a] Note that UGC 06877 (HAPLESS 1) is an AGN (Osterbrock & Dahari, 1983), with contamination from non-thermal continuum emission in the UV (Markaryan et al., 1979). Therefore no value for SFR_{FUV} is recorded.

we also calculated the Specific Star Formation Rate (SSFR), the SFR per stellar mass. Histograms of the distributions of SFR and SSFR for the HAPLESS galaxies are shown in Figure 5.8, and the values for each source can be found in Table 5.3. The calculated SFRs range from 0.01 to 7.12 $\mathrm{M_{\odot} yr^{-1}}$, with a median SFR of 0.18 $\mathrm{M_{\odot} yr^{-1}}$. Derived SSFRs range from 1.6×10^{-12} to $1.4 \times 10^{-9}\,\mathrm{yr^{-1}}$, with a median SSFR of $1.3 \times 10^{-10}\,\mathrm{yr^{-1}}$.

5.4 CONCLUSION

In this chapter, I report the various derived properties I calculated for the HAPLESS galaxies. I demonstrated that a single-component modified blackbody ('greybody') model provides unsuitable fits to the dust SEDs of this unique sample; therefore, I instead used a two-component model to derive their dust masses and temperatures (Section 5.1). I also used optical colours and luminosities to determine the stellar masses of the HAPLESS galaxies (Section 5.2), along with their UV and MIR luminosities to estimate their star formation rates (Section 5.3).

CHAPTER 6

HAPLESS: COMPARISON TO OTHER SURVEYS OF DUSTY GALAXIES

> *'Before you criticise someone, you should walk a mile in their shoes. That way, when you criticise them, you are a mile away from them, and you have their shoes.'*
>
> JACK HANDEY

HAPLESS provides us with a unique sample for studying dust in the local universe. The various derived properties discussed in Chapter 5 provide us a wealth of information about the galaxies in the sample. But in order to establish what new insights HAPLESS can provide, it needs context. Therefore in this chapter, I compare HAPLESS to other surveys of dust in nearby galaxies. The work presented in this chapter is published in Clark et al. (*submitted*).

6.1 THE REFERENCE SAMPLES

We compared HAPLESS to two other surveys of dust in local galaxies; the *Herschel* Reference Survey, and the *Planck* sample of Clemens et al. (2013) and Negrello et al. (2013). Throughout this chapter – with the exception of Section 6.4 – we consider our entire sample; however those galaxies that are not in the luminosity-limited subset of HAPLESS are plotted in figures as hollow circles.

6.1.1 THE HERSCHEL REFERENCE SURVEY

With its stated objective to be the 'benchmark study of dust in the nearby universe', the *Herschel* Reference Survey (HRS, Boselli et al. 2010) has resolution and sensitivity unrivalled by anything that has come before. The HRS chose K_S-band brightness as its selection criteria, because it is the part of the stellar emission spectrum that suffers least from extinction, and is known to be a good proxy for stellar mass. The velocity range of the HRS ($1050 \leq V \leq 1750$ km s^{-1}), with corrections made to account for the velocity dispersion of the galaxies of the Virgo Cluster, corresponds to a distance range of $15 \leq D \leq 25$ Mpc (whereas the HAPLESS distance range is $15 \leq D \leq 46$ Mpc).

The apparent magnitude limit of the late type galaxies in HRS is $K_S \leq 12$, which equates to an absolute magnitude limit between $-17.43 \geq K_S \geq -18.54$, depending on the distance of the source between the HRS limits. Note that for early type galaxies, a brighter flux limit of $K_S \leq 8.7$ is applied. From this we can ascertain that between 4 and 15 of the 42 HAPLESS galaxies would have been insufficiently luminous in K_S-band to have been included in the HRS. We also note that only 3 HAPLESS galaxies overlap with the distance range of HRS and of these, only one would have been bright enough for the HRS selection. These faint HAPLESS galaxies are low stellar mass systems that tend to have very blue FUV-K_S colours; 13 of the potentially-missing 15 satisfy our FUV-$K_S < 3.5$ criterion. Galaxies seen by *H*-ATLAS that are faint in K_S-band, but nonetheless dusty, represent an orthogonal population to the HRS, and reveal selection biases imposed on targeted dust surveys that *H*-ATLAS, with its blind sample, is not susceptible to. Another difference between the samples is that the HRS contains numeous early type galaxies, partly due to the stellar mass selection, and partly due to the extensive overlap (46%) of the HRS sample with the Virgo cluster.

To allow for a valid direct comparison of HAPLESS to the HRS, we determined dust masses and temperatures for the HRS galaxies ourselves, using our own SED-fitting method (as detailed in Section 5.1) with their published PACS (Cortese et al., 2014), SPIRE (Ciesla et al., 2012), and WISE (Ciesla et al., 2014) photometry, along with IRAS 60 μm data we acquired using SCANPI in the same manner as for the HAPLESS galaxies (described in Section 4.2.2.1). We likewise calculated L_{TIR} values for the HRS using the same method as for HAPLESS. We corrected the HRS PACS fluxes to account for an issue in `Scanamorphos`, the pipeline that was used to reduce the HRS PACS data (Cortese et al., 2014). This issue arises from a mis-handling of the reference pixel area. We corrected for this by multiplying the published HRS fluxes at 100 and 160 μm by 1.01 and 0.93 respectively. These values represent the average change (with scatter $\sim 2\%$) in extended-source flux in maps produced with corrected versions of `Scanamorphos`.

We note that our dust masses for the HRS galaxies are on average a factor of ~ 2.2 higher than in Ciesla et al. (2014) because they use a lower dust mass absorption coefficient value of κ_d of $\kappa_{500} = 0.1\,\mathrm{m^2\,kg^{-1}}$. Smith et al. (2012b) also find that the submm emission of two HRS sources, the giant elliptical galaxies M87 and M84, contain significant contamination from their AGN. As such, we do not attempt to fit the SEDs of these sources.

The published stellar masses of the HRS (Cortese et al., 2012b) were calculated in the same way as our own. The UV GALEX and optical SDSS photometry of the HRS is described in Cortese et al. (2012a), whilst their NIR K_S-band photometry (Boselli et al., 2010) was acquired from the 2-Micron All-Sky Survey (2MASS, Jarrett et al. 2000). To calculate the star formation rates of the HRS galaxies, we employed the same technique as for the HAPLESS galaxies (Section 5.3), for which we used the published HRS WISE and GALEX photometry. As for the HAPLESS galaxies, we obtain morphologies for the HRS from EFIGI (Baillard et al., 2011).

6.1.2 PLANCK

Negrello et al. (2013) used the *Planck* Early Release Compact Source Catalogue (ERCSC, Planck Collaboration et al., 2011b) to assemble a sample of nearby galaxies. Their flux-limited sample contains 234 dusty galaxies brighter than 1.8 Jy at 550 μm, at distances $\lesssim$ 100 Mpc (with the vast majority lying at $D < 50\,\mathrm{Mpc}$); the authors estimate the sample to be 80% complete. Clemens et al. (2013) have used this sample to perform a study of the properties of nearby dusty galaxies. We hereafter refer to this as the *Planck* C13N13 (Clemens et al. 2013 and Negrello et al. 2013) sample.

Whilst the *Planck*-selected sample benefits from being blind and all-sky (excepting the galactic plane zone of avoidance), *Planck* suffers from reduced sensitivity and resolution compared to *Herschel* ($3.8'$ in contrast to $18''$). Only 3 of the HAPLESS galaxies exceed the 1.8 Jy 550 μm flux limit necessary to feature in the *Planck* C13N13 sample (and none of those are members of the curious blue subset).

Clemens et al. (2013) also derived dust masses and temperatures for their sources by fitting two-component modified blackbody SEDs with $\beta = 2$, which is consistent with our method. For the *Planck* C13N13 sample, the authors adopted a value for the dust absorption coefficient of $\kappa_{850} = 0.0383\ \mathrm{m^2\ kg^{-1}}$, in contrast to the value in this work of $\kappa_{850} = 0.077\ \mathrm{m^2\ kg^{-1}}$. As a result, we have divided their dust masses by a factor of 2.01 to permit comparison.

The *Planck* C13N13 stellar masses and star formation rates were estimated using the MAGPHYS multiwavelength SED-fitting package (da Cunha et al., 2008), which produces stellar masses which agree exceptionally well with the Zibetti et al. (2009) method we employ (De Vis et al., *in prep.*); both methods also assume the Chabrier IMF. Once again, we use EFIGI morphologies (Baillard et al., 2011).

Whilst almost identical sets of observed and derived properties are shared by HAPLESS and the HRS, a more limited set of parameters is available for *Planck* C13N13; as a result, not all of the following analyses can include the *Planck* sample.

6.2 COLOUR AND MAGNITUDE PROPERTIES

As described in Section 3.1.1, we find FUV-K_S colour to be an effective way of identifying the subset of curious blue galaxies in our sample, using a colour cut of FUV-$K_S < 3.5$. We find that 64% (27) of the HAPLESS galaxies satisfy this criterion, compared to only 27% of the HRS galaxies with FUV-K_S colours available (which make up 85% of their sample). Given that the HRS is K_S-band-selected, it is to be expected that its galaxies will tend to exhibit redder FUV-K_S colour. The distributions of FUV-K_S colours for HAPLESS and the HRS are shown in the upper pane of Figure 6.1. Whilst the HRS more-or-less equally samples a wide range of FUV-K_S colours, with a median of 4.6 (Table 6.1), the blindly-selected HAPLESS galaxies tend to occupy a much narrower range of colours, with a median of 2.8. A Kolmogorov-Smirnov (K-S) test indicates that the likelihood of the null hypothesis that the two samples being drawn from the same underlying population is 10^{-8} (Table 6.1).

As demonstrated by Gil de Paz et al. (2007), FUV-K_S colour is a strong indicator of morphology, as is also seen in the central pane of Figure 6.1. The very blue FUV-K_S colours of the HAPLESS galaxies indicate that the dust-selected universe is dominated by very late type galaxies.

The lower pane of Figure 6.1 is a colour-magnitude plot constructed using FUV-K_S colour and K_S-band magnitude. Both the blue cloud and red sequence can be seen in the distribution of the HRS, at (3, -19.5) and (8.5, -22); however our HAPLESS sample is skewed towards bluer colours such that the bimodality is missing in this sample; indeed, most of the HAPLESS galaxies are in fact bluer than the blue cloud peak seen in the HRS distribution.

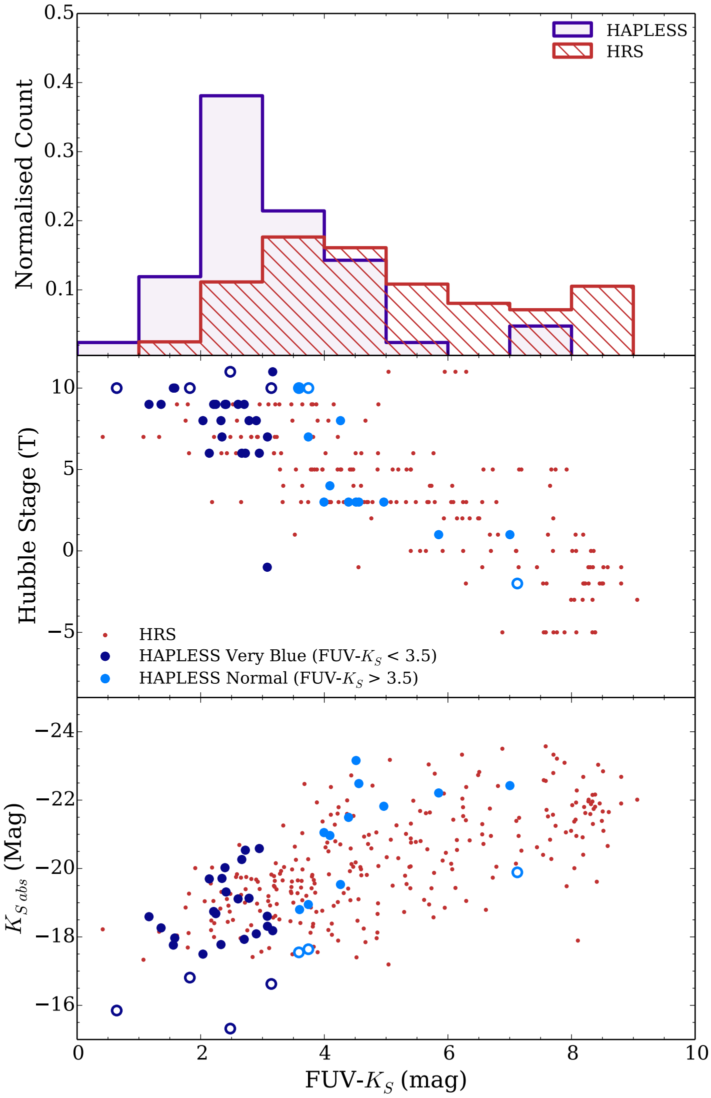

FIGURE 6.1 *Upper:* The distributions of FUV-K_S colour for the HAPLESS (blue) and the HRS (red) samples. The galaxies of the blind HAPLESS sample tend to be significantly bluer than those of the K_S-band selected HRS. *Central*: Morphology against FUV-K_S colour for HAPLESS and the HRS. *Lower:* Absolute K_S-band magnitude against FUV-K_S colour for HAPLESS and the HRS. Hollow circles indicate galaxies not in our luminosity-limited sub-sample.

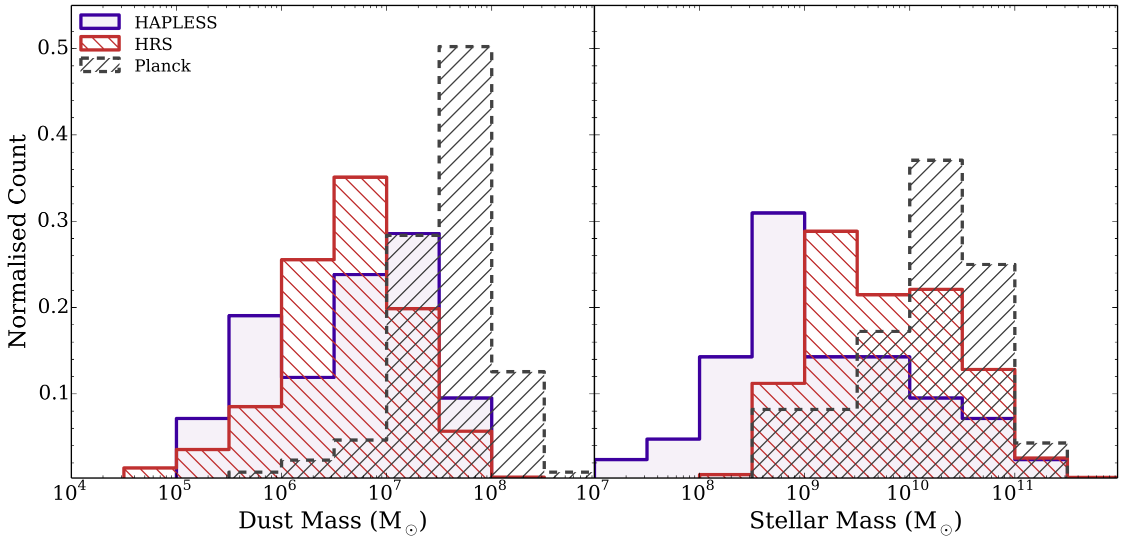

FIGURE 6.2 The dust and stellar mass properties of the HAPLESS, HRS, and *Planck* C13N13 galaxies. *Left:* The distribution of dust masses. *Right:* The distributions of stellar masses. Note that Clemens et al. (2013) derive the stellar masses for the *Planck* C13N13 sample using MAGPHYS, whilst for the HAPLESS and HRS samples we use Equation 5.3; however the stellar masses produced by both methods are in excellent agreement with each other for the HAPLESS sample (De Vis et al., *in prep.*).

6.3 DUST AND STELLAR MASS

The left pane of Figure 6.2 compares the dust mass distributions of HAPLESS, HRS, and *Planck* C13N13. The effect of the 1.8 Jy flux limit at 550 μm in the *Planck* C13N13 sample is immediately apparent; only galaxies with high dust masses (and a few less massive but very nearby galaxies) were bright enough to be included in their sample, which has a median dust mass of $4.2 \times 10^7\,M_\odot$. The HAPLESS and the HRS samples have different selection effects but ultimately have comparable median dust masses of 5.6×10^6 and $4.6 \times 10^6\,M_\odot$ respectively (Table 6.1).

The three samples also exhibit notably different distributions in stellar mass, as shown in the right pane of Figure 6.2. The flux limit of the *Planck* C13N13 sample naturally biases it towards more massive galaxies; whilst HAPLESS spans the broadest range of stellar masses overall, but is skewed towards low stellar mass systems. The median stellar masses of the three samples span over an order of magnitude, with $9.8 \times 10^8\,M_\odot$, $4.9 \times 10^9\,M_\odot$, and $1.8 \times 10^{10}\,M_\odot$ for the HAPLESS, HRS, and *Planck* C13N13 galaxies respectively. The combination of lower stellar masses, but moderate-to-high dust masses, mean the HAPLESS galaxies are very

TABLE 6.1 Median parameters derived for the local-volume surveys in this work, including the very blue (FUV-$K_S < 3.5$) subset of the HAPLESS sample. Results from Kolmogorov-Smirnov (K-S) tests between HAPLESS and the HRS and *Planck* C13N13 samples are also shown, indicating the likelihood of the null hypothesis that two samples are drawn from the same underlying population.

Sample	FUV-K_S (mag)	T_c (K)	M_d ($10^6\,M_\odot$)	$M_\star$ ($10^8\,M_\odot$)	$M_d/M_\star$ (10^{-3})	SSFR ($10^{-11}\,\mathrm{yr}^{-1}$)	L_{TIR} ($10^8\,L_\odot$)
HAPLESS	2.8	14.6	5.3	1.0	4.4	12.9	9.6
HAPLESS Very Blue	2.4	14.2	4.8	0.6	6.5	20.7	6.2
HRS	4.6	18.5	4.6	4.9	1.2	4.1	19.4
Planck	–	17.7	41.9	17.4	2.5	6.9	73.3
K-S (HRS)	10^{-8}	10^{-4}	0.15	10^{-6}	10^{-6}	10^{-5}	10^{-3}
K-S (*Planck*)	–	10^{-3}	10^{-13}	10^{-11}	10^{-3}	0.01	10^{-8}

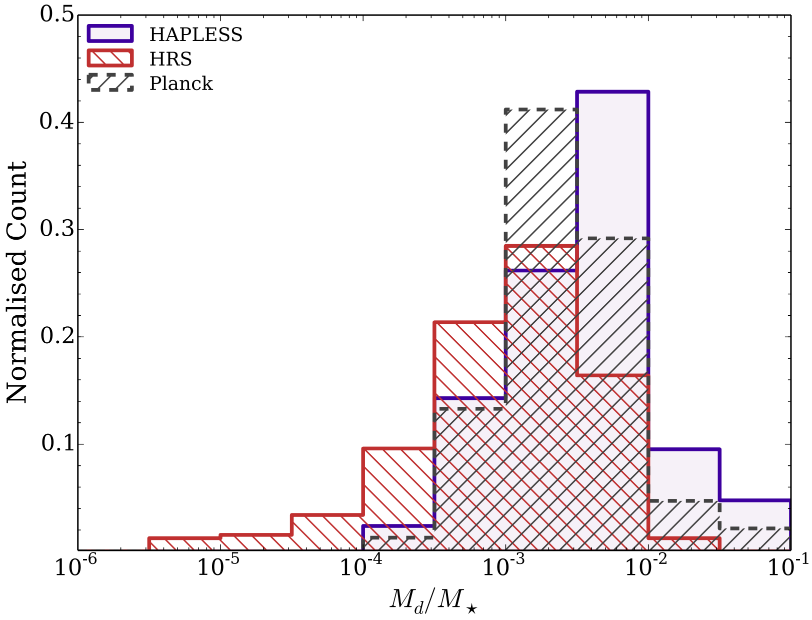

FIGURE 6.3 The distributions of $M_d/M_\star$ (ie, specific dust mass) for the HAPLESS, HRS, and *Planck* C13N13 galaxies. HAPLESS contains a much higher proportion of very dust-rich galaxies than either of the other two samples.

dust rich, as can be seen in Figure 6.3, possessing the highest median $M_d/M_\star$ (ie, specific dust mass) of the three surveys, at 4.4×10^{-3} (the HRS and *Planck* C13N13 samples have median values of 1.2×10^{-3} and 2.5×10^{-3} respectively, see Table 6.1). The very blue subset have an even higher median dust-to-stellar mass ratio of 6.5×10^{-3}. *Despite accounting for only 6% of the stellar mass in the HAPLESS sample, the curious very blue galaxies account for over 35% of the dust mass.*

6.4 THE DUST MASS VOLUME DENSITY

As described in Chapter 1, the Dust Mass Function (DMF) is very poorly constrained, despite being one of the fundamental characterisations of dust in the Universe. We are in a position to compare the dust mass volume densities DMFs of the HAPLESS, HRS, and *Planck* C13N13 samples, along with those of other literature studies. Given the 161.6 $\deg^2$ sky area of the *H*-ATLAS GAMA fields, and the 15–46 Mpc distance range we employ here, HAPLESS samples a volume of 1,540 Mpc^3.

To determine the total dust mass present in the HAPLESS volume, we calculate the combined dust mass of the individual sources, with the masses of the 7

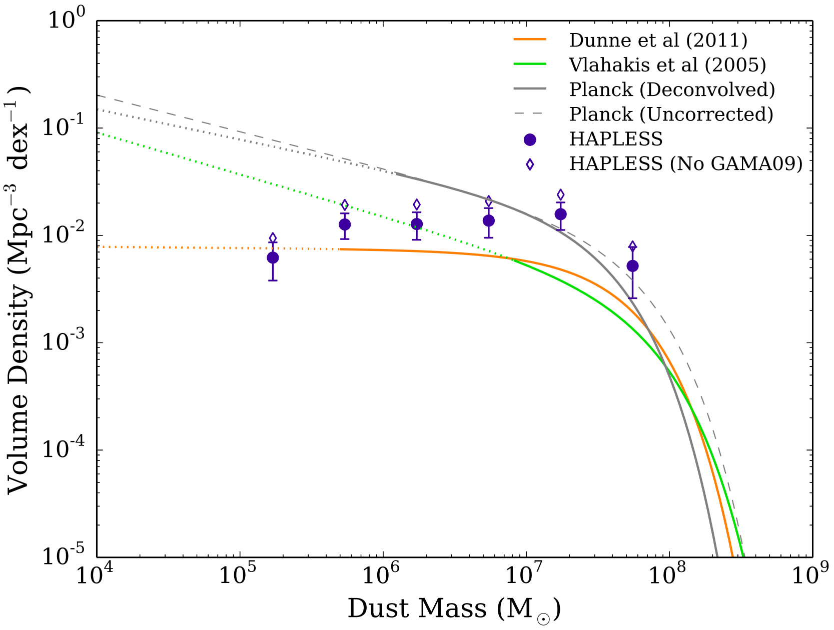

FIGURE 6.4 The HAPLESS dust mass function, compared with those of *Planck* C13N13, Vlahakis et al. (2005), and the *H*-ATLAS Science Demonstration Phase data from Dunne et al. (2011). All have been scaled to the same cosmology and value of κ_d employed here. The error bars on the points represent Poisson uncertainty. The hollow diamonds are the points produced when the extremely under-dense GAMA09 field is omitted from the HAPLESS sample. The solid lines indicate the range sampled by each of the functions from the literature, whilst the dashed lines show the region for which they are extrapolating. The naïve *Planck* C13N13 function represents the Clemens et al. (2013) published fit, whilst the deconvolved *Planck* C13N13 function represents our fit to their data points, taking account of the Eddington bias introduced by their large ($\sim$ 30%) distance uncertainties.

luminosity-incomplete sources weighted to account for the fraction of our volume in which they can be detected. We do this by means of an adaptation of the $1/V_{max}$ method of Schmidt (1968), with the total volume dust mass given by:

$$M_{tot} = \sum \left(M_d \frac{V_{tot}}{V_{acc}} \right) \tag{6.1}$$

where M_{tot} is the dust mass density, V_{tot} is the total sample volume, and V_{acc} is the accessible volume for a given source (in the case of the luminosity-complete sources detectable in our entire volume, we treat $V_{acc} = V_{tot}$). This gives a total dust mass of $(5.7 \pm 1.0) \times 10^8\,\mathrm{M}_\odot$. The uncertainty on this value represents the quadrature sum of the uncertainties on the dust masses of the individual sources, and uncertainty arising from Poisson statistics.

The resulting dust mass density of the HAPLESS volume is $\rho_d = (3.7 \pm 0.7) \times 10^5\,\mathrm{M}_\odot\,\mathrm{Mpc}^{-3}$ – however, this value could be misleading. The HAPLESS volume over-samples low-density environments; the GAMA09 field has been noted by previous authors for its paucity of galaxies at low redshift (Driver et al., 2011). Indeed, we note in Chapter 3 that the *H*-ATLAS GAMA09 field, which accounts for one third of our sampled volume, contains only a single HAPLESS object, UGC 04684 (HAPLESS 39). The result of this is that the GAMA09 portion of the HAPLESS volume has a dust mass volume density of only $(0.2 \pm 0.2) \times 10^5\,\mathrm{M_\odot\,Mpc^{-3}}$; this is 22 times lower than the $(5.4 \pm 1.0) \times 10^5\,\mathrm{M_\odot\,Mpc^{-3}}$ value of the combined GAMA12 and GAMA15 portions, which make up the remaining two-thirds of the HAPLESS volume, and together account for 98% of the total sample dust mass. It is important to bear in mind the large cosmic variance of the HAPLESS volume, which we estimate to be 166% (see Chapter 3).

The luminosity limit of $L_{250} = 2.8 \times 10^7\,\mathrm{L_\odot}$ for the complete sub-sample of HAPLESS, and its average dust temperature of 14.6 K, implies it has an approximate dust mass limit of $7.4 \times 10^5\,\mathrm{M_\odot}$ (assuming a dust SED of the kind described in Chapter 5).

The Figure 6.4 compares HAPLESS (with diamonds marking the HAPLESS volume density when *excluding* the severely under-dense GAMA09 field) to the dust mass functions of Dunne et al. (2011), Vlahakis et al. (2005), and Clemens et al. (2013), each discussed individually below. The literature DMFs have been corrected to the same cosmology[1] and value of κ_d as used in this work. All employ standard Schechter functions (see Section 1.4.1) of the form:

$$\phi = \phi^\star \left(\frac{M}{M^\star}\right)^\alpha e^{-\frac{M}{M^\star}} \tag{6.2}$$

The Clemens et al. (2013) best fit Schechter function does not take account of the large ($\sim$30%) uncertainties in the redshift independent distances they use (Negrello et al., 2013). Errors of this size on the distance measurements will cause scatter of $\sim$70% in the dust masses, and since there are more low mass galaxies than high mass ones, more are scattered towards the high mass end, effectively introducing significant Eddington bias (Eddington, 1913) into their DMF. As shown by Loveday et al. (1992), this means that an observed DMF is effectively a Schechter function *convolved with a Gaussian*, with σ the size of the scatter in the parameter of interest. As such, we performed our own fit to their quoted data points, and extract the underlying Schechter parameters via deconvolution; both DMFs are included in Figure 6.4. We also note that the units of $\phi^\star$ they give in their Table 2 are

---

[1] Cosmologies computed using Ned Wright's Cosmology Calculator (Wright, 2006): `http://www.astro.ucla.edu/~wright/CosmoCalc.html`

actually Mpc^{-3} for their own fits, and *not* $\mathrm{Mpc}^{-3}\,\mathrm{dex}^{-1}$, as they state their paper. The values they quote for $\phi^{\star}$ for Dunne et al. (2011) and Vlahakis et al. (2005) are however in the correct $\mathrm{Mpc}^{-3}\,\mathrm{dex}^{-1}$ units (Negrello, *priv. comm.*).

The HAPLESS data points are higher than the DMFs of Dunne et al. (2011) and Vlahakis et al. (2005) for the entirety of the mass range they directly sample, and lie above the *Planck* C13N13 DMF down to a mass of $\sim 10^{7}\,\mathrm{M}_{\odot}$ (galaxies with dust masses down to this level account for 86% of the total HAPLESS dust mass). Below this point, the various dust mass functions diverge from the HAPLESS data points, and from one another. The Vlahakis et al. (2005) and *Planck* C13N13 DMFs sample the low-mass slope to very different degrees, but are in reasonable agreement with one another nonetheless, whilst the Dunne et al. (2011) DMF suggests a flatter low-mass slope; however all estimates are compatible with each other to within their $1\,\sigma$ uncertainties.

In order to compare the HAPLESS dust mass volume density, ρ_{d}, to the other the samples, we integrate their best-fit Schechter functions (parameters listed in Table 6.2) down to the approximate HAPLESS dust mass limit of $7.4 \times 10^{5}\,\mathrm{M}_{\odot}$.

The corresponding values for the dust mass volume density are: $\rho_{d} = (2.5 \pm 0.6) \times 10^{5}\,\mathrm{M}_{\odot}\,\mathrm{Mpc}^{-3}$ for Clemens et al. (2013); $\rho_{d} = (1.3 \pm 0.2) \times 10^{5}\,\mathrm{M}_{\odot}\,\mathrm{Mpc}^{-3}$ for Dunne et al. (2011); and $\rho_{d} = 1.1 \times 10^{5}\,\mathrm{M}_{\odot}\,\mathrm{Mpc}^{-3}$ for Vlahakis et al. (2005). The quoted uncertainty is from retaining the fractional uncertainty of the integrated value quoted in the original work, where applicable. The best fitting parameters quoted by these authors, and the corresponding dust mass volume densities integrated down to our approximate dust mass limit, are given in Table 6.2.

The SED fitting we conduct in this work yields a total dust mass for the HRS of $(2.5 \pm 0.2) \times 10^{9}\,\mathrm{M}_{\odot}$. The right ascension, declination, and distance ranges defined in Boselli et al. (2010) mean that the HRS encompasses a volume of 4,600 Mpc^{3}, therefore corresponding to a dust mass volume density of $(5.5 \pm 0.3) \times 10^{5}\,\mathrm{M}_{\odot}\,\mathrm{Mpc}^{-3}$. We note that this value is almost identical to the value obtained from HAPLESS when excluding the severely under-dense GAMA09 field. However, the HRS opted to centre their volume upon the Virgo Cluster; 46% (148) of the HRS galaxies are located within Virgo (as defined by the Virgo Cluster Catalogue, Binggeli et al., 1985), and more still are in groups deep within the supercluster. This bias towards very high-density environments makes the dust mass volume density of the HRS difficult to compare fairly to other samples. Also, the HRS is not a truly complete, volume limited sample; rather, it is flux limited in K_{S}-band. There is no way to correct for the incompleteness in dust mass arising from the K_{S}-band flux limited selection.

TABLE 6.2 The dust mass volume densities and (where applicable) the best-fit Schechter function parameters of the various dust mass functions compared in this work. All have been scaled to the same cosmology and value of κ_d employed here. In the case of ρ_d values derived from Schechter functions, these were arrived at by integrating down to the approximate HAPLESS dust mass limit.

Sample	α	$M^\star$ ($10^7\,M_\odot$)	$\phi^\star$ ($10^{-3}\,\mathrm{Mpc}^{-3}\,\mathrm{dex}^{-1}$)	ρ_d ($10^5\,M_\odot\,\mathrm{Mpc}^{-3}$)	Origin
HAPLESS	–	–	–	3.7 ± 0.7	This work
Planck C13N13 (uncorrected)	-1.34	5.27	11.0	3.2 ± 0.7	Clemens et al. (2013)
Planck C13N13 (deconvolved)	-1.28	3.17	15.6	2.5 ± 0.6	Clemens et al. (2013) / this work
H-ATLAS SDP	-1.01	4.22	7.19^a	1.3 ± 0.2^a	Dunne et al. (2011)
SLUGS	-1.39	6.49	2.97	1.1	Vlahakis et al. (2005)
MGC L_B/M_d	–	–	–	2.2 ± 0.7	Driver et al. (2007b)
HRS	–	–	–	5.5 ± 0.3^b	This work

[a] Note that this incorporate the 1.42 correction factor applied by Dunne et al. (2011) to account for the previously-documented (Driver et al., 2011).

[b] 46% of the HRS galaxies lie within the Virgo Cluster, hence it is strongly biased towards extremely high-density environments.

The *H*-ATLAS Science Demonstration Phase (SDP) result for $0 < z < 0.1$ from Dunne et al. (2011) (plotted in orange in Figure 6.4) is based on the first 16 $\deg^2$ field of *H*-ATLAS. Their dust mass function as plotted here includes the correction factor of 1.42 applied by Dunne et al. (2011) to account for the known under-density of the GAMA09 field at $z < 0.1$, relative to the SDSS average (Driver et al., 2011). Despite this correction, the Dunne et al. (2011) DMF yields the second-lowest dust mass volume density of all the surveys compared here – a factor of 2.8 less than that of of HAPLESS. The $0 < z < 0.1$ Dunne et al. (2011) DMF suffers significantly from cosmic variance, particularly as the volume probed by the faint end part of the Dunne et al. (2011) DMF is small.

The *Planck* DMF of Clemens et al. (2013) is the least vulnerable to cosmic variance, being all-sky. However, although *Planck* C13N13 fully samples the HAPLESS volume, the survey's high flux limit of 1.8 Jy at 550 μm means that it detects just 3 (8%) of the HAPLESS galaxies (HAPLESS 6, 21, and 29), thereby missing 59% of the total dust mass we find in our sample. Despite this, Clemens et al. (2013) estimate of the dust mass volume density (integrated down to our approximate dust mass limit, with appropriate corrections for their mis-stated units) is compatible, in extremis, with our own. We note, however, that 167 (71%) of galaxies in the *Planck* C13N13 sample have no FIR photometry available. In these cases, the SED is entirely unconstrained between 22 and 350 μm. This wavelength range accounts for the vast majority of the total infrared luminosity – and, critically, contains the peak of the dust SED. Hence, for 71% of their sample, Clemens et al. (2013) have very little ability to constrain the dust temperature of their galaxies. The importance of the dust temperature will be discussed in Sections 6.4.1 and 6.5.

Vlahakis et al. (2005) used IRAS-submm colour relations from the SLUGS survey to estimate 850 μm fluxes, and hence dust masses, for all IRAS galaxies in the PSCz catalogue (Saunders et al., 2000). In order to use their 850 μm flux estimates and IRAS fluxes to yield a dust mass, they needed to assume a temperature for the SEDs, and their 'cold' fit assumes a cold dust temperature of 20 K – which seemed reasonable at the time based on submm studies of IRAS galaxies by Dunne & Eales (2001). We now know that low mass, late-type, blue, star-forming galaxies typically have dust temperatures 5–10 K colder than this (Boselli et al., 2010; Clemens et al., 2013; Kennicutt et al., 2011; Smith et al., 2012a). Overestimating the average temperature of the dust leads to an underestimation of the dust mass, and also means that more galaxies are likely missing from the IRAS PSCz than thought by Vlahakis et al. (2005). This was indeed shown by Negrello et al. (2013) in their comparison of the *Planck* 850 μm luminosity function with that of Vlahakis et al.

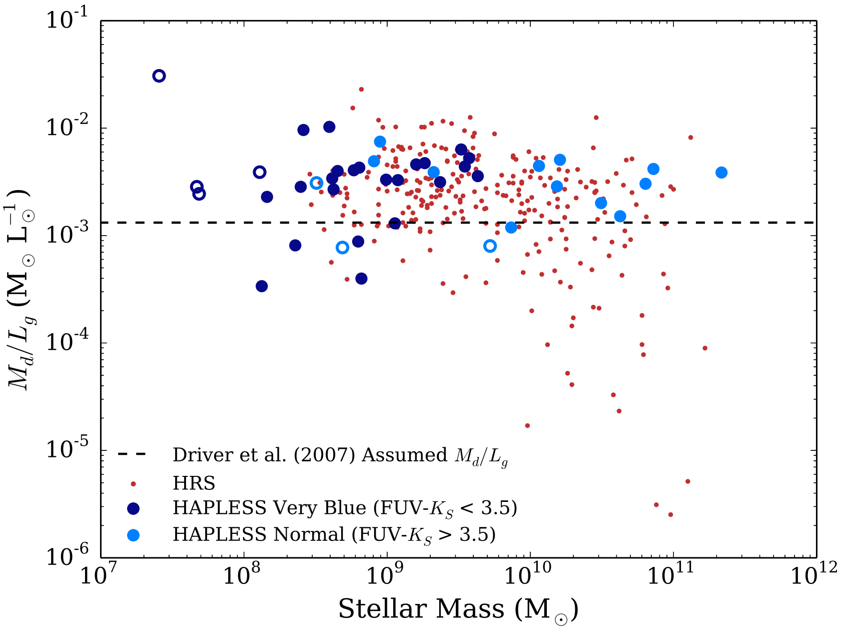

FIGURE 6.5 The ratio of dust mass to g-band luminosity against stellar mass for the HRS and HAPLESS samples. The dashed line shows the value of constant $M_d/L_g = 1.32 \times 10^{-3}$ assumed by Driver et al., 2007b, when converting optical luminosities to dust mass. Note that this value has been scaled by a factor of 0.59 to account for their different κ_d, and by a factor of 1.15 to convert from B-band luminosity. 83% of the HAPLESS galaxies (in both the full and luminosity limited sub-sample) lie above this line; the median HAPLESS value is $M_d/L_g = 3.36 \times 10^{-3}$.

(2005) and Dunne et al. (2000). It is therefore unsurprising that the Vlahakis et al. (2005) DMF (plotted in green in Figure 6.4) gives rise to the lowest of the dust mass volume density estimates compared here.

Our value is similarly in disagreement with the Driver et al. (2007b) estimate of $(2.2 \pm 0.7) \times 10^5\,\mathrm{M_\odot\,Mpc^{-3}}$, which they arrived at by assuming a constant ratio of unattenuated B-band luminosity to dust mass for the galaxies of the Millennium Galaxy Catalogue (MGC, Liske et al., 2003). We have normalised for the value of κ_d used by Driver et al. (2007b) (which is 70% lower than the one used here, Popescu, *priv. comm.*). However we do not attempt to integrate their function down to our dust mass limit, as it is not based upon direct measurements of actual dust masses. The dust mass-to-light ratio assumed by Driver et al. (2007b) in estimating their dust mass is lower than that measured in both the HAPLESS sample and the HRS, which will partially explain the difference – see Figure 6.5. Note that Clemens et al. (2013) misquote the Driver et al. (2007b) dust mass density in their paper. They do not account for the h scaling in Driver's quoted value, nor the value of κ_d used by Popescu & Tuffs (2002), which is a factor 1.7 lower than that used here (not equal

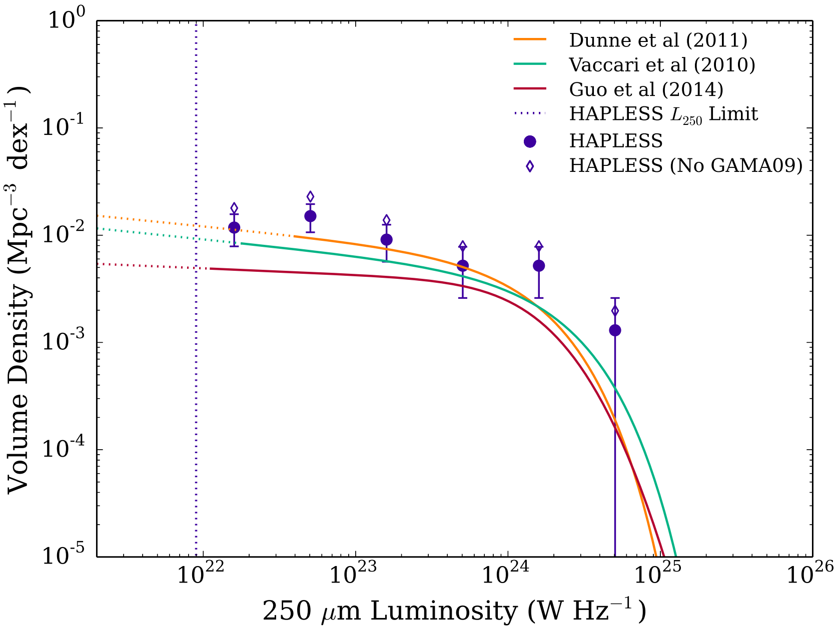

FIGURE 6.6 The 250 µm luminosity function of HAPLESS, compared with the $z < 0.1$ *H*-ATLAS samples of Dunne et al. (2011) and Guo et al. (2014), and the $z < 0.2$ sample of Vaccari et al. (2010). All have been scaled to the same cosmology employed here. We apply the appropriate corrections from Rigby et al. (2011) to our luminosity function, to account for the statistical effects of flux boosting and source blending. The error bars on the points represent Poisson uncertainty. The hollow diamonds are the points produced when the extremely under-dense GAMA09 field is omitted from the HAPLESS sample. The solid lines indicate the range sampled by each of the functions from the literature, whilst the dashed lines show the region for which they are extrapolating.

to ours, as they state). Therefore the Driver et al. (2007b) value is lower than their estimate – not, as they claim, higher.

Whilst HAPLESS is unavoidably incomplete in terms of dust mass, this should not be the case for 250 µm luminosity, where our luminosity-limited subsample (as defined in Chapter 3) is complete down to down to $L_{250} = 2.8 \times 10^{7}\ \mathrm{L}_{\odot}$. The luminosity function for HAPLESS is shown in Figure 6.6. We corrected our luminosity function for flux boosting (whereby fluxes can increased due to the noise characteristics of the maps) and source blending (whereby multiple sources in close proximity will appear to be a single artificially-bright source) according to the prescriptions of Rigby et al. (2011).

Comparing the luminosities of our galaxies to the luminosity functions of previous authors can provide us with a way to assess the relative density of the HAPLESS volume (ie, whether it is particularly under- or over-dense). Also plotted in Figure 6.6 is the 16 deg^{2} *H*-ATLAS SDP $0 < z < 0.1$ luminosity function of

TABLE 6.3 The best-fit Schechter function parameters of the various luminosity functions compared in this work. All have been scaled to the same cosmology employed here.

Sample	α	$L^{\star}$ $(10^{24}\,\mathrm{W\,Hz})$	$\phi^{\star}$ $(10^{-3}\,\mathrm{Mpc^{-3}\,dex^{-1}})$	Origin
H-ATLAS SDP	-1.14	1.53	6.00[a]	Dunne et al. (2011)
H-ATLAS Phase-1[b]	-1.06	1.12	3.70	Guo et al. (2014)
HerMES	-1.14[c]	2.19[c]	4.22[c]	Vaccari et al. (2010) / this work

[a] Note that this incorporate the 1.42 correction factor applied by Dunne et al. (2011) to account for the previously-documented (Driver et al., 2011).

[b] Guo et al. (2014) use a modified Schechter function to fit their LF, with an additional parameter of $\sigma = 0.30$.

[c] Vaccari et al. (2010) do not provide the parameters to their 250 µm Schechter fit; these values represent our best fit to their quoted data points.

Dunne et al. (2011) (plotted in orange, and scaled by their under-density correction factor of 1.42), the 161.6 deg^2 *H*-ATLAS Phase-1 $0 < z < 0.1$ luminosity function of Guo et al. (2014) (plotted in red), and the 14.7 deg^2 HerMES (*Herschel* Multi-tiered Extragalactic Survey, Oliver et al., 2012) $0 < z < 0.2$ luminosity function of Vaccari et al. (2010) (plotted in teal; this is our best fit to their quoted data points, as they do not state the Schechter parameters of their 250 μm LF). It should be noted that the Vaccari et al. (2010) LF, by sampling a volume out to $z = 0.2$, will likely feature evolution relative to the other samples, given the rapid evolution in submm luminosity reported by Dunne et al. (2011). The Schechter function parameters for these fits are given in Table 6.3. The good agreement between these luminosity functions and our own indicates that the HAPLESS volume represents a region of fairly typical 250 μm luminosity density. The fact that we find a greater dust mass volume density than other surveys suggests that HAPLESS is more sensitive to very cold dust in galaxies; leading to a greater dust mass for a given submm luminosity. We address this further in Sections 6.4.1 and 6.5.

6.4.1 GALAXIES POTENTIALLY MISSING FROM THE SAMPLE

Whilst we can correct for some types of incompleteness in our sample (by, for example, using the simulations of Rigby et al., 2011) it is difficult to correct for more subtle effects, such as the translation from 250 μm luminosity limits to dust mass limits, and the effects of incompleteness in the optical–submm cross-IDs (for a full discussion see Dunne et al., 2011).

Whether or not we detect a given mass of dust is strongly dependant upon the temperature of that dust. This is well illustrated by Figure 6.7, which compares the relation between 250 μm luminosity and dust mass for the HAPLESS and HRS. There is a scatter of $\sim$ 1 dex in this relationship. The galaxies in HAPLESS generally have more dust mass for a given 250 μm luminosity than the galaxies of the HRS or Dunne et al. (2011) samples because they are consistently colder.

A relatively large mass of dust would still be missed by our survey if it were sufficiently cold; $5.3 \times 10^5\,\mathrm{M}_\odot$ of dust at 10 K would not be detected, even at the inner edge of our distance range (note that 6 of the HAPLESS galaxies contain less dust *mass* than this limit, but have higher cold dust temperatures). And whilst $5.0 \times 10^6\,\mathrm{M}_\odot$ of dust at 10 K would be detectable in all but the outer 5% of our volume, it would not be luminous enough to be included in our in our luminosity-limited sub-sample – even though 42% of the galaxies that *do* meet the luminosity limit in fact contain *less* dust than this. In relation to the DMF, this effect also

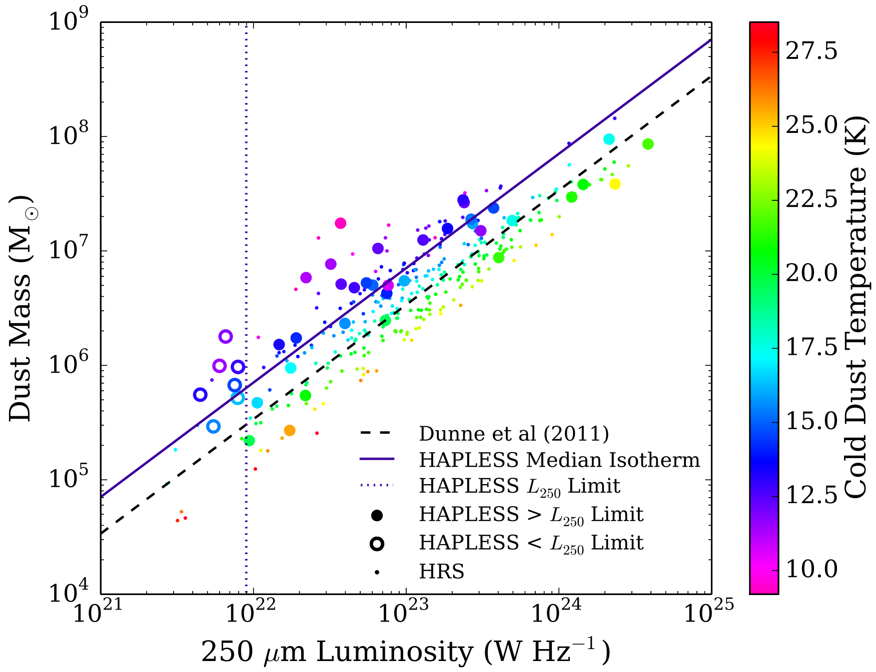

FIGURE 6.7 Dust mass against 250 µm luminosity for HAPLESS and the HRS, colour-coded by cold dust temperature. The solid blue line traces the isotherm corresponding to the median HAPLESS cold dust temperature of 14.6 K. The dashed black line is the best-fit trend found by Dunne et al. (2011) for this relation in their data; for both their plot and our own, this relation passes through the ∼19 K isotherm, indicating that for a given 250 µm luminosity and temperature, we would find the same dust mass. However, the HAPLESS galaxies tend to be colder than those in the HRS and Dunne et al. (2011) samples, hence they generally have a greater dust mass for a given luminosity. Hollow circles indicate galaxies not in our luminosity-limited sub-sample.

has a very significant influence upon a source's accessible volume. If we consider the volume accessible to a source with $M_d = 10^7\,M_\odot$ at a dust temperature of 14 K, compared to that for a source with the same dust mass but at a temperature of 20 K, we find that the warmer source *with the same dust mass* has an accessible volume *8 times greater* than the colder one. HAPLESS samples a far smaller, more local volume than the other surveys discussed in this section, and does so to a higher degree of sensitivity, rendering it much less susceptible to this effect. Conversely, even very warm dust can go undetected, if it represents little enough mass.

The *H*-ATLAS source extraction procedure (Rigby et al., 2011) operates by extracting $>5\,\sigma$ point sources from the maps. However it is, in theory, possible for extended sources to not meet the $5\,\sigma$ threshold at any one point, yet still represent a significant amount of flux overall; such sources would go undetected in the Phase-1 catalogue, and therefore would not be included in HAPLESS. However, the source extraction process was simulated by Rigby et al. (2011), including the effects of missing extended sources in this way, and these corrections have been applied in Figure 6.6. Furthermore, the corrections were modest – only a few percent lower completeness was found for the extended source simulations compared to the point source simulations. Thus we do not believe this has a large effect upon our dust or luminosity functions.

In matching an *H*-ATLAS source with an optical counterpart, an algorithmic likelihood ratio approach is taken where the separation between the optical and submm positions, the *r*-band magnitude, and the signal-to-noise of the 250 μm detection, are all taken into account to derive the likelihood that a given optical galaxy is genuinely associated with the SPIRE source in question. For very extended sources this algorithm can run into difficulties as the positional error distribution is no longer following a theoretical decline with increasing submm SNR. The resolved sizes of the galaxy become an issue – centroiding of the SDSS detection algorithm and shredding of the optical galaxy into multiple sources all can play havoc. For this reason, we have visually inspected the *H*-ATLAS maps at the location of every optical galaxy in the NASA/IPAC Extrgalactic Database (NED[2]) within the volume range of HAPLESS, and corrected any missing IDs (of which there were 3, see Chapter 3). Thus we are also confident our sample does not suffer from incompleteness due to missing optical identifications.

However, should a bright background source be present within a faint extended foreground source, the *H*-ATLAS submm–optical cross-ID procedure would deem both to be unreliable confused matches. The lower the surface brightness, and the greater the angular size, of a foreground source, the more likely this effect is to occur, potentially introducing systematic incompleteness in such objects.

Given the approximate HAPLESS dust mass limit of $7.4 \times 10^5\,M_\odot$, we can use the Schechter fits of previous authors' dust mass functions to estimate the fraction of the total dust mass in the HAPLESS volume that has gone undetected. The Clemens et al. (2013) *Planck* C13N13 fit implies that 7% of the dust mass in the local volume is in galaxies with dust masses less than our approximate limit – however their lowest dust mass is $\approx 8.3 \times 10^6\,M_\odot$. Vlahakis et al. (2005) specifically set out to constrain the low-mass slope, and find a similar dust mass function to Clemens et al. (2013), suggesting we are missing 8% of the total local dust mass. However, the very flat low-mass slope of the Dunne et al. (2011) fit implies that HAPLESS is only missing 2% of the total dust mass in our volume. Regardless, all of these

---

[2] `http://ned.ipac.caltech.edu/`

estimates suggest that HAPLESS represents a reasonably complete census of dust in the sampled volume. Future work exploiting the full *H*-ATLAS survey, which covers $\sim 600\,\mathrm{deg}^2$ of sky (compared to the $161.6\,\mathrm{deg}^2$ surveyed in this work), will be able to address these matters with far greater statistical power.

6.5 COLD, BLUE GALAXIES

Given the effects of dust temperature in limiting our completeness in the dust mass function, here we explore some relations between dust temperature and other galaxy properties in the three samples, to see what kinds of populations may be most at risk from selection bias. The first pane of Figure 6.8 shows the cold dust temperature distributions of the three samples. The HRS and *Planck* C13N13 distributions are similar, with medians of 18.5 and 17.7 K respectively. The HAPLESS distribution, however, is strikingly different; with a broad peak in the 12–16 K range, and a median temperature of 14.6 K; we find that 71% (30) of the HAPLESS galaxies have dust temperatures colder than both the HRS and *Planck* C13N13 medians (see Table 6.1).

The relationship between cold dust temperature and galaxy morphology for the HAPLESS, HRS, and *Planck* C13N13 galaxies is shown in the 2nd pane of Figure 6.8. A strong correlation is present; the dust in later galaxy types tends to be much colder than that in earlier types (Skibba et al., 2011; Smith et al., 2012c) and in low metallicity dwarf galaxies (Rémy-Ruyer et al., 2013). The HAPLESS galaxies are heavily skewed towards the late type and very cold end of the distribution. The 3rd pane compares stellar mass with cold dust temperature (following Bourne et al. 2012). No significant correlation is seen for HAPLESS according to Spearman correlation tests; however there is weak but statistically significant correlation amongst the other samples, and when all three samples are combined. The Spearman rank coefficients are 0.23, 0.39, 0.23, and 0.31 for HAPLESS, HRS, *Planck* C13N13, and all three combined, respectively (Table 6.4).

The last pane of Figure 6.8 also shows a strong inverse correlation between cold dust temperature and $M_d/M_\star$; this is particularly tight for galaxies with cold dust temperatures below $\sim 15\,\mathrm{K}$. This lack of cold galaxies with low $M_d/M_\star$ may be due to the detection bias against low dust mass objects with cold temperatures discussed in Section 6.4.1. Warmer galaxies can still be above the flux limit with smaller quantities of dust. As we know most of our cold galaxies are also low in

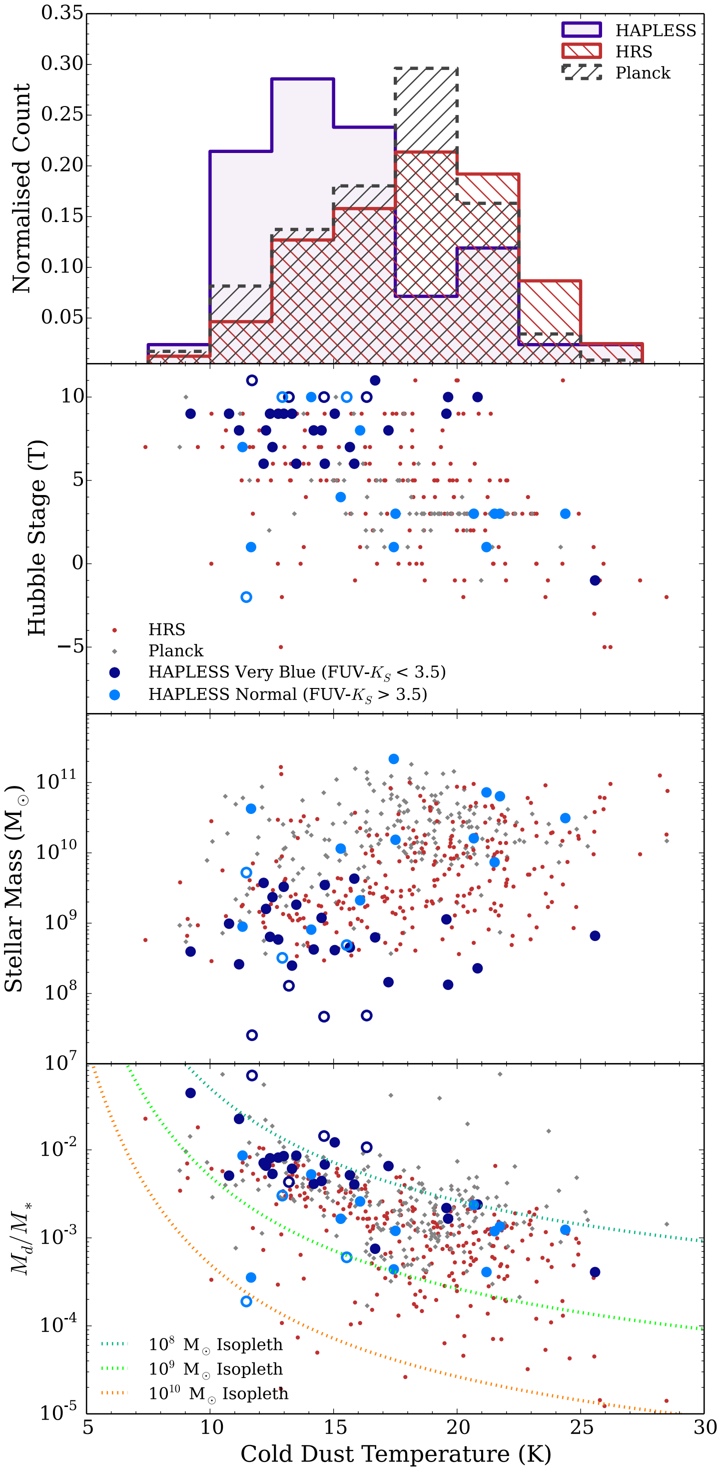

FIGURE 6.8 Cold dust temperatures relations for the HAPLESS, HRS, and *Planck* C13N13 galaxies. *From top-to-bottom – 1*st*:* The distribution of cold dust temperatures. *2*nd*:* The relation between morphological type and cold dust temperature; HAPLESS is heavily skewed towards cold late-type galaxies. *3*rd*:* Stellar mass versus cold dust temperature. *4*th*:* $M_d/M_\star$ against cold dust temperature; the dotted lines are isopleths of constant stellar mass, indicating the $M_d/M_\star$ required to be luminous enough to be included in the luminosity-limited sub-sample. Hollow circles indicate galaxies not in our luminosity-limited sub-sample.

stellar mass, this selection bias is a likely explanation for the tightening of the scatter toward lower temperatures. Isopleths are plotted to show the $M_d/M_\star$ necessary to a source to be luminous enough to be included in our luminosity-complete sub-sample, for given stellar masses, at different cold dust temperatures.

The 1st pane of Figure 6.9 demonstrates that bluer FUV-K_S colours are generally associated with colder dust temperatures, with the curious very blue subset of HAPLESS strongly clustered towards lower temperatures. The 2nd, 3rd, and 4th panes of Figure 6.9 show that bluer FUV-K_S colours correlate strongly with lower stellar masses, but higher values of $M_d/M_\star$ – with the net effect that dust mass actually does not vary with FUV-K_S colour. It is interesting to note that across the 3.5 orders of magnitude of $M_d/M_\star$ sampled by HAPLESS and the HRS, no galaxies are so dusty that extinction takes over and FUV-K_S colours become redder - this is in stark contrast to the Dust-Obscured Galaxies (DOGs) observed at higher redshifts, where dust-richness gives rise to severe extinction, resulting in red UV-NIR colours (Dey et al., 2008; Calanog et al., 2013).

The correlation between 'blueness' and colder dust temperatures in Figure 6.9 is surprising, as blue FUV-K_S colours suggests galaxies with plentiful ongoing star-formation – and one might naïvely expect this would indicate an intense interstellar UV radiation field, leading to more dust heating. In Figure 6.10 we examine L_{FUV}/L_{TIR} in relation to dust temperature, $M_d/M_\star$, and FUV-K_S colour. L_{FUV}/L_{TIR} indicates the number of UV photons escaping a galaxy unabsorbed, relative to the amount of energy which is absorbed by dust and thermally re-emitted in the IR. In the case where most dust emission is powered by absorption of UV photons rather than optical photons, this is equivalent to a measure of the UV transparency.

The upper pane of Figure 6.10 shows that the cold dust temperatures of the curious very blue HAPLESS galaxies decrease with increasing L_{FUV}/L_{TIR}. This suggests that the reason for the low cold temperatures is because a large fraction of their UV luminosity escapes unabsorbed by dust. This could be due to some physical difference in the composition of the dust (grains that are more efficient absorbers/emitters) or because the dust is distributed differently in these sources.

The central pane of Figure 6.10 shows that the more dust-rich a galaxy is (as defined by $M_d/M_\star$), the *smaller* the fraction of the UV luminosity that suffers dust absorption. The lower pane of Figure 6.10 demonstrates a tight correlation between L_{FUV}/L_{TIR} and FUV-K_S colour – except for galaxies on the red sequence (FUV-$K_S \gtrsim 6$). In these systems there is a range of L_{FUV}/L_{TIR} at the same colour.

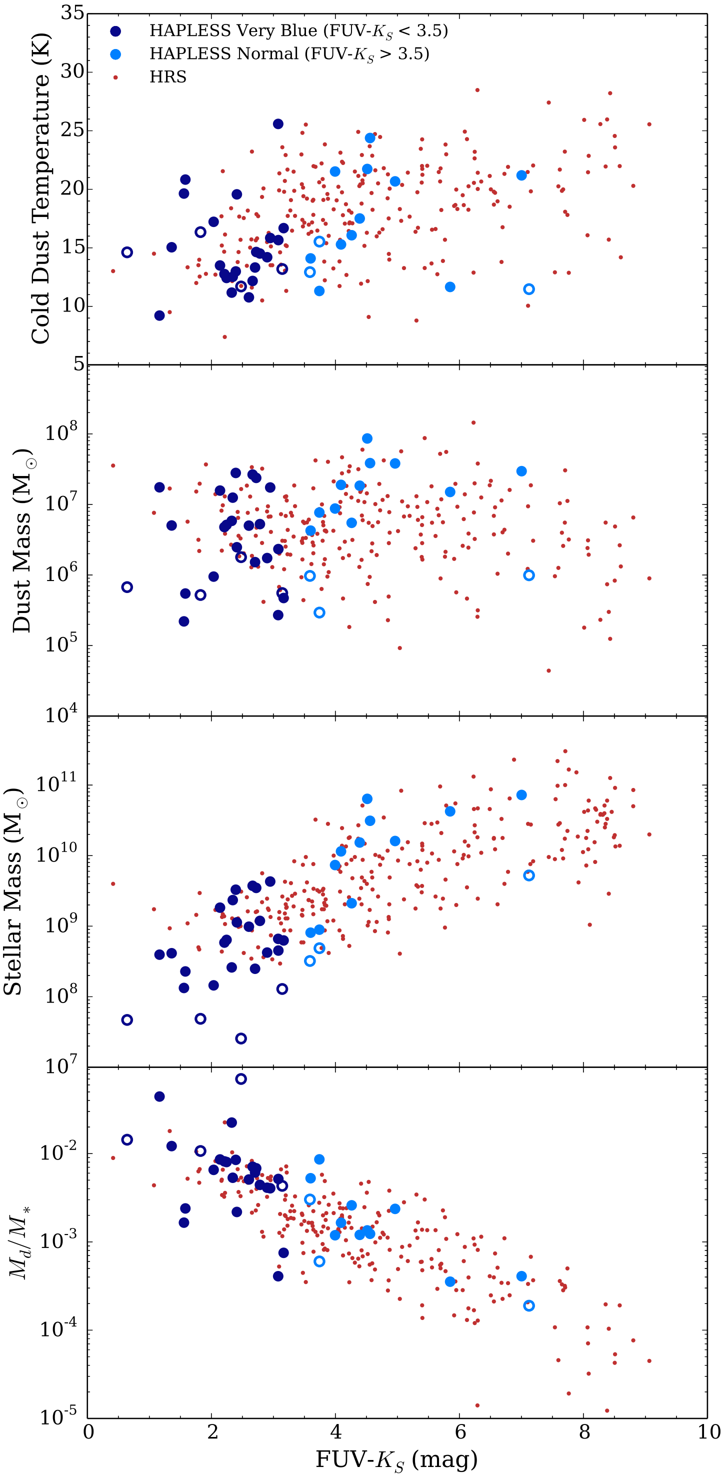

FIGURE 6.9 Scaling relations with FUV-K_S colour for the galaxies of HAPLESS and the HRS. *From top-to-bottom – 1st*: FUV-K_S cold dust temperature against colour; HAPLESS shows a preponderance of cold blue galaxies, which only make up a small fraction of the HRS. *2nd*: Dust mass against FUV-K_S colour. *3rd*: Stellar mass against FUV-K_S colour. *4th*: $M_d/M_\star$ (ie, specific dust mass) against FUV-K_S colour, showing the strong relationship between colour and dust-richness. Hollow circles indicate galaxies not in our luminosity-limited sub-sample.

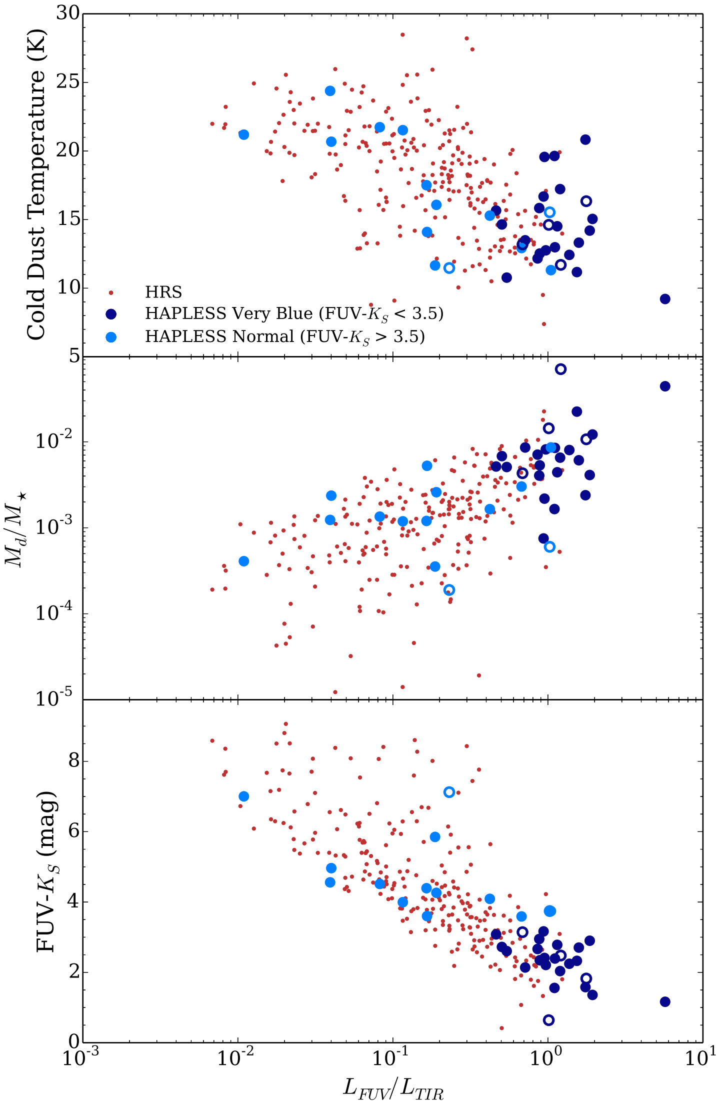

FIGURE 6.10 Scaling relations with L_{FUV}/L_{TIR} for the HAPLESS and HRS. *Upper:* Cold dust temperature against L_{FUV}/L_{TIR}. *Centre:* $M_d/M_\star$ against L_{FUV}/L_{TIR}; counter-intuitively, the more dust-rich a galaxy, the larger the proportion of FUV photons that go unabsorbed. *Lower:* FUV-K_S colour against L_{FUV}/L_{TIR}; correlation is very tight for bluer galaxies, but extremely weak for redder galaxies. Hollow circles indicate galaxies not in our luminosity-limited sub-sample.

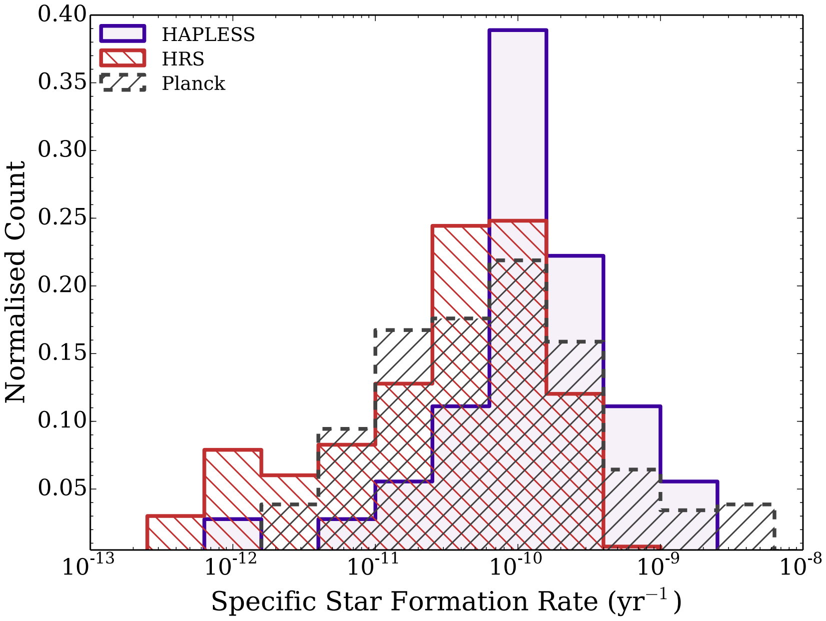

FIGURE 6.11 The distribution of SSFRs derived for the HAPLESS, HRS, and *Planck* C13N13 samples. Whilst the HRS and *Planck* C13N13 samples show a broad range of SSFRs, the HAPLESS galaxies generally occupy of much narrow range of values, of relatively high SSFRs.

Recalling that L_{FUV}/L_{TIR} is really only an attenuation measure if most IR luminosity is powered by UV photons (as opposed to optical ones), this wide range of values for L_{FUV}/L_{TIR} on the red sequence may indicate that the dust heating in this population is not dominated by UV radiation. Dust in early type galaxies is often acquired during interactions (Gomez et al., 2010; Smith et al., 2012c; Rowlands et al., 2012) which may produce a range of dust geometries and therefore a wide range of values for L_{FUV}/L_{TIR}.

6.6 STAR FORMATION RELATIONS

Figure 6.11 shows the SSFR distributions of all three samples. The HAPLESS galaxies tend towards high SSFRs, with a median of $1.3 \times 10^{-10}\,\text{yr}^{-1}$. Only 15% of the HRS and 34% of the *Planck* C13N13 galaxies exhibit SSFRs greater than this (having medians of 4.1×10^{-11} and $6.9 \times 10^{-11}\,\text{yr}^{-1}$ respectively). The upper pane of Figure 6.12 demonstrates that FUV-K_S colour is a very good indicator of SSFR, which stands to reason – FUV luminosity traces recent star formation, whilst K_S-band luminosity is an excellent indicator of a galaxy's total stellar mass. Our colour criterion of FUV-$K_S < 3.5$ corresponds to a SSFR $\sim 10^{-11}\,\text{yr}^{-1}$; the HAPLESS

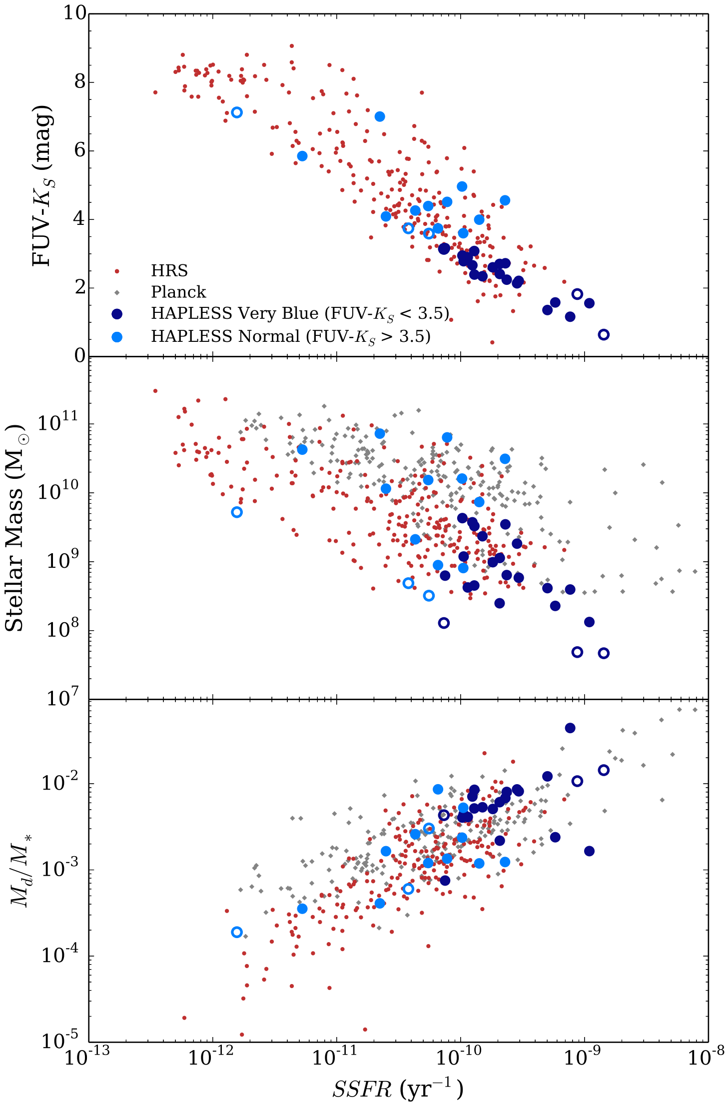

FIGURE 6.12 Scaling relations with SSFR for the HAPLESS, HRS, and *Planck* C13N13 galaxies. *Upper:* FUV-K_S colour against SSFR; the two are tightly related, with our FUV-$K_S < 3.5$ colour criterion corresponding to a SSFR $\sim 1.1 \times 10^{-10}\,\text{yr}^{-1}$. *Centre:* Stellar mass against SSFR. *Lower:* $M_d / M_\star$ (ie, specific dust mass) against SSFR; higher SSFRs are consistently associated with more dust-rich systems. Hollow circles indicate galaxies not in our luminosity-limited sub-sample.

galaxies bluer than this have a median SSFR of $2.1 \times 10^{-10}\,\mathrm{yr}^{-1}$.

The central pane of Figure 6.12 also shows that systems with lower stellar masses consistently have higher SSFRs. The low stellar masses and high SSFRs of the curious blue HAPLESS galaxies place them all in line with the same trend exhibited by the *Planck* C13N13 and HRS samples. This trend agrees with the relationship found in higher stellar mass objects from the GALEX Arecibo SDSS Survey (GASS) in Schiminovich et al. (2010); whilst they only probe galaxies with $M_{\star} > 10^{10}\,\mathrm{M}_{\odot}$, we are able to show that this relationship continues to lower stellar masses. There are a number of *Planck* C13N13 objects with extremely high SSFRs that have much higher stellar masses than would be expected; this subset includes well-known aggressively star-forming systems such as Arp 220 and Arp 299. The third pane of Figure 6.12 shows similarly strong correlation between SSFR and $M_d/M_{\star}$. This is unsurprising, given that dust likely traces the dense ISM where star-formation occurs (Cortese et al., 2012a; Smith et al., 2012b; Rowlands et al., 2014a). Overall, the curious blue HAPLESS galaxies are distributed in good agreement with the overall trends; this suggests that these galaxies do not depart from usual correlations with $M_d/M_{\star}$ and SSFR, and that despite their particularly high SSFRs, these objects are not forming stars in a fundamentally different manner to the galaxies of the other samples.

6.7 WHAT IS HEATING THE COLD DUST?

Dust heating in galaxies can occur in a variety of ways (see Kennicutt & Evans, 2012b; Dunne, 2013). Warm dust is thought to be associated with star-forming dense molecular clouds, with newly formed stars heating the dust to temperatures $>60\,\mathrm{K}$ (Kennicutt, 1998; Kennicutt et al., 2009; Bendo et al., 2010). Cold dust is instead associated with the diffuse ISM (Rowan-Robinson & Crawford, 1989; Tuffs & Popescu, 2005; Boquien et al., 2011; Bendo et al., 2012) though high energy photons from 'leaky' star forming regions could also contribute to heating this cold component (Law et al., 2011; Clemens et al., 2013; Hughes et al., 2014). As well as the intrinsic heating source, the amount of heating will also depend on the distribution of dust and stars within a galaxy, and the optical properties of the dust (see Foyle et al., 2013). If star formation activity is the primary driver of the heating of cold dust, we would expect the dust in the HAPLESS galaxies to be amongst the hottest – which is very much not the case (Figure 6.8). In this section, we wish to investigate the relative importance of both the young and the old stellar population in heating the bulk dust mass (ie, the cold component).

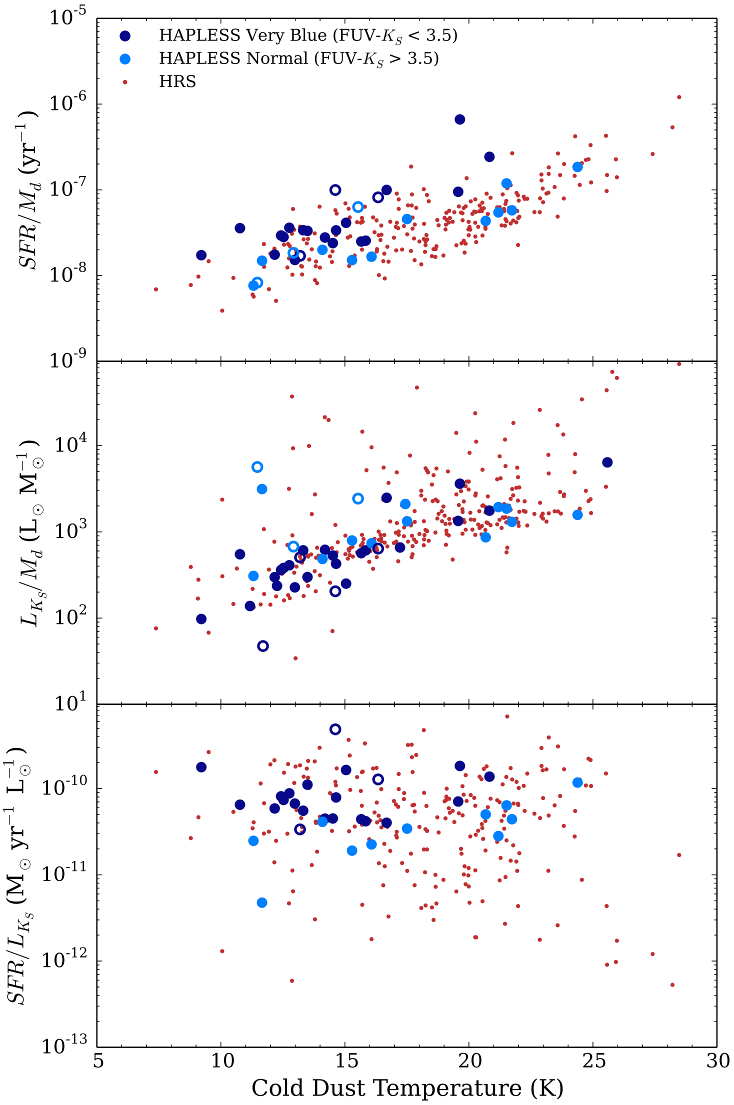

FIGURE 6.13 The influence of star formation and the older stellar population upon the temperature of the cold dust in the HAPLESS and HRS galaxies. *Upper:* SFR/M_d; *Centre:* L_{K_S}/M_d and *Lower:* SFR/L_{K_S} against T_c. The SFR/L_{K_S} should indicate the relative influence of star formation and the older stellar population on T_c. Hollow circles indicate galaxies not in our luminosity-limited sub-sample.

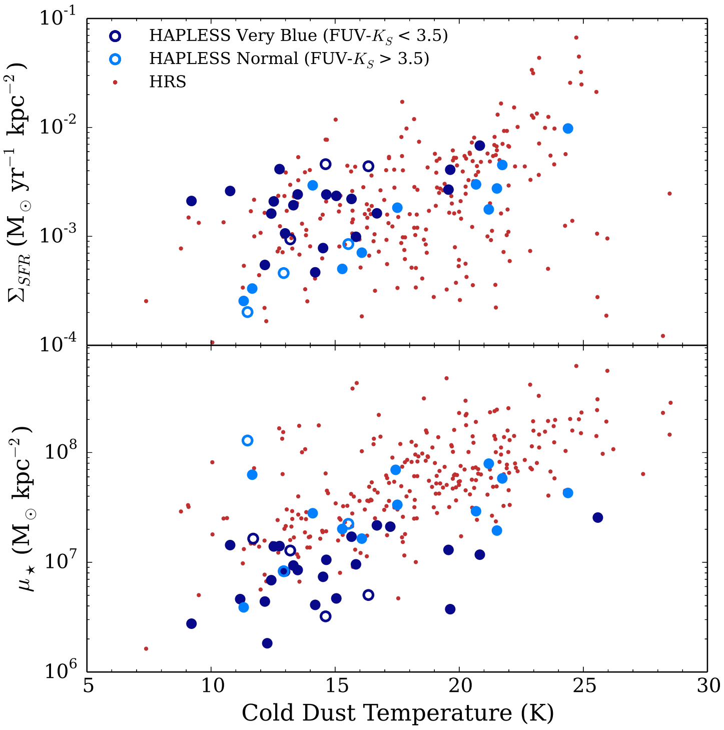

FIGURE 6.14 The variation of SFR surface density, Σ_{SFR}, (*upper*), and the stellar mass surface density, $\mu_\star$, (*lower*), with cold dust temperature for the HAPLESS and HRS galaxies.

Our choice of 'heating' parameter is influenced by the study of Foyle et al. (2013), who determined that it was the amount of star formation (or alternatively old stellar radiation field) *per unit dust mass* which should determine the temperature of the bulk dust component, not simply the *amount* of star formation or old stars, or even their surface density. If there is simply more dust to be heated by a particular radiation field, then its average temperature will be lower. To explore this, we plot SFR/M_d, L_{K_S}/M_d, and SFR/L_{K_S} versus cold dust temperature in Figure 6.13, and the SFR surface density Σ_{SFR} and stellar mass surface density ($\mu_\star$) versus T_c in Figure 6.14. Surface densities were estimated using the r-band $R25$ (Table 3.2) to determine the optical radius in kpc, assuming that each galaxy is circular as a first approximation.

In the upper pane of Figure 6.13 we see that higher values of SFR/M_d correlate significantly with higher cold dust temperatures, with a Spearman r coefficient of 0.74 for the combined surveys (0.71 for HAPLESS, 0.75 for HRS, see Table 6.4). It is difficult to see that this relationship could be a selection effect, as warmer galaxies are always easier to detect for a given mass of dust.

As a proxy for the energy from old stellar photons per unit dust mass, we also plot L_{K_S}/M_d versus T_c in Figure 6.13, and again significant positive correlation is seen, with Spearman rank 0.69 for the combined surveys (0.64 and 0.67 for HAPLESS and the HRS respectively, see Table 6.4). These correlations suggest that whilst star formation has a definite influence upon the temperature of the cold dust component, it is not the sole driver in these surveys.

Kirkpatrick et al. (2014) use 500 μm luminosity as a proxy for dust mass, and 3.6 μm luminosity to trace the radiation field of the older stellar population, in a study of star-forming spirals with average $M_\star = 8.2 \times 10^9\,\mathrm{M}_\odot$. In contrast to this work, they find no significant correlation for their sample of normal star forming disk galaxies. However they consider resolved regions within their galaxies and so photons are required to be absorbed within the same pixel from which they were emitted in order to produce a correlation. It is not clear whether this sample would produce the same trends if only the global integrated values were considered, as we do here.

To gauge the relative importance of the young and old stellar populations in heating the bulk of the dust mass, the lower pane of Figure 6.13 compares SFR/L_{K_S} against T_c. No correlation is seen, but the blue HAPLESS sources tend to exhibit higher values of SFR/L_{K_S} for a given dust temperature. This is in contrast to Kirkpatrick et al. (2014), who find that $SFR/L_{3.6}$ and T_c are positively correlated on resolved scales in nearby star forming spiral galaxies; although this correlation cannot solely be due to their resolved comparison as they do not see any radial dependence in this trend.

Finally, we also examine the surface density of star formation and stellar mass against T_c in Figure 6.14. Both HAPLESS and HRS show correlations with the stellar mass surface density, but the HRS sample has a tighter correlation with a steeper slope, with Spearman rank coefficients of 0.44 and 0.63 for HAPLESS and the HRS respectively (note that the HAPLESS correlation is not statistically significant due to the small size of the sample, see Table 6.4). Also we note that the stellar mass surface density is consistently higher for HRS galaxies at a given dust temperature. In contrast, the HAPLESS galaxies do show a weak correlation between star formation surface density and dust temperature ($r = 0.32$) while the HRS does not ($r = 0.04$). More specifically, the HAPLESS sample shows a range of Σ_{SFR} at the coldest dust temperatures, but require a higher Σ_{SFR} to reach the highest temperatures; the HRS sample instead shows a range of ΣSFR at all temperatures.

This suggests that while both the young and old stellar radiation fields (using $\mu_\star$ and Σ_{SFR} as proxies respectively) play a role in heating the dust in both

TABLE 6.4 Spearman rank coefficients for the correlation of various parameters with cold dust temperature for the HAPLESS and HRS samples. Shown for each is the likelihood of the null hypothesis that a correlation at least as good as that seen could have arisen by chance.

Parameter versus T_c	HAPLESS		HRS		HRS + HAPLESS	
	r	$P(null)$	r	$P(null)$	r	$P(null)$
$M_\star$	0.24	0.14	0.39	$< 10^{-5}$	0.31	$< 10^{-5}$
SFR/M_d	0.71	$< 10^{-5}$	0.75	$< 10^{-5}$	0.74	$< 10^{-5}$
L_{K_S}/M_d	0.64	$< 10^{-5}$	0.67	$< 10^{-5}$	0.69	$< 10^{-5}$
$\mu_\star$	0.44	10^{-3}	0.63	$< 10^{-5}$	0.65	$< 10^{-5}$
Σ_{SFR}	0.32	10^{-2}	0.04	0.42	0.08	0.14

samples, the dust heating in galaxies selected by HRS is more strongly influenced by the old stellar population and galaxies selected in HAPLESS are more strongly heated by the young stellar population.

Therefore, it seems that neither star formation nor the older stellar population solely govern the cold dust temperature in the HAPLESS and HRS galaxies. The systems with the coldest dust temperatures are consistently associated with lots of star formation relative to their older stellar population; but, the inverse *cannot* be said.

6.8 CONCLUSION

In this chapter, I compare HAPLESS, a blind dust-selected sample of nearby galaxies, to other surveys of dust in galaxies in the local volume. The HAPLESS galaxies are exceptionally dust rich, with a median $M_d/M_\star$ greater by a factor of ~ 3.7 than the galaxies observed as part of the *Herschel* Reference Survey (the largest targeted sample of nearby galaxies surveyed with *Herschel*), and a factor of 1.8 than galaxies in the *Planck* Early Release Compact Source Catalogue sample of Clemens et al. (2013) and Negrello et al. (2013) (hereafter referred to as *Planck* C13N13). The curious very blue HAPLESS galaxies, whilst accounting for only 6% of the stellar mass in our sample, contain over 35% of the dust mass.

The HAPLESS systems show a strong propensity towards very late morphological types and extremely blue FUV-K_S colours, relative to the other surveys. They also exhibit extremely low cold dust temperatures, with a median of only 14.6 K. We find that the more dust-rich a galaxy (as defined by $M_d/M_\star$), the *smaller* the fraction of its UV luminosity that suffers dust absorption – this effect is observed to be particularly dramatic in the case of the curious very blue objects. Either the emissivity or geometry of the dust in these systems must be highly unusual. The 'leakiness' of the dust in these galaxies appears to be the cause of their low dust temperatures.

We find that the coldest dust seen in the local universe is consistently associated with galaxies that have lots of star formation relative to their older stellar population. Nonetheless, both the amount of star formation and evolved stars in a galaxy, relative to its dust mass, are found to be strongly correlated with the cold dust temperature for both HAPLESS and the HRS. Both star formation and evolved stellar population surface density are found to correlate with dust temperature for HAPLESS; however, for the stellar mass selected HRS, this is only true for the latter.

The dust mass volume density of the local universe from the 250 μm luminosity limited portion of our sample is $(3.7 \pm 0.7) \times 10^{5}\,\mathrm{M}_{\odot}\,\mathrm{Mpc}^{-3}$, which is higher than other estimates from *H*-ATLAS, other submm, and optical surveys – although is consistent with recent results from *Planck*. Much of this difference seems to arise from the low dust temperatures of the galaxies in our sample; we systematically observe temperatures lower than the ~ 20 K routinely assumed in the literature. Although our volume suffers from a high cosmic variance of $\sim 166\%$, the HAPLESS 250 μm luminosity function is in good agreement with surveys of far larger volumes, suggesting that we do *not* sample an over-dense region of space (at least with respect to dust luminosity). Comparing our flux limit to the dust mass functions of previous studies suggests that HAPLESS could be missing up to 8% of the dust in the local volume.

CHAPTER 7

HAPLESS: REVEALING IMMATURE GALAXIES IN THE LOCAL VOLUME

> *'Youth, what man's age is like to be, doth show;*
> *We may our ends by our beginnings know.'*
>
> SIR JOHN DENHAM

CHAPTER 6 revealed that HAPLESS, a sample of galaxies selected purely on the basis of their submillimetre luminosity, contains systems that display a host of unusual properties compared to the objects commonly found in other surveys. In this chapter, I explore the role that the gas content of the HAPLESS galaxies has to play in their remarkable characteristics, and examine what this unique sample can tell us about the on-going evolution of galaxies in the local universe. The work in this chapter is published in Clark et al. (*submitted.*), except for the gas depletion work, which will appear in De Vis et al. (*in prep.*).

7.1 GAS PROPERTIES OF THE HAPLESS GALAXIES

The high SSFRs of the HAPLESS galaxies, and their generally low stellar masses, suggest that these are either objects going through an intense but unsustainable phase of heightened star formation, or that they possess large gas reservoirs from which to form stars over a long period of time.

To address this I searched the literature for the highest-resolution 21 cm observations available for each of the HAPLESS sources. I found 15 of the galaxies have observations in the literature; the instrument and reference for each can be

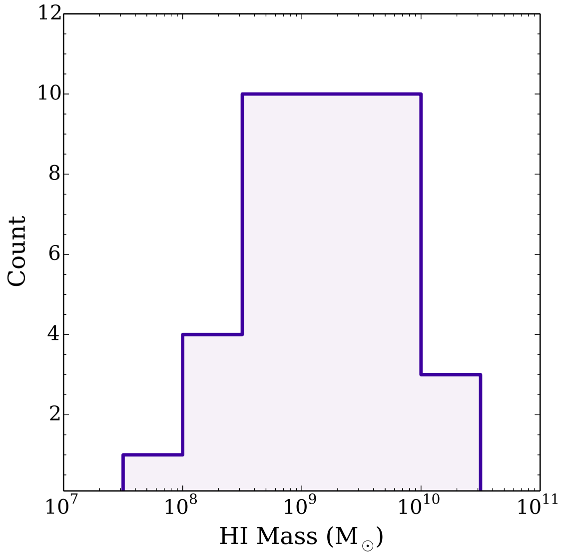

FIGURE 7.1 The distribution of HI masses exhibited by the HAPLESS galaxies, calculated using Equation 7.1 for the 31 sources with 21 cm fluxes available in the literature or HIPASS.

found in Table 7.1. For the remaining sources, I then used the HI Parkes All-Sky Survey (HIPASS, Meyer et al., 2004; Zwaan et al., 2004; Wong et al., 2006) to search for HIPASS sources within the Full-Width Half-Maximum (FWHM) of the Parkes beam (14.75′) centred on the positions of the HAPLESS galaxies.

To avoid the risk of contamination due to confusion, I only accepted matches for which there were no other known galaxies within 14.75′ radius on the sky, nor within 500 km s^{-1} in velocity. Less than 1% of sources in the HIPASS catalogues have line-widths $> 500\,\mathrm{kms}^{-1}$. Using this matching technique, I was able to identify 16 additional 21 cm detections associated with the HAPLESS galaxies.

For the 11 sources with neither HIPASS nor literature HI detections available, HI data for 7 were provided by the ALFALFA (Arecibo Legacy Fast ALFA, Giovanelli et al., 2005) survey (Haynes, *priv. comm.*).

Combined with the literature observations, this provides us with HI measurements for 38 of the 42 objects (90%) in our sample. To calculate the HI masses, I used the standard prescription:

$$M_{HI} = 2.36 \times 10^5 S_{int} D^2 \tag{7.1}$$

where M_{HI} is the mass of atomic hydrogen in Solar units, S_{int} is the integrated 21 cm line flux density in Jy km s^{-1}, and D is the source distance in Mpc.

A histogram of the HI mass distribution of the HAPLESS galaxies is shown

TABLE 7.1 HI properties of the HAPLESS galaxies. The origin column indicates whether 21 cm data comes from the HIPASS or ALFALFA catalogues, or published literature values (note that R_v and W_{50} are not available for all sources with 21 cm measurements). HI masses were calculated using Equation 7.1, with upper limits derived using Equation 7.4. The gas fraction f_g^{HI} is defined by Equation 7.2, and the effective atomic gas depletion timescale τ_g^{HI} is defined by Equation 7.3.

HAPLESS	S_{int} (Jy km s^{-1})	R_v (km s^{-1})	W_{50} (km s^{-1})	Telescope	Origin	M_{HI} (log$_{10}$ M$_\odot$)	f_g^{HI}	τ_g^{HI} (log$_{10}$ yr)
1	1.30	1146	78	GBT 91 m	Courtois et al. (2011)	8.08	0.13	-
2	1.39	1308	-	Arecibo	Salzer (1992)	8.36	0.60	-
3	23.70	1387	222	Parkes	HIPASS	9.56	0.67	9.85
4	0.86	1439	140	VLA-D	Taylor et al. (1995)	8.24	0.22	9.57
5	0.44	-	-	Arecibo	Impey et al. (2001)	7.83	0.18	9.58
6	72.00	1462	306	Parkes	HIPASS	10.16	0.19	9.47
7	60.90	1539	243	Parkes	HIPASS	10.03	0.74	10.36
8	5.70	-	-	Arecibo	Sulentic & Arp (1983)	9.08	0.52	9.71
9	46.90	1537	198	Parkes	HIPASS	9.94	0.96	10.63
10	35.80	1528	287	WRST	Popping & Braun (2011)	9.82	0.31	9.90
11	5.90	1624	187	Parkes	HIPASS	9.17	0.62	10.40
12	3.97	1560	176	Arecibo	ALFALFA	8.90	0.66	10.14
13	0.38	1713	26	Arecibo	ALFALFA	7.87	0.37	10.90
14	27.10	1638	198	Parkes	HIPASS	9.76	0.47	9.59
15	1.08	1652	72	Arecibo	ALFALFA[a]	8.34	0.35	10.07
16	4.26	1673	205	Arecibo	ALFALFA	8.97	0.32	10.01
17	3.50	1749	120	VLA-D	Taylor et al. (1995)	8.96	0.88	9.80
18	-	-	-	-	-	< 8.69	< 0.46	< 9.39
19	26.90	1729	225	Parkes	HIPASS	9.85	0.82	-
20	43.50	1736	431	GBT 300 ft	Davis & Seaquist (1983)	9.98	0.12	9.78
21	30.70	1724	556	WRST	Popping & Braun (2011)	9.83	0.03	-
22	-	-	-	-	-	< 8.72	< 0.09	< 10.72

[a] Classified by ALFALFA as a low SNR source (SNR = 5).

TABLE 7.1 – *Continued*

HAPLESS	S_{int} (Jy km s^{-1})	V_r (km s^{-1})	W_{50} (km s^{-1})	Telescope	Origin	M_{HI} ($\log_{10}$ M$_{\odot}$)	f_g^{HI}	τ_g^{HI} ($\log_{10}$ yr)
23	25.60	1748	294	Parkes	HIPASS	9.78	0.28	9.56
24	2.89	1859	100	VLA-D	Taylor et al. (1995)	8.93	0.95	10.31
25	5.30	-	-	Parkes	Bottinelli et al. (1990)	9.08	0.03	9.73
26	27.90	1760	184	Parkes	HIPASS	9.80	0.66	10.18
27	8.40	1836	224	Parkes	HIPASS	9.31	0.83	10.63
28	5.50	1878	150	Parkes	HIPASS	9.16	0.17	9.14
29	44.50	1897	317	GBT 300 ft	Davis & Seaquist (1983)	10.07	0.28	9.22
30	3.80	-	-	NED	NED[b]	9.00	0.62	9.83
31	13.30	1891	177	Parkes	HIPASS	9.64	0.51	10.00
32	1.81	1916	113	Arecibo	ALFALFA	8.71	0.39	9.78
33	6.10	1973	60	VLA-D	Taylor et al. (1995)	9.35	0.91	10.23
34	6.50	2033	99	Parkes	HIPASS	9.37	0.86	9.90
35	3.22	-	-	Arecibo	Schneider et al. (1990)	9.11	0.52	10.01
36	2.04	2143	98	Arecibo	ALFALFA	8.93	0.77	-
37	-	-	-	-	-	<9.06	<0.09	<9.56
38	1.41	2433	127	Arecibo	ALFALFA	8.79	0.71	10.08
39	8.80	2510	148	Parkes	HIPASS	9.55	0.60	10.01
40	3.40	1622	148	Parkes	HIPASS	8.87	0.43	9.61
41	6.40	1098	124	Parkes	HIPASS	8.65	0.90	9.83
42	-	-	-	-	-	<8.78	<0.96	-

[b] A 21 cm S_{int} value for HAPLESS 30 (UGC 09470) is available on NED, but no reference is provided. Despite this, the corresponding HI properties of HAPLESS 30 are typical of the HAPLESS sample, thus we opt to include it.

in Figure 7.1, whilst the HI properties for each source are listed in Table 7.1. Amongst those HAPLESS galaxies with 21 cm detections, the derived HI gas masses range from 6.8×10^7 to $1.5 \times 10^{10}\,\mathrm{M}_\odot$, with a median mass of $1.4 \times 10^9\,\mathrm{M}_\odot$ (see Table 7.2).

To quantify how gas-rich a galaxy is, we calculate the atomic gas fraction f_g^{HI} for galaxies with detected HI masses; this is defined as:

$$f_g^{HI} = \frac{M_{HI}}{M_{HI} + M_\star} \tag{7.2}$$

where f_g^{HI} provides a lower limit (as molecular gas is not considered in this work) on the fraction of the baryonic mass in the gas phase.

Given the HI mass and SFR for each galaxy, we also calculate the effective atomic gas depletion timescale, τ_g^{HI}, defined as:

$$\tau_g^{HI} = \frac{M_{HI}}{SFR} \tag{7.3}$$

where τ_g^{HI} is the time, in years, that it would take a galaxy to exhaust its observed reservoir of HI, given its current effective rate of star formation. This is not in any way intended to a precise estimate, as it obviously ignores the effects of feedback, interactions, and the entire star-forming molecular gas component. Rather, it serves as a crude way of indicating how sustainable a galaxy's current rate of star formation is. This provides a way to gauge whether a galaxy is a starburst, fated to consume its available supply of gas in short order; or a stable system undergoing star formation at a rate it can maintain for a long time.

Given the relatively poor angular resolution of HIPASS, care should be taken that using this survey to determine HI masses is not biasing us towards gas-rich objects. Certainly, the median HI mass of the galaxies with 21 cm fluxes from the literature is 3 times lower than those with 21 cm fluxes taken from HIPASS. However, this is to be expected, as the low sensitivity of HIPASS means that it will only detect larger masses of HI. A K-S test indicates that the distribution of f_g^{HI} values derived from the HIPASS and non-HIPASS HI masses are compatible with being drawn from the same underlying distribution ($P(null) = 0.21$); ie, gas-*richness* of our sources with HIPASS gas masses are not systematically different.

The remaining 4 HAPLESS sources fall below the HIPASS detection limit, which typically ranges from $(1.6 \times 10^8 < M_{HI} < 9.8 \times 10^8)\,\mathrm{M}_\odot$ at the distance range of our sample (Haynes et al., 2011). Of the 4 undetected sources, 2 (50%) fall into the curious very blue subset (FUV-$K_S < 3.5$). A $3\,\sigma$ upper limit on the HI mass on the undetected sources was determined using the following prescription from

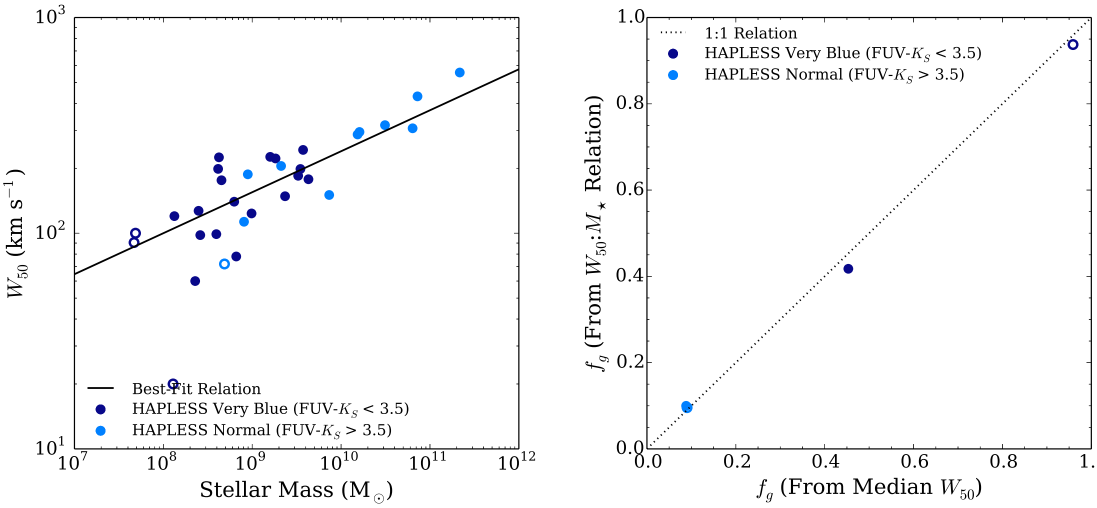

FIGURE 7.2 Using the HI-detected HAPLESS galaxies to inform upper limits for HI-undetected galaxies in our sample. *Left:* The best-fit relationship (solid line) between W_{50} and $M_\star$ for the HI-detected sources. *Right:* Comparison of the upper limit gas fraction (Equation 7.2) estimated using (*y-axis*) the W_{50} : $M_\star$ relationship to derive W_{50} for the undetected sources, and using (*x-axis*) the median W_{50} for the detected sample. The black dotted line shows a 1:1 relationship.

Stevens et al. (2004):

$$M_{HI} \leq 2.36 \times 10^5 D^2 (3\sigma) \sqrt{18} \sqrt{W_{50}} \tag{7.4}$$

where σ is the RMS noise in a single channel (0.013 Jy), D is the distance in Mpc, and the $\sqrt{18}$ term accounts for the number of uncorrelated channels (the velocity resolution of HIPASS is 18 km s^{-1}). Initially, the median value of $W_{50} = 187\,\mathrm{km\,s^{-1}}$ for the HI-detected HAPLESS galaxies was used to estimate the upper limits on the HI mass, gas fraction and depletion timescale for undetected sources (Table 7.1). To check this was a valid assumption, the stellar mass was plotted against W_{50} for the HI-detected galaxies (Figure 7.2, left pane) and a best-fit relationship was derived ($\log_{10} W_{50} = 0.19 \log_{10} M_\star + 0.48$). This relationship was then used to determine a value for W_{50} applicable in the case of each of the *undetected* sources, given their stellar masses; upper limits on the gas mass and the gas fractions were determined using this relation. The resulting upper limits of f_g^{HI} are compared to the values estimated using the median W_{50} parameter in the right pane of Figure 7.2, where the two methods are in excellent agreement, suggesting our use of the median value in Equation 7.4 to calculate upper limits is appropriate. Note that amongst our HI-undetected objects, we are missing both gas-poor-but-massive ($f_g^{HI} < 0.09$, $M_\star > 10^{10}\,\mathrm{M_\odot}$) galaxies, and small galaxies

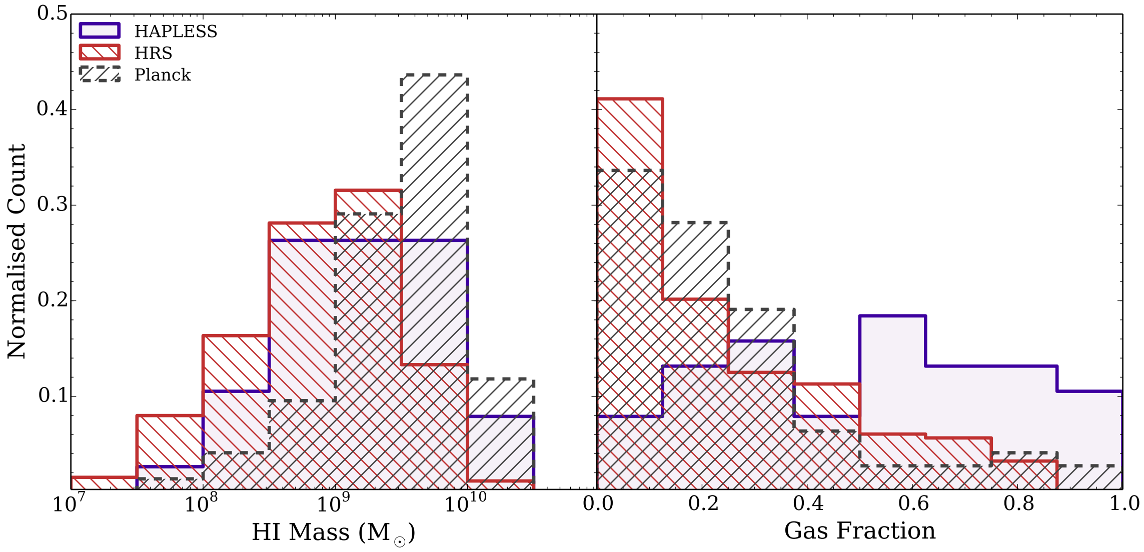

FIGURE 7.3 The atomic gas properties of the HAPLESS, HRS, and *Planck* C13N13 galaxies (note that upper limits are not included). *Left:* The HI mass distribution. *Right:* The gas fraction (Equation 7.2) distribution. The HAPLESS sources have much higher gas fractions than seen in the other FIR surveys of local galaxies.

which may be gas rich ($f_g^{HI} < 0.96$, $M_\star < 10^9\,\mathrm{M}_\odot$). Upper limits on the depletion times were calculated for the 3 HI-undetected sources with SFRs (Chapter 5). Gas fractions and gas depletion times (with upper limits where appropriate) for each source are listed in Table 7.1, with median values in Table 7.2.

7.2 COMPARISON TO OTHER LOCAL SAMPLES

In this section, I compare the gas properties of HAPLESS with those of the galaxies of the HRS and *Planck* C13N13 surveys (Chapter 6). HI masses are available for 263 (81%) of the HRS galaxies, taken from Boselli et al. (2014a), in which they were compiled and homogenised from the literature. HI masses for 220 (94%) of the *Planck* sample were provided by Marcel Clemens (*priv. comm.*), and were derived from the average HI mass quoted for each source in the HyperLeda database[1].

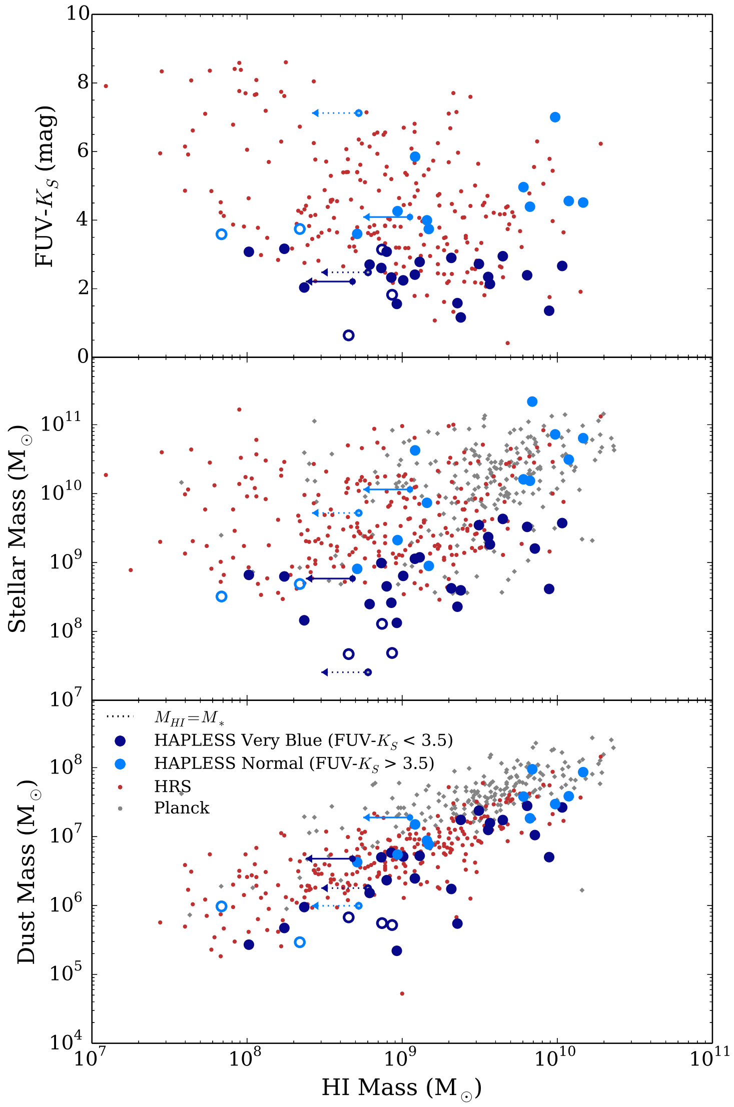

FIGURE 7.4 Scaling relations with M_{HI} for the HAPLESS, HRS and *Planck* C13N13 samples. *From top-to-bottom:* FUV-K_S, stellar mass and dust mass against HI Mass. Hollow circles indicate galaxies not in our luminosity-limited sub-sample. Upper limits are shown for galaxies with no 21 cm detection (dotted in the case of galaxies not in our 250 μm luminosity-limited sub-sample).

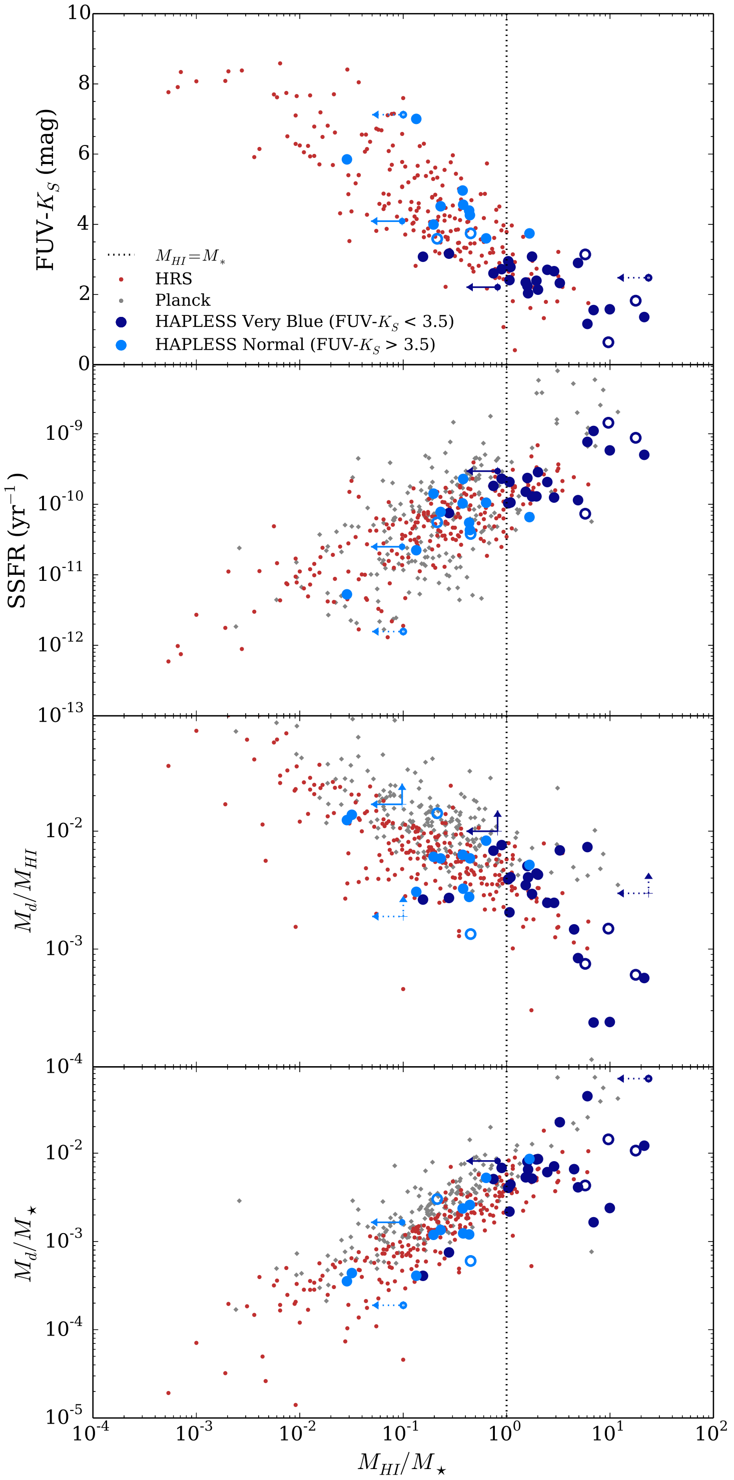

FIGURE 7.5 Trends with $M_{HI}/M_\star$ (ie, gas richness) for the HAPLESS, HRS and *Planck* C13N13 samples. *From top-to-bottom – 1st:* FUV-K_S versus $M_{HI}/M_\star$. Bluer colours are strongly associated with higher gas-to-stellar mass fractions. *2nd:* $M_{HI}/M_\star$ against SSFR. *3rd:* M_d/M_{HI} against $M_{HI}/M_\star$. *4th:* $M_d/M_\star$ against $M_{HI}/M_\star$. The vertical dotted line indicates where $M_{HI} = M_\star$. Hollow circles indicate galaxies not in our luminosity-limited sub-sample. Upper limits are shown for galaxies with no 21 cm detection (dotted in the case of galaxies not in our 250 µm luminosity-limited sub-sample).

7.2.1 SCALING RELATIONS WITH ATOMIC GAS MASS

The left pane of Figure 7.3 shows the HI mass distribution of the three samples; note that only 90% (38) of the HAPLESS galaxies have HI detections. The median HAPLESS HI mass of 1.4×10^9 M$_\odot$ (Table 7.2) is greater than the HRS median of 8.5×10^8 M$_\odot$ – despite the median HAPLESS stellar mass being 4 times *less* than that of the HRS. The bias of the *Planck* C13N13 sample towards more massive objects is clear in its distribution; its median HI mass is 3.6×10^9 M$_\odot$.

The gas fractions (Equation 7.2) of the HAPLESS galaxies, shown in the right pane of Figure 7.3, are extremely high, ranging from 0.03 to 0.96, with a median value of 0.52. Of the HAPLESS galaxies with HI detections, 55% (21) have baryonic masses which are in fact dominated by their atomic gas component. This is without any consideration of the molecular gas component, the inclusion of which would only serve to drive up the gas fractions still further. Equally striking is how greatly the HAPLESS gas fraction distribution differs from those of the other samples. As can be seen in the central pane of Figure 7.3, the HRS and *Planck* C13N13 distributions are strongly skewed towards lower gas fractions (and have medians of 0.18 and 0.17 respectively – Table 7.2); this is in stark contrast to the HAPLESS distribution, which is essentially flat across its entire range. Indeed, a K-S test finds that the gas fractions of the HAPLESS galaxies are compatible with being drawn from a flat underlying distribution ($P(null) = 0.97$).

Figure 7.4 presents the scaling relationships between HI mass and other properties of the galaxies - in every case the curious blue HAPLESS galaxies are offset from the overall trends seen in other *Herschel* local samples. Greater HI masses are associated with bluer FUV-K_S colours; the curious blue HAPLESS galaxies consistently represent the bluest galaxies for a given HI mass. As expected, galaxies with high HI masses tend to have large stellar masses – but the curious blue HAPLESS galaxies trace the edge of this distribution. All of the HAPLESS sources have low stellar masses given their HI mass; their collective offset from the main trend is as much as an order of magnitude. The correlation between dust mass and HI mass in Figure 7.4 is more obvious, as both are measures of the amount of interstellar material in a galaxy, though the bluest HAPLESS galaxies always have less dust for a given atomic gas mass.

The reason for these trends become clearer in Figure 7.5, where we now compare the local volume samples in terms of to their *gas richness*; ie, $M_{HI}/M_{\star}$. This shows that bluer FUV-K_S colour is strongly correlated with higher levels of

---

[1] `http://leda.univ-lyon1.fr/`

TABLE 7.2 Median gas parameters derived for the HAPLESS, HRS, and *Planck* C13N13 samples, along with the medians for the extremely blue subset of HAPLESS (for which FUV-$K_S < 3.5$). Also given are the results from Kolmogorov-Smirnov (K-S) tests, indicating the likelihood of the null hypothesis that two samples are drawn from the same underlying population.

Sample	M_{HI} ($M_\odot$)	M_d / M_{HI}	f_g^{HI}	τ_g^{HI} (Gyr)	M_B ($M_\odot$)
HAPLESS[a]	1.4×10^9	3.9×10^{-3}	0.52	7.89[a]	2.5×10^9
HAPLESS Very Blue[b]	2.1×10^9	2.7×10^{-3}	0.66	10.20[b]	2.3×10^9
HRS[c]	8.5×10^8	6.2×10^{-3}	0.18	4.54[c]	5.5×10^9
Planck C13N13[d]	3.6×10^9	1.2×10^{-2}	0.17	3.16[d]	2.2×10^{10}
K-S (HAPLESS - HRS)	0.03	10^{-2}	10^{-5}	0.03	10^{-2}
K-S (HAPLESS - *Planck*)	10^{-3}	10^{-10}	10^{-7}	10^{-5}	10^{-10}

[a] 90% of the HAPLESS galaxies have HI detections. 79% of the HAPLESS galaxies have both HI detections and SFR estimates.

[b] 93% of the very blue HAPLESS galaxies have HI detections. 78% of the very blue HAPLESS galaxies have both HI detections and SFR estimates.

[c] 81% of the HRS galaxies have HI detections. 72% of the HAPLESS galaxies have both HI detections and SFR estimates.

[d] 94% of the *Planck* C13N13 galaxies have HI detections, all of which also have SFR estimates.

gas richness. We also note that the edges of this distribution appear to be quite sharp; for a given FUV-K_S colour, only a small range of $M_{HI} / M_\star$ seems permissible. The curious blue HAPLESS galaxies (FUV-$K_S < 3.5$) are the most gas-rich of all – of the 25 with HI detections, 20 (80%) contain *a greater mass of atomic hydrogen than stars*, and their median gas fraction is 0.66. Of the remaining 13 HAPLESS galaxies, for which FUV-$K_S > 3.5$, with HI detections, only 1 galaxy contains more HI than stars. It transpires that the FUV-$K_S < 3.5$ colour criterion adopted to identify the curious very blue objects in Section 3.1.1 corresponds to the divide between gas-dominated and star-dominated galaxies. There is also a positive correlation between SSFR and gas-richness (see 2nd pane of Figure 7.5), in agreement with many previous studies (Noeske et al., 2007b; Catinella et al., 2010, 2012; Boselli et al., 2014b).

The dust-to-gas ratio of the samples (M_d / M_{HI}) are compared in the 3rd pane of Figure 7.5. Until now we have described the HAPLESS galaxies, especially the curious blue subset, as being very dust-rich compared to other FIR surveys, in light of their high values of $M_d / M_\star$ (Chapter 6). But Figures 7.4 and 7.5 show that the HAPLESS galaxies are in fact *dust-poor* in terms of their gas mass. The median value (Table 7.2) of M_d/M_{HI} for the HRS and *Planck* C13N13 galaxies are 6.2×10^{-3} and 1.2×10^{-2} (ie, gas-to-dust ratios of ≈ 160 and ≈ 90), whilst the median for the HAPLESS galaxies is 3.9×10^{-3} (gas-to-dust ≈ 260). Furthermore, the median M_d/M_{HI} of the curious blue subset is only 2.7×10^{-3} (gas-to-dust ≈ 370) – ie, dust makes up less than 0.3% of the ISM in these galaxies (compared oft-quoted value of 1% for typical spirals). Therefore, if we assume that the dust traces the dense molecular ISM (Smith et al., 2012b; Rowlands et al., 2014a), this would suggest that the molecular gas component of the HAPLESS galaxies makes up only a small fraction of their total gas reservoir ($<1\%$, an order of magnitude lower than in typical spirals). Alternatively, these galaxies may have particularly large ratios of M_{H2}/M_d. Deep molecular gas maps are required to test if there really is a difference in the molecular gas, atomic gas, and dust ratios in the HAPLESS systems. This is beyond the scope of this work, but will be the subject of follow-up studies.

The 4th pane of Figure 7.5 demonstrates that HAPLESS has some of the highest $M_d/M_\star$ ratios in the local universe, *and* consistently exhibits greater gas-richness ($M_{HI}/M_\star$) for a given level of dust-richness ($M_d/M_\star$).

7.2.2 ATOMIC GAS DEPLETION TIMESCALES

The high SSFRs (Figure 6.11) and low stellar masses (Figure 6.2) of the HAPLESS galaxies (as discussed in Chapter 6) suggest these are either galaxies going through an intense but unsustainable phase of heightened star formation, or that they have large gas reservoirs from which to form stars over a long period of time.

The distribution of atomic gas depletion times (Equation 7.3) of the HAPLESS, HRS and *Planck* C13N13 samples are displayed in Figure 7.6. Surprisingly, despite having the highest average SSFR, HAPLESS also has the *longest* median gas depletion time (Table 7.2), at 7.9 Gyr. The HRS and *Planck* C13N13 medians are considerably lower, at 4.5 and 3.2 Gyr respectively. This would strongly imply that we are not observing the HAPLESS galaxies during a short-lived and unsustainable phase of increased star-forming activity – despite their high SSFRs. This is corroborated by the upper pane of Figure 7.7; there is no correlation between SSFR and atomic gas depletion amongst HAPLESS and the HRS, whilst the galaxies of *Planck* C13N13 with particularly high SSFRs potentially show a weak tendency to have shorter depletion timescales. Certainly, the curious very blue HAPLESS galaxies show a strong tendency to cluster in the region representing high values for both parameters. A high SSFR cannot be used as an indicator of unsustainable star formation, as noted by previous authors (Noeske et al., 2007a; Schiminovich

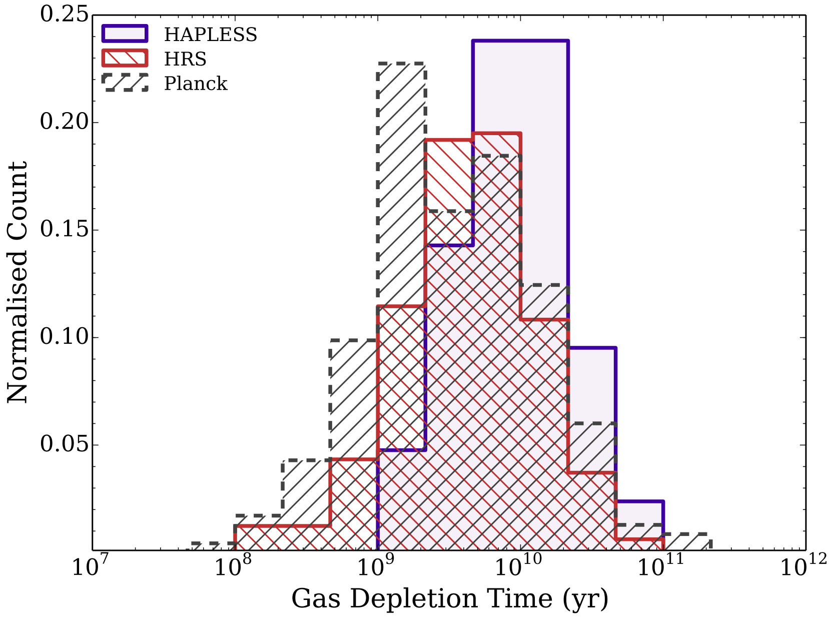

FIGURE 7.6 The atomic gas depletion time distributions for the HAPLESS, HRS, and *Planck* C13N13 galaxies. HAPLESS has the largest typical depletion timescales compared to the other FIR local-volume surveys.

et al., 2010; Bauer et al., 2013).

Rowlands et al. (2014a) use dust as a tracer of the molecular ISM to examine the variation of the molecular Star Formation Efficiency (SFE$_m$) with stellar mass, finding it roughly constant below $10^{10}\,M_\odot$. Schiminovich et al. (2010) perform a similar analysis using data from the GALEX Arecibo SDSS Survey (GASS, Catinella et al., 2008, a survey dedicated to study the gas atomic gas properties of galaxies), but instead consider the HI Star Formation Efficiency, defined as SFE$_{HI}$ $= SFR/M_{HI}$ (ie, what fraction of the atomic gas reservoir of a galaxy is being converted into stars per unit time). SFR/M_{HI} is simply the inverse of the gas depletion time τ_g^{HI}. They find that SFE$_{HI}$ does not vary with stellar mass. However, GASS only samples massive galaxies, with $M_\star > 10^{10}\,M_\odot$. We are in a position to test whether the SFE$_{HI}$ stays invariant with stellar mass down to stellar masses two orders of magnitude lower than probed by GASS, plotted in Figure 7.7. There is a lot of scatter in SFR/M_{HI} for the FIR surveys compared in this work, although when binned, it is consistent with a constant SFR/M_{HI} of $1 \times 10^{-10}\,\mathrm{yr}^{-1}$ (corresponding to a gas depletion timescale of 10 Gyr) within the uncertainty. The majority of the curious blue HAPLESS sources sit below this level, in line with their longer depletion times (Figure 7.6). Nonetheless, SFE$_{HI}$ remains broadly constant down to the lowest stellar masses we probe.

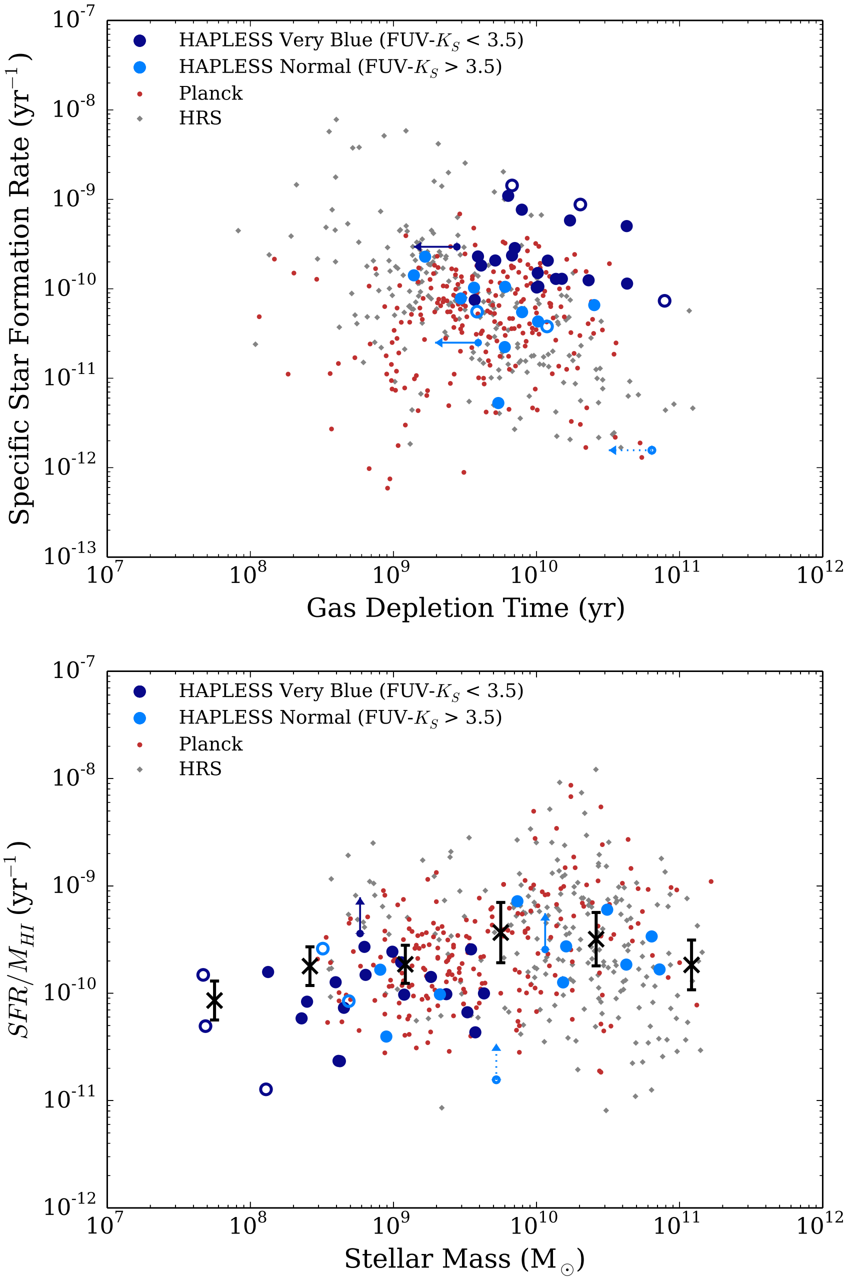

FIGURE 7.7 *Upper:* Plot of SSFR against atomic gas depletion time. Very little correlation is in evidence; a high SSFR generally does not indicate that a galaxy is undergoing an unsustainable phase of star formation. *Lower:* SFR/M_{HI} against the stellar mass for the HAPLESS, HRS and *Planck* C13N13 samples. Hollow circles indicate galaxies not in our luminosity-limited sub-sample. HIPASS 3σ upper limits (determined according to Equation 7.4) are shown for galaxies with no 21 cm detection (dotted in the case of galaxies not in our 250 µm luminosity-limited sub-sample). Black points show the average values in bins of 0.5 dex with the standard error on the mean of each interval shown by the error bars.)

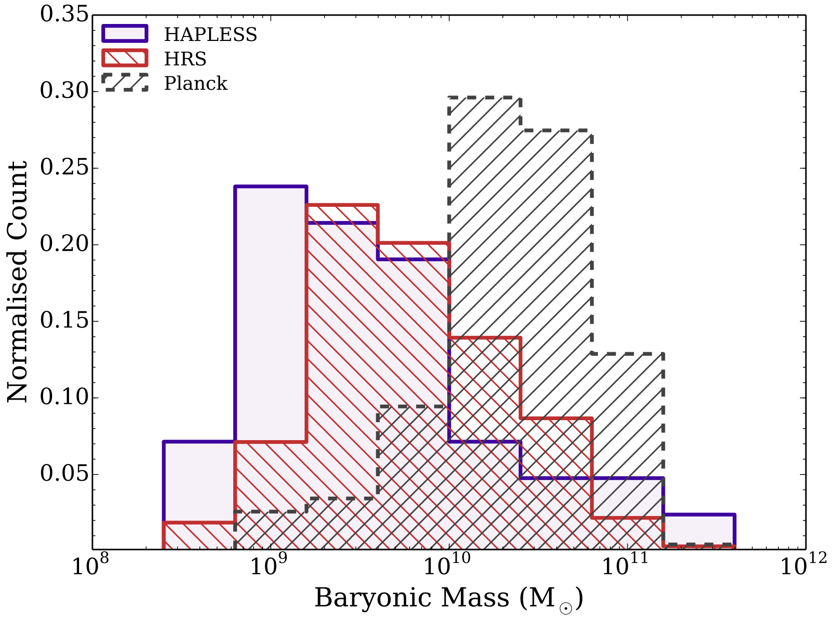

FIGURE 7.8 The baryonic mass distributions of the HAPLESS, HRS, and *Planck* C13N13 samples. Baryonic mass was calculated using Equation 7.5, for all galaxies that have values for both stellar and HI mass.

The HAPLESS galaxies have both the highest SSFRs (Figure 6.11) and longest gas depletion times (Figure 7.6); this is particularly true of the curious blue HAPLESS galaxies, which exhibit a median depletion time of 10.20 Gyrs – double that of HRS, and three times that of *Planck* C13N13. Indeed, of the 21 curious blue HAPLESS galaxies with estimates for τ_g^{HI}, 7 (33%) have values in excess of the Hubble time. This suggests that in contrast to their high SSFRs representing a brief phase of increased star formation, these systems are engaged in star formation activity which can be sustained over the long term. The HAPLESS sources appear to have converted less of their gas into stars, and could be in an immature phase of evolution. Previous studies of low-stellar-mass, high-SSFR galaxies have concluded likewise (Noeske et al., 2007a), and we will investigate this further in Section 7.3.

7.2.3 BARYONIC MASS SCALING RELATIONSHIPS

The use of stellar mass to represent 'specific' relations such as dust-richness and SSFR may not be appropriate for galaxies where stars make up only a small fraction of the total baryonic mass. To provide a more objective frame of reference, we consider instead the baryonic mass:

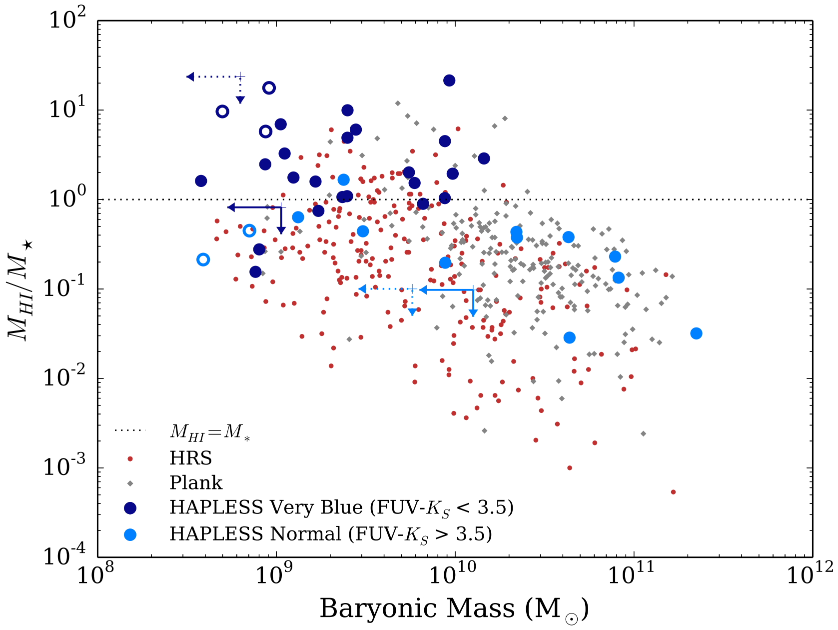

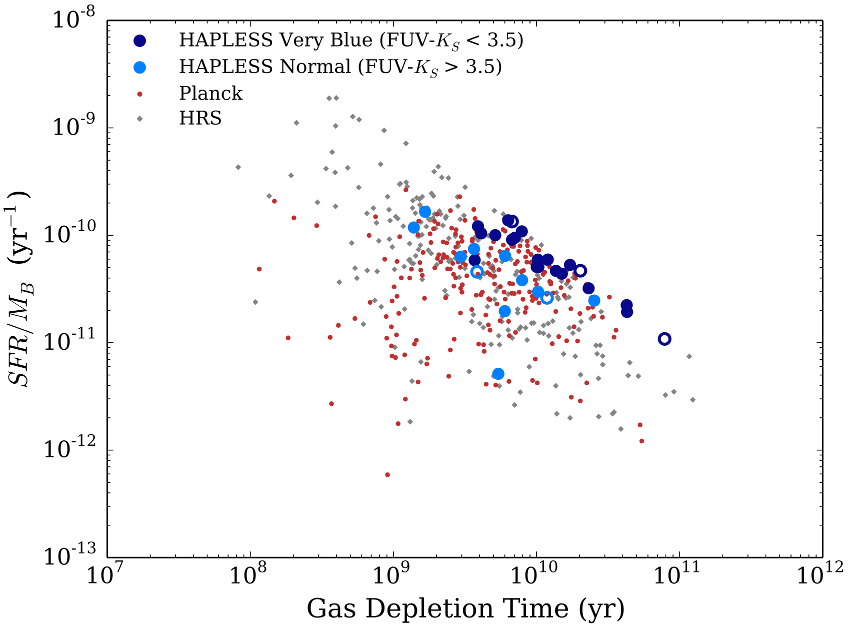

FIGURE 7.9 *Upper:* $M_{HI}/M_\star$ against the baryonic mass of the HAPLESS, HRS and *Planck* C13N13 samples. The dotted line indicates $M_{HI}/M_\star = 1$. *Lower:SFR*/M_B against atomic gas depletion times for the HAPLESS, HRS, and *Planck* C13N13 galaxies. Hollow circles indicate galaxies not in our luminosity-limited sub-sample. HIPASS 3σ upper limits (determined according to Equation 7.4) are shown for galaxies with no 21 cm detection (dotted in the case of galaxies not in our 250 µm luminosity-limited sub-sample).

$$M_B = M_\star + M_{HI} \tag{7.5}$$

where we continue to ignore the contribution of the molecular gas component so that M_B is a lower limit. The baryonic mass distributions for all three samples are shown in Figure 7.8. Whilst HAPLESS and the HRS have very different distributions of stellar mass and HI mass (Figures 6.2 and 7.3), these differences are greatly reduced once we consider baryonic mass.

Figure 7.9 (upper pane) compares baryonic mass to $M_{HI}/M_\star$ for the HAPLESS, HRS, and *Planck* C13N13 galaxies. Across all three samples, we see a trend where galaxies with large baryonic masses tend to have depleted more of their gas than smaller objects (this is an aspect of 'downsizing', reviewed in Chapter 1). As the HRS is essentially a stellar-mass-selected sample, it is biased towards objects that have already converted a large fraction of their gas into stars. The high flux limit of the *Planck* C13N13 sample means that is biased towards more massive, hence more gas-poor galaxies – but selecting ISM-rich examples of these massive systems. Our HAPLESS sample is strongly biased towards ISM-rich objects in general – ie, a blind submm survey consistently selects the most gas-rich galaxies of a given baryonic mass.

Comparing the atomic gas depletion time to SFR/M_B (upper pane of Figure 7.9) instead of SFR/M_{HI} (lower pane of Figure 7.7), we see that galaxies with higher SFRs relative to their baryonic mass tend to deplete their gas more rapidly. The trend exhibits a sharp cutoff traced by the curious blue HAPLESS galaxies, arising from the fact that these galaxies are extraordinarily gas rich; as $f_g^{HI} \rightarrow 1$, $SFR/M_B \rightarrow SFR/M_{HI}$, which is simply the inverse of τ_g^{HI}. This further suggests that the high SSFRs and long atomic gas depletion timescales of the HAPLESS galaxies arise from the fact they are relatively immature, and yet to build up much stellar mass. This will be investigated further in Section 7.3 .

7.3 THE EVOLUTION OF GAS AND DUST IN THE LOCAL UNIVERSE

In this Section, we will attempt to explain the dust masses and high gas fractions of the HAPLESS sources using a chemical and dust evolution model to follow the build up of heavy elements and dust over time as gas is converted into stars. We assume a closed box model as the optimistic case for the build up of dust (that is, we do not consider inflows and outflows of gas) and instead simply follow the gas (and gas fraction f_g^{HI}) as it is converted into stars using a star formation rate $\psi(t)$ and an IMF $\phi(m)$ (using the Chabrier, 2003 IMF consistent with Chapter 5).

7.3.1 THE CHEMICAL MODEL

The equations we use to follow the evolution of gas and dust in the HAPLESS galaxies are:

$$M_{tot} = M_g + M_\star, \tag{7.6}$$

where M_g is the gas mass and $M_\star$ is the stellar mass. The gas mass evolution with time is described by:

$$\frac{dM_g}{dt} = -\psi(t) + e(t). \tag{7.7}$$

where $\psi(t)$ is the rate at which gas is depleted by the SFR, and $e(t)$ is the rate at which it is returned as stars die.

Assuming that mass loss occurs suddenly at the end of stellar evolution at time $\tau_m(m)$ (Schaller et al., 1992), the ejected mass, $e(t)$, from stars is:

$$e(t) = \int_{m_{\tau_m}}^{m_U} [m - m_R(m)]\, \psi(t - \tau_m)\phi(m)dm \tag{7.8}$$

where $m_{R(m)}$ (from Prantzos et al., 1993) is the remnant mass and m_{τ_m} is the mass of a star whose age is that of a system where a star formed at $(t - \tau_m)$ has died at τ_m. The evolution over time of the mass of metals in the ISM, M_Z, is described by:

$$\frac{d(M_Z)}{dt} = -Z(t)\psi(t) + e_z(t) \tag{7.9}$$

where Z is the fraction of heavy elements by mass in the gas phase. The mass of heavy elements ejected by stars at the end of their lives is denoted by $e_{z(t)}$:

$$\begin{aligned} e_z(t) \;&=\; \int_{m_{\tau_m}}^{m_U} \left([m - m_R(m)]\, Z(t - \tau_m) + mp_z\right) \\ &\quad\times \psi(t - \tau_m)\phi(m)dm \end{aligned} \tag{7.10}$$

Yields from stars (mp_z) are taken from the theoretical models of Maeder (1992) and van den Hoek & Groenewegen (1997). Similarly, the evolution of the mass of dust with time is described by:

$$
\begin{aligned}
\frac{dM_d}{dt} \quad = \quad & \int_{m_{\tau_m}}^{m_U} \left([m - m_R(m)] \, Z(t-\tau_m)\delta_{old} + mp_z\delta_{new} \right) \\
& \times \psi(t-\tau_m)\phi(m)dm - (M_d/M_g)\psi(t)
\end{aligned}
\tag{7.11}
$$

where dust is built up from two sources: the fraction of the heavy elements that are recycled through star formation and ejected in stellar winds (δ_{old}), and the fraction of new elements freshly synthesised in stars and ejected in both supernovae and stellar winds (δ_{new}). The final term describes dust removed from the interstellar medium due to astration. More details of the model can be found in Morgan & Edmunds (2003) and Rowlands et al. (2014b) (which are in turn adapted from the prescriptions of Tinsley, 1980).

We follow Rowlands et al. (2014b) and assume two possible scenarios for dust formation by stars: firstly, where dust is only contributed via the stellar winds of evolved Low-to-Intermediate Mass Stars (LIMS); and secondly, where dust is contributed via both LIMS and SuperNovae (SNe). Whether the majority of dust in galaxies is contributed by LIMS or SNe is a long-standing question (see the review in Chapter 1, and also Gomez, 2013). We use the dust yields from LIMS consistent with FIR observations (Ladjal et al., 2010) and theoretical models (Ventura et al., 2012). For simplicity, we assume supernova dust yields from Todini & Ferrara (2001), which are consistent with the upper range of dust masses observed in historical SN remnants including our recent results (discussed in Chapter 2) based on observations of the Crab Nebula (Gomez et al., 2012b, see also Dunne et al., 2003, 2009; Rho et al., 2009; Barlow et al., 2010; Matsuura et al., 2011; Indebetouw et al., 2014). As also discussed in Chapter 2, Type-Ia SNe are assumed to be negligible contributors to the dust budget (Morgan et al., 2003; Gomez et al., 2009, 2012a). Note that we have no dust destruction in our model as we want to follow the maximum build up of dust mass at a given time (see Rowlands et al., 2014b).

7.3.2 FIDUCIAL STAR FORMATION HISTORIES

An important parameter of the model is the SFR at a given time. To model our HAPLESS sources, we tested four fiducial Star Formation Histories (SFHs), shown in Figure 7.10 and listed in Table 7.3. The range in the SFHs are consistent with the range in observed parameters for the HAPLESS sample (Chapter 5). In brief, these SFHs are *(i)* SFH A - consistent with the Milky Way (Yin et al., 2009); *(ii)* SFH B - an exponentially declining low SFR and a short burst at $\sim 1\,\mathrm{Gyr}$; *(iii)*

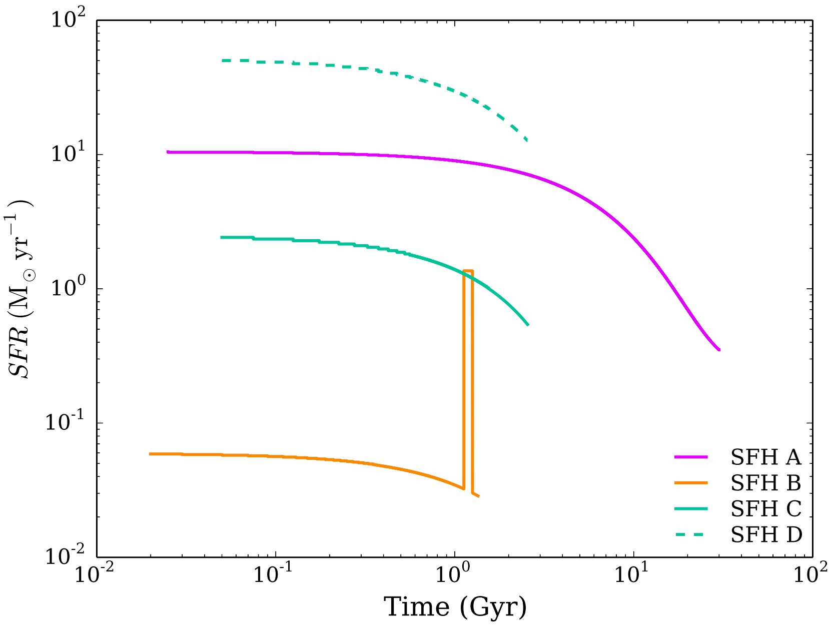

FIGURE 7.10 The star formation histories used to model the HAPLESS galaxies, see Table 7.3. SFH A follows the evolution of the MW (pink, solid track). SFH B (orange, solid line) has initial SFR 0.058 $M_\odot$ yr^{-1} with a burst at 1 Gyr. SFH C (turquoise) has initial SFR 2.4 $M_\odot$ yr^{-1} and exponentially declines until truncated at 2.5 Gyr. SFR D (turquoise dashed) is a scaled version of SFR C ($\times$20).

SFH C - a higher SF exponentially declining rate, and *(iv)* SFH D - a scaled-up version of SFR C (increased by a factor of 20). The latter SFH is designed to illustrate the evolution of a low-mass system which is consuming its gas more rapidly. Using these fiducial SFHs, we follow the evolution of the dust mass (relative to the baryonic mass) as the gas fraction decreases. The initial gas mass is set to $M_g(0) = 4 \times 10^{10}\,M_\odot$ for the Milky Way, and for the other models (Table 7.3) we selected a range of observed gas masses, and used the observed gas fractions to infer the initial gas mass. Note that these fiducial SFHs are consistent with the observed SFRs and gas fractions of the HAPLESS galaxies (truncated at time $t_{\rm end}$, Table 7.3) and are also compatible with the range of SFHs derived from complex multi-wavelength modelling of their SEDs using the MAGPHYS prescription (De Vis et al., *in prep.*).

7.3.3 IMMATURE LOCAL GALAXIES IN H-ATLAS

The model results are shown in Figure 7.11. First, we compare the dust evolution for a galaxy similar to the MW (SFH A) assuming dust contributed from

TABLE 7.3 The fiducial star formation histories (A–D) and initial gas masses used in this work to model the HAPLESS galaxies. SFH A is from Yin et al., 2009. Also given is the time ($t_{\rm end}$) where the SFH is truncated to match the present SFRs and gas fractions of the HAPLESS sample.

SFH	$g(0)$ (M$_\odot$)	$\psi(0)$ (M$_\odot$ yr^{-1})	Burst? (Y/N)	$t_{\rm end}$ (Gyr)	$\psi(t_{\rm end})$ (M$_\odot$ yr^{-1})	$f_g(t_{\rm end})$
A (MW)	4.0×10^{10}	10	N	20	0.7	0.11
B	3.0×10^{9}	0.06	Y	1.35	0.029	0.95
C	5.5×10^{9}	2.5	N	2.8	0.5	0.64
D	5.5×10^{9}	49	N	0.1	48	0.31

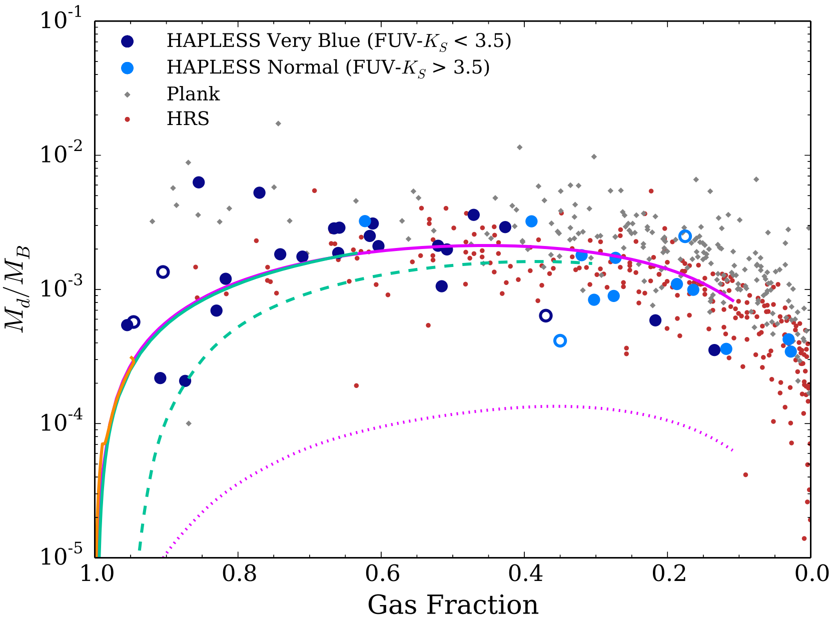

FIGURE 7.11 M_B/M_d against gas fraction for the three samples. Note that the x-axis of this plot goes from a gas fraction of 1 to 0, and is therefore a proxy for the time since the system started forming stars. The curves show the results from the chemical evolution model for different SFHs (Table 7.3) including SFR A – consistent with the Milky Way (purple); SFR B – exponentially declining SFR with low initial SFR and a burst (orange); SFH C – exponentially declining rate, but higher initial SFR (tourquoise); and finally SFR D – a scaled version of SFR C (tourquoise dashed). The dotted purple line is the track from SFR A (MW) with dust from LIMS only.

LIMS only (dotted pink line). Second, we include dust from LIMS and SNe in combination (solid pink line) and see that the levels of M_d/M_B for LIMS dust never reach the high levels observed in the HAPLESS, HRS and *Planck* C13N13 samples. This is true for all the SFHs modeled here and is in line with results from other studies, including Morgan & Edmunds (2003), Matsuura et al. (2009), Dunne et al. (2011), Gall et al. (2011), and Rowlands et al. (2014b). With dust from both SNe and LIMS (solid and dashed lines), SFH models A–C all sit on the same evolutionary track in Figure 7.11, due to the models with lower star formation rates (SFHs B & C) than the MW (SFH A) also having lower initial gas masses; ie the models lie on the same constant SFR/M_{HI} tracks. These are in good agreement with the HAPLESS galaxies (at high gas fractions) and the HRS galaxies (at lower gas fractions). The *Planck* C13N13 galaxies (clustered towards lower gas fractions) have somewhat elevated M_d/M_B compared to the models presented here. When we multiply SFH C by a factor of 20 (SFH D) but keep the initial gas mass the same, the evolutionary path (dashed) is offset, due to the available gas reservoir being consumed faster. The dust mass is significantly reduced due to the higher level of astration.

The evolutionary path suggested in Figure 7.11 indicates that a galaxy's dust mass will peak when its gas fraction falls to ~ 0.5 (as predicted by Eales & Edmunds, 1996, 1997). Therefore this is the stage of a galaxy's development when it is most likely to meet the inclusion threshold of a dust-selected sample such as HAPLESS – the median gas fraction of which is indeed 0.5. The stellar-mass selection of the HRS means that it is biased towards galaxies where most of the gas has already been converted into stars, hence it severely under-samples the gas-rich portion of this evolutionary path. Similarly, the tendancy of the *Planck* C13N13 sample to mainly select more massive galaxies means that it too is biased towards systems where most of the gas has already been depleted (see also Figure 7.9). A blind dust survey appears to an exceptionally efficient way to select galaxies across the entire range of gas fractions, crucially including systems which are less far down their evolutionary path – ie, are immature. Such systems are dramatically undersampled by other submm surveys of the local volume. Thus we are selecting galaxies at a much earlier stage in their evolution, and this is the reason for their low stellar masses, dust-richness with respect to $M_\star$ (near their peak M_d), and low ratios of dust-to-atomic-gas ratios.

7.4 CONCLUSION

In this chapter, I present the gas properties of HAPLESS, a dust-selected sample of nearby galaxies, drawn from the blind *H*-ATLAS survey in the distance range $15 < D < 46$. We found that the HAPLESS galaxies are extraordinarily gas rich. Of the HAPLESS galaxies, 21 (being 50% of the total sample, and 55% of those with HI detections) have atomic gas masses greater than or equivalent to their stellar mass – the median sample gas fraction is 0.52. Gas fractions > 0.8 are exhibited by 19% of the sample (being 21% of those with HI detections). The median gas-to-dust ratio of the HAPLESS sample is ≈ 260, 2–3 times larger than in other local FIR surveys. The median atomic gas depletion timescale is 7.9 Gyr, also significantly greater than seen in other local volume samples.

The subset of very blue HAPLESS galaxies (FUV-$K_S < 3.5$) has a median gas fraction of 0.66, gas-to-dust ratio of ≈ 370, and atomic gas depletion timescale of 10.2 Gyr – all 3–5 times greater than seen in other dust surveys of the local volume.

The large atomic gas depletion timescales (despite their high SSFRs) and low stellar masses of these very blue galaxies suggests that they have not yet consumed much of their atomic gas reservoirs, and can continue forming stars for a long time. Their atomic gas star formation efficiency is consistent with that of more typical galaxies, suggesting that they are not forming stars in a fundamentally different manner.

A chemical and dust evolution model confirms that these galaxies are not forming their stars in a different way to galaxies at higher stellar masses, but that they are simply in an early stage of converting their gas into stars. Gas inflows are not needed to explain their high gas fractions. A dust-selected survey such as *H*-ATLAS is a particularly efficient way of identifying young galaxies of this kind. The bluest galaxies appear to be the most immature, they should therefore provide valuable insights into the chemical evolution of young galaxies.

CHAPTER 8
CONCLUSION

> *''Tis much better to do a little with certainty, and leave the rest for others that come after you, than to explain all things by conjecture without making sure of any thing.'*
>
> SIR ISAAC NEWTON

IN this thesis, I have used multiwavelength observations, centred around the unique FIR and submm window provided by *Herschel*, to study the origins and evolution of dust in the local Universe. This has involved two distinct research projects. Firstly, using *Herschel* observations of three recent Milky Way supernovæ to establish the contribution made by supernovæ to the dust budget of galaxies; this is recounted in Chapter 2. Secondly, using *Herschel* to study a volume-limited sample of nearby galaxies selected solely on the basis of the emission from their dust; this work is described in Chapters 3, 4, 5, 6, and 7.

8.1 KEY RESULTS I – DUST IN SUPERNOVA REMNANTS

Herschel observations of the remnants of Kepler's and Tycho's supernovæ were used to look for evidence of dust created in the explosions. These remnants are the results of Type-Ia events (SN1604 and SN1572), and were observed as part of the MESS survey. In both cases, previous works found a very low mass of luminous hot dust; *Herschel* allowed us to search for the existence of any previous missed cold dust. The *Herschel* observations of both remnants are dominated by unrelated galactic cirrus along the line of sight, and show no indication of any cold dust associated with the supernovæ. Dust temperature maps, created by means of resolved SED fitting, traced where the expanding remnants are interacting with the surrounding material (ISM in the case of Tycho, and CSM in the case of Kepler), but showed no evidence of features corresponding to newly-created supernova dust. This suggests that Type-Ia supernovæ do not make a significant contribution to the galactic dust budget.

The Crab Nebula, the result of the Type-II supernova SN1054, was also observed by *Herschel* as part of the MESS survey. Synchrotron radiation accounts for a large fraction of the total emission from the Crab, to the extent that it actually dominates in much of the submm. Modelling the flux in the synchrotron-dominated 3.6–8 µm *Spitzer* and 550–10,000 µm *Planck* bands indicated that the synchrotron emission is well-described by a power law , with a spectral index of $\alpha = 0.4121 \pm 0.0041$, and an anchor flux of $S_0 = 1,434 \pm 62$ Jy at a wavelength of 300 mm. With the synchrotron component subtracted (and the contribution due to line emission accounted for using the available ISO, *Spitzer*, and *Herschel* spectroscopy), it was possible to disentangle any flux due to thermal dust emission. The Crab's dust SED was well-fit by a one-greybody model, with $T_d = 63.1\,\mathrm{K}$, dust mass of $M_d = 0.21\,\mathrm{M}_\odot$, and $\beta = 0.61$. I created the first ever map of the distribution of cold dust in a supernova remnant by means of a resolved component separation, which revealed that the dust is found primarily in the filamentary ejecta. Combined with the minimal amount of interstellar material in the region of the Crab Nebula, this means that we can be confident that this dust was manufactured by the supernova. The location of the dust in the dense filament regions, and the remnant's lack of a reverse shock, strongly suggests that this dust will survive in the long term, and be injected into the galactic dust budget. This is the first – and to date, only – detection of dust in a supernova remnant for which this can be said.

8.2 KEY RESULTS II – A BLIND SURVEY OF THE LOCAL DUSTY UNIVERSE

I used the *H*-ATLAS survey to assemble HAPLESS: the *Herschel*-ATLAS Phase-1 Limited Extent Spatial Sample – a blind, volume-limited, dust-selected sample of nearby galaxies. Noticeable amongst HAPLESS are a subset of curious very blue galaxies. Often irregular and/or flocculent in morphology, with extremely blue UV-NIR colours, these galaxies appear to be prominent in the local dusty universe, making up 64% of the HAPLESS sample. I found a colour criterion of FUV-$K_S < 3.5$ to be an effective way of identifying these intriguing systems.

Existing multiwavelength photometry of *H*-ATLAS sources was provided by GAMA, whose photometric pipeline was designed primarily for more distant galaxies, of much smaller angular size than the very nearby objects found in HAPLESS. Because of this, much of the GAMA photometry of the HAPLESS sample was found to be unusable. I therefore designed, created, and tested a purpose-built photometric pipeline – CAAPR: Chris' Adequate Aperture Photometry Routine. The emphasis for CAAPR was that it not only produce reliable fluxes, but also reliable uncertainties. The photometry conducted using CAAPR demonstrated that the GAMA pipeline severely underestimated the brightness of many of the HAPLESS galaxies. With CAAPR, the average increase in observed flux is by a factor of 1.6 in the FUV and 1.4 in *r*-band, relative to the GAMA photometry.

8.2.1 A GREAT DIVERSITY OF DUSTY GALAXIES REVEALED

The dust in the HAPLESS galaxies appears to be very cold; two-component modified blackbody SED fitting indicates that their cold dust temperatures range from 9.2 to 25.6 K, with a median temperature of 14.6 K. Their dust masses range from 2.2×10^5 to $9.5 \times 10^7\,M_\odot$, with a median dust mass of $5.3 \times 10^6\,M_\odot$. The HAPLESS galaxies tend to have relatively low stellar masses, ranging from 5.6×10^7 to $2.2 \times 10^{11}\,M_\odot$, with a median stellar mass of $9.8 \times 10^8\,M_\odot$. The SFRs of the HAPLESS galaxies range from 0.01 to $7.12\,M_\odot yr^{-1}$, with a median SFR of $0.18\,M_\odot yr^{-1}$; given their low stellar masses, this corresponds to generally large SSFRs, ranging from 1.6×10^{-12} to $1.4 \times 10^{-9}\,yr^{-1}$, with a median SSFR of $1.3 \times 10^{-10}\,yr^{-1}$. The curious very blue HAPLESS galaxies, whilst accounting for only 6% of the stellar mass in our sample, contain over 35% of the dust mass.

In comparison to other submm surveys of dust in local galaxies, the HAPLESS systems show a strong propensity towards very late morphological types and extremely blue FUV-K_S colours. They are also exceptionally dust rich, a median $M_d/M_\star$ greater by a factor of 1.8–3.7 that that seen in other surveys. We find that the more dust-rich a galaxy (as defined by $M_d/M_\star$), the *smaller* the fraction of its UV luminosity that suffers dust absorption – this effect is observed to be particularly dramatic in the case of the curious very blue objects. Either the emissivity or geometry of the dust in these systems must be highly unusual. The 'leakiness' of the dust in these galaxies appears to be the cause of their low dust temperatures. We find that the coldest dust seen in the local universe is consistently associated with galaxies that have lots of star formation relative to their older stellar population; nonetheless, both the amount of star formation and evolved stars in a galaxy are found to be strongly correlated with the cold dust temperature. The dust mass volume density of the local universe from the 250 µm luminosity limited portion of our sample is $(3.7 \pm 0.7) \times 10^5\,M_\odot\,\mathrm{Mpc}^{-3}$, which is higher than for any local universe dust survey – however, the HAPLESS 250 µm luminosity function is in good agreement with surveys of far larger volumes, suggesting that we do *not* sample an over-dense region of space. Comparing our flux limit to the dust mass functions of previous studies suggests that HAPLESS misses up to 8% of the dust in the local volume. The preponderance of very cold dust temperatures found in HAPLESS suggests that such objects are commonplace, and have been overlooked by previous surveys due to their relatively low luminosities – leading them to underestimate the dust mass volume density of the local Universe.

8.2.2 IMMATURE GALAXIES IN THE LOCAL UNIVERSE

The HAPLESS galaxies are extraordinarily gas rich. Of the HAPLESS galaxies with HI detections, 58% have atomic gas masses greater than or equivalent to their stellar mass, and 19% of the entire sample have gas fractions >0.8 – the median HAPLESS gas fraction is 0.52. The median gas-to-dust ratio of HAPLESS is ≈ 260, 2–3 times larger than in other local FIR surveys, whilst the subset of very blue HAPLESS galaxies (FUV-$K_S < 3.5$) has a median gas fraction of 0.66, gas-to-dust ratio of ≈ 370, and atomic gas depletion timescale of 10 Gyr – all 3–5 times greater than seen in other dust surveys of the local volume. A chemical and dust evolution model indicates that these in an early stage of converting their gas into stars. A dust-selected survey such as *H*-ATLAS is a particularly efficient way of identifying young galaxies of this kind. The bluest galaxies appear to be the most immature, and should therefore provide valuable insights into the chemical evolution of young galaxies.

8.3 FUTURE WORK

8.3.1 FURTHER SEARCHES FOR DUST IN TYPE-IA SUPERNOVÆ

Regarding the manufacture of dust in supernovæ, the most severe limits on our understanding are imposed by the paucity of recent supernovæ in the Milky Way. But in lieu of waiting for the next one to occur, it would be informative to perform more thorough searches for manufactured dust in the Type-Ia remnants, especially in light of the predicted (Dwek, 1998), but seemingly missing, iron dust component. As detailed in Chapter 2, the available molecular line observations (CO) proved to be limited tracers of the foreground galactic cirrus in the regions of Kepler's and Tycho's SNRs; particularly in the case of Kepler's. Observations with a wider range of molecular lines and species (particularly at lower energies, given the cold cirrus temperatures suggested by the dust temperature mapping), at higher resolution and sensitivity, with a wider field of view for calibration, might permit practical subtraction of the foreground dust component, hence revealing faint emission associated with manufactured supernova dust.

Perhaps more useful would be observations at longer wavelengths; highly iron-rich dust, predicted by some to be produced by Type-Ia supernovae (Dwek, 2004), could well have different properties to the usual carbonaceous and silicate dust species (Gomez et al., 2005). Should it be a particularly efficient emitter, it would have a low equilibrium temperature, resulting in a faint SED that would peak at longer wavelengths; this could have been missed by *Herschel* and other submm observatories. The new generation of mm-range instruments, such as ALMA (the Atacama Large Millimeter Array, Wootten & Thompson, 2009) and NIKA2 (the New Instrument of KID Arrays 2, Monfardini et al., 2014), provide the sensitivity to probe at the longer wavelengths where such dust could emit – wavelengths where the cirrus contribution would be far less severe, and where the synchrotron component could still be precisely accounted for.

8.3.2 TOWARDS A GREATER UNDERSTANDING OF IMMATURE GALAXIES IN THE LOCAL UNIVERSE

Much of the work in Chapters 3, 4, 5, 6, and 7 has been concerned with the curious very blue HAPLESS galaxies. These gas-rich immature local galaxies are of great interest, and a follow-up observational campaign is already in progress.

The very blue HAPLESS galaxies have extremely high gas-to-dust (M_{HI}/M_d) with a median ratio of ≈ 370, 3–5 times greater than seen in that other FIR and submm surveys of the local volume. Given that dust is generally expected to be a good tracer of the molecular ISM, this would lead us to assume that the very blue HAPLESS galaxies are relatively poor in molecular gas. Initial observations of the ^{12}CO(2-1) line were made for a small pilot sample consisting of UGC 9215, NGC 5496, and NGC 5584 (HAPLESS 3, 7 and 14), with EMIR (Eight MIxed Reciever) on the IRAM (Institut de Radioastronomie Millimétrique) 30 m telescope.

Preliminary inspection of this data suggests that not only are these galaxies poor in molecular gas, they are an order of magnitude poorer even than suggested by their high gas-to-dust ratios.

Given that molecular gas is the raw material required for star formation, it is hard to understand how they are able to maintain such high star formation rates, if they indeed are so poor in molecular gas. One possibility is that X_{CO}, the converstion factor used to scale from CO to H_2, is particularly large in these galaxies. We currently lack metallicity data for HAPLESS, other than estimates from SDSS spectroscopy of the central $3''$ of each galaxy; whilst these suggest unremarkable metallicities of $0.85\,Z_{\odot}$, such a small region will not be representative of the galaxy at large. Such metallicities are also far greater than observed in immature late-type progenitors at high redshift (Phillipps & Edmunds, 1996). To resolve this, we have applied to use MUSE (Multi Unit Spectroscopic Explorer) on the VLT (Very Large Telescope) to obtain resolved optical spectroscopy for these galaxies. As well as informing the value of X_{CO}, resolved metallicities will indicate the chemical evolution of these young systems, and the manner which they are assembling themselves.

Another explanation for the apparent lack of molecular gas in these galaxies is that a larger than usual fraction of their ISM is in the hot dense phase (compared to normal spirals), and so is poorly traced by ^{12}CO(2-1) observations. To answer this question, we have applied to use the SHFI (Swedish Heterodyne Facility Instrument, Vassilev et al., 2008) instrument on APEX (the Atacama Pathfinder Experiment) to observe the ^{12}CO(3-2) transition in these galaxies. Note, however, that it would be surprising if so little of these system's molecular gas is cold, given how cold their dust is.

High-resolution 21 cm mapping of selected HAPLESS galaxies is currently being carried out with the Very Large Array (VLA, $14''$ resolution at 21 cm in 'C' configuration) and Giant Metre-wave Radio Telescope (GMRT, $3''$ resolution at 21 cm), to reveal their distribution of atomic hydrogen; at present, most of the galaxies in our sample only have unresolved Parkes or Arecibo coverage available. In combination with the IRAM and APEX observations, this will allow us to investigate the conditions in these systems' atomic-to-molecular transition.

Whilst replete with fascinating objects, HAPLESS is still a relatively small sample, consisting of only 42 sources, compared to the 323 and 234 galaxies in the HRS and *Planck* C13N13 surveys. However, this work only used the 161.6 $\deg^2$ of the *H*-ATLAS Phase-1 data. The full *H*-ATLAS dataset consists of almost 600 $\deg^2$ of coverage, an area $\approx$3.5 times greater. Combined with ongoing improvements

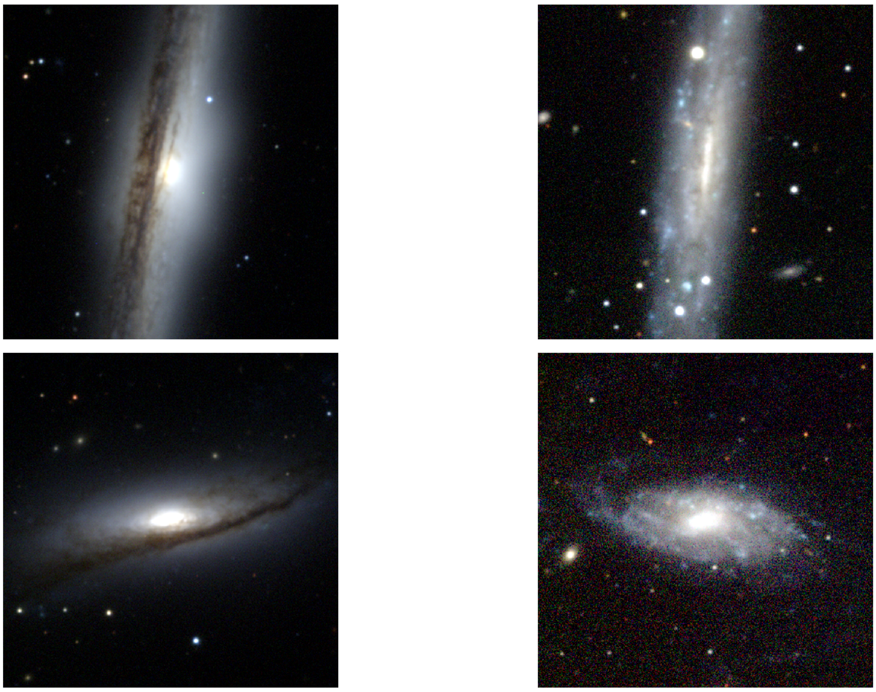

FIGURE 8.1 Optical SDSS *gri*-band imagery of 4 of the HAPLESS galaxies. The galaxies on the left, NGC 5746 and NGC 5719 (HAPLESS 21 and 20), are two of the most dust-poor HAPLESS objects, and yet have very prominent dust lanes; the galaxies on the right, UGC 9299 and NGC 5496 (HAPLESS 9 and 7) are approximately 25 times more dust rich, and yet visual inspection shows very little evidence for extinction. Each image is 150″ across.

to the source-extraction process (Maddox et al., *in prep.*), a local galaxy sample created using all of *H*-ATLAS should be expected to contain 150–200 sources – making it one of the largest surveys of dust in nearby galaxies. A particular benefit of conducting follow-up work using the entire 600 deg^2 of *H*-ATLAS would be a massive reduction in the influence of cosmic variance, allowing for a far more exact determination of the dust mass volume density of the local Universe.

An especially interesting result of this work is the apparent correlation between dust-richness ($M_d/M_\star$), and *lack* of absorption by dust, as detailed in Chapter 6. This can actually be seen from visual inspection of our galaxies. On the left of Figure 8.1, two of the most dust-poor HAPLESS galaxies, NGC 5746 and NGC 5719 (HAPLESS 21 and 20), are displayed; they have $M_d/M_\star$ of 4.4×10^{-4} and 4.1×10^{-4} respectively. But despite being so dust-poor, they have very prominent dust lanes, easily visible in these images. On the right of Figure 8.1 two of the very blue immature HAPLESS galaxies, UGC 9299 and NGC 5496 (HAPLESS 9 and 7), are shown; they have $M_d/M_\star$ of 0.012 and 0.007, approximately 25 times greater than in the galaxies on the left. But despite being so dust-rich, these galaxies show very little evidence for dust in extinction. In the future, I would be keen to carry out resolved SED-fitting to map out the dust mass distribution in these galaxies, to determine if this trend between dust-richness and lack of absorption carries on to a local level. The resulting temperature maps of these galaxies would also be valuable. Fitting the integrated SEDs of the very blue HAPLESS galaxies indicated dust temperatures of only 12–14 K (see Chapter 5) – however, these are global values. There must therefore be regions in these systems that are even colder than that. Resolved temperature maps would allow me to identify these very cold regions, and constrain the physical conditions there – some of the most unusual dusty environments yet discovered.

BIBLIOGRAPHY

Abazajian K. N. et al., 2009, ApJS, 182, 543

Acharova I. A., Mishurov Y. N., Kovtyukh V. V., 2012, MNRAS, 420, 1590

Ade P. A. R., Pisano G., Tucker C., Weaver S., 2006, in Society of Photo-Optical Instrumentation Engineers (SPIE) Conference Series, Vol. 6275, Society of Photo-Optical Instrumentation Engineers (SPIE) Conference Series

Adelman-McCarthy J. K. et al., 2008, ApJS, 175, 297

Ahn C. P. et al., 2012, ApJS, 203, 21

Aller H. D., Reynolds S. P., 1985, ApJ, 293, L73

André P., Basu S., Inutsuka S., 2009, The formation and evolution of prestellar cores, Chabrier G., ed., Cambridge University Press, p. 254

Andrews S. K., Kelvin L. S., Driver S. P., Robotham A. S. G., 2014, PASA, 31, 4

Astropy Collaboration et al., 2013, A&A, 558, A33

Auld R. et al., 2013, MNRAS, 428, 1880

Bacon F., 1626, Sylva Sylvarum. London

Baillard A. et al., 2011, A&A, 532, A74

Baldry I. K. et al., 2012, MNRAS, 421, 621

Bandiera R., Neri R., Cesaroni R., 2002, A&A, 386, 1044

Barlow M. J., 1978, MNRAS, 183, 367

Barlow M. J. et al., 2010, A&A, 518, L138

Barlow M. J. et al., 2013, Science, 342, 1343

Barnes J. E., Hernquist L., 1992, ARA&A, 30, 705

Bauer A. E. et al., 2013, MNRAS, 434, 209

Bendo G. J. et al., 2012, MNRAS, 419, 1833

Bendo G. J. et al., 2013, MNRAS, 433, 3062

Bendo G. J. et al., 2010, A&A, 518, L65

Bertin E., Arnouts S., 1996, A&AS, 117, 393

Binggeli B., Sandage A., Tammann G. A., 1985, AJ, 90, 1681

Blair W., Borkowski K., Ghavamian P., Long K., Reynolds S., Sankrit R., 2004, Spitzer Proposal, 3413

Blair W. P., Ghavamian P., Long K. S., Williams B. J., Borkowski K. J., Reynolds S. P., Sankrit R., 2007, ApJ, 662, 998

Blanton M. R. et al., 2001, AJ, 121, 2358

Bohren C. F., Huffman D. R., 1983, Absorption and scattering of light by small particles

Boquien M. et al., 2011, AJ, 142, 111

Borkowski K. J., Sarazin C. L., Blondin J. M., 1994, ApJ, 429, 710

Boselli A., Cortese L., Boquien M., 2014a, A&A, 564, A65

Boselli A., Cortese L., Boquien M., Boissier S., Catinella B., Lagos C., Saintonge A., 2014b, A&A, 564, A66

Boselli A. et al., 2010, PASP, 122, 261

Bottinelli L., Gouguenheim L., Fouque P., Paturel G., 1990, A&AS, 82, 391

Bourne N. et al., 2012, MNRAS, 421, 3027

Buat V. et al., 2008, A&A, 483, 107

Buat V., Giovannoli E., Takeuchi T. T., Heinis S., Yuan F.-T., Burgarella D., Noll S., Iglesias-Páramo J., 2011, A&A, 529, A22

Buat V. et al., 2012, A&A, 545, A141

Buat V. et al., 2007, ApJS, 173, 404

Buitrago F., Trujillo I., Conselice C. J., Häußler B., 2013, MNRAS, 428, 1460

Bunker A., Spinrad H., Stern D., Thompson R., Moustakas L., Davis M., Dey A., 2000, ArXiv Astrophysics e-prints

Cai Z.-Y., Yang J., Lu D.-R., 2009, Chinese Astronomy and Astrophysics, 33, 393

Calanog J. A. et al., 2013, ApJ, 775, 61

Calvi R., Poggianti B. M., Fasano G., Vulcani B., 2012, MNRAS, 419, L14

Calzetti D. et al., 2005, ApJ, 633, 871

Casey C. M. et al., 2014, ArXiv e-prints

Catinella B., Schiminovich D., Kauffmann G., 2008, in American Institute of Physics Conference Series, Vol. 1035, The Evolution of Galaxies Through the Neutral Hydrogen Window, Minchin R., Momjian E., eds., pp. 252–255

Catinella B. et al., 2012, A&A, 544, A65

Catinella B. et al., 2010, MNRAS, 403, 683

Chabrier G., 2003, PASP, 115, 763

Ciesla L. et al., 2014, A&A, 565, A128

Ciesla L. et al., 2012, A&A, 543, A161

Clayton D. D., Deneault E. A.-N., Meyer B. S., 2001, ApJ, 562, 480

Clemens M. S. et al., 2013, MNRAS, 433, 695

Cluver M. E. et al., 2014, ApJ, 782, 90

Colless M. et al., 2003, ArXiv Astrophysics e-prints

Combes F., 2007, in IAU Symposium, Vol. 235, IAU Symposium, Combes F., Palouš J., eds., pp. 19–23

Conselice C. J., Blackburne J. A., Papovich C., 2005, ApJ, 620, 564

Cortese L. et al., 2012a, A&A, 544, A101

Cortese L. et al., 2012b, A&A, 540, A52

Cortese L. et al., 2014, MNRAS, 440, 942

Courtois H. M., Tully R. B., Makarov D. I., Mitronova S., Koribalski B., Karachentsev I. D., Fisher J. R., 2011, MNRAS, 414, 2005

Cowie L. L., Songaila A., Hu E. M., Cohen J. G., 1996, AJ, 112, 839

Crossley J. H., Sjouwerman L. O., Fomalont E. B., Radziwill N. M., 2007, in Bulletin of the American Astronomical Society, Vol. 39, American Astronomical Society Meeting Abstracts, p. 132.03

Croton D. J. et al., 2006, MNRAS, 365, 11

da Cunha E., Charlot S., Elbaz D., 2008, MNRAS, 388, 1595

Davis L. E., Seaquist E. R., 1983, ApJS, 53, 269

de Graauw T. et al., 2010, A&A, 518, L6

DeLaney T., Koralesky B., Rudnick L., Dickel J. R., 2002, ApJ, 580, 914

Delgado-Inglada G., Rodríguez M., García-Rojas J., Peña M., Ruiz M. T., 2011, in Revista Mexicana de Astronomia y Astrofisica, vol. 27, Vol. 40, Revista Mexicana de Astronomia y Astrofisica Conference Series, pp. 165–166

Demyk K. et al., 2001, A&A, 368, L38

Demyk K. et al., 2013, in Proceedings of The Life Cycle of Dust in the Universe: Observations, Theory, and Laboratory Experiments (LCDU2013). 18-22 November, 2013. Taipei, Taiwan.

Denissenkov P. A., Herwig F., Truran J. W., Paxton B., 2013, ApJ, 772, 37

Devereux N. A., Young J. S., 1990, ApJ, 350, L25

Dey A. et al., 2008, ApJ, 677, 943

Di Criscienzo M. et al., 2013, MNRAS, 433, 313

D'Onghia E., Vogelsberger M., Hernquist L., 2013, ApJ, 766, 34

Draine B. T., 2009, in Astronomical Society of the Pacific Conference Series, Vol. 414, Cosmic Dust - Near and Far, Henning T., Grün E., Steinacker J., eds., p. 453

Draine B. T., Lee H. M., 1984, ApJ, 285, 89

Draine B. T., Salpeter E. E., 1979, ApJ, 231, 438

Dressler A., 1980, ApJ, 236, 351

Driver S. P., Allen P. D., Liske J., Graham A. W., 2007a, ApJ, 657, L85

Driver S. P. et al., 2011, MNRAS, 413, 971

Driver S. P., Liske J., Cross N. J. G., De Propris R., Allen P. D., 2005, MNRAS, 360, 81

Driver S. P. et al., 2009, Astronomy and Geophysics, 50, 050000

Driver S. P., Popescu C. C., Tuffs R. J., Liske J., Graham A. W., Allen P. D., de Propris R., 2007b, MNRAS, 379, 1022

Driver S. P., Robotham A. S. G., 2010, MNRAS, 407, 2131

Driver S. P., Robotham A. S. G., Bland-Hawthorn J., Brown M., Hopkins A., Liske J., Phillipps S., Wilkins S., 2013, MNRAS, 430, 2622

Dunne L., 2013, in Proceedings of The Life Cycle of Dust in the Universe: Observations, Theory, and Laboratory Experiments (LCDU2013). 18-22 November, 2013. Taipei, Taiwan.

Dunne L., Eales S., Edmunds M., Ivison R., Alexander P., Clements D. L., 2000, MNRAS, 315, 115

Dunne L., Eales S., Ivison R., Morgan H., Edmunds M., 2003, Nature, 424, 285

Dunne L., Eales S. A., 2001, MNRAS, 327, 697

Dunne L. et al., 2011, MNRAS, 417, 1510

Dunne L. et al., 2009, MNRAS, 394, 1307

Dwek E., 1998, in Astronomical Society of the Pacific Conference Series, Vol. 133, Science With The NGST, Smith E. P., Koratkar A., eds., p. 249

Dwek E., 2004, ApJ, 607, 848

Dwek E., Cherchneff I., 2011, ApJ, 727, 63

Dwek E., Galliano F., Jones A. P., 2007, ApJ, 662, 927

Dwek E., Scalo J. M., 1980, ApJ, 239, 193

Eales S. et al., 2010, PASP, 122, 499

Eales S. et al., 2012, ApJ, 761, 168

Eales S. A., Edmunds M. G., 1996, MNRAS, 280, 1167

Eales S. A., Edmunds M. G., 1997, MNRAS, 286, 732

Eddington A. S., 1913, MNRAS, 73, 359

Edge A., Sutherland W., 2013, VIKING (VISTA Kilo-degree Infrared Galaxy Survey Data Release 1. Tech. rep., ESO

Edge A., Sutherland W., Kuijken K., Driver S., McMahon R., Eales S., Emerson J. P., 2013, The Messenger, 154, 32

Ferrarotti A. S., Gail H.-P., 2006, A&A, 447, 553

Fesen R. A. et al., 2006, ApJ, 645, 283

Fitzpatrick E. L., 1999, PASP, 111, 63

Fitzpatrick E. L., 2004, in Astronomical Society of the Pacific Conference Series, Vol. 309, Astrophysics of Dust, Witt A. N., Clayton G. C., Draine B. T., eds., p. 33

Fontanot F., De Lucia G., Monaco P., Somerville R. S., Santini P., 2009, MNRAS, 397, 1776

Ford G. P. et al., 2013, ApJ, 769, 55

Foyle K. et al., 2013, MNRAS, 432, 2182

Galametz M. et al., 2012, MNRAS, 425, 763

Galametz M. et al., 2013, MNRAS, 431, 1956

Gall C., Andersen A. C., Hjorth J., 2011, A&A, 528, A14

Gil de Paz A. et al., 2007, ApJS, 173, 185

Giovanelli R. et al., 2005, AJ, 130, 2598

Glazebrook K., 2013, PASA, 30, 56

Gomez H., 2013, in Proceedings of The Life Cycle of Dust in the Universe: Observations, Theory, and Laboratory Experiments (LCDU2013). 18-22 November, 2013. Taipei, Taiwan.

Gomez H., Dunne L., Eales S., Gomez E., Edmunds M., 2005, Monthly Notices of the Royal Astronomical Society, 361

Gomez H. L. et al., 2010, A&A, 518, L45

Gomez H. L. et al., 2012a, MNRAS, 420, 3557

Gomez H. L. et al., 2009, MNRAS, 397, 1621

Gomez H. L. et al., 2012b, ApJ, 760, 96

Gordon K. D., 2005, in American Institute of Physics Conference Series, Vol. 761, The Spectral Energy Distributions of Gas-Rich Galaxies: Confronting Models with Data, Popescu C. C., Tuffs R. J., eds., pp. 134–140

Gordon K. D., Clayton G. C., Misselt K. A., Landolt A. U., Wolff M. J., 2003, ApJ, 594, 279

Gould R. J., Salpeter E. E., 1963, ApJ, 138, 393

Green D. A., 2001, in American Institute of Physics Conference Series, Vol. 558, American Institute of Physics Conference Series, Aharonian F. A., Völk H. J., eds., pp. 59–70

Green D. A., Tuffs R. J., Popescu C. C., 2004, MNRAS, 355, 1315

Griffin M. et al., 2008, in Society of Photo-Optical Instrumentation Engineers (SPIE) Conference Series, Vol. 7010, Society of Photo-Optical Instrumentation Engineers (SPIE) Conference Series, p. 6

Griffin M. J. et al., 2010, A&A, 518, L3

Griffin M. J. et al., 2013, MNRAS, 434, 992

Groenewegen M. A. T. et al., 2011, A&A, 526, A162

Grossi M. et al., 2010, A&A, 518, L52

Guo Q. et al., 2014, MNRAS, 442, 2253

Hao C.-N., Kennicutt R. C., Johnson B. D., Calzetti D., Dale D. A., Moustakas J., 2011, ApJ, 741, 124

Haynes M. P. et al., 2011, AJ, 142, 170

Heavens A., Panter B., Jimenez R., Dunlop J., 2004, Nature, 428, 625

Herschel W., 1811, Royal Society of London Philosophical Transactions Series I, 101, 269

Hester J. J., 2008, ARA&A, 46, 127

Hill D. T. et al., 2011, MNRAS, 412, 765

Hirashita H., Buat V., Inoue A. K., 2003, A&A, 410, 83

Hopkins A. M., Beacom J. F., 2006, ApJ, 651, 142

Hopkins P. F., Bundy K., Hernquist L., Ellis R. S., 2007, ApJ, 659, 976

Hughes D. H. et al., 1998, Nature, 394, 241

Hughes J. P., 1999, ApJ, 527, 298

Hughes T. M. et al., 2014, A&A, 565, A4

Hunter J. D., 2007, Computing In Science & Engineering, 9, 90

Ibar E. et al., 2010, MNRAS, 409, 38

Ibar E. et al., 2013, MNRAS, 434, 3218

Impey C., Burkholder V., Sprayberry D., 2001, AJ, 122, 2341

Indebetouw R. et al., 2014, ApJ, 782, L2

Inoue A. K., Buat V., Burgarella D., Panuzzo P., Takeuchi T. T., Iglesias-Páramo J., 2006, MNRAS, 370, 380

Irwin M., 2010, "UKIRT Newsletter", 26, 14

James A., Dunne L., Eales S., Edmunds M. G., 2002, MNRAS, 335, 753

Jarrett T. H., Chester T., Cutri R., Schneider S., Skrutskie M., Huchra J. P., 2000, AJ, 119, 2498

Jarrett T. H. et al., 2013, AJ, 145, 6

Jenkins E., 2013, in Proceedings of The Life Cycle of Dust in the Universe: Observations, Theory, and Laboratory Experiments (LCDU2013). 18-22 November, 2013. Taipei, Taiwan.

Jenkins E. B., 2009, ApJ, 700, 1299

Jensen A. G., Snow T. P., 2007, ApJ, 669, 378

Jones A., 2013, in Proceedings of The Life Cycle of Dust in the Universe: Observations, Theory, and Laboratory Experiments (LCDU2013). 18-22 November, 2013. Taipei, Taiwan.

Jones A. P., 2004, in Astronomical Society of the Pacific Conference Series, Vol. 309, Astrophysics of Dust, Witt A. N., Clayton G. C., Draine B. T., eds., p. 347

Jones A. P., Nuth J. A., 2011, A&A, 530, A44

Jones A. P., Tielens A. G. G. M., Hollenbach D. J., 1996, ApJ, 469, 740

Jones A. P., Tielens A. G. G. M., Hollenbach D. J., McKee C. F., 1994, ApJ, 433, 797

Kamenetzky J. et al., 2013, ApJ, 773, L34

Kapteyn J. C., 1909, Contributions from the Mount Wilson Observatory / Carnegie Institution of Washington, 31, 1

Kelly B. C., Shetty R., Stutz A. M., Kauffmann J., Goodman A. A., Launhardt R., 2012, ApJ, 752, 55

Kennicutt R. C. et al., 2011, PASP, 123, 1347

Kennicutt R. C., Evans N. J., 2012a, ARA&A, 50, 531

Kennicutt R. C., Evans N. J., 2012b, ARA&A, 50, 531

Kennicutt, Jr. R. C., 1998, ApJ, 498, 541

Kennicutt, Jr. R. C. et al., 2009, ApJ, 703, 1672

Kepler J., 1606, De Stella Nova in Pede Serpentarii. Prague

Kim S.-H., Martin P. G., 1994, ApJ, 431, 783

Kim S.-H., Martin P. G., Hendry P. D., 1994, ApJ, 422, 164

Kirchhoff G., 1860, Annalen der Physik, 185, 275

Kirkpatrick A. et al., 2013, ApJ, 778, 51

Kirkpatrick A. et al., 2014, ApJ, 789, 130

Krause O., Birkmann S. M., Rieke G. H., Lemke D., Klaas U., Hines D. C., Gordon K. D., 2004, Nature, 432, 596

Krause O., Tanaka M., Usuda T., Hattori T., Goto M., Birkmann S., Nomoto K., 2008, Nature, 456, 617

Kroupa P., 2001, MNRAS, 322, 231

Ladjal D. et al., 2010, A&A, 518, L141

Law K.-H., Gordon K. D., Misselt K. A., 2011, ApJ, 738, 124

Lawrence A. et al., 2007, MNRAS, 379, 1599

Lee J. C. et al., 2009, ApJ, 706, 599

Liddle A., 2003, An Introduction to Modern Cosmology, Second Edition

Linde A. D., 1982, Physics Letters B, 108, 389

Liske J., Lemon D. J., Driver S. P., Cross N. J. G., Couch W. J., 2003, MNRAS, 344, 307

Loveday J., Peterson B. A., Efstathiou G., Maddox S. J., 1992, ApJ, 390, 338

Macías-Pérez J. F., Mayet F., Aumont J., Désert F.-X., 2010, ApJ, 711, 417

Madau P., Dickinson M., 2014, ARA&A, 52, 415

Maddox S. J. et al., 2010, A&A, 518, L11

Maeder A., 1992, A&A, 264, 105

Maguire K. et al., 2013, MNRAS, 436, 222

Markaryan B. E., Lipovetskii V. A., Stepanyan D. A., 1979, Astrophysics, 15, 363

Matsuura M. et al., 2009, MNRAS, 396, 918

Matsuura M. et al., 2011, Science, 333, 1258

Meyer M. J. et al., 2004, MNRAS, 350, 1195

Mihos J. C., Hernquist L., 1994, ApJ, 431, L9

Miyaji S., Nomoto K., Yokoi K., Sugimoto D., 1980, PASJ, 32, 303

Monfardini A. et al., 2014, Journal of Low Temperature Physics, 176, 787

Morgan H. L., Dunne L., Eales S. A., Ivison R. J., Edmunds M. G., 2003, ApJ, 597, L33

Morgan H. L., Edmunds M. G., 2003, MNRAS, 343, 427

Morrissey P. et al., 2007, ApJS, 173, 682

Negrello M. et al., 2013, MNRAS, 429, 1309

Neistein E., van den Bosch F. C., Dekel A., 2006, MNRAS, 372, 933

Neugebauer G. et al., 1984, ApJ, 278, L1

Nielsen M. T. B., Nelemans G., Voss R., Toonen S., 2014, A&A, 563, A16

Noeske K. G. et al., 2007a, ApJ, 660, L47

Noeske K. G. et al., 2007b, ApJ, 660, L43

Nomoto K., Tominaga N., Umeda H., Kobayashi C., Maeda K., 2006, Nuclear Physics A, 777, 424

Nozawa T., Maeda K., Kozasa T., Tanaka M., Nomoto K., Umeda H., 2011, ApJ, 736, 45

Ochsenbein F., Bauer P., Marcout J., 2000, A&AS, 143, 23

Oliver S. J. et al., 2012, MNRAS, 424, 1614

Osterbrock D. E., Dahari O., 1983, ApJ, 273, 478

Overcast W. C., 2010, Master's thesis, University of Tennessee, Knoxville

Pascale E. et al., 2011, MNRAS, 415, 911

Patton D. R., Torrey P., Ellison S. L., Mendel J. T., Scudder J. M., 2013, MNRAS, 433, L59

Peng Y.-j., Lilly S. J., Renzini A., Carollo M., 2014, ApJ, 790, 95

Phillipps S., Driver S. P., Couch W. J., Smith R. M., 1998, ApJ, 498, L119

Phillipps S., Edmunds M. G., 1996, MNRAS, 281, 362

Pier J. R., Munn J. A., Hindsley R. B., Hennessy G. S., Kent S. M., Lupton R. H., Ivezić Ž., 2003, AJ, 125, 1559

Pilbratt G. L. et al., 2010, A&A, 518, L1

Planck Collaboration et al., 2014a, A&A, 564, A45

Planck Collaboration et al., 2014b, A&A, 564, A45

Planck Collaboration et al., 2013, ArXiv e-prints

Planck Collaboration et al., 2011a, A&A, 536, A1

Planck Collaboration et al., 2011b, A&A, 536, A7

Poglitsch A. et al., 2010, A&A, 518, L2

Popescu C. C., Tuffs R. J., 2002, in Reviews in Modern Astronomy, Vol. 15, Reviews in Modern Astronomy, Schielicke R. E., ed., p. 239

Popping A., Braun R., 2011, A&A, 528, A28

Prantzos N., Vangioni-Flam E., Cassé M., 1993, Origin and evolution of the elements. Proceedings.

Reach W. T., Rho J., 1999, ApJ, 511, 836

Rémy-Ruyer A. et al., 2013, A&A, 557, A95

Reynolds S. P., Borkowski K. J., Hwang U., Hughes J. P., Badenes C., Laming J. M., Blondin J. M., 2007, ApJ, 668, L135

Reynoso E. M., Velázquez P. F., Dubner G. M., Goss W. M., 1999, AJ, 117, 1827

Rho J., Reach W. T., Tappe A., Hwang U., Slavin J. D., Kozasa T., Dunne L., 2009, ApJ, 700, 579

Riaz B., Mullan D. J., Gizis J. E., 2006, ApJ, 650, 1133

Richards G. T. et al., 2006, AJ, 131, 2766

Rieke G. H., Alonso-Herrero A., Weiner B. J., Pérez-González P. G., Blaylock M., Donley J. L., Marcillac D., 2009, ApJ, 692, 556

Riess A. G. et al., 2011, ApJ, 730, 119

Rigby E. E. et al., 2011, MNRAS, 415, 2336

Robotham A. S. G., Driver S. P., 2011, MNRAS, 413, 2570

Rouleau F., Martin P. G., 1991, ApJ, 377, 526

Roussel H., 2013, PASP, 125, 1126

Rowan-Robinson M., Crawford J., 1989, MNRAS, 238, 523

Rowlands K. et al., 2014a, MNRAS, 441, 1017

Rowlands K., Dunne L., Maddox S., Maddox, 2012, in IAU Symposium, Vol. 284, IAU Symposium, Tuffs R. J., Popescu C. C., eds., pp. 259–261

Rowlands K., Gomez H. L., Dunne L., Aragón-Salamanca A., Dye S., Maddox S., da Cunha E., Werf P. v. d., 2014b, MNRAS, 441, 1040

Saken J. M., Fesen R. A., Shull J. M., 1992, ApJS, 81, 715

Salzer J. J., 1992, AJ, 103, 385

Sanders D. B., Mazzarella J. M., Kim D.-C., Surace J. A., Soifer B. T., 2003, AJ, 126, 1607

Sargent B. A. et al., 2010, ApJ, 716, 878

Saunders W. et al., 2000, MNRAS, 317, 55

Schaefer B. E., Pagnotta A., 2012, Nature, 481, 164

Schaller G., Schaerer D., Meynet G., Maeder A., 1992, A&AS, 96, 269

Schechter P., 1976, ApJ, 203, 297

Schiminovich D. et al., 2010, MNRAS, 408, 919

Schlegel D. J., Finkbeiner D. P., Davis M., 1998, ApJ, 500, 525

Schmidt M., 1968, ApJ, 151, 393

Schneider S. E., Thuan T. X., Magri C., Wadiak J. E., 1990, ApJS, 72, 245

Shetty R., Kauffmann J., Schnee S., Goodman A. A., 2009, ApJ, 696, 676

Silverman J. M. et al., 2013, ApJS, 207, 3

Skibba R. A. et al., 2011, ApJ, 738, 89

Smith D. J. B. et al., 2012a, MNRAS, 427, 703

Smith D. J. B. et al., 2011, MNRAS, 416, 857

Smith D. J. B. et al., 2013, MNRAS, 436, 2435

Smith M. W. L. et al., 2012b, ApJ, 756, 40

Smith M. W. L. et al., 2012c, ApJ, 748, 123

Springel V., Di Matteo T., Hernquist L., 2005, MNRAS, 361, 776

Starobinskii A. A., 1978, Soviet Astronomy Letters, 4, 82

Stevens J. B., Webster R. L., Barnes D. G., Pisano D. J., Drinkwater M. J., 2004, Publications of the Astronomical Society of Australia, 21, 318

Stoughton C. et al., 2002, AJ, 123, 485

Struve F. G. W., 1847, Etudes d'Astronomie Stellaire : Sur la voie lactee et sur la distance des etoiles fixes

Sulentic J. W., Arp H., 1983, AJ, 88, 489

Swinyard B., Wild W., 2010, ISSI Scientific Reports Series, 9, 241

Tabatabaei F. S. et al., 2014, A&A, 561, A95

Takahashi K., Yoshida T., Umeda H., 2013, ApJ, 771, 28

Taylor C. L., Brinks E., Grashuis R. M., Skillman E. D., 1995, ApJS, 99, 427

Taylor M. B., 2005, in Astronomical Society of the Pacific Conference Series, Vol. 347, Astronomical Data Analysis Software and Systems XIV, Shopbell P., Britton M., Ebert R., eds., p. 29

Temim T., Dwek E., 2013, ApJ, 774, 8

Temim T. et al., 2006, AJ, 132, 1610

Temim T., Sonneborn G., Dwek E., Arendt R. G., Gehrz R. D., Slane P., Roellig T. L., 2012, ArXiv e-prints

Tielens A. G. G. M., Allamandola L. J., 1987, in Astrophysics and Space Science Library, Vol. 134, Interstellar Processes, Hollenbach D. J., Thronson Jr. H. A., eds., pp. 397–469

Tinsley B. M., 1980, Fund. Cosmic Phys., 5, 287

Todini P., Ferrara A., 2001, MNRAS, 325, 726

Tonry J. L., Blakeslee J. P., Ajhar E. A., Dressler A., 2000, ApJ, 530, 625

Tonry J. L., Dressler A., Blakeslee J. P., Ajhar E. A., Fletcher A. B., Luppino G. A., Metzger M. R., Moore C. B., 2001, ApJ, 546, 681

Tout C. A., 2005, in Astronomical Society of the Pacific Conference Series, Vol. 330, The Astrophysics of Cataclysmic Variables and Related Objects, Hameury J.-M., Lasota J.-P., eds., p. 279

Trimble V., 1968, AJ, 73, 535

Trumpler R. J., 1930, Lick Observatory Bulletin, 14, 154

Tuffs R. J., Popescu C. C., 2005, in American Institute of Physics Conference Series, Vol. 761, The Spectral Energy Distributions of Gas-Rich Galaxies: Confronting Models with Data, Popescu C. C., Tuffs R. J., eds., pp. 344–363

Tycho B., 1573, De Nova et Nullius Aevi Memoria Prius Visa Stella. Copenhagen

Vaccari M. et al., 2010, A&A, 518, L20

Valiante E., Lutz D., Sturm E., Genzel R., Chapin E. L., 2009, ApJ, 701, 1814

van den Hoek L. B., Groenewegen M. A. T., 1997, A&AS, 123, 305

Vassilev V. et al., 2008, A&A, 490, 1157

Ventura P. et al., 2012, MNRAS, 424, 2345

Vlahakis C., Dunne L., Eales S., 2005, MNRAS, 364, 1253

Walt S. v. d., Colbert S. C., Varoquaux G., 2011, Computing in Science & Engineering, 13

Warren J. S. et al., 2005, ApJ, 634, 376

Wenger M. et al., 2000, A&AS, 143, 9

Werner M. W. et al., 2004, ApJS, 154, 1

Whittet D. C. B., 1992, Dust in the galactic environment

Wong O. I. et al., 2006, MNRAS, 371, 1855

Woosley S. E., Heger A., 2007, Phys. Rep., 442, 269

Woosley S. E., Weaver T. A., 1995, ApJS, 101, 181

Wootten A., Thompson A. R., 2009, IEEE Proceedings, 97, 1463

Wright E. L., 2006, PASP, 118, 1711

Wright E. L. et al., 2010, AJ, 140, 1868

Yang W., 1054, Song Huiyao. Bianjing (Kaifeng)

Yin J., Hou J. L., Prantzos N., Boissier S., Chang R. X., Shen S. Y., Zhang B., 2009, A&A, 505, 497

York D. G. et al., 2000, AJ, 120, 1579

Zibetti S., Charlot S., Rix H.-W., 2009, MNRAS, 400, 1181

Zubko V. G., Mennella V., Colangeli L., Bussoletti E., 1996, MNRAS, 282, 1321

Zwaan M. A. et al., 2004, MNRAS, 350, 1210

‘This too shall pass.’

OLD PERSIAN SAYING